STRUCTURE-PROPERTY RELATIONSHIPS IN DE VRIES SMECTIC A LIQUID CRYSTALS*

by

MARK JAMES CONROY MORAN

B.Sc., Queen's University, 2004

M.Sc., Queen's University, 2007

A thesis submitted to the

Faculty of the Graduate School of the

University of Colorado in partial fulfillment

of the requirement for the degree of

Doctor of Philosophy

Department of Chemistry and Biochemistry

2015

signature page

This thesis entitled:
Structure-Property Relationships in de Vries Smectic A* Liquid Crystals
written by Mark James Conroy Moran
has been approved for the Department of Chemistry and Biochemistry

(Professor David M. Walba)

(Professor Joseph E. Maclennan)

Date______________

The final copy of this thesis has been examined by the signatories, and we
Find that both the content and the form meet acceptable presentation standards
Of scholarly work in the above mentioned discipline.

Abstract

Moran, Mark James Conroy (Ph.D., Chemistry)

Structure-Property Relationships in de Vries Smectic A liquid Crystals

Thesis directed by Professor David M. Walba

Liquid crystals (LCs) have become inextricably linked with the display industry in recent years. As screen sizes increase the response time of the LC must decrease to maintain picture quality. A rare subset of the chiral smectic A (SmA*) , known as the de Vries SmA* phase, shows fast switching times, large electroclinic tilts, native gray-scale and small layer shrinkage when driven by an electric field, making it an attractive alternative to SmC* materials for next-generation displays. The de Vries SmA* phase is typically formed by molecules with one or more tails that strongly suppress out-of-layer fluctuations.

The first part of this thesis describes a set of mesogens with four different liquid crystalline cores built on a scaffold possessing a phenyl and biphenyl moiety linked by an ester with two peripheral alkoxy side-chains (tails). One side-chain is the (*S*)-1-methylheptyloxy group ortho to a trifluoromethyl group. The second side chain is varied between an n-alkoxy-, n-alkenyloxy- and semifluorinated tails, all of the same length. The latter two tails have been shown to suppress out-of-layer fluctuations. Only the LCs built on the hydroquinone stereopolar unit (**W652/W657/W530**) show the desired liquid crystalline phases (SmA* and SmC*) over a convenient temperature range. Surprisingly, **W652**, which possesses no strong out-of-layer suppressing group, shows the de Vries SmA* phase, suggesting the core may be as important as the tails in the design of de Vries smecticss.

The second part of this thesis develops structure-property relationships of compounds built on the hydroquinone stereopolar unit, which is particularly good at promoting the de Vries SmA* phase. The set of lateral polar groups (H, Me, Cl, CF_3 or NO_2) and achiral tails were varied. The effect on the width of the SmA* phases, the clearing point, saturated electroclinic tilt, layer shrinkage from SmA* to SmC* and spontaneous polarization in the SmC* phase were examined. Materials with a large electronegative lateral polar group and strongly out-of-layer suppressing tails give the most desirable properties.

Acknowledgements

I would like to thank Dr. Dave Walba for his support, patience and guidance. Additionally, I would like to thank Dr. Noel Clark, Dr. Matt Glaser and Dr. Joseph Maclennan for their insight and fruitful conversations.

I would like to acknowledge the talent group of scientists with whom I have worked. From the Department of Chemistry: Dr. Rebecca Callahan, Eric Carlson, Dr. Tao Gong, Eduard Guzman, Dr. Nan Hu, Lee Foley, Dr. Maria Kolber, Dr. Eva Korblova, Dr. Jan Porada, Dr. Jacquie Richardson, Timothy Rochelle, Alyssa Scarborough, Dr. Michael Springer, Dr. Ethan Tsai, Dayan Wei, Dr. Hong Yang. From the Department of Physics: Art Klittnick, Dr. Duong Nguyen, Dr. Cheol Park, Dr. Yongqiang Shen, Renfan Shao, Greg Smith, Michael Tuchband, Rayshan Visvanathan, Dr. Chenhui Zhu. Finally, international collaborators: Dr. Tomasso Bellini, Dr. Edgardo Garcia, Dr. Patrick Keller, Dr. Dong Ki Yoon.

Special thanks to Dr. Rich Shoemaker, our NMR guru, for his assistance in characterization of materials.

I'd like to thank all of the staff associated with the Soft Matter Materials Research Center, in particular Christine Morrow and Annette Baumgartner.

Finally, I'd like to thank my parents Gordon and Margaret Ann for their unconditional love and support.

Table of Contents

1. CHAPTER 1. INTRODUCTION I

1.1 Classifications of liquid crystals xviii

1.2 Calamitic liquid crystals xx

1.2.1 The nematic phase xx

1.2.2 The smectic A phase xxi

1.2.3 The de Vries SmA xxi

1.2.4 The smectic C phase xxii

1.3 Chiral phases xxiii

1.3.1 The cholesteric phase xxiii

1.3.2 The chiral smectic A phase xxiv

1.3.3 The chiral de Vries SmA phase xxv

1.3.4 The chiral smectic C phase xxvi

1.4 Techniques xxviii

1.4.1 Polarized Light Microscopy xxviii

1.4.2 Differential Scanning Calorimetry xxxi

1.5 References xxxiii

CHAPTER 2. OPTIMIZATION OF DE VRIES CORES XXXIV

2.1 Introduction xxxiv

2.2 Molecular origins of de Vries behaviour xxxvii

2.2.1 W530, W317 and W415 xxxvii

2.2.1.1 W530 xxxvii

2.2.1.2 W317 xxxix

2.2.1.3 W415 xli

2.3 Design principle & synthesis xlii

2.4 Core Optimization xlviii

2.4.1 Core A xlviii
2.4.1.1 W551 xlviii
2.4.1.2 W659 xlix
2.4.1.3 W667 li
2.4.2 Core B lii
2.4.2.1 W652 lii
2.4.2.2 W657 lvii
2.4.2.3 W530 lxi
2.4.3 Core C lxii
2.4.3.1 W558 lxii
2.4.3.2 W661 lxv
2.4.3.3 W668 lxvi
2.4.4 Core D lxvii
2.4.4.1 W665 lxvii
2.4.4.2 W666 lxvii
2.4.4.3 W669 lxviii
2.4.5 Conclusions lxxi
2.5 W705 lxxv
2.6 Synthesis lxxx
2.7 References xcviii
CHAPTER 3. EFFECT OF LATERAL SUBSTITUENT ON BULK PROPERTIES CI
3.1 Intro ci
3.2 Design and Synthesis cii
3.3 Effect of Hydrogen as Lateral Polar Group cvi
3.3.1 W697 cvi
3.3.2 W698 cx
3.3.3 W699 cxiii

3.4 Effect of Methyl as Lateral Polar Group .... **cxvi**

3.4.1 W733 cxvi

3.4.2 W734 cxix

3.4.3 W735 cxxii

3.5 Effect of Chloro as Lateral Polar Group .... **cxxv**

3.5.1 W713 cxxv

3.5.2 W714 cxxix

3.5.3 W715 cxxxiii

3.6 Effect of Nitro as Lateral Polar Group .... **cxxxvi**

3.6.1 W314 cxxxvi

3.6.2 W717 cxl

3.6.3 W718 cxlv

3.7 Trends .... **cxlix**

3.7.1 Effect of Lateral Polar Group and Tail on the Clearing Point cxlix

3.7.2 Effect of Lateral Polar Group and Tail on the Width of the SmA* Phase cli

3.7.3 Effect of Lateral Polar Group and Tail on the Saturated Electroclinic Tilt cliii

3.7.4 Summary of the Effect of Lateral Polar Group and Tail on the Birefringence clv

3.7.5 Summary of the Effect of Lateral Polar Group and Tail on the Spontaneous Polarization clvii

3.8 New Materials to Supplement this Work .... **clix**

3.9 Synthesis .... **clxi**

3.10 References .... **clxxix**

BIBLIOGRAPHY **163**

List of Figures

Figure 1.1: Common morphologies of lyotropic LCs. The concentration of water decreases from left to right. xix

Figure 1.2 Prototypical compounds of discotic, calamitic and bent-core liquid crystal compounds. xx

Figure 1.3 Idealized representation of the: (a) nematic (b) SmA and (c) SmC phase. The phases are more disordered than illustrated. xxi

Figure 1.4 The hollow cone representation of the de Vries SmA phase. The molecular long axes (n) are tilted, by an angle θ, with respect the layer normal (z). The azimuthal angle (ϕ) is disordered. xxii

Figure 1.5 Schematic representation of the highly polarizable core being more tilted (θ_{opt}) than the fully extended molecule ($\theta_{X\text{-}Ray}$) in the SmC phase. xxiii

Figure 1.6 Schematic represntation of the helical twist of the N* phase. xxiv

Figure 1.7 Schmatic representaion of the electroclinic effect. The application of an electric field to a SmA* phase, in a cell with bookshelf layer geometry, reduces symmetry and induces tilt. xxv

Figure 1.8 Representation of the electroclinic effect in the de Vries SmA* phase. With no electric field, E = 0 (left), the molecules are evenly distributed about the tilt cone, the optic axis (OA) is parallel to the layer normal and the birefringence is at a minimum. At small electric fields (centre) the molecules become biased to one side of the cone, tilting the OA and increasing the birefringence. At large E (right) the bias is increased and the phase becomes a field induced SmC* phase. The OA and birefringence become maxima; Ψ_{max} and Δn max respectively. xxvi

Figure 1.9 The helielectric order of the SmC* phase. The polarization rotates from layer to layer. xxvii

Figure 1.10: Switching between two surface-stabilized tilt states of a ferroelectric liquid crystal by application of an electric field. xxviii

Figure 1.11 Schematic representation of a birefringent sample between crossed polarizers.^{x} xxx

Figure 1.12 Schematic representation of a compensator used to measure birefringence in liquid crystal samples. xxxi

Figure 1.13 DSC trace of W657. The red curve is on heating while the blue curve is on cooling. The integral of the peak is proportional to the change in entropy between the phases. xxxii

Figure 2.1: Schematic representation of the the formation of zig-zag defects in the SmA* phase. The bookshelf geometry of the SmA* phase (top left) and, with layer spacing d_A (bottom left) is subjected to an electric field. This causes the molecules to tilt (top right). The volume of the cell remains constant which causes the layers to buckle (bottom right). xxxv

Figure 2.2: a) Double-peak profile of W530 at 41 °C. From the left as the negative voltage is reduced the LC transitions from a field-induced SmC* to a de vries SmA* phase (first peak). This crosses 0 V and as the positive voltage increases the LC transitions into a field-induced SmC* phase, which is tilted in the opposite direction as with the large negative voltage. b) Model of the de Vries SmA phase in which the phase is an in-layer cybotactic SmC.[xxii] xxxix

Figure 2.3 Electroclinic response of W317 xli

Figure 2.4 Electroclinic response of W415 xlii

Figure 2.5 Conformational analysis of 1-butene. This is a model for how the E-5-decenyloxy tail of W415 behaves near the unsaturation. xlii

Figure 2.6 The four isomers of a phenyl, biphenyl linked by an ester that possesses a trifluoromethyl ortho to a 1-methylheptyloxy tail. xliii

Figure 2.7 DSC of W551 xlix

Figure 2.8 Layer spacing of W551 as a function of temperature. xlix

Figure 2.9 DSC of W659 l

Figure 2.10 Layer spacing of W659 as a function of temperature. li

Figure 2.11 DSC of W667 lii

Figure 2.12 DSC of W652 liii

Figure 2.13 Layer spacing of W652 as a function of temperature. liv

Figure 2.14: a) Representative compounds synthesized by the Lemieux group that show significant layer expansion in the SmA phase and anomalous expansion in the SmC phase. b) Ratio of X-Ray Layer spacing to the Layer spacing at the SmA - SmC phase transition, showing expansion of the layer spacing in de Vries SmA materials.[xxxiv] liv

Figure 2.15 The electroclinic tilt of W652 as a function of applied field at various temperatures in the SmA* phase lvi

Figure 2.16 The birefringence (Δn) of W652 as a function of applied field at various temperatures in the SmA* phase. lvi

Figure 2.17 Field-induced polarization of W652 at T-T_{A-C} = 1 K. lvi

Figure 2.18 DSC of W657 lviii

Figure 2.19 Layer spacing of W657 as a function of temperature. lviii

Figure 2.20 The electroclinic tilt of W657 as a function of applied field at various temperatures in the SmA* phase. lx

Figure 2.21 The birefringence (Δn) of W657 as a function of applied field at various temperatures in the SmA* phase. lx

Figure 2.22 The field-induced polarization of W652 as a function of applied field at various temperatures in the SmA* phase. lxi

Figure 2.23 X-Ray layer spacing of W530[xxxvi] lxii

Figure 2.24 a) Electroclininc tilt of W530 as a funtion of applied field at various temperatures. b) ratio of birefringence vs. maximum birefringence of W530 as a function of applied field at various temperatures.[xxxvi] lxii

Figure 2.25 DSC of W558 lxiv

Figure 2.26 Layer spacing of W558 as a function of temperature. lxiv

Figure 2.27 DSC of W661 lxv

Figure 2.28 DSC of W668 lxvi

Figure 2.29 DSC of W665 lxvii

Figure 2.30 DSC of W666 lxviii

Figure 2.31 DSC of W669 lxix

Figure 2.32 X-Ray layer spacing of W669 at various temperatures lxix

Figure 2.33 The electroclinic tilt of W669 as a function of applied field at various temperatures in the SmA* phase lxx

Figure 2.34 Birefringence of W669 as a function of applied field at various temperatures in the SmA* phase. lxxi

Figure 2.35 Schematic representation fof the longitudinal dipole of the moiety bearing the non-chiral tail of Core C (left) and Core B (right) lxxiv

Figure 2.36: Schematic representation of the effect of the orientation of the transverse dipole on the polarization. If the transverse dipole orients towards the tilt plane (left) the polarization will be small, while if the transverse dipole aligns towards to the polar axis then the polarization will be large. lxxv

Figure 2.37 DSC of W705....... lxxvi

Figure 2.38 Layer spacing of W705 as a function of temperature. lxxvii

Figure 2.39 The electroclinic tilt of W705 as a function of applied field at various temperatures in the SmA* phase lxxviii

Figure 2.40 The electroclinic tilt of W705 as a function of applied field at various temperatures in the SmA* phase. The field is limited to ca. 10 V mm in which the electroclinic response is linear and shows very little temperature dependence. lxxviii

Figure 2.41 The birefringence (Δn) of W705 as a function of applied field at various temperatures in the SmA* phase. lxxix

Figure 2.42 Field-induced polarization inthe SmA* phase of W705 at various temperatures. lxxx

Figure 3.1 DSC of W697 cvii

Figure 3.2 Layer spacing of W697 as a function of temperature. cviii

Figure 3.3 The electroclinic tilt of W697 as a function of applied field at various temperatures in the SmA* phase cix

Figure 3.4 The birefringence (Δn) of W697 as a function of applied field at various temperatures in the SmA* phase. cix

Figure 3.5 DSC of W698 cx

Figure 3.6 Layer spacing of W698 as a function of temperature. cxi

Figure 3.7 The electroclinic tilt of W698 as a function of applied field at various temperatures in the SmA* phase cxii

Figure 3.8 The birefringence (Δn) of W698 as a function of applied field at various temperatures in the SmA* phase. cxiii

Figure 3.9 DSC of W699 cxiv

Figure 3.10 Layer spacing of W699 as a function of temperature. cxiv

Figure 3.11 The electroclinic tilt of W699 as a function of applied field at various temperatures in the SmA* phase cxv

Figure 3.12 The birefringence (Δn) of W699 as a function of applied field at various temperatures in the SmA* phase. cxvi

Figure 3.13 DSC of W733....... cxvii

Figure 3.14 Layer spacing of W733 as a function of temperature. cxvii

Figure 3.15 The electroclinic tilt of W733 as a function of applied field at various temperatures in the SmA* phase cxviii

Figure 3.16 The birefringence (Δn) of W733 as a function of applied field at various temperatures in the SmA* phase. cxix

Figure 3.17 DSC of W734....... cxx

Figure 3.18 Layer spacing of W734 as a function of temperature. cxx

Figure 3.19 The electroclinic tilt of W734 as a function of applied field at various temperatures in the SmA* phase cxxii

Figure 3.20 The birefringence (Δn) of W734 as a function of applied field at various temperatures in the SmA* phase cxxii

Figure 3.21 DSC of W735....... cxxiii

Figure 3.22 Layer spacing of W735 as a function of temperature. cxxiii

Figure 3.23 The electroclinic tilt of W735 as a function of applied field at various temperatures in the SmA* phase cxxv

Figure 3.24 The birefringence (Δn) of W735 as a function of applied field at various temperatures in the SmA* phase. cxxv

Figure 3.25 DSC of W713....... cxxvi

Figure 3.26 Layer spacing of W713 as a function of temperature. cxxvi

Figure 3.27 The electroclinic tilt of W713 as a function of applied field at various temperatures in the SmA* phase cxxviii

Figure 3.28 The birefringence (Δn) of W713 as a function of applied field at various temperatures in the SmA* phase. cxxviii

Figure 3.29 Field-induced polarization of W713 cxxix

Figure 3.30 DSC of W714 cxxx

Figure 3.31 Layer spacing of W714 as a function of temperature. cxxx

Figure 3.32 The electroclinic tilt of W714 as a function of applied field at various temperatures in the SmA* phase cxxxii

Figure 3.33 The birefringence (Δn) of W714 as a function of applied field at various temperatures in the SmA* phase. cxxxii

Figure 3.34 Field-induced polarization of W714 cxxxii

Figure 3.35 DSC of W715 cxxxiii

Figure 3.36 Layer spacing of W715 as a function of temperature. cxxxiv

Figure 3.37 The electroclinic tilt of W715 as a function of applied field at various temperatures in the SmA* phase cxxxv

Figure 3.38 The birefringence (Δn) of W715 as a function of applied field at various temperatures in the SmA* phase. cxxxvi

Figure 3.39 Field-induced polarization of W715 cxxxvi

Figure 3.40 DSC of W314 cxxxvii

Figure 3.41 Layer spacing of W314 as a function of temperature. cxxxviii

Figure 3.42 The electroclinic tilt of W314 as a function of applied field at various temperatures in the SmA* phase cxxxix

Figure 3.43 The birefringence (Δn) of W314 as a function of applied field at various temperatures in the SmA* phase. cxl

Figure 3.44 Field-induced polarization of W314 at various temperatures cxl

Figure 3.45 DSC of W717 cxli

Figure 3.46 Layer spacing of W717 as a function of temperature. cxlii

Figure 3.47 The electroclinic tilt of W717 as a function of applied field at various temperatures in the SmA* phase cxliv

Figure 3.48 The birefringence (Δn) of W717 as a function of applied field at various temperatures in the SmA* phase cxliv

Figure 3.49 Field-induced polarization of W717 at various temperatures cxlv

Figure 3.50 DSC of W718 cxlvi

Figure 3.51 Layer spacing of W718 as a function of temperature. cxlvi

Figure 3.52 The electroclinic tilt of W718 as a function of applied field at various temperatures in the SmA* phase cxlviii

Figure 3.53 The birefringence (Δn) of W718 as a function of applied field at various temperatures in the SmA* phase. cxlviii

Figure 3.54 Field induced polarization of W718 at various temperatures cxlix

List of Schemes

Scheme 2-1 a) NBS, HBF_4 • Et_2O, CH_3CN b) (R)-2-octanol, $P((Ph)_3)_4$, DEAD, THF c) ^nBuLi, THF, CO_2, $HCl_{(aq)}$ d) 4-(4-alkoxyphenyl)phenol, DCC, DMAP, CH_2Cl_2 xliv

Scheme 2-2 a) ^nBuLi, THF. $B(OMe)_3$, H_2O_2, NaOH, H_2O b) 4-(4'-alkoxyphenyl)benzoic acid, DCC, DMAP, CH_2Cl_2 xlv

Scheme 2-3 a) ^nBuLi, THF, $B(OMe)_3$, MeOH b) 4-benzyloxybromobenzene, $Pd(P(Ph)_3)_4$, Na_2CO_3, H_2O, THF c) H_2, Pd/C, EtOH, $CHCl_3$ d) 4-alkoxybenzoic acid, DCC, DMAP, CH_2Cl_2 xlvi

Scheme 2-4 a) methyl-4-iodobenzoate, $Pd(P(Ph)_3)_4$, Na_2CO_3, H_2O, THF b) NaOH, H_2O, EtOH c) phenol, DCC, DMAP, CH_2Cl_2 xlvii

Scheme 2-5 a) 4-7,7,8,8,9,9,10,10,10nonafluorodecyloxybenzoic acid , DCC, DMAP, CH_2Cl_2 xlviii

Scheme 3-1 a) (R)-2-octanol, $P((Ph)_3)_4$, DEAD, THF b) NaOH, H_2O, EtOH c) 4-(4'-alkoxyphenyl)benzoic acid, EDC, DMAP, CH_2Cl_2 ciii

Scheme 3-2 a) Pivalic anhydride, CH2Cl2 b) (R)-2-octanol, $P((Ph)_3)_4$, DEAD, THF c) NaOH, H_2O, EtOH d) 4-(4'-alkoxyphenyl)benzoic acid, EDC, DMAP, CH_2Cl_2 civ

Scheme 3-3 a) N-Chlorosuccinimide, p-Toluenesulfonic acid, CH_2Cl_2 b) (*R*)-2-octanol, $P((Ph)_3)_4$, DEAD, THF c) NaOH, H_2O, EtOH d) 4-(4'-alkoxyphenyl)benzoic acid, EDC, DMAP, CH_2Cl_2 cv

Scheme 3-4 a) Sodium nitrite, $HCl_{(aq)}$, acetic anhydride, EtOAc b) (*R*)-2-octanol, $P((Ph)_3)_4$, DEAD, THF c) NaOH, H_2O, EtOH d) 4-(4'-alkoxyphenyl)benzoic acid, DCC, DMAP, CH_2Cl_2 cvi

List of Tables

Table 2.1 Phase transitions for compounds built on the Core A, Core B, Core C and Core D scaffolds....lxxii

Table 3.1 Summary of the clearing point, van der Waals volume and the Hammett substituent constant for compounds built on the Core B scaffold....cli

Table 3.2 Summary of the saturated tilt for compounds built on the Core B scaffold....cliii

Table 3.3 The saturated tilt of compounds built on the Core B scaffold.... clv

Table 3.4 Summary of the minimum and maximum birefringence near the SmA* - SmC* phase transition as well as the birefringence at $T-T_{A-C}$ = 5 K for compounds built on the Core B scaffold....clvii

Table 3.5 A summary of the dipole moment (D) of the benzene deriviatives of the lateral polar group from compounds built on the Core B scaffold and the corresponding spontaneous polarization at $T-T_{A-C}$ = 5 K.... clix

Chapter 1. Introduction

1.1 Classifications of liquid crystals

Liquid crystal (LC) phases are an intermediate state of matter between the ordered crystal phase and the disordered isotropic liquid phase. Like liquids, they flow easily and are relatively incompressible. Like crystals, LCs show orientational order, however, the positional order is shown in zero, one or two dimensions. These phases, due to their intermediate properties, are termed mesophases and compounds that show them are termed mesogens. The thermodynamic driving force to form LC phases is nanophase segregation between core and side-chains (*vide infra*). LCs can be classed as either lyotropic, which form mesophases in the presence of a solvent, or thermotropic, which form mesophases in the absence of a solvent.[1]

Lyotropic LCs are formed by compounds possessing a hydrophilic polar, typically ionic, head group and one or more hydrophobic aliphatic tails in the presence of a solvent.[2] These types of molecules are referred to as amphiphiles. If the lyotropic LC is added to polar solvent the hydrophilic head group will interact favourably, while the aliphatic group will sequester into tail-rich domains, as shown in Figure 0.1. If the solvent is non-polar the tails will interact favourably with the solvent and the polar head groups will aggregate. The principal factor in mesophase formation and morphology in lyotropic LCs is concentration of the mesogen, however, temperature can also have an effect. A typical example of lyotropic behavior is the formation of liposomes or micelles by phospholipids.

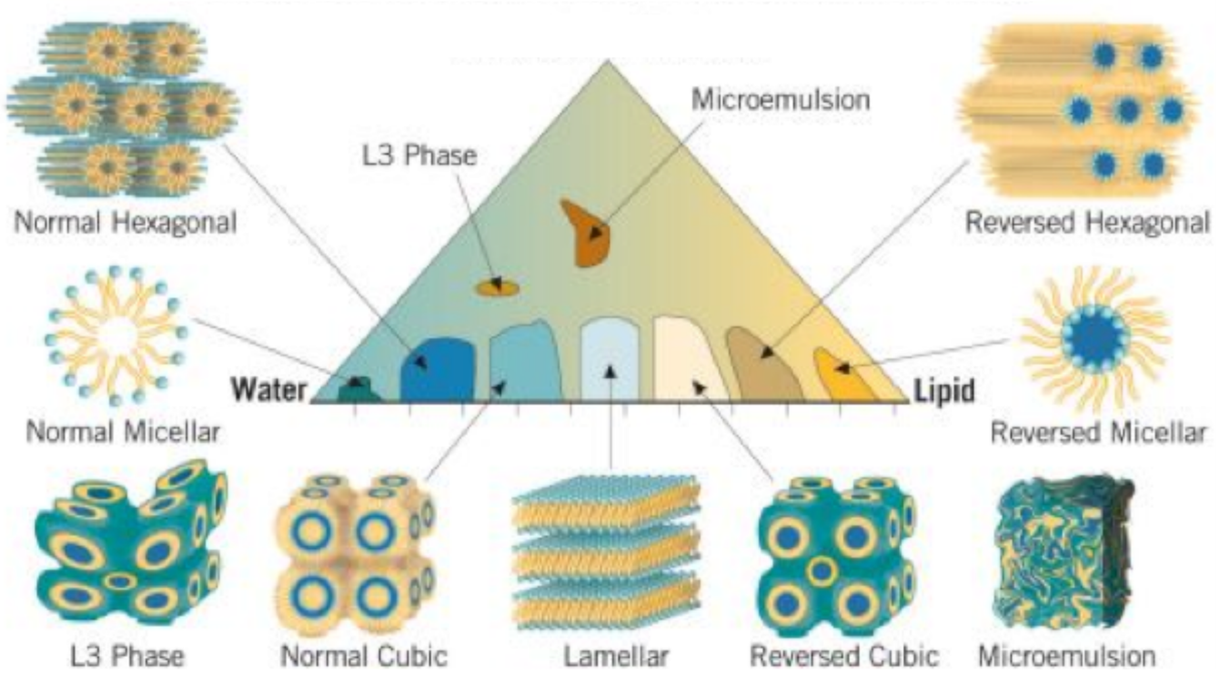

Figure 0.1: Common morphologies of lyotropic LCs. The concentration of water decreases from left to right.[3]

Thermotropic liquid crystals form mesophases in the absence of a solvent and change morphology with temperature. One simple system that shows thermotropic behaviour is semi-fluorinated alkanes, which align anti-parallel into diffuse layers. Most calamitics, however, possess a rigid, poly-aromatic core with one or more pendant aliphatic side-chains. The aromatic cores tend to nano-phase segregate to increase π-stacking interactions, while the fluid side-chains, by virtue of strong London dispersion forces, also tend to segregate. There are three broad classes of thermotropics: discotics, which are disc-shaped and self-assemble into columns; calamitics, which are rod-shaped and self-assemble into nematic and smectic phases; and bent-core, which are banana-shaped and self-assemble into nematic, smectic and columnar phases. Prototypical compounds of each class of thermotropic compound are shown in Figure 1.2. This thesis will focus on thermotropic liquid crystals with calamitic and bent-core shape anisotropy.

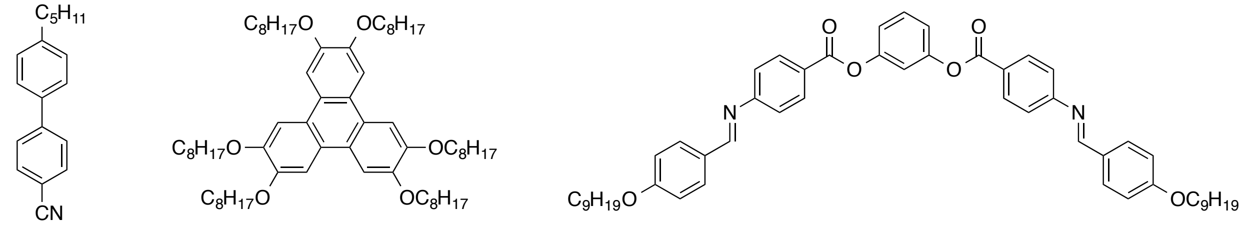

Calamitic **Discotic** **Bent-core**

Figure 0.2 Prototypical compounds of discotic, calamitic and bent-core liquid crystal compounds.

1.2 Calamitic liquid crystals

Many liquid crystals show more than one mesophase (polymorphism). Some LC phases exist only on cooling and are termed monotropic. These phases exist only in a super-cooled state and are kinetically stable. With time, monotropic phases will transition to the more thermodynamically stable phase. Phases that are stable on heating and cooling are termed enantiotropic, and are the thermodynamically stable phase. There are many known liquid crystalline phases for calamitic compounds with the three most ubiquitous being the nematic (N), the smectic A (SmA), and the smectic C (SmC).

1.2.1 The nematic phase

The nematic phase is characterized by the molecular long axes being aligned along the director (**n**), on the time average as there are large variations in the alignment, with isotropic positional order on the time average as shown in Figure 1.3a. High polarization anisotropy and aspect ratio, short alkyl tails and lack polar groups tend to promote the nematic phase.

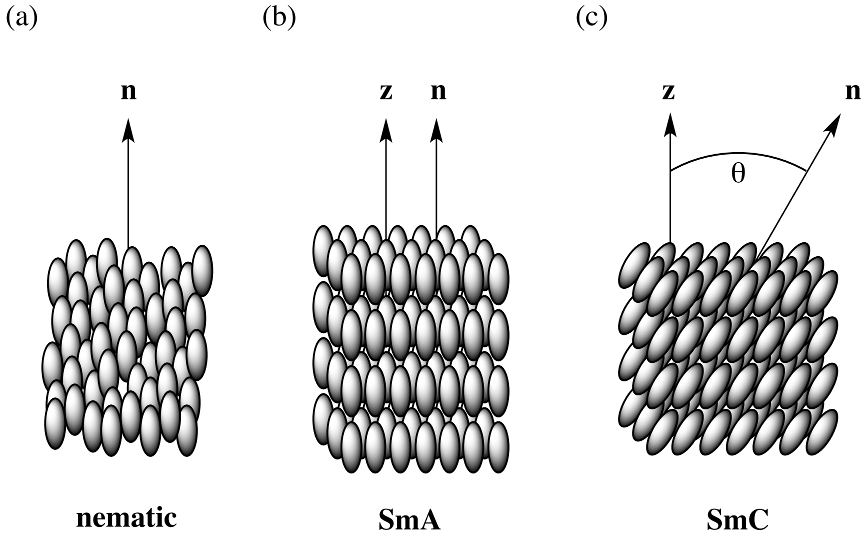

Figure 0.3 Idealized representation of the: (a) nematic (b) SmA and (c) SmC phase. The phases are more disordered than illustrated.

1.2.2 The smectic A phase

The SmA phase is characterized by diffuse layers with the alignment of molecular long axes along the director (**n**) parallel to the layer normal (**z**) as shown in Figure 1.3b. The cores of SmA mesogens freely rotate and layer-to-layer fluctuations are fast. Molecules that possess long alkyl side chains and out-of-layer suppressing groups (i.e. semi-fluorinated alkyl groups and carbosilanes) typically form smectic phases.

1.2.3 The de Vries SmA

The de Vries SmA is characterized by diffuse layers with alignment of the molecular long axes along the director (**n**), which are tilted with respect to the layer normal (**z**). The tilt (θ) shows no long-range azimuthal (ϕ) correlation and is typically temperature independent. The lack of azimuthal correlation can be imagined as the molecules being confined to a hollow cone, on which the molecules can precess.[4] The hollow cone model is shown in Figure 1.4. When viewed between crossed polarizers the optic axis appear to be oriented along **n**, as in the traditional SmA phase. Molecules that have a propensity for smectic phases typically through the suppression of out-of-layer fluctuations, tends to promote the formation of the de Vries SmA phase.

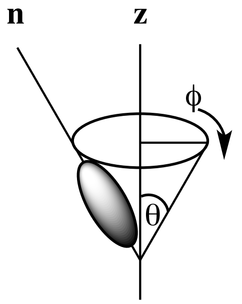

Figure 0.4 The hollow cone representation of the de Vries SmA phase. The molecular long axes (n) are tilted, by an angle θ, with respect the layer normal (z). The azimuthal angle (ϕ) is disordered.

1.2.4 The smectic C phase

The SmC phase is characterized by a diffuse layer structure with the molecular long axes aligned along the director (**n**), which is tilted with respect to the layer normal (**z**) as shown in Figure 1.3c. The tilt angle (θ) is azimuthally coherent and the magnitude of θ increases with decreasing temperature. In 1978 Durand compared the optical tilt (θ_{opt}), observed by polarized light microscopy (PLM), is typically larger than the X-Ray tilt ($\theta_{X\text{-}Ray}$), with the ratio typically ca. 0.8. The latter is calculated by geometry using the fully extended molecular length and the layer spacing. He hypothesized that the cores, which have a larger polarization anisotropy than the tails, are more tilted than the side-chains as shown in Figure 1.5.[5]

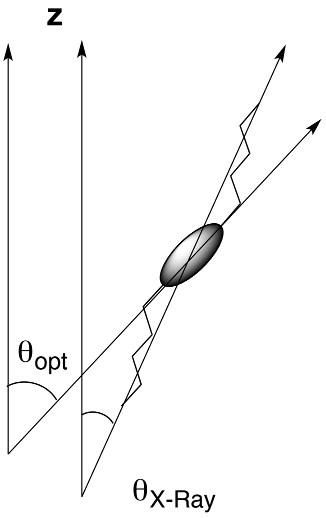

Figure 0.5 Schematic representation of the highly polarizable core being more tilted (θ_{opt}) than the fully extended molecule ($\theta_{X\text{-}Ray}$) in the SmC phase.

1.3 Chiral phases

The phase descriptions above apply to mesophases formed by non-chiral, or macroscopically racemic, molecules. Each phase, however, has additional unique properties when composed of enantiomerically enriched chiral molecules.

1.3.1 The cholesteric phase

The cholesteric phase, or chiral nematic (N*), possesses locally the alignment properties of the N phase but incorporates a helical pitch as shown in Figure 1.6. The degree of twisting is characterized by the pitch (p), which describes the distance for one complete rotation, which is temperature dependent. Some N* materials show selective reflection, which occurs when the wavelength (λ) of circularly polarized light matches the pitch of the N* phase. If the handedness of the circularly polarized light is the same as the N* material the light is incapable of penetrating the material and is reflected. This thermographic phenomenon is employed in LC thermometers.[2]

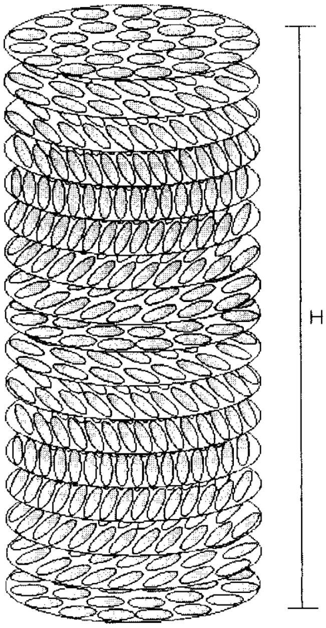

Figure 0.6 Schematic represntation of the helical twist of the N* phase.

1.3.2 The chiral smectic A phase

The chiral SmA phase (SmA*), like it's achiral analogue, is characterized by a diffuse layer structure, however, there are no bulk chiral properties, such as twist, due to the very fast rotation of the core; the fast rotation of the core prevents polar alignment (piezoelectricity). In the presence of an electric field (E), however, the permanent dipole couples to the electric field, which gives rise to a rotational bias. The alignment of molecular dipoles reduces the symmetry and induces tilt (θ) perpendicular to the applied field (Figure 1.7). The field-induced tilting is known as the electroclinic effect.[6] The induced tilt increases linearly with applied field, for small E, and the electroclinic susceptibility (e_c) is given by:

$$e_c = \frac{\partial \theta}{\partial E}$$

The tilt susceptibility increases with decreasing temperature, becoming largest near the SmA*-SmC* transition. Materials with large e_c were considered promising for optical applications that require gray-scale.[7] Layer contraction at large tilt, however, greatly reduces the device performance.

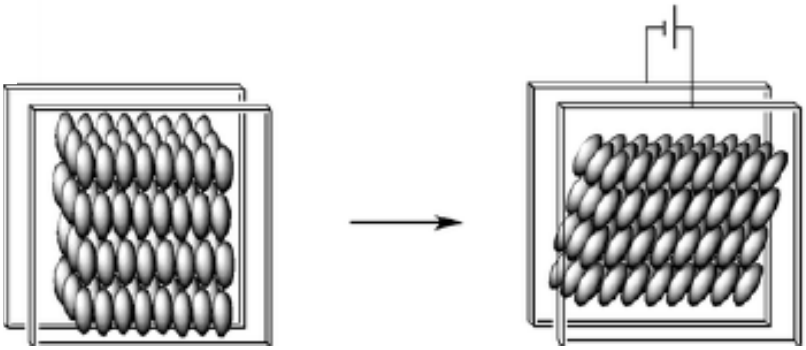

Figure 0.7 Schmatic representaion of the electroclinic effect. The application of an electric field to a SmA* phase, in a cell with bookshelf layer geometry, reduces symmetry and induces tilt.

1.3.3 The chiral de Vries SmA phase

The chiral de Vries SmA phase (de Vries SmA*) possesses a diffuse layered structure, like the achiral analogue, and like the SmA* phase fast rotation of the core prevents piezoelectric alignment. In the presence of an electric field the chirality couples to the field and gives rise to a rotational bias, as shown in Figure 1.8. The molecules, being tilted and confined to the tilt cone, respond to an electric field with an increase in the azimuthal order parameter. This increase in azimuthal order parameter leads to an increase the optical tilt angle and the birefringence. With the application of small electric fields the electroptic response is typically linear, except when just above the SmA* - SmC* phase transition. De Vries SmA* materials possess several properties that make them attractive for next generation gray-scale devices, including: large e_c, θ_{opt} and absence of field-induced layer shrinkage.

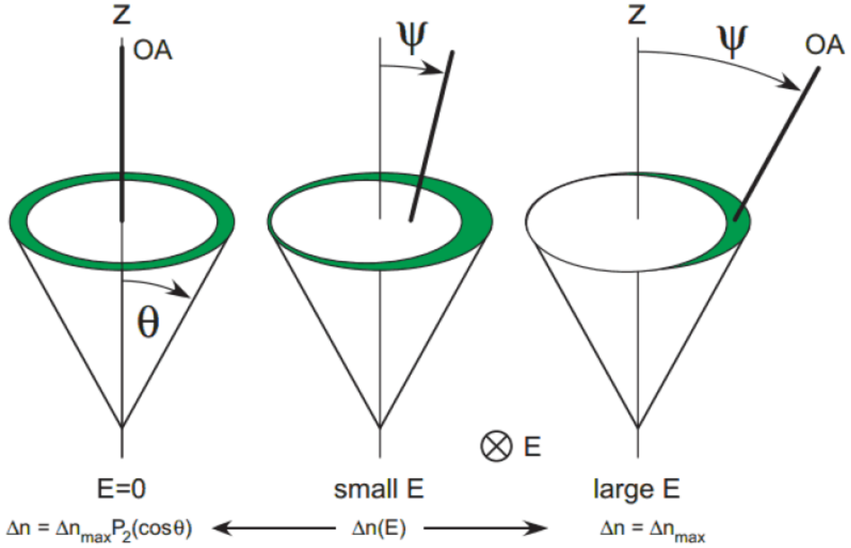

Figure 0.8 Representation of the electroclinic effect in the de Vries SmA* phase. With no electric field, E = 0 (left), the molecules are evenly distributed about the tilt cone, the optic axis (OA) is parallel to the layer normal and the birefringence is at a minimum. At small electric fields (centre) the molecules become biased to one side of the cone, tilting the OA and increasing the birefringence. At large E (right) the bias is increased and the phase becomes a field induced SmC* phase. The OA and birefringence become maxima; Ψ_{max} and Δn max respectively.

1.3.4 The chiral smectic C phase

In 1975 Meyer predicted that a chiral smectic C phase (SmC*) would be ferroelectric based on a symmetry argument.[8] The SmC phase possesses C_{2h} symmetry, which is non-polar, but if it were composed of chiral molecules then the symmetry is reduced to C_2, which is polar. This polarity would be manifest as a spontaneous, ferroelectric polarization as the permanent dipoles would be aligned and the tilt coherent from layer to layer. In the bulk, however, the SmC* phase is heli-electric as the polarization precesses from layer to layer, as shown in Figure 1.9.

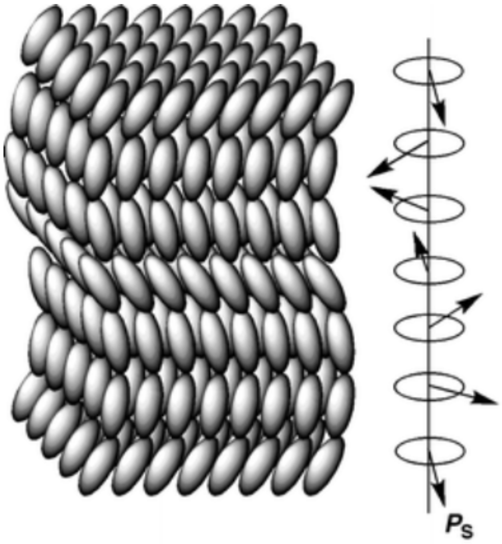

Figure 0.9 The helielectric order of the SmC* phase. The polarization rotates from layer to layer.

The helix can be unwound when boundary conditions are imposed, as shown by Clark and Lagerwall.[9] They placed a small amount of SmC* material between parallel rubbed polyimide coated glass plates, creating a thin film. The rubbed polymer forced the molecules at the surface to align with long axes parallel to the plane of the glass keeping the azimuth coherent from layer to layer, resulting in a surface-stabilized ferroelectric liquid crystal (SSFLC). The SSFLC can be driven with an electric field to either of the two surface-stabilized tilt states (+θ and –θ), as shown in Figure 1.10, by reorientation of the molecules about the tilt cone in what is called the Goldstone mode. The Goldstone mode, in SSFLCs, has a barrier and no switching can occur until a threshold voltage (V_{th}) has been applied.

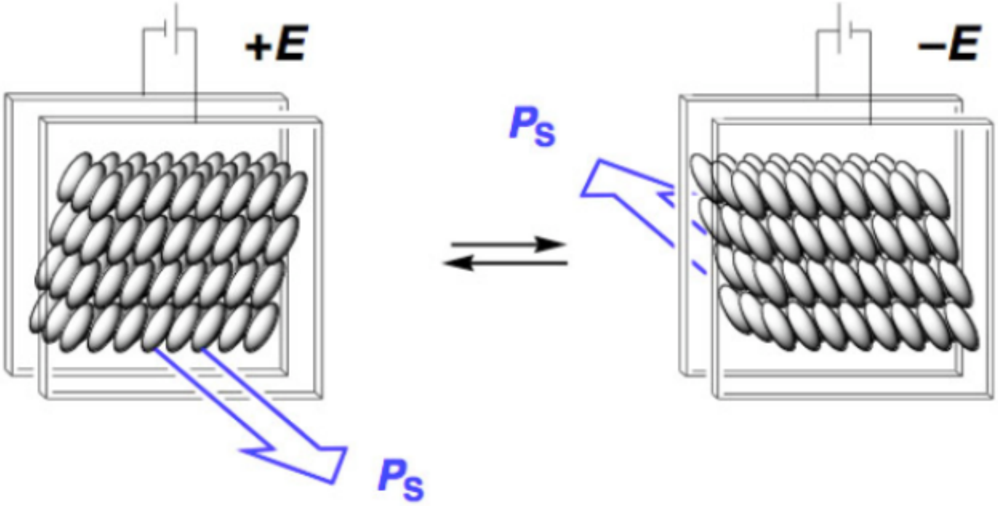

Figure 0.10: Switching between two surface-stabilized tilt states of a ferroelectric liquid crystal by application of an electric field.

1.4 Techniques

There are several techniques used for characterizing small organic molecules such as nuclear magnetic resonance (NMR), both ^{1}H and ^{13}C, mass spectrometry and elemental analysis. Bulk mesophase characterization is accomplished primarily with polarized light microscopy (PLM), including birefringence determination, with supplementary information provided by differential scanning calorimetry (DSC).

1.4.1 Polarized Light Microscopy

PLM is a technique used to identify mesophases and phase transition temperatures. Mesophases are anisotropic and possess two, or more, unique indices of refraction, a phenomenon known as birefringence. In the microscope, non-polarized light first passes through a polarizer to produce plane-polarized light. This light, when passing through a birefringent sample, is split into its two component beams known as the ordinary and extraordinary waves, as shown in Figure 1.11.[10] These waves are retarded, to different extents, by the indices of refraction. This leads, upon recombination, to elliptically polarized light. This light in general passes through a second polarizer, typically called the analyzer, which is oriented perpendicular to the first polarizer. If the sample is isotropic, or in a non-birefringent orientation, such as the molecular long axes aligned along a polarizer or a homeotropically aligned SmA phase, then no light passes through the analyzer and it appears dark.

Liquid crystal samples are typically studied in liquid crystal cells in PLM. The substrates are typically glass and coated with indium tin oxide (ITO), which is a transparent conductor. The ITO layer is then coated with an alignment layer, typically a polymer or a surfactant. For alignment parallel to the surface, rubbed polyimide is typically used, the molecules aligning along the rubbing direction. In the case of alignment perpendicular to the surface (homeotropic) a surfactant, such as cetyltrimethylammonium bromide, is used. Once the sample is loaded in the cell and aligned, electric fields are used to measure the electro-optical response. Things that can be measured include tilt angle, birefringence and spontaneous polarization. The latter is measured using the triangular wave method.

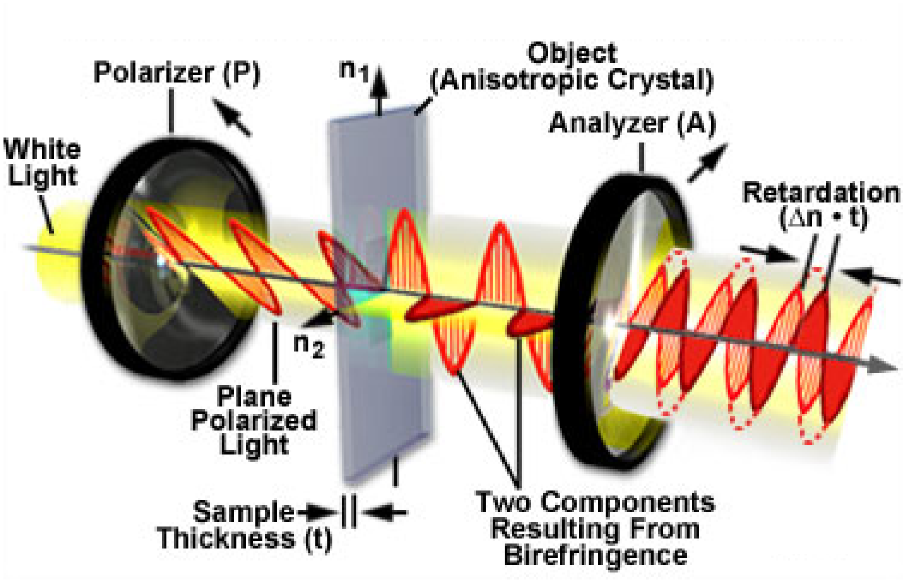

Figure 0.11 Schematic representation of a birefringent sample between crossed polarizers.[10]

The measurement of birefringence, the difference between the two unique refractive indices, was accomplished with a Zeiss (Germany) Berek compensator (Figure 1.12). The light source of the PLM was made monochromatic by use of a coloured filter. The well aligned, planar geometry liquid crystal cell would be oriented such that the long axis of the liquid crystal was aligned with one of the polarizers and then rotated 45°, such that the layers were perpendicular to the compensator, and the sample was at maximum brightness. The compensator plate was rotated, increasing the path length of the light through the compensator, until the sample appeared dark. The compensator plate angle was noted and birefringence could be determined from the plate angle, via phase shift, and sample thickness by:

$$\Delta n = \frac{phase\ shift\ (nm)}{cell\ thickness\ (nm)}$$

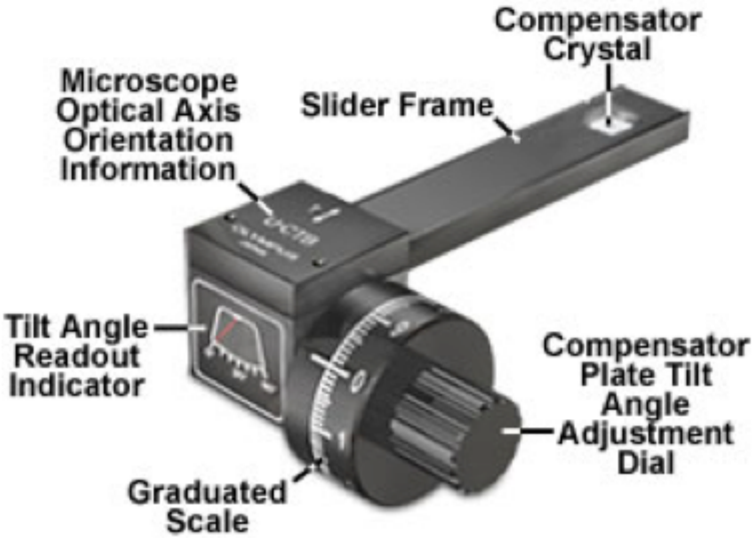

Figure 0.12 Schematic representation of a compensator used to measure birefringence in liquid crystal samples. [11]

1.4.2 Differential Scanning Calorimetry

A differential scanning calorimeter is an instrument used to determine both phase transition temperatures and the corresponding entropy change between phases. In this technique two aluminum pans, one filled with sample and the other empty, referred to as the reference pan, are heated at the same rate. Since the material in the pan has a specific heat capacity different than air, the amount of energy input into the same pans to keep them at the same temperature is different, but the difference is roughly constant over small temperature ranges. For a phase transition there is some heat absorbed, or lost, that will affect the rate of temperature change of the two pans. This is manifest as a peak in the DSC (Figure 1.13). The magnitude of the peak can imply the type of phase transition (first or second order) and is instrumental in showing that liquid crystals are far more liquid than crystal, since the enthalpy required to melt the crystal phase to a liquid crystal phase is significantly larger, in most cases, than to melt a liquid crystal phase to an isotropic liquid phase.

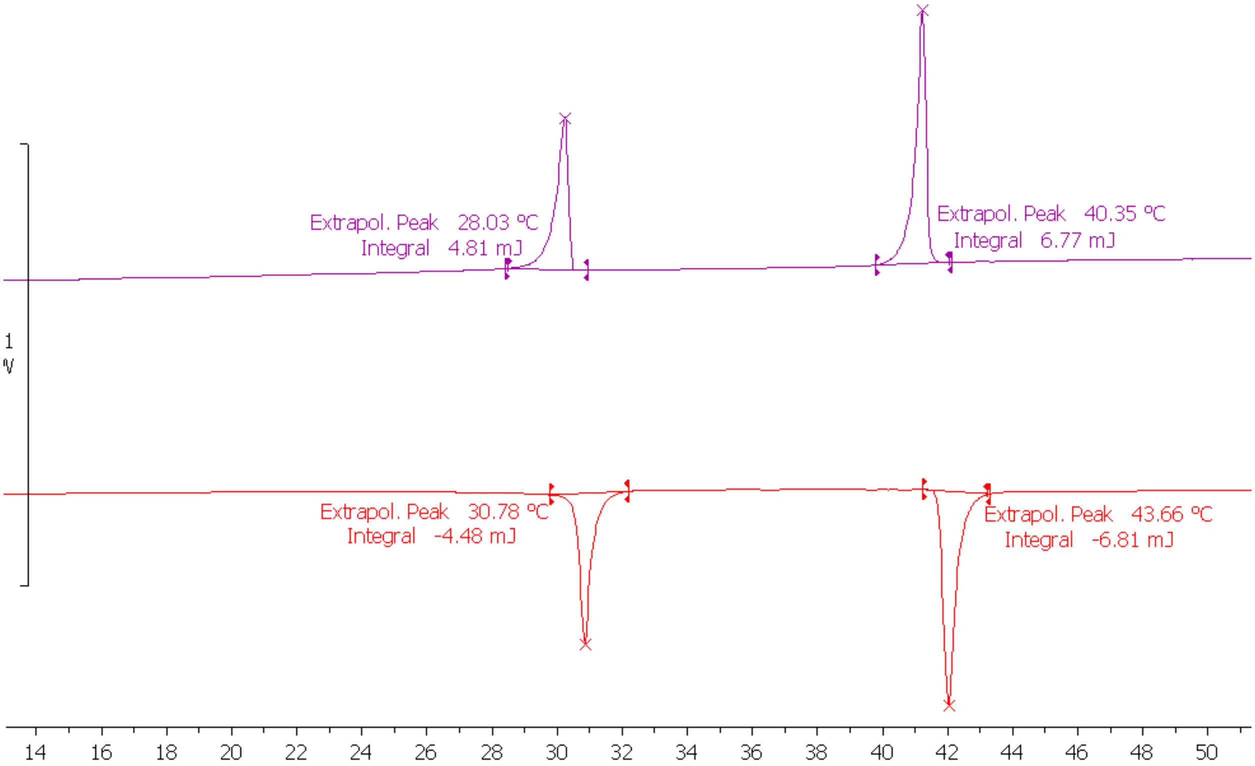

Figure 0.13 DSC trace of W657. The red curve is on heating while the blue curve is on cooling. The integral of the peak is proportional to the change in entropy between the phases.

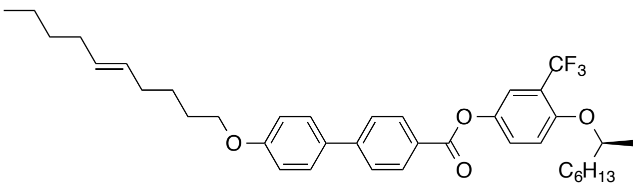

W657

I - 40 °C - SmA* - 28 °C - SmC*

1.5 References

1. Collings, P. J. Liquid Crystals: Nature's Delicate Phase of Matter; Princeton University Press: Princeton, **1990**.

2. D. Demus, J. Goodby, G. W. Gray, H.-W. Spiess and V. Vill, (**1998**). Handbook of Liquid Crystals. Weinheim: Wiley VCH.

3. Particle Sciences – Technical Briefs, **2012**, Vol. 04.

4. de Vries, A. *Mol. Cryst. Liq. Cryst. Lett.* **1977**, *41*, 27.

5. Bartolino, R.; Doucet, J.and Durand, G. *Ann. Phys. (Paris)*, **1978**, *3*, 389.

6. Garoff, S. and Meyer, R. *Physical Review Letters* **1977**, *38*, 848.

7. Andersson, G.; Dahl, I.; Komitov, L.; Laggerwall, S. T.; Skarp, K. and Stebler. B. *J. Appl. Phys.* **1989**, *66*, 4983.

8. R. B. Meyer, L. Liebert, L. Strzelecki and P. Keller, *J. Phys. (France)*, **1975**, *36*, L-69.

9. Clark, N. A. and Lagerwall, S. *Appl. Phys. Lett.* **1980**, *36*, 899.

10. Murphy, D. B.; Spring, K. R.; Fellers, T. J.; Davidson, M. W. *http://www.microscopyu.com/articles/polarized/birefringenceintro.html.*

11. Davidson, M. W. *http://micro.magnet.fsu.edu/primer/techniques/polarized/berekcompensator.html.*

Chapter 2. Optimization of de Vries Cores

2.1 Introduction

A significant problem facing liquid crystal-based technology is the need for well-aligned materials with very fast response times. Nematic liquid crystals, on which the LC display industry is built, are very easily aligned but are slow relative to ferroelectrics. As screen sizes continue to increase a paradigm shift from nematics to ferroelectrics will be required to maintain high optical quality with sufficiently fast response times as ferroelectrics are ca. 10^3 times faster than nematics.

The SmC* phase is an attractive solution to decrease the response time of devices, however, if the SmC* phase is grown directly from the isotropic melt it is typically very difficult to align. Materials possessing an isotropic, N*, SmA* and SmC* phase sequence (INAC) are typically employed to obtain better alignment. The SmC* phase is well aligned since the alignment of the nematic phase is retained as the morphology changes. The fundamental problem with INAC materials is that upon transition from the SmA* to SmC* phase, the layers contract. Since the volume of LC in the device is fixed, and material is forced to fill space, the layers buckle, which results in zigzag, or chevron, defects as shown in Figure 2.1. These defects greatly reduce the contrast ratio – the difference between bright and dark states - of a device.

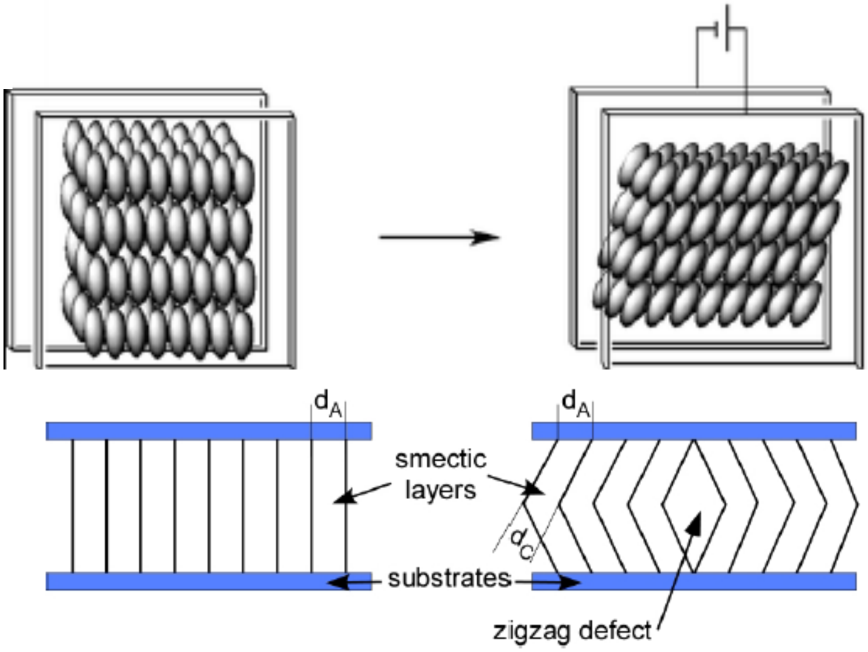

Figure 0.1: Schematic representation of the the formation of zig-zag defects in the SmA* phase. The bookshelf geometry of the SmA* phase (top left) and, with layer spacing d_A (bottom left) is subjected to an electric field. This causes the molecules to tilt (top right). The volume of the cell remains constant which causes the layers to buckle (bottom right).

The SmA* is another phase that could be employed for next-generation display devices. The electroclinic effect, as described by Meyer and Garoff in 1976, is the coupling of an applied electric field with the permanent transverse dipole of the chiral molecules.[1] The transverse dipole is perpendicular to the molecular long axis. This coupling reduces the symmetry and induces tilt. The electroclinic effect is particularly attractive since it is fast relative to the dielectric switching of the nematic phase. Additionally, the magnitude of the tilt is proportional to the applied field, which offers native gray-scale. The SmC* phase relies on very fast switching for gray-scale optics. The electroclinic tilt, like the tilt of the SmC* phase, causes layer shrinkage, which gives rise to chevron defects in the SmA* phase. The ideal phase for display applications would be easy to align; possess native gray-scale;

switch faster than current technology and not develop defects by either change in bulk morphology or application of an electric field.

Adriaan de Vries first described this “ideal” phase in 1977 when he discovered a material with anomalously small layer shrinkage from the SmA phase to SmC phase.[2] This led to the development of the “diffuse cone model” which states that molecules in the SmA phase are tilted with random azimuthal order (see 1.2.3). If observed between crossed polarizers the phase is optically uniaxial and has been termed the “de Vries SmA”. If the de Vries SmA material is chiral then the transverse dipole can couple to an electric field giving an electro-optic response where the azimuthal angle is biased in one direction (Figure 1.8). This gives an apparent optical tilt similar to the electroclinic effect, but without any change in the cone angle. Since the cone angle remains constant there is no contraction of the layers with an applied electric field thus no layering defects are introduced. Additionally, de Vries SmA* materials typically have very large saturated electroclinic tilts (>20^o), while most traditional SmA* materials show saturated electroclinic tilts of a few degrees (< 5^o) and require much larger fields. These larger tilts offer larger gray-scale. An ideal material would possess a tilt of 22.5^o as between crossed polarizers maximum brightness and darkness are achieved at 45^o and 0^o with respect to the polarizer, respectively.

Other characteristics of the de Vries SmA phase include an increase in birefringence with increasing tilt; “shallow” chevrons; the lack of a nematic phase; first order SmA* - SmC* phase transitions; electrostatic V-shaped switching for materials with high polarization; bistable electro-optic switching and bookshelf geometry for low polarization materials; and a large surface electroclinic effect.[3] While not all de Vries SmA materials possess all of these characteristics several are typically present. Until recently a directed approach to the design of new de Vries SmA materials eluded chemists.

2.2 Molecular origins of de Vries behaviour

Our group has proposed a general structural feature required to form the de Vries SmA phase. Similar to inducing anticlinic antiferroelectric behaviour in SmC* materials, the de Vries SmA phase is promoted by suppressing of out-of-layer fluctuations.[4] This is typically accomplished either by introducing nano-phase segregating moieties (e.g. semi-fluorinated hydrocarbons or siloxanes), which tend to promote smectic phases, or by shape anisotropy in the tail, such as incorporation of steric bulk near the layer interface or introducing a "kink", like in a 2-octyloxy tail.[5] This suppression of out-of-layer fluctuations conveniently explains the lack of nematic phase for de Vries SmA materials, as the nematic phase relies on translational motion similar to out-of-layer fluctuations.[3] Other groups, however, believe that the de Vries SmA phase is caused by a frustration between the SmA and SmC phase, analogous to the twist grain boundary phase (TGB*) which is caused by the frustration between the propensity to twist in the N* phase and the desire to form layers.[6] Additionally, they believe that de Vries SmA materials possess a large smectic order parameter and a very small nematic order parameter.[7]

2.2.1 W530, W317 and W415

2.2.1.1 W530

One material designed and synthesized by the Walba group is **W530**.[8] This compound incorporates two moieties that suppress out-of-layer fluctuations. At one periphery is a semi-fluorinated alkyl group, which is known to strongly promote smectic phases.[9] At the other periphery is an O-2-methylheptyloxy tail. The tail, when attached to an ester, as in **MHPOBC**, is thought to adopt a conformation where the tail is nearly parallel to the layers, thus inhibiting out-of-layer fluctuations.[5] It is unknown if it adopts a similar conformation when linked by an ethereal oxygen. As **W530** approaches the SmA* to SmC* phase transition it shows a double-peak profile in the polarization reversal current as shown in Figure 2.2a. This profile is characteristic of an antiferroelectric material, however, in a de Vries SmA* material the interpretation is slightly different. Starting from a large applied electric field in the SmA* temperature range results in a field-induced SmC* phase. Upon lowering the voltage a threshold is crossed and the material transitions to the de Vries SmA* phase with the tilt biased in the same direction as the field-induced SmC*. This accounts for the first peak. The field then changes sign and the voltage increases. This causes the molecules to tilt in the opposite direction, while maintaining the de Vries SmA* phase. As the field increases a threshold voltage is reached and the material transitions to a field induced SmC*. This accounts for the second peak. This double-peak behaviour is typically only observed in materials with a first order SmA*-SmC* phase transition. An early hypothesis was that the de Vries SmA* phase was composed of sub-optical anticlinic domains which gives rise to the double-peak profile.[10] Recent modeling done by the Glaser group at the University of Colorado has suggested that the de Vries SmA* phase is similar to a cybotactic SmC* phase as shown in Figure 2.2b.[11]

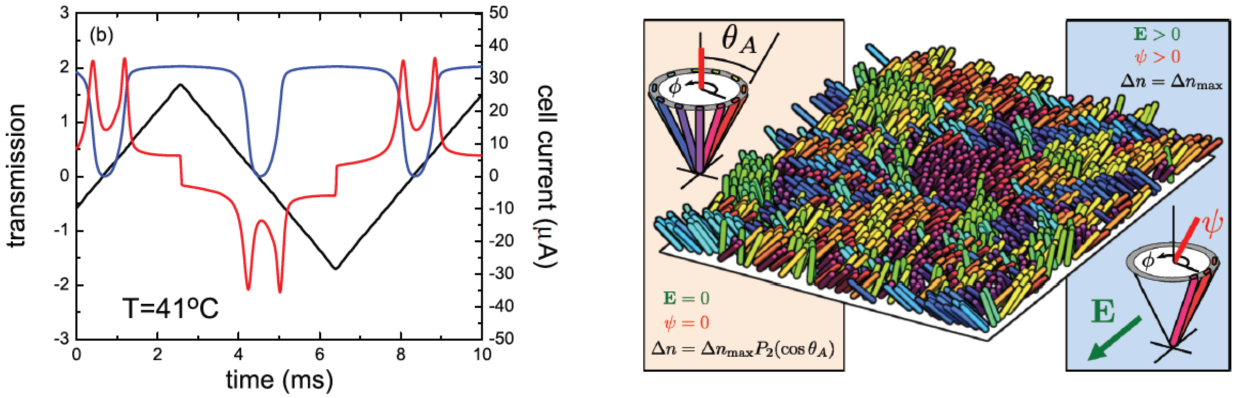

a)

b)

Figure 0.2: a) Double-peak profile of W530 at 41 ^{o}C. From the left as the negative voltage is reduced the LC transitions from a field-induced SmC* to a de vries SmA* phase (first peak). This crosses 0 V and as the positive voltage increases the LC transitions into a field-induced SmC* phase, which is tilted in the opposite direction as with the large negative voltage. b) Model of the de Vries SmA phase in which the phase is an in-layer cybotactic SmC.[11]

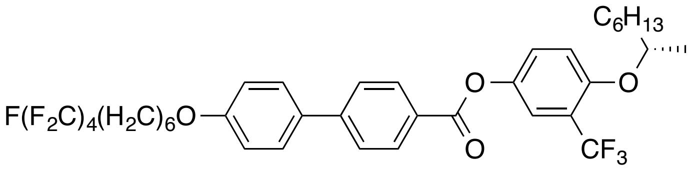

W530

I - 94 ^{o}C - SmA* - 39 ^{o}C - SmC*

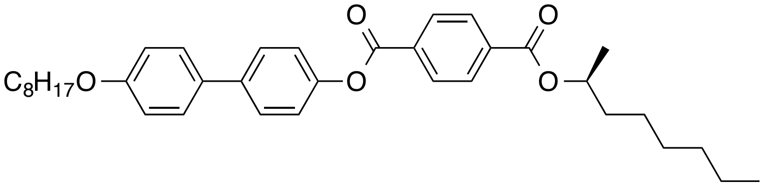

MHPOBC

2.2.1.2 W317

An interesting pair of molecules to compare, designed and synthesized by the Walba group, is **W317** and **W415**.x-y These two compounds have remarkably similar molecular structure but exceptionally different mesophase behaviour, particularly in the SmA* phase. **W317** shows an isotropic to the traditional SmA* phase transition at 76 °C which transitions to the SmB* phase at 23 °C. **W415**, conversely, shows an isotropic to de Vries SmA* phase at 34 °C which transitions to the SmC* phase at 26 °C.

W317 possesses an n-decyloxy tail, which does not strongly suppress out-of-layer fluctuations, and is a representative of a rare class of traditional SmA materials known as anti-de Vries.[12] Anti-de Vries SmA molecules act as a rigid rod in the SmA phases evidenced by a ratio of $\theta_{X\text{-}Ray}$ to θ_{opt} of unity. This phenomenon gives maximum layer shrinkage for a given tilt. Additionally, **W317** possesses a very large tilt susceptibility relative to most SmA* materials.[13] The tilt susceptibility typically increases non-linearly as you approach a SmA* to SmC* transition. This property makes devices based on the electroclinic effect difficult to implement as small variations in temperature can have significant effects on performance. **W317**, however, has a relatively temperature independent e_c as you approach the SmA* to SmB* transition as shown in Figure 2.3. The lack of a SmC* phase is thought to be the origin of the temperature independent electroclinic tilt susceptibility.

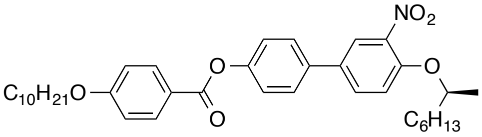

W317

I - 76 °C - SmA* - 23 °C - SmB* - -7 °C - Cr

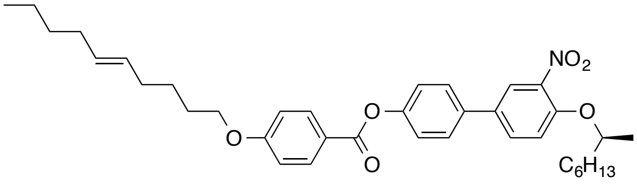

W415

I - 34 °C - SmA* - 26 °C - SmC* - 0 °C - Cr

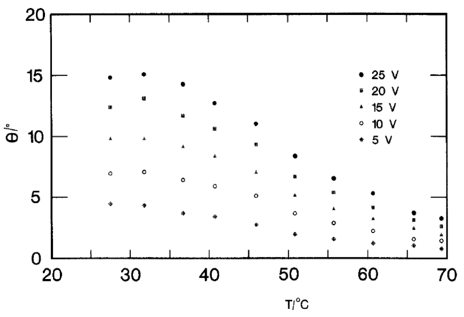

Figure 0.3 Electroclinic response of W317[14]

2.2.1.3 W415

W415 is remarkably similar to **W317** except that an *E*-5 unsaturation has been introduced to the decyloxy tail.[15] As a result **W415** forms a de Vries SmA* phase, which is surprising as an alkene is not expected to be a strong out-of-layer suppressing group. The electroclinic response of **W415**, which is typical of a de Vries SmA* material, as a function of temperature is shown in Figure 2.4. There are a few possible mechanisms by which an alkene can suppress out-of-layer fluctuations. First, weak π-π interactions could help segregate the double bond into pseudo layers, however, since the LC can align either parallel or anti-parallel with respect to neighbouring molecules, it may not be a significant factor. Secondly, shape anisotropy may play an important role. 1-butene can be used as a model system to examine the conformations of the *E*-5-decene tail near the unsaturation. Figure 2.5 shows the stable conformations of 1-butene and their relative energies in the gas phase.[16] The *skew* conformation resembles the anti conformation of an n-alkane, but with a kink, which may suppress out-of-layer fluctuations. The *syn* conformation, which is only 0.5 kcal/mol higher in energy than the *skew* conformation, is significantly more bent and should suppress out-of-layer fluctuations. In a condensed phase the *syn* conformation could be higher in relative energy than in the gas phase, suggesting that the *skew* conformation likely dominates. Regardless, the *E*-5 decenyloxy tail shows promise for next generation de Vries materials with clearing points significantly lower than their saturated homologues, although they show narrower SmA* phases than the saturated analogues.

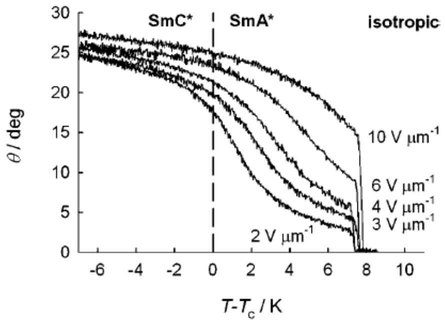

Figure 0.4 Electroclinic response of W415[17]

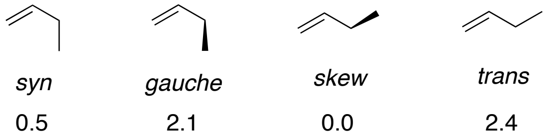

Figure 0.5 Conformational analysis of 1-butene. This is a model for how the E-5-decenyloxy tail of W415 behaves near the unsaturation.

2.3 Design principle & synthesis

The primary goal of this research was to thoroughly investigate structure-property relations and optimize the core for implementation in new de Vries materials. **W415** and **W530** gave a basic scaffold on which a series of compounds could be synthesized. The core consists of three phenyl rings with one ester linkage and an alkoxy group at each periphery. This combination can be assembled in four unique ways (Figure 2.6). The stereopolar unit consists of a lateral trifluoromethyl group *ortho* to a unichiral 2-O-methylheptyloxy group. Trifluoromethyl was chosen for its chemical stability and large transverse dipole to induce high polarization, a property desirable for next-generation FLCs. The second tail for the series would be either n-decyloxy, employed in **W317**, *E*-5-decenyloxy, employed in **W415** and 7,7,8,8,9,9,10,10,10-nonafluorodecyloxy, employed in **W530**. While materials possessing an n-decyloxy tail are not expected to show the de Vries SmA* phase, due to lack of a strong nano-phase segregating moiety, they could show the rare anti-de Vries SmA* phase or other interesting electrooptic properties similar to those observed in **W317** *(vide supra*). The other two tails should promote de Vries SmA* phases and it may be possible to determine which tail is a stronger de Vries SmA* promoting moiety.

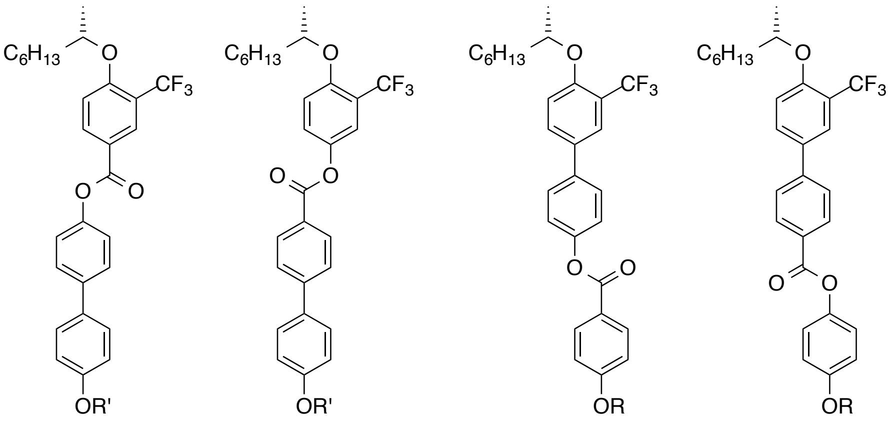

Core A **Core B** **Core C** **Core D**

Figure 0.6 The four isomers of a phenyl, biphenyl linked by an ester that possesses a trifluoromethyl ortho to a 1-methylheptyloxy tail.

The first series of compounds is built on the 4-(4-phenyloxy) phenyl trifluromethylalkoxyphenyl benzoate core (**Core A**). The synthesis of this series is shown in Scheme 2-1. 2-trifluoromethyl phenol, **1**, was brominated using NBS to afford **2** followed by Mitsunobu coupling[18] with (*R*)-2-octanol to afford **3**. The aryl bromide, **3**, was treated with n-butyl lithium and trapped with solid carbon dioxide followed by an acid workup. The resultant benzoic acid derivative **5** was then coupled to three mono-alkylated biphenol derivatives (*i.e.* n-decyloxy, E-5-decenyloxy and 7,7,8,8,9,9,10,10,10-nonafluorodecyloxy) via Steglich coupling[19] to afford **W551**, **W659** and **W667.**

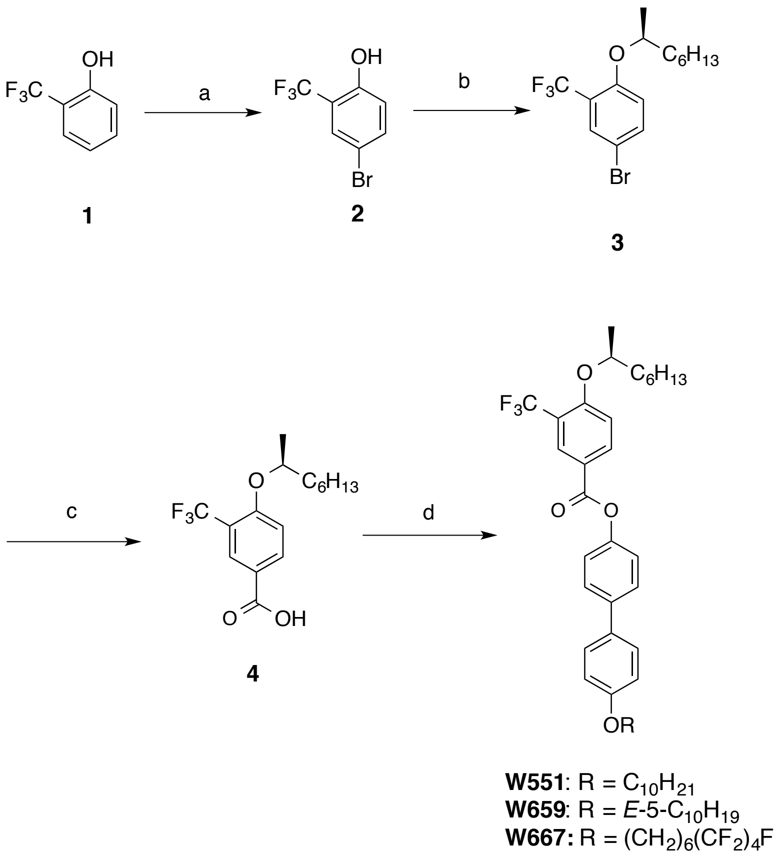

Scheme 0-1 a) NBS, HBF_4 • Et_2O, CH_3CN b) (R)-2-octanol, $P((Ph)_3)_4$, DEAD, THF c) $^{n}BuLi$, THF, CO_2, $HCl_{(aq)}$ d) 4-(4-alkoxyphenyl)phenol, DCC, DMAP, CH_2Cl_2

The second series is built on the 3-trifluoromethyl-4-alkoxyphenyl 4-(4-phenyloxy)phenyl benzoate core (**Core B**), the same core as **W530.** The synthesis of this series is shown in Scheme 2-2. Aryl bromide, **3**, was treated with n-butyl lithium, trapped with trimethylborate and worked up with peroxides to afford the hydroquinone derivative **5**. **5** was then coupled to the three alkoxybiphenyl acids (*i.e.* n-decyloxy, E-5-decenyloxy and 7,7,8,8,9,9,10,10,10-nonafluorodecyloxy) via Steglich coupling[19] to afford **W652**, **W657** and **W530**.

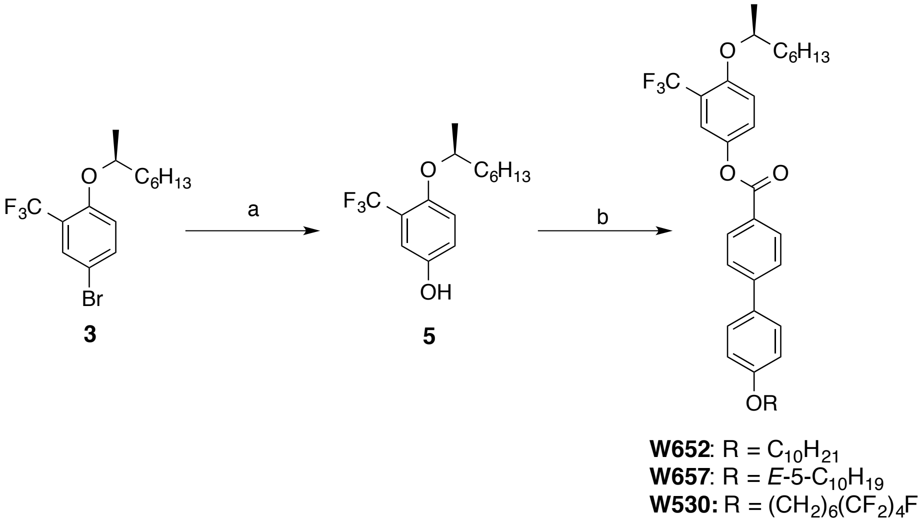

Scheme 0-2 a) ^{n}BuLi, THF. B(OMe)$_3$, H_2O_2, NaOH, H_2O b) 4-(4'-alkoxyphenyl)benzoic acid, DCC, DMAP, CH_2Cl_2

The third set of compounds is built on the 4-(4-alkoxy-3-trifluoromethylphenyl)phenyl-4-alkoxybenzoate core (**Core C**), which is the same as **W317** and **W415**, except the nitro group has been replaced with a trifluoromethyl group. The synthesis of this series is shown in Scheme 2-2. Aryl bromide, **3,** was treated with n-butyl lithium and trapped with trimethyl borate to afford **6**. This was then coupled to 4-benzyloxybromobenzene in the presence of tetrakis (triphenylphosphine) palladium (0)[20] to afford **7**. The benzyl protecting group was removed via hydrogenation in the presence of palladium on charcoal to afford **8**. The mono-alkylated biphenol derivative, **8**, was coupled to three 4-alkoxybenzoic acid derivatives (*i.e.* n-decyloxy, E-5-decenyloxy and 7,7,8,8,9,9,10,10,10-nonafluorodecyloxy) via Steglich coupling[19] to afford **W558**, **W661** and **W668**.

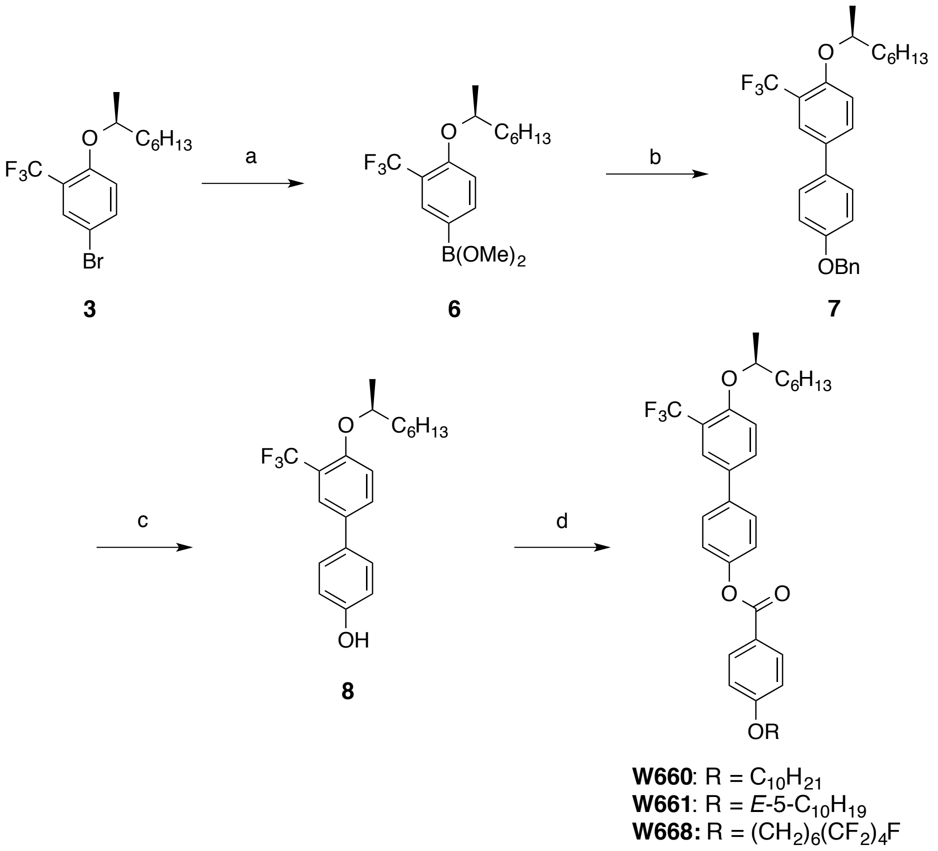

Scheme 0-3 a) ^{n}BuLi, THF, $B(OMe)_3$, MeOH b) 4-benzyloxybromobenzene, $Pd(P(Ph)_3)_4$, Na_2CO_3, H_2O, THF c) H_2, Pd/C, EtOH, $CHCl_3$ d) 4-alkoxybenzoic acid, DCC, DMAP, CH_2Cl_2

The fourth set of compounds is built upon the 4-alkoxyphenyl 4-(3-trifluoromethyl-4-alkoxyphenyl)benzoate scaffold (**Core D**). The synthesis of this series is shown in Scheme 2-2. Boronic ester derivative, **6**, was coupled to methyl 4-iodobenzoate in the presence of tetrakis (triphenylphosphine) palladium (0)[20] to afford the biphenyl derivative **9**. The methyl ester was cleaved by hydrolysis to afford **10**, which was subsequently coupled to three mono-alkylated hydroquinone derivatives (*i.e.* n-decyloxy, *E*-5-decenyloxy and 7,7,8,8,9,9,10,10,10-nonafluorodecyloxy) via Steglich coupling[19] to afford **W665**, **W666** and **W669**.

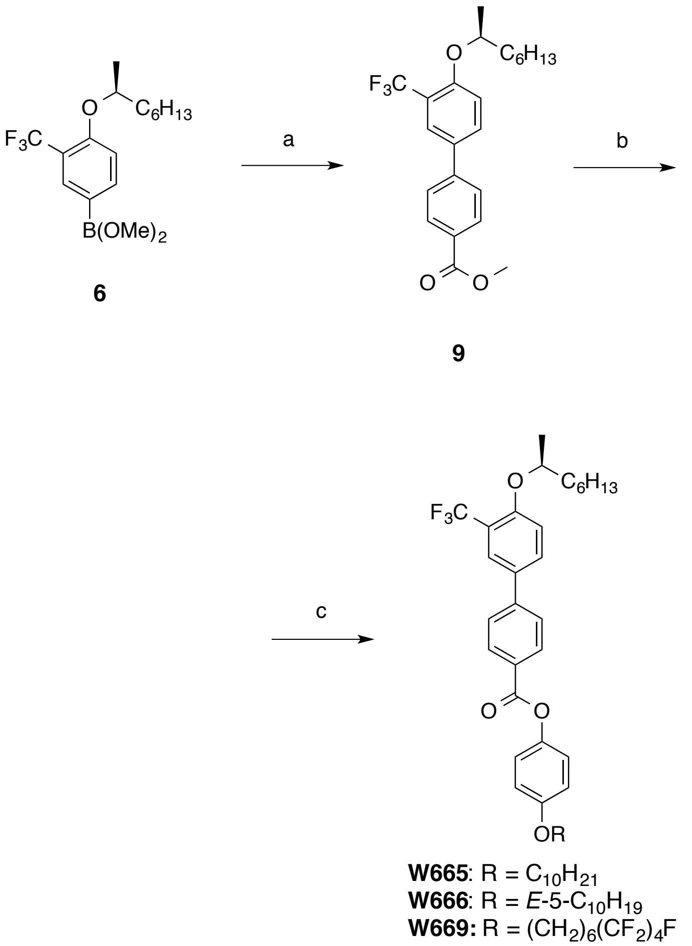

Scheme 0-4 a) methyl-4-iodobenzoate, $Pd(P(Ph)_3)_4$, Na_2CO_3, H_2O, THF b) NaOH, H_2O, EtOH c) phenol, DCC, DMAP, CH_2Cl_2

W317 and **W415** have shown interesting properties in the SmA* phase. **W415** shows the de Vries SmA* phase, suggesting that the core could be an interesting scaffold to develop new de Vries materials. The semi-fluorinated tail employed in **W530** was used on the **W317/W415** core and is expected to possess the SmA* phase. The mono-alkylated nitrobiphenol derivative, **11,** was coupled to 4-7,7,8,8,9,9,10,10,10-nonafluorodecyloxybenzoic acid under Steglich coupling[19] conditions to afford **W705**.

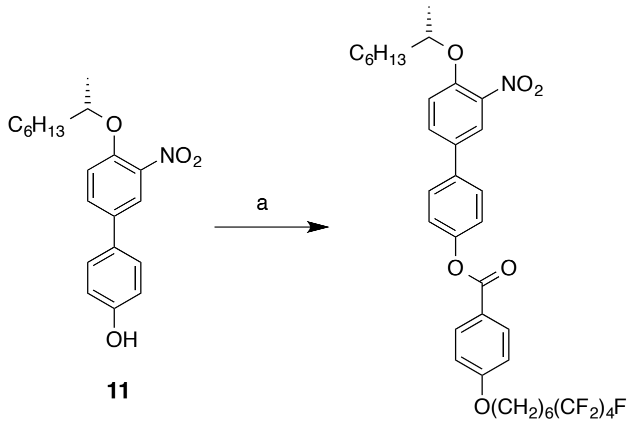

11

W705

Scheme 0-5 a) 4-7,7,8,8,9,9,10,10,10nonafluorodecyloxybenzoic acid , DCC, DMAP, CH_2Cl_2

2.4 Core Optimization

2.4.1 Core A

2.4.1.1 W551

W551 employs an n-decyloxy tail on **Core A** and has been reported with phase transitions, but without other physical properties.[21] **W551**, by DSC, shows an enantiotropic I – SmC* phase transition at 49 °C which then transitions to a second phase at 29 °C. The DSC of **W551** is shown in Figure 2.7. The I-SmC* phase transition is lower than the 55 °C reported, however, the phase transition temperature observed by X-ray is 54 °C, which is much closer to the literature value.[22] The low temperature SmX phase was previously unreported. The enthalpy of transition from the SmC* to the SmX phase is very small and thus not likely a crystal phase. The X-ray layer spacing the SmC* phase is 29.5 Å and is nearly constant over the entire temperature range. At 34 °C the layer spacing increases to 31 Å. Since this layer spacing is significantly shorter than the molecular length the SmX phase is could be a higher order SmC* phase (e.g. SmI, SmF). The X-Ray layer spacing of **W551** is shown in Figure 2.8.

Since **W551** lacks a SmA* phase, and the alignment in commercial liquid crystal cells was very poor, electrooptic properties were not investigated.

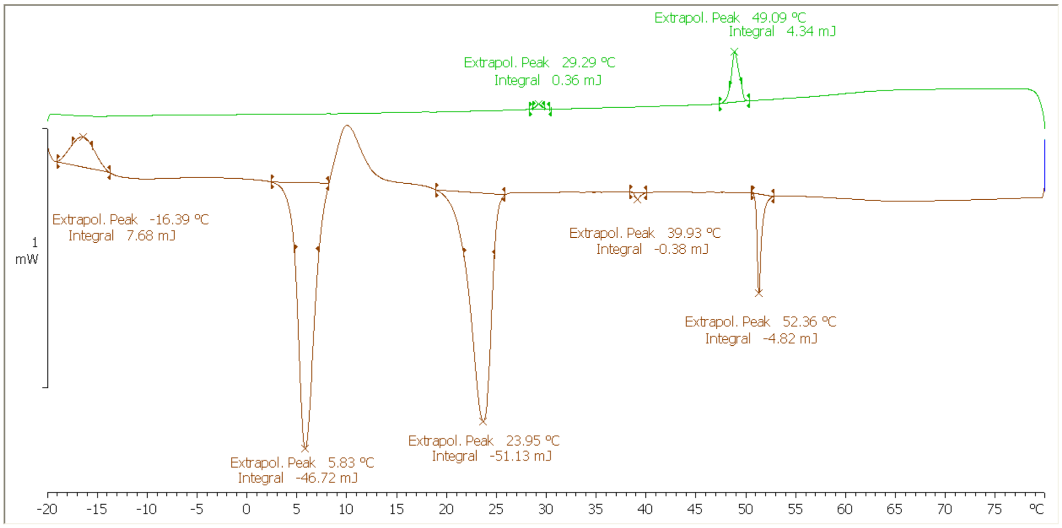

Figure 0.7 DSC of W551

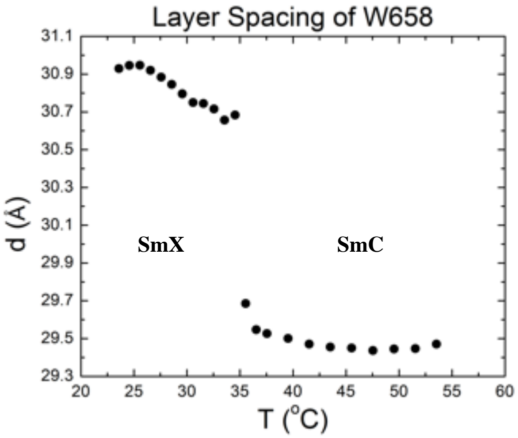

Figure 0.8 Layer spacing of W551 as a function of temperature.

2.4.1.2 W659

W659 employs an *E*-5-decenyloxy tail on **Core A** and is a novel material. **W659**, by DSC, shows an enantiotropic I – SmC* phase transition at 30 °C which then transitions to a second phase at 8 °C. The I - SmC* phase transition is lower than the 55 °C of **W658**, this is consistent with a lower clearing point for the *E*-5decenyloxy tail relative to the decyloxy tail observed in **W415** and **W317**, respectively. The DSC of **W659** is shown if Figure 2.9. The enthalpy of transition from the SmC* to the X phase is large and the low temperature X phase could be a crystal phase. The layer spacing in the X phase was not determined, since it is impractical to obtain data well below room temperature. The X-ray layer spacing the SmC* phase is 26.5 Å and is nearly constant over the entire temperature range. This suggests a SmC* phase that is more tilted than **W658** since there is a 3 Å difference in the layer spacing, which is much larger than the expected molecular length difference. The X-Ray later spacing as a function of temperature is shown in Figure 2.10.

Since **W659** does not show a SmA* phase, and the SmC* phase shows very poor alignment in commercial liquid crystals cells, its electrooptic properties were not explored.

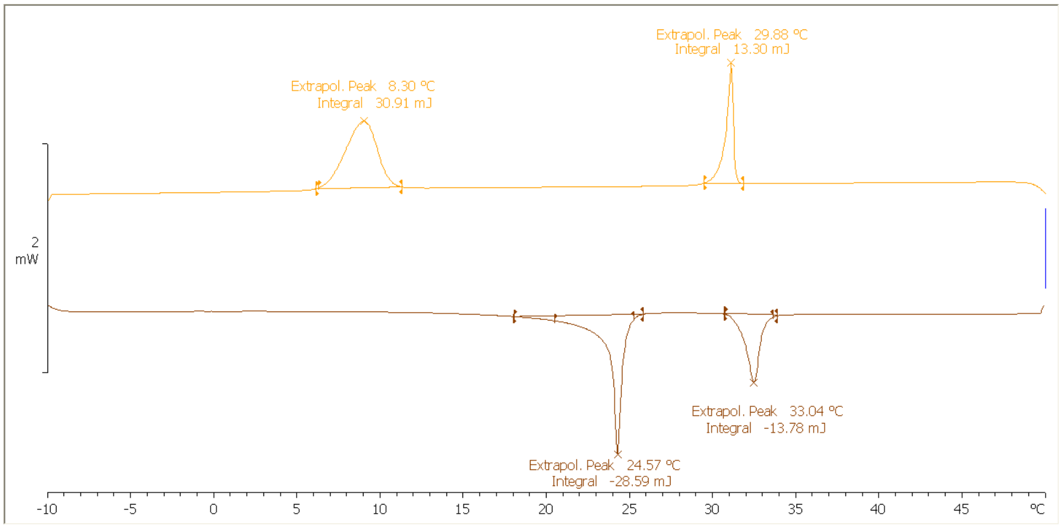

Figure 0.9 DSC of W659

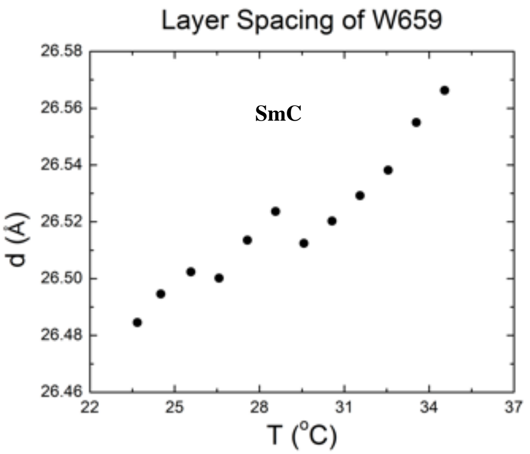

Figure 0.10 Layer spacing of W659 as a function of temperature.

2.4.1.3 W667

W667 possesses **Core A** scaffold with the same semi-fluorinated tail employed in **W530** and is a novel compound. **W667**, by virtue of a strongly out-of-layer suppressing moiety, is expected to show the de Vries SmA* phase, if it possesses the SmA* phase. By DSC there is an isotropic liquid to an unidentified smectic phase at 72 °C. This phase transitions into a second phase at 71 °C. The DSC of **W667** is shown in Figure 2.11. The high temperature phase is difficult to characterize due to the narrow temperature range, however, observations in PLM suggest that it is a SmC* phase like analogues **W551** and **W667**. The low temperature phase is an isotropic glassy phase, evidenced by low birefringence and no longer being able to easily shear the sample on a glass slide with cover slip. The exact nature of this phase has not been explored.

Since **W667** does not possess a SmA* phase the electrooptics were not explored. **Core A** does not seem suitable for developing new de Vries materials.

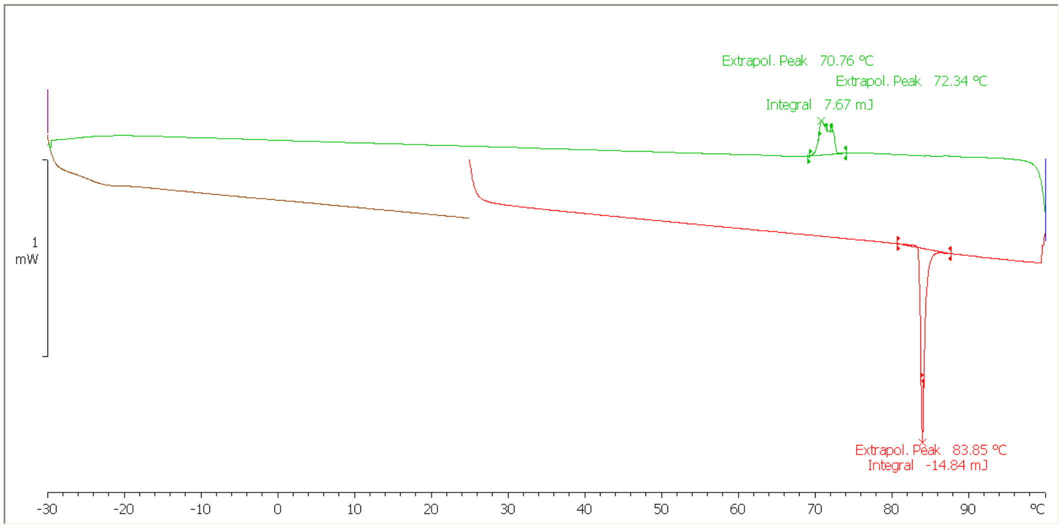

Figure 0.11 DSC of W667

2.4.2 Core B

2.4.2.1 W652

W652 is built on **Core B**, the same core as **W530**, but incorporates an n-decyloxy tail. **W652** is not predicted to possess a de Vries SmA* phase as the only moiety that suppresses out of layer fluctuation is the 2-O-methylheptyloxy tail, which in other systems (*e.g.* **W317**) has been ineffective at promoting de Vries SmA* behaviour. It may, however, show interesting electrooptics, such as temperature insensitivity of the electroclinic tilt susceptibility, shown by **W317**.[13]

W652 possesses enantiotropic SmA* and SmC* phases. The SmA* forms from the isotropic melt at 79 °C, transitions to the SmC* at 50 °C and crystallizes at 33 °C. The SmA* - SmC* phase transition appears to be very weakly first order, which is consistent with a traditional SmA* phase transitioning to the SmC* phase (Figure 2.12). The phase transition temperatures were recorded by DSC and are about 3 K lower than transitions observed by POM. The X-Ray layer spacing of **W652** (Figure 2.13) suggests that, surprisingly, it could possess the de Vries SmA* phase. The layer spacing of **W652** increases from 34.5 Å at 87 °C to 35.7 at 55 °C, which corresponds to 0.006 Å K^{-1}. Layer expansion is common in the traditional SmA* phase. The layer expansion in **W652**, however, is very small (ca. 3%) which is much smaller than the 10% seen in **W317**. De Vries materials, such as **W530** and **W415**, typically show almost no change in layer spacing in the SmA* phase. A series of de Vries materials synthesized by the Lemieux group (Figure 2.14a) have shown large layer expansion in the SmA* phase (Figure 2.14b), suggesting that the de Vries SmA* phase does not necessarily require a flat layer spacing profile.[23] These materials, however, form partial bilayers and show anomalous expansion in the SmC* phase. Additionally, at the SmA* - SmC* phase transition the layer spacing is 35.7 Å, which is significantly shorter than the estimated molecular length of 37.8 Å. In the SmC* phase the layers contract to 33.6 Å at T-$T_{A\text{-}C}$ = -10 K, which is a layer shrinkage of ca. 6%.

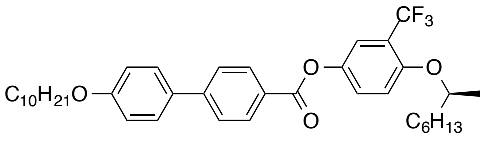

W652

I - 80 °C - SmA* - 50 °C - SmC* - 33 °C - Cr

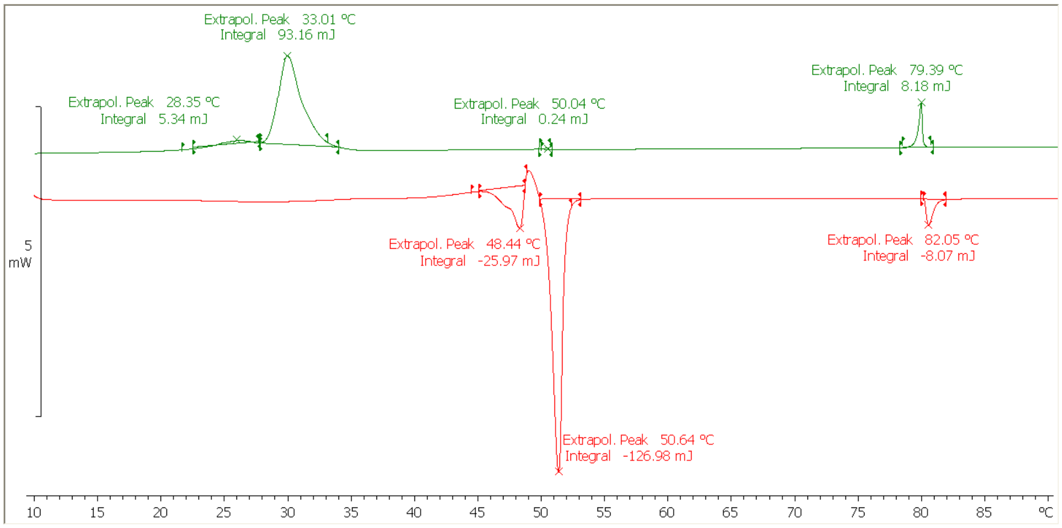

Figure 0.12 DSC of W652

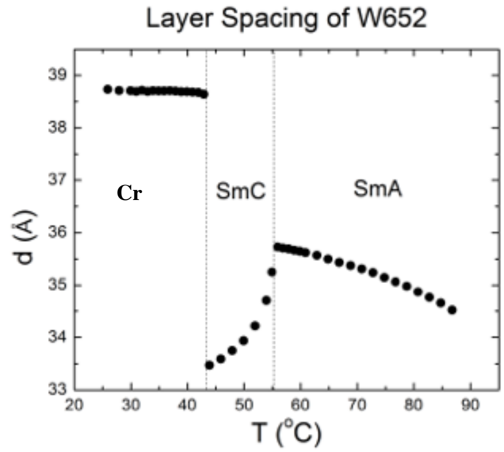

Figure 0.13 Layer spacing of W652 as a function of temperature.

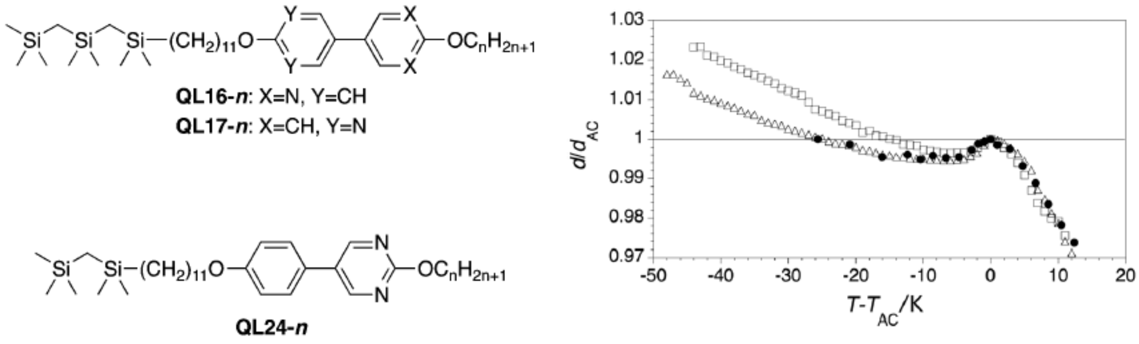

a) b)

Figure 0.14: a) Representative compounds synthesized by the Lemieux group that show significant layer expansion in the SmA phase and anomalous expansion in the SmC phase. b) Ratio of X-Ray Layer spacing to the Layer spacing at the SmA - SmC phase transition, showing expansion of the layer spacing in de Vries SmA materials.[23]

The electro-optics of **W652** add further evidence to it being a de Vries SmA* material. The electroclinic tilt becomes apparent at ca. 82 °C, approximately 30 K above the SmA* to SmC* phase transition. The electroclinic tilt as a function of applied field for **W652** at various temperatures is shown in Figure 2.15. In most traditional SmA* materials there is a very small electroclinic tilt which becomes apparent very close to the SmA* - SmC* phase transition. **W652** lacks a strongly first order SmA* - SmC* phase transition and thus does not show a sigmoidal response, or double-peak profile in the current reversal, with increasing applied field near the SmA* - SmC* phase transition, as observed in **W530**. The saturated tilt angle of **W652** is 26^{o} and larger than the 20^{o} X-Ray tilt calculated from the molecular length and layer spacing at the SmA* - SmC* phase transition. Saturated electroclinic tilt is achieved at ca. 3 K above the SmA* - SmC* phase transition with an electric field of ca. 25 V μm^{-1}, indicating a strong electroclinic effect. The saturated tilt of **W652** is larger than the 16^{o} of **W317**[13] and less than the 33^{o} of chemically similar **W530**[8], which is a prototypical de Vries SmA* material. The birefringence increases from 0.155, with no applied field, to 0.165, at 25 V μm^{-1}, at T-T$_{A\text{-}C}$ = 3 K. This is an increase of 7%, which is much less than the 30% observed in **W530**. The birefringence of **W652** as a function of applied field at various temperatures is shown in Figure 2.16. This increase, however, is relatively large relative to traditional SmA* materials, which show no increase in birefringence with applied field. There is a small increase in birefringence at T-T$_{A\text{-}C}$ = -5 K to 0.167. **W652** shows a field-induced polarization of 51 nC cm^{-2} at T-T$_{A\text{-}C}$ = 1 K and shows linear behaviour with increasing electric field (Figure 2.17). The polarization is expected to show the same shape of curve as the birefringence and electroclinic tilt as explained by a simple Langevin model.[24] The induced polarization is not evident further away from the SmA* - SmC* phase transition. The P$_{S}$ of **W652** is ca. 94 nC cm^{-2} with a tilt of 27^{o} at T-T$_{A\text{-}C}$ = -5 K. The polarization in the SmA* phase is relatively small even as you approach the SmA*-SmC* phase transition.

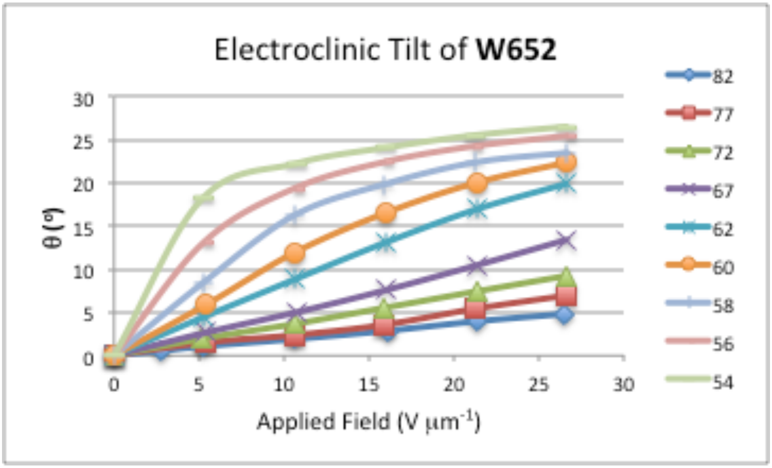

Figure 0.15 The electroclinic tilt of W652 as a function of applied field at various temperatures in the SmA* phase

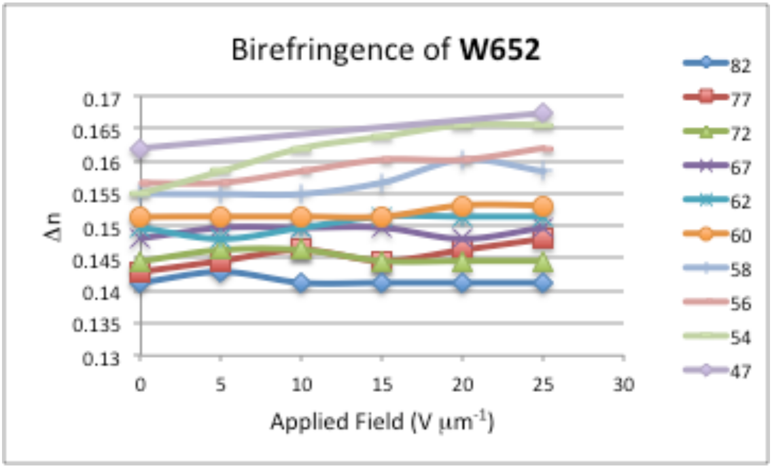

Figure 0.16 The birefringence (Δn) of W652 as a function of applied field at various temperatures in the SmA* phase.

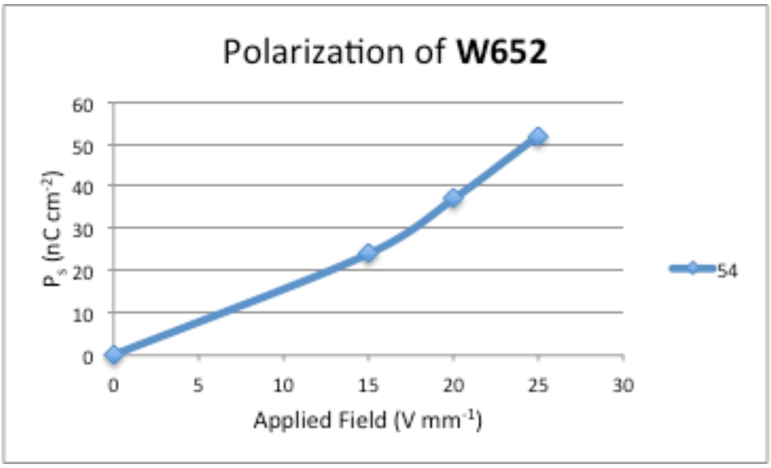

Figure 0.17 Field-induced polarization of W652 at T-T_{A-C} = 1 K.

2.4.2.2 W657

W657 possesses **Core B** with the same *E*-5-decenyloxy tail employed in **W415**. This compound increases the number of liquid crystals incorporating the *E*-5-decenyloxy tail. This is of particular interest since the *E*-5-decenyloxy tail may be strongly de Vries promoting, based on **W415.** On cooling from the isotropic melt the SmA* phase forms at 40 ^{o}C and transitions to the SmC* phase at 28 ^{o}C. No further phase transitions are observed on cooling to temperatures as low as -30 ^{o}C (Figure 2.18). The phase transitions recorded by DSC are about 2 K lower than transitions observed by POM. The SmA* to SmC* phase is strongly first order, which is common for de Vries SmA* materials. The layer spacing in the SmA* phase, which is nearly constant at ca. 32 Å from 45 ^{o}C to 33 ^{o}C (Figure 2.19), is significantly shorter than the molecular of 37.5 Å estimated by a combination of *ab initio* methods and the layer spacing of **W317** at the SmB* to crystal phase transition. The layer spacing of **W657** is shorter than the 33.8 Å of the prototypical de Vries compound **W530**, which also possesses **Core B**. This difference is not particularly large, as the semi-fluorinated tail is expected to be ca. 0.7 Å longer than the E-5-decenyloxy tail. The layer spacing of **W657** is also significantly shorter than the layer spacing of **W652** in the SmA* phase, suggesting a larger tilt. The layer spacing at T – $T_{A\text{-}C}$ = -10 K is 29.8 Å, which corresponds to a layer shrinkage of ca. 7%.

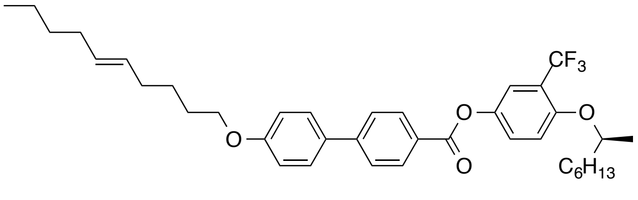

W657

I - 40 ^{o}C - SmA* - 28 ^{o}C - SmC*

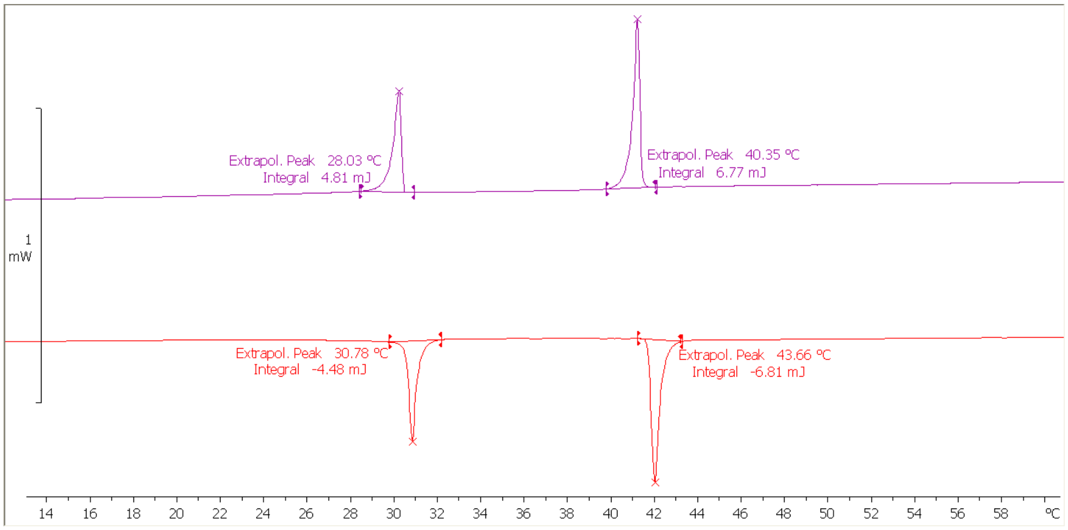

Figure 0.18 DSC of W657

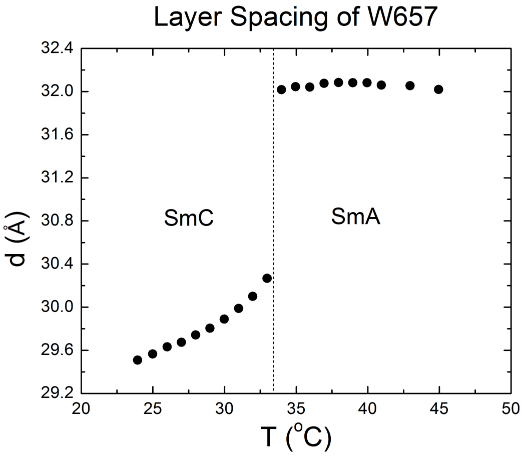

Figure 0.19 Layer spacing of W657 as a function of temperature.

The electrooptics of **W657** are consistent with a de Vries SmA* material that shows a strongly first order phase transition from the SmA* to SmC* phase. The tilt vs. applied field curve shows a strongly sigmoidal response, as shown in Figure 2.20. The saturated electroclinic tilt is approximately 33° and is achievable ca. 5 K above the SmA*-SmC* phase transition, indicating a very strong electroclinic effect. The electroclinic effect of **W657** is larger than the 26° observed in **W652**, which is also de Vries, which is expected as the smaller layer spacing of **W657** suggests that it is more tilted. **W657** shows the same saturated electroclinic tilt as **W530**. The optical tilt of **W657** is slightly larger than the calculated X-Ray tilt of 31°. The birefringence of **W657** behaves in a sigmoidal manner, much like electroclinic tilt. At ca. 7 K above the SmA* to SmC* transition, at higher applied fields, non-linear behaviour is observed as the material begins to transition to a field-induced SmC* phase. The birefringence of **W652** at $T-T_{A-C} = 1$ K changes from 0.120 at no applied field to 0.160 at 25 V μm^{-1}, a change of ca. 25%. This change is very large and close to the 30% observed in the prototypical de Vries compound **W530**. The 25% change is significantly larger than the 7% increase observed in **W652**, suggesting that compounds that show first order SmA* - SmC* phase transitions show larger birefringence changes. The birefringence of **W657** as a function of applied field at various temperatures is shown in Figure 2.21. This could result from an incomplete bias of the azimuthal angle in materials with weakly first order phase transitions, evidenced by a single peak in the polarization reversal current. The polarization reversal current in the SmA* phase of **W657** shows a double-peak response, consistent with a strongly first order SmA* - SmC* phase transition. The maximum field-induced polarization is ca. 200 nC cm^{-2} (Figure 2.22). The polarization vs. applied field curve is expected to strongly resemble the electroclinic tilt and birefringence vs. applied field curves.[24] Due to equipment malfunction, data at low applied field could not be obtained. Efforts are ongoing to collect data in the low field regime. The P_S of **W657** at $T-T_{A-C} = -5$ K is 210 nC cm^{-2} with a tilt of 36°. The polarization is almost twice as large as observed in **W652** and **W530**.

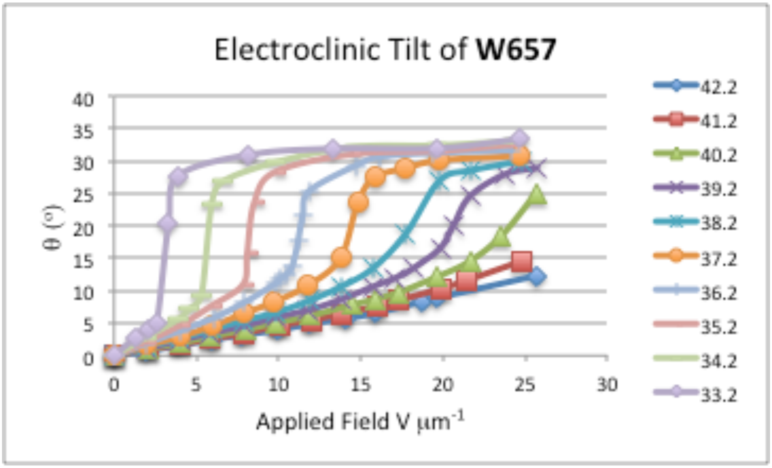

Figure 0.20 The electroclinic tilt of W657 as a function of applied field at various temperatures in the SmA* phase.

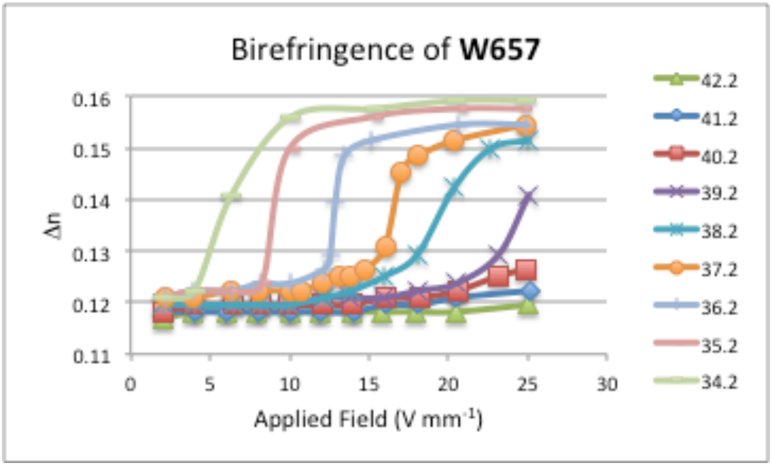

Figure 0.21 The birefringence (Δn) of W657 as a function of applied field at various temperatures in the SmA* phase.

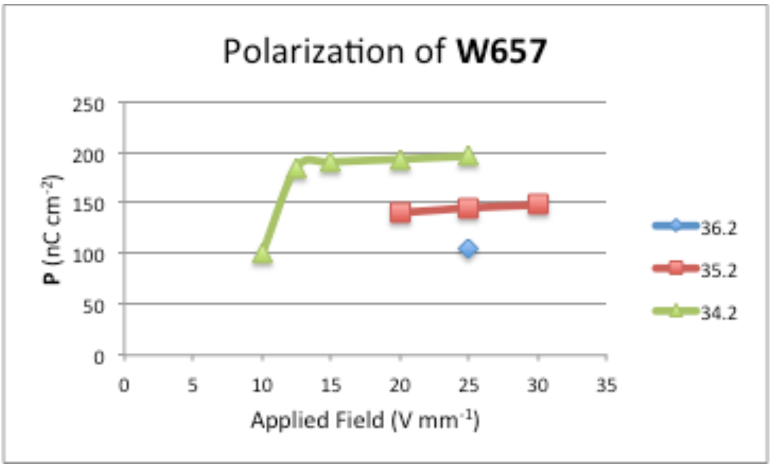

Figure 0.22 The field-induced polarization of W652 as a function of applied field at various temperatures in the SmA* phase.

2.4.2.3 W530

W530 transitions from the isotropic liquid phase to the de Vries SmA* phase at 92 °C, which transitions to the SmA* phase at 46 °C. The layer spacing of **W530** is relatively constant at 33.7 Å in the SmA* phase and shows a layer shrinkage of ca. 3% at $T\text{-}T_{A\text{-}C} = -10$ K (Figure 2.23). The saturated tilt of **W530** in the SmA* phase is 33° (Figure 2.24a), which is larger than the estimated X-Ray tilt of 28°. The birefringence shows an increase of 30% with increasing field near the SmA* - SmC* phase transition (Figure 2.24b). The polarization in the SmC* at $T - T_{A\text{-}C} = -5$ K is 105 nC cm^{-2}, which is about 50% of that of **W652** at the same reduced temperature.[8,25]

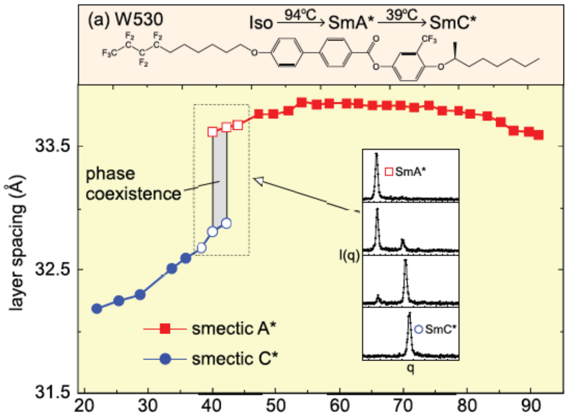

Figure 0.23 X-Ray layer spacing of W530[25]

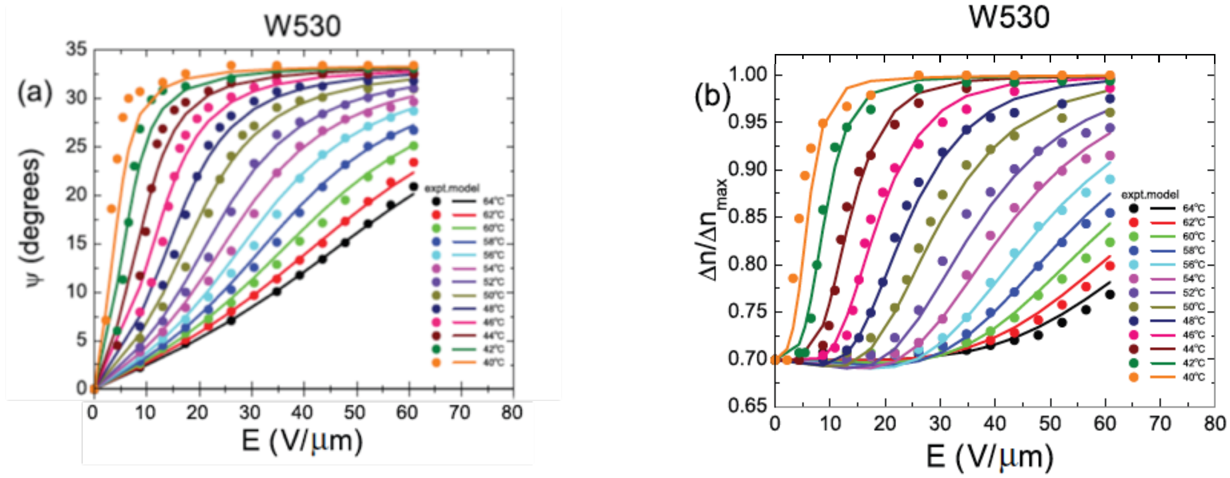

Figure 0.24 a) Electroclininc tilt of W530 as a funtion of applied field at various temperatures. b) ratio of birefringence vs. maximum birefringence of W530 as a function of applied field at various temperatures.[25]

2.4.3 Core C

2.4.3.1 <u>W558</u>

The third series of compounds employs the same core as **W317** and **W415** with a lateral trifluoromethyl group replacing the nitro group (**Core C**). This substitution improves chemical stability, as the NO_2 group is susceptible to photochemical reactions, while maintaining relatively large polarization due to the large lateral dipole. **W558**, which possesses an n-decyloxy tail, while not expected to possess the de Vries SmA* phase, is of particular interest due to the similarity to **W317**, which shows the traditional SmA* phase. This is a known material, however, the X-Ray layer spacing and electrooptical properties have not been reported.[21] On cooling, the isotropic liquid phase transitions to the SmA* phase at 48°C. The SmA* phase transitions to the SmC* phase, via a second order phase transition, at 18°C and then crystallizes at -2°C. These phase transitions were recorded by DSC, which is shown in Figure 2.25. The I – SmA* phase transition is consistent with the literature value, however, the SmA* - SmC* phase transition was not reported in the original publication.[21] Phase transitions observed by POM and X-Ray were a few degrees higher. The SmA* phase expands from 36.2 Å at 48 °C to 37.8 Å at 23 °C, which is the SmA* - SmC* phase transition, as shown in Figure 2.26. This is a ca. 6% layer expansion and such layer expansion is common in the traditional SmA* phase. The layer spacing near the SmA*-SmC* phase transition is identical to the 37.8 Å of **W317** at the SmB* - crystal phase transition. Interestingly, **W652** shows less layer expansion than **W558** and the layer spacing at the SmA* - SmC* phase transition in 2 Å shorter. This comparison of the layer spacing suggest that **W558** is behaves more like **W317** than **W652**, and thus possesses a traditional SmA* phase. The SmC* phase has a layer spacing of 36.3 Å at $T-T_{A-C}$ = -10 K, which corresponds to a layer shrinkage of ca. 5%.

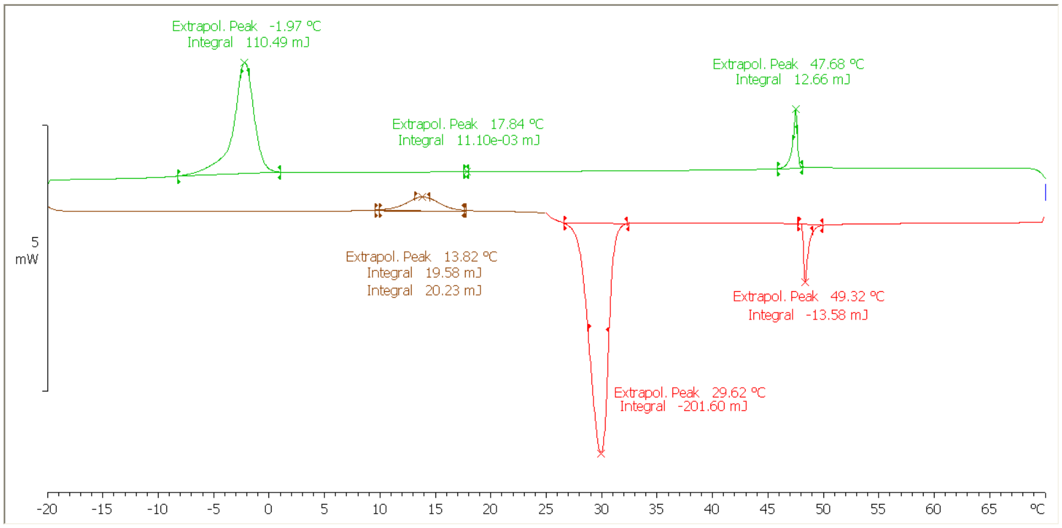

Figure 0.25 DSC of W558

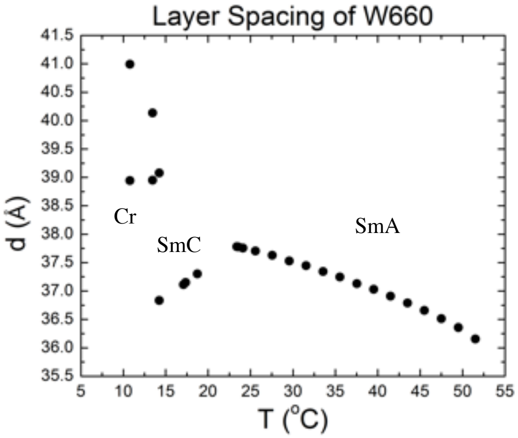

Figure 0.26 Layer spacing of W558 as a function of temperature.

The electrooptics of the SmA* phase of **W558** were not explored. Electrooptic measurements below room temperature are particularly difficult with the microscope setup, since the hot stage is heated and cooled simultaneously which creates large temperature gradients through the cell. The temperature sensor is far from the sample and severe suppression of the isotropic - SmA* phase transition (as much as 10 K) is observed when using the chiller. This is unfortunate, since **W558** could show interesting properties, such as non-divergent electroclinic tilt and an anti-de Vries electroclinic tilt, like the chemically similar **W317**. If a cooling system, which could be set to a temperature, without a heating offset could be acquired the electrooptic properties could be reliably measured.

2.4.3.2 W661

W661 is built on the **Core C** scaffold and employs an *E*-5-decenyloxy tail. This is chemically identical to **W415** except the lateral nitro group is replaced with a trifluoromethyl group. **W661** transitions from an isotropic liquid to a smectic phase at -17 ^{o}C. The DSC of W661 is shown in Figure 2.27. The nature of this phase was not studied as it is in an impractical temperature range. Like **W558, W661** shows suppression of the isotropic - SmA* phase transition relative to the lateral nitro analogue. The ca. 50 K depression is likely a result of the significantly larger lateral group, as the van der Waals radius of trifluoromethyl is ca. 42.6 cm^{3} mol^{-1} while nitro has a van der Waals radius of 18 cm^{3} mol^{-1}.[26] The larger trifluoromethyl group likely suppresses mesogenicity by preventing the cores from close-packing in a smectic phase.

The electrooptics of **W661** were not explored, as measurements below room temperature are impractical (*vide supra*).

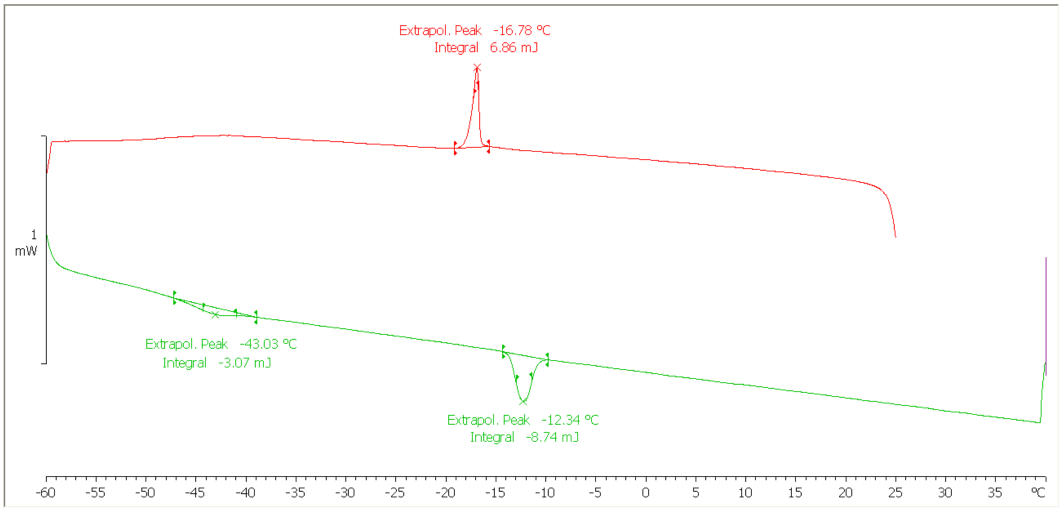

Figure 0.27 DSC of W661

2.4.3.3 W668

W668 possesses the same core as **W558** and **W661** but employs the semi-fluorinated tail used in **W530**, which is expected to promote the de Vries SmA* phase. **W668** shows an enantiotropic SmA* phase and a very broad SmC* phase, which does not crystallize as low as -50 ^{o}C. **W668** transitions from an isotropic liquid to the SmA* phase at 58 ^{o}C then to the SmC* phase at 2 ^{o}C. The DSC of **W668** is shown if Figure 2.28. The SmA* to SmC* phase transition is weakly first order, which implies that the SmA* of **W668** could be de Vries.

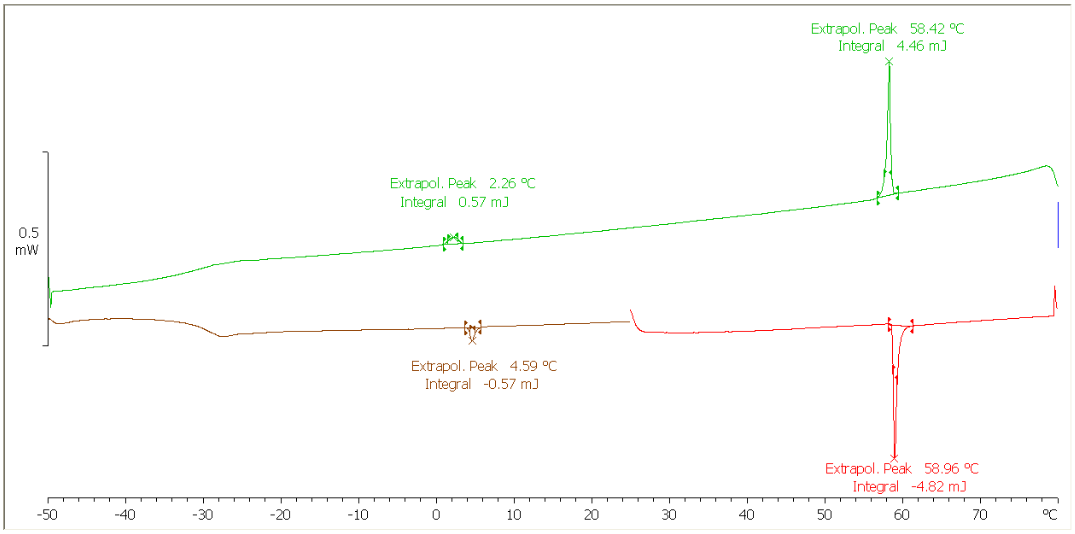

Figure 0.28 DSC of W668

The electrooptics of **W668** were not investigated due to the SmA*-SmC* phase transition being well below room temperature and measurements in this temperature regime are unreliable (*vide supra*). The electrooptic response far away from the SmA*-SmC* phase transition is expected to be linear for both traditional and de Vries SmA* materials. Even very strongly de Vries materials, such as **W657** and **W530** only begin to larger electroclinic tilts 15 K above the SmA* - SmC* phase transition.

2.4.4 Core D

2.4.4.1 W665

The fourth series of compounds is built on the **Core D** scaffold. **W665**, which employs an n-decyloxy tail, is not expected to be de Vries as it lacks nano-phase segregating units, although if **Core D** shows strong core-core correlation than it could be de Vries, like **W652**. **W665** shows a monotropic isotropic - SmA* phase transition at 38 ^{o}C which then crystallizes, slowly, at 23 ^{o}C. There is only a crystal to isotropic phase transition on heating, which occurs at 57 ^{o}C. The phase transitions temperatures of **W665** were measured by DSC, which is shown in Figure 2.29.

W665, in a 4mm liquid crystal cell, shows an isotropic liquid to crystal phase at 38 ^{o}C. As a result the electrooptics of the SmA* phase could not be investigated.

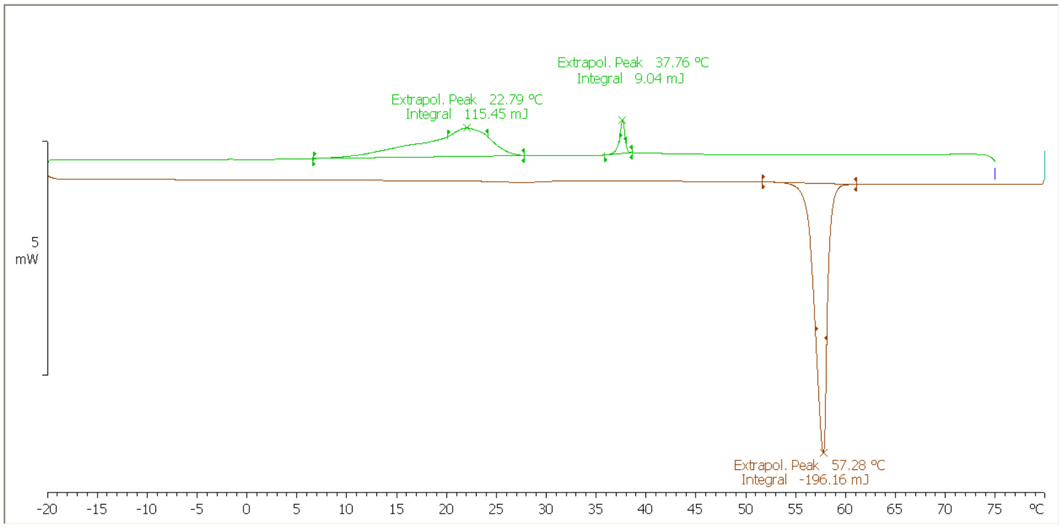

Figure 0.29 DSC of W665

2.4.4.2 W666

W666 is built on the **Core D** scaffold and possesses an *E*-5-deceneyloxy tail. **W666** transitions from a crystal phase to isotropic liquid at 43 ^{o}C, as observed by DSC. The DSC of **W666** is shown in Figure 2.30. The isotopic liquid transitions to an unknown phase at 6 ^{o}C.

The I – X phase transition occurs significantly below room temperature. The identity of the X phase was not investigated. Near room temperature, on an untreated glass slide with coverslip, there is an isotropic glassy phase, similar to that observed in **W667.** This phase transition is not observed in the DSC.

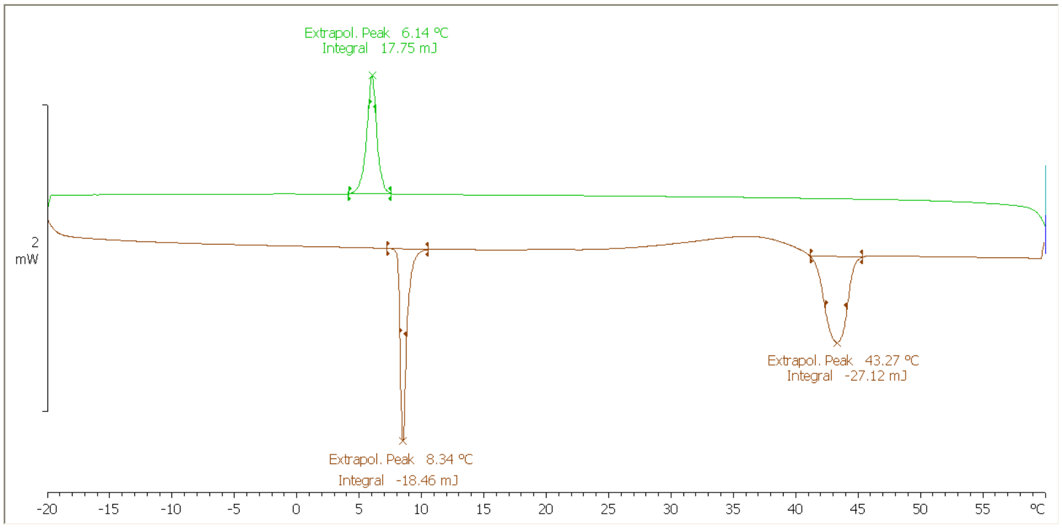

Figure 0.30 DSC of W666

2.4.4.3 W669

W669 is built on the **Core D** scaffold and possesses the 7,7,8,8,9,9,10,10,10-nonafluorodecyloxy tail. **W669** shows enantiotropic SmA* and SmC* phases, with the SmA* phase forming, from the isotropic melt, at 62 ^{o}C and the SmC* phase at 28 ^{o}C. These phase transition temperatures were measured by DSC, which is shown in Figure 2.31. The layer spacing of **W669** (Figure 2.32) increases from 33.7 Å at 60 ^{o}C to 34.1 Å at 30 ^{o}C, which corresponds to a 1% increase.This is less than **W652**, which also possesses a weakly first order SmA* - SmC* phase transition. The layer spacing in the SmA* phase is significantly shorter than the estimated molecular length of 38.3 Å, suggesting **W669** possesses the de Vries SmA* phase. Since the electrooptics of **W665** could not be investigated it is unknown whether the de Vries phase is being promoted solely by the tail, or if the core also significantly contributes, like **Core B**.

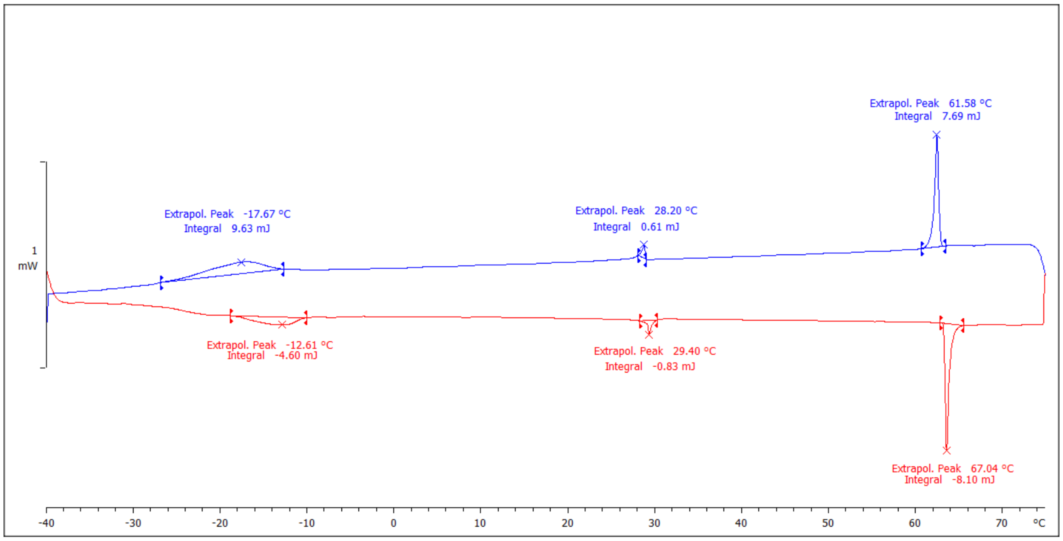

Figure 0.31 DSC of W669

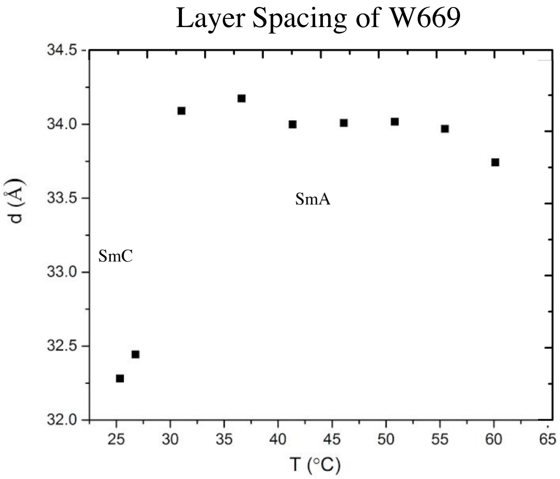

Figure 0.32 X-Ray layer spacing of W669 at various temperatures

The electrooptics of **W669** are consistent with a de Vries SmA* material that shows a weakly first order phase transition from the SmA* to SmC* phase, such as **W652**. The tilt vs. applied field does not show a sigmoidal response, as shown in Figure 2.33. The saturated electroclinic tilt is approximately 25° and is achievable ca. 3 K above the SmA*-SmC* phase transition, indicating a strong electroclinic effect. The electroclinic effect of

W669 is approximately the same as the 26^{o} observed in **W652**, which is also de Vries. **W669** shows a smaller saturated electroclinic tilt as **W530** and **W657**, which show strongly first order SmA* - SmC* phase transitions. The saturated tilt of **W669** is smaller than the calculated X-Ray tilt of 27^{o}. The birefringence of **W669**, surprisingly, behaves in a weakly sigmoidal manner at T-$T_{A\text{-}C}$ = 3 K (Figure 2.34). The birefringence of **W652** at T-$T_{A\text{-}C}$ = 1 K changes from 0.103 at 5 V mm^{-1} to 0.119 at 20 V mm^{-1}, a change of ca. 13%. This change is large, further suggesting that **W669** is de Vries, however, it is smaller than the 25% and 30% observed in prototypical de Vries compounds **W657** and **W530**, respectively. No field-induced polarization was measured in the SmA* phase. The P_s of **W669** at T – TA-C = -5 K is 77 nC cm^{-2} with a tilt of 30^{o}. The polarization is similar to the P_s observed in **W652** and **W530**.

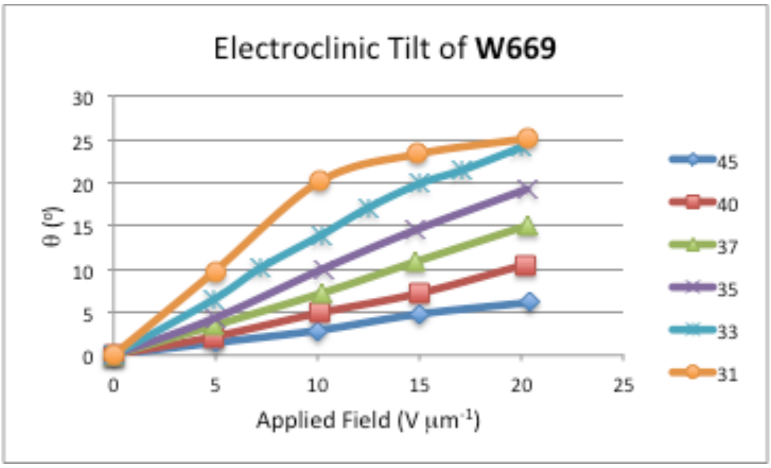

Figure 0.33 The electroclinic tilt of W669 as a function of applied field at various temperatures in the SmA* phase

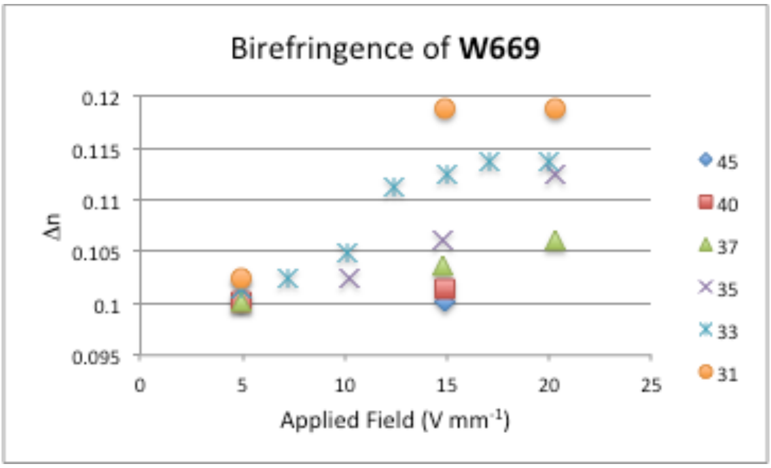

Figure 0.34 Birefringence of W669 as a function of applied field at various temperatures in the SmA* phase.

2.4.5 Conclusions

The summary of the mesophases and their transition temperatures of the compounds synthesized on the **Core A – D** scaffold is shown in Table 2.1. **Core B** shows the highest stability liquid crystals, measured by average clearing point, of the compounds investigated. This is likely a result of particularly strong core-core interactions, since the effect of the tails should be common across all series. What is particularly interesting is that **Core B** also shows the "de Vries" SmA* phases for all analogues investigated, including **W652**, which doesn't possess a tail that strongly suppresses out-of-layer fluctuations. Since core-core interactions are stronger in tilted smectics, by virtue of closer packing, it is possible that mesogens possessing **Core B** form very small aggregates of locally coherently tilted with no correlation between domains (Figure 2.1). The strong core-core interactions of Core B as the driving force for the de Vries SmA* phase is consistent with the Glaser model. Liquid crystals built on the **Core C** scaffold shows the least stable liquid crystal phases, as measured by average clearing point. This suggests that **Core C** shows the weakest core-core interactions. This is of particular note since **W558**, the trifluoromethyl analogue of **W317**, like **W317**, shows the traditional SmA* phase. The lack of strong core-core interactions reduces the propensity to tilt, and thus forms the traditional SmA* phase. Interestingly, by incorporating tails that strongly suppress out-of-layer fluctuations, such as semi-fluorinated or *E*-5-decenyl, the reduction of entropy drives the cores to interact more strongly and induce tilt and thus a de Vries SmA* phase. This phenomenon is seen in **W415** and **W705** (*vide infra*). Mesogens build on **Core A** and **Core D** do not reliably show the SmA* and SmC* phases. **W699**, which is built on Core D, is the only compound from either series that shows both the SmA* and SmC* phase. It shows the de Vries SmA* phase, however, it is unknown how strong of a de Vries promoting group the core is since W665 and W666 do not show the SmA* and SmC* phase.

Stereopolar Unit	Compound	Phase Transitions on Cooling (°C)
Core A	**W658**	I - 49 - SmC* - 29 - SmX$_2$
	W659	I - 29 - SmC*
	W667	72 - SmC* - 71 X$_2$
Core B	**W652**	I - 79 - SmA* - 50 - SmC* - 33 - Cr
	W657	I - 40 - SmA* - 28 - SmC*
	W530	I - 90 - SmA* - 54 - SmC*
Core C	**W660**	I - 48 - SmA* - 18 - SmC*- -2 - Cr
	W661	I - (-17) - SmX
	W668	I- 58 - SmA* - 2 - SmX
Core D	**W665**	38 - SmA* (monotropic)
	W666	I - 6 - SmA*
	W669	I – 63 – SmA* – 30 SmC*

Table 0.1 Phase transitions for compounds built on the Core A, Core B, Core C and Core D scaffolds.

An interesting set of related compounds are **W697** (discussed in detail in Chapter 3) and **W702**[27,28]. These compounds differ in the orientation of the ester linkage between the biphenyl and phenyl units and which core moiety possesses the chiral tail. These compounds, **W697** and **W702**, are analogues of **W652,** a de Vries SmA* material, and **W558**, a traditional SmA* material, respectively, except the lateral trifluoromethyl group is replaced with a hydrogen. Of particular interest is that **W697**, a core shown to promote the de Vries SmA* phase, shows an isotropic to SmA* phase transition[27], while **W702**, a core shown to promote the traditional SmA* phase, shows an isotropic to nematic phase transition[28]. This suggests that the orientation of the phenyl and biphenyl units in **Core B** shows stronger core-core interactions than **Core C**, via suppression of a nematic phase. This effect can be overcome in **Core C** by introducing sufficiently de Vries promoting tails (e.g. *E*-5-decenyloxy in **W415**). The origin of this effect is subtle, however, one possible explanation is that the part of the core where the non-chiral tail is connected possesses a large longitudinal dipole. **Core B**, by virtue of a second phenyl ring, possesses a much larger dipole than **Core C**, as shown in Figure 2.35. The interaction of the longitudinal dipoles of **Core B** could drive the in layer tilt and, thus, promote the de Vries SmA* phase.

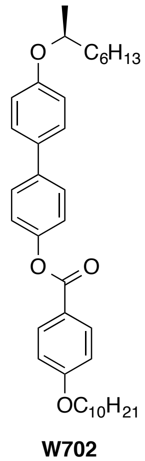

W702

I - 120 - N - 108 - SmA - 71- SmX$_1$ - 32 - SmX$_2$

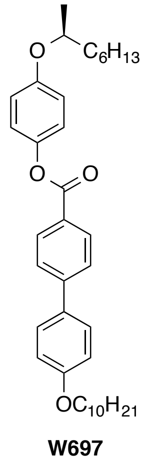

W697

I - 142 - SmA - 123 - SmC - 37 - Cr

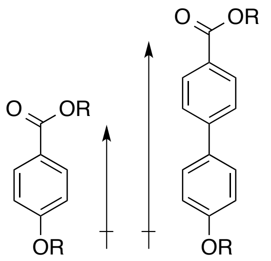

Figure 0.35 Schematic representation fof the longitudinal dipole of the moiety bearing the non-chiral tail of Core C (left) and Core B (right)

Compounds that possess the 7,7,8,8,9,9,10,10,10-nonafluorodecyloxy tail, built on the **Core A-D** scaffold, give the broadest SmA* phase. Compounds that possess this tail also show the lowest polarization in the SmC* phase at $T-T_{A-C}$ = -5 K. Compounds that possess the *E*-5-decenyloxy tail shows the narrowest SmA* phase and the largest polarization at 5 K below the SmA* - SmC* phase transition. The volume of the semi-fluorinated tail is larger than the alkene, so there may be more alkenyl molecules per unit area relative to semi-fluorinated molecules, which would increase polarization.[29] The larger number of molecules in a unit area is confirmed by the birefringence as the maximum birefringence of **W657** in the field-induced SmC* phase is ca. 33% larger than in **W530**, at the same reduced temperature. It is unlikely, however, that there are twice as many molecules per unit area, so secondary effects also contribute to this discrepancy. The orientational order parameter of the core may be significantly higher in compounds with the alkene tail relative to the semi-fluorinated tail. If this is the case, it is possible that π-π interactions of the alkene moiety could be the origin. Since parallel and anti-parallel alignment of adjacent molecules is equally likely in most smectics this effect is expected to be small. A second possibility is the transverse dipole of compounds possessing the *E*-5-decentyloxy tail may be rotated towards the polar axis relative to compounds possessing the alkyl and semi-fluorinated tails (Figure 2.36).[30] Since the alkene tail possesses non-anti conformations in the tail these could affect the orientation of the core within the layer.[16] The alkyl tail shows intermediate phase width and polarization relative to the alkene and semi-fluorinated tail. The magnitude is closer to the semi-fluorinated analogues suggesting that the transverse dipole is oriented in a similar direction relative to the tilt plane.

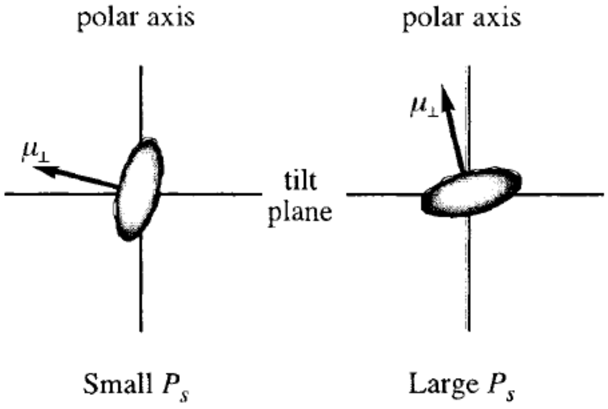

Figure 0.36: Schematic representation of the effect of the orientation of the transverse dipole on the polarization. If the transverse dipole orients towards the tilt plane (left) the polarization will be small, while if the transverse dipole aligns towards to the polar axis then the polarization will be large.

In Chapter 3 the effect of the lateral polar group on polarization, tilt, and the generality of compounds possessing the same orientation of phenyl and biphenyl units as **Core B** will be explored.

2.5 W705

W530, amongst other compounds, have shown that semi-fluorinated tails can be a powerful method to induce de Vries behaviour in SmA materials. With desire to expand the library of de Vries materials, and the knowledge that **Core C** can show the de Vries SmA* phase, the semi-fluorinated tail of **W530** was incorporated onto the **W317/W415** scaffold (**W705**). This material is expected to possess the de Vries SmA* phase, potentially with a wider SmA* phase than **W530** based on the relative stability of the SmA* phase of **W317/W415** relative to **W652/W657**.

W705 possesses an enantiotropic SmA* and SmC* phase. The SmA* phase forms from the isotropic melt at 125 °C and transitions to the SmC* phase at 28 °C. These transition temperatures were measured by X-Ray diffraction, as the SmA* - SmC* phase transition is not detectable by DSC (Figure 2.37). This suggests a strongly second order phase transition, which is consistent with a traditional SmA* - SmC* phase transition. **W705** shows layer expansion, from 35 Å at 125 °C to 36.3 Å at 27 °C, in the SmA* phase, as shown in Figure 2.38. The layer spacing at the SmA* - SmC* phase transition is significantly shorter than the estimated molecular length of ca. 38.3 Å, suggesting **W705** is de Vries, but with a smaller cone angle than chemically similar **W415**. This gives an X-Ray tilt of ca. 18°. This suggests that the SmA* phase of **W705** is de Vries, however, it has a much smaller cone angle than **W415**. The later spacing at $T\text{-}T_{A\text{-}C}$ = -5 K is 35.9 Å, which is a layer shrinkage of ca. 1%.

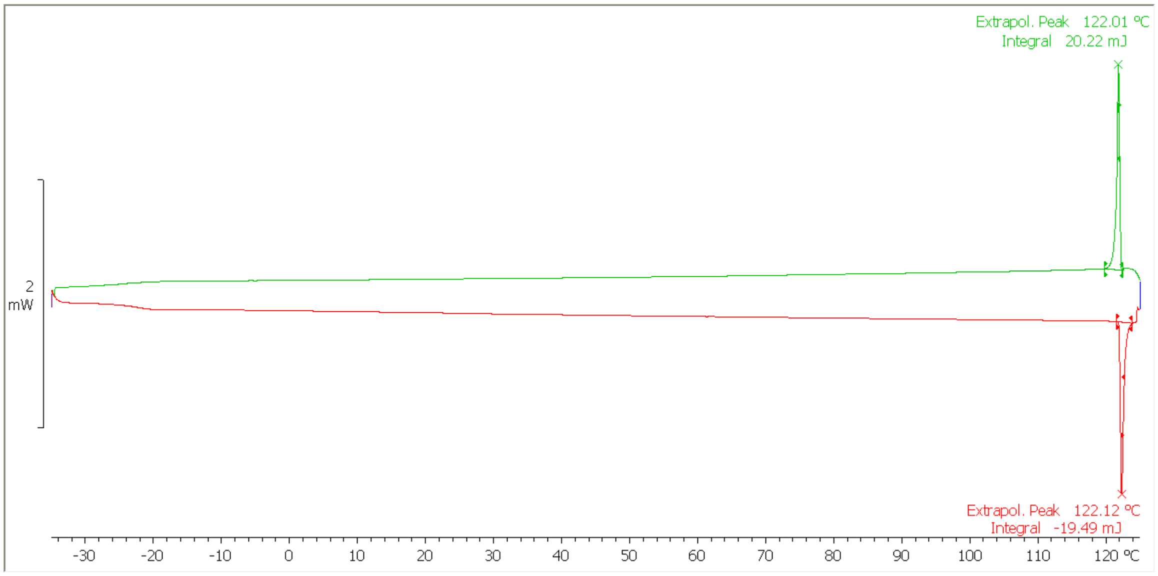

Figure 0.37 DSC of W705

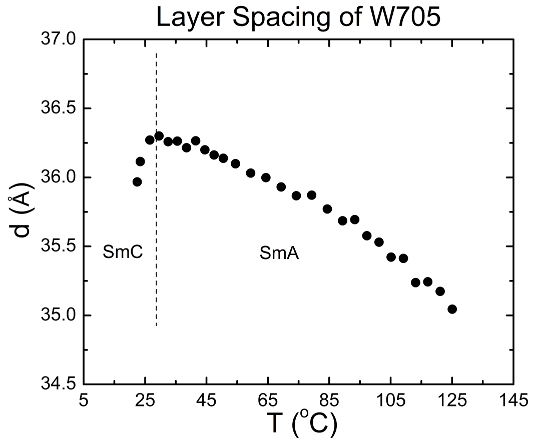

Figure 0.38 Layer spacing of W705 as a function of temperature.

W705 begins to show significant electroclinic tilt (ca. 15°) at T-$T_{A\text{-}C}$ = 18 K (Figure 3.39), which is very large as most materials do not show an electroclinic tilt until very close to the SmA*-SmC* phase transition. **W705** shows a saturated tilt of ca. 22° at T-$T_{A\text{-}C}$ = 2 K. This is slightly larger than the X-Ray tilt of 18°. The saturated electroclinic tilt of **W705** is larger than the saturated tilt of 16° for **W317** and smaller than the 28° of **W415**. Amazingly, at low applied fields, up to ca. 10 V μm^{-1}, **W705** shows small temperature dependence in the electroclinic tilt susceptibility, as shown in Figure 3.40. At 34 °C e_c is ca. 1.6 ° $\mu m\ V^{-1}$ while at 29 °C, only 2 K above the SmA* - SmC* phase transition, e_c is ca. 1.9 ° $\mu m\ V^{-1}$. **W652**, for example, over a similar change in reduced temperatures increases from 1 $\mu m\ V^{-1}$ to 3 $\mu m\ V^{-1}$ at fields up to 5 V μm^{-1}. **W705** does not behave strongly like **W317** or **W415**. The best comparison is likely **W652** which shows the de Vries SmA* phase with layer expansion through the SmA* phase and a very weakly first order SmA* - SmC* phase transition. This suggests the *E*-5-decenyloxy tail is significantly better at promoting traditional properties in the de Vries SmA* phase (e.g. flay layer profile and strong first order SmA* - SmC* phase transition) then the 7, 7, 8, 8, 9, 9, 10, 10, 10-nonafluorodecyloxy tail.

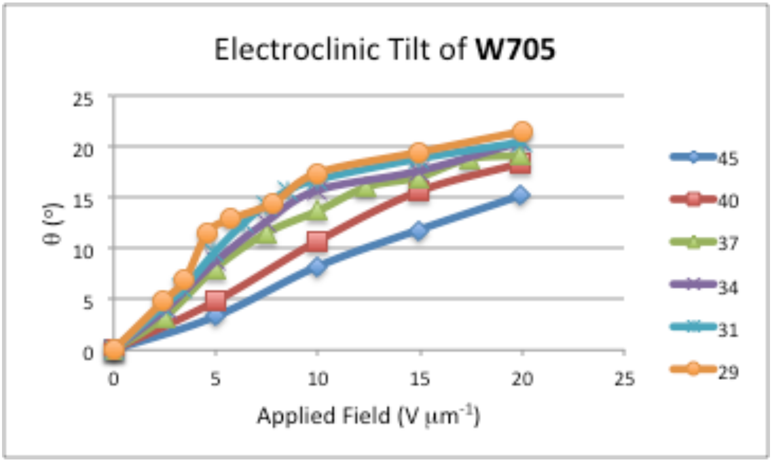

Figure 0.39 The electroclinic tilt of W705 as a function of applied field at various temperatures in the SmA* phase

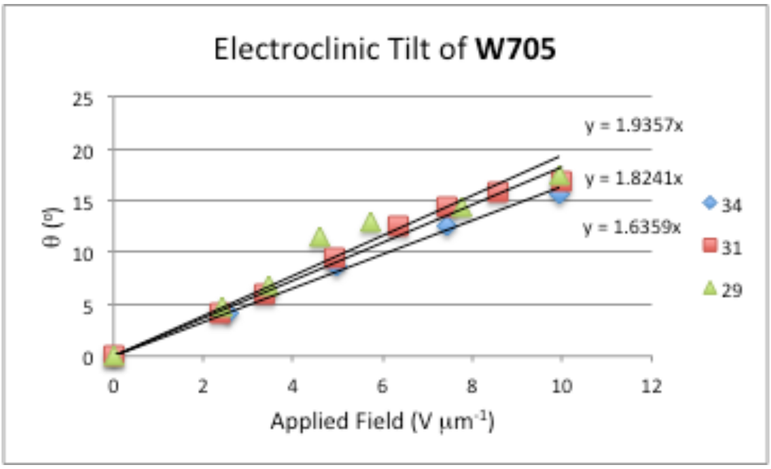

Figure 0.40 The electroclinic tilt of W705 as a function of applied field at various temperatures in the SmA* phase. The field is limited to ca. 10 V mm in which the electroclinic response is linear and shows very little temperature dependence.

The birefringence of **W705** is temperature increases with increasing field, which is a characteristic of the de Vries SmA* phase. At 29 ^{o}C, ca. 2 K above the SmA* - SmC* phase transition, the birefringence increases from 0.108 at 2.5 V μm^{-1} low field to 0.118 at 20 V μm^{-1}, a change of ca. 8% (Figure 2.41). This field induced change of birefringence similar to those observed in other de Vries possessing compounds that show weakly first order SmA* - SmC* phase transitions, such as **W652**. The field-induced polarization of **W705** as a function of applied filed is shown in Figure 2.42. At T-T$_{A\text{-}C}$ = 2 K at 20 V μm^{-1} the field induced polarization reaches a maximum of 100 nC cm^{-2} and, like the electroclinic tilt and birefringence, does not show a sigmoidal response. This polarization is ca. 2x larger than that observed in **W652** at a similar reduced temperature. The increase can likely be attributed to the larger transverse dipole associated with the nitro group relative to the trifluoromethyl group. The polarization reversal current shows one peak, which is consistent with de Vries SmA* materials that show weakly first order SmA* - SmC* phase transitions.

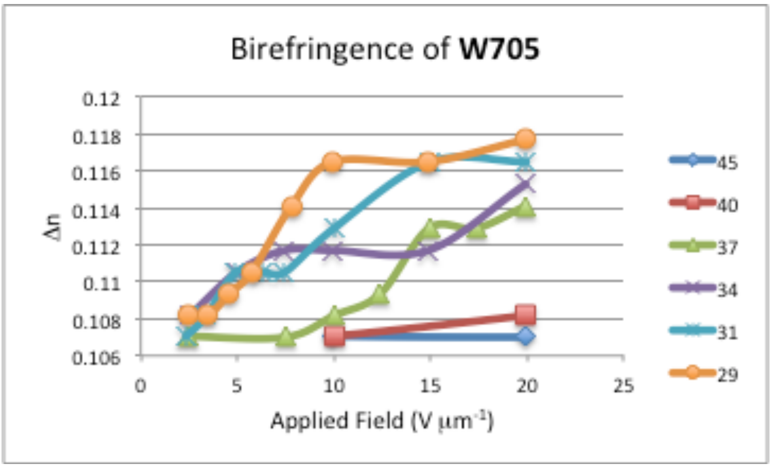

Figure 0.41 The birefringence (Δn) of W705 as a function of applied field at various temperatures in the SmA* phase.

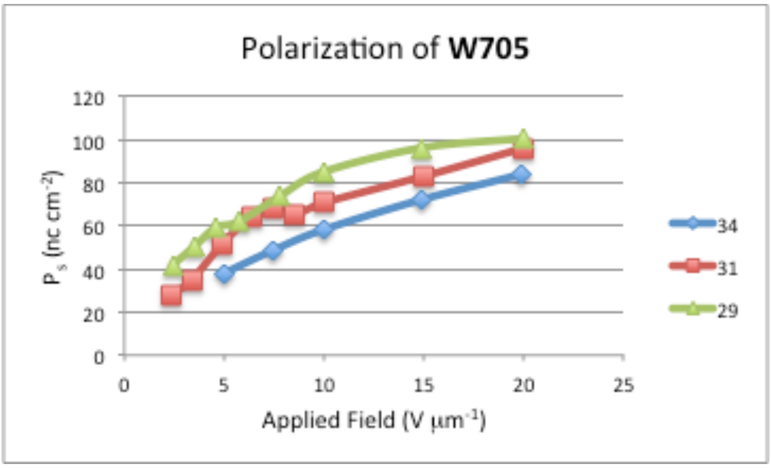

Figure 0.42 Field-induced polarization inthe SmA* phase of W705 at various temperatures.

2.6 Synthesis

Commercially available reagents were used as purchased without further purification unless otherwise noted. THF was purified by distillation from a sodium/ benzophenone ketyl still under an argon atmosphere prior to use. All non-aqueous reactions were performed in oven-dried glassware under an atmosphere of dry argon unless otherwise noted. All aqueous solutions used for reaction work up were saturated unless otherwise noted. All flash chromatography was performed with silica gel (40-63 µm, 230-400 mesh) purchased from Silicycle or American International Chemical. Analytical thin layer chromatography (TLC) was performed on Silica G TLC plates w/ UV with a thickness of 200 µm, purchased from Sorbent Technologies. Compounds were visualized with short-wave UV, or by staining phosphomolybdic acid, which was heated to visualize spots.

New compounds in the synthetic route were routinely characterized by NMR spectroscopy. ^{1}H and ^{13}C NMR spectra were recorded using a Varian Unity INOVA-500, or a Bruker AM-400 spectrometer. ^{1}H NMR spectra are reported in parts per million (ppm) relative to residual solvent peaks (7.26 for $CDCl_3$). ^{13}C NMR spectra are reported in parts per million (ppm) relative to residual solvent peaks (77.23 for $CDCl_3$).

For the mesogenic materials, phase transition temperatures were determined by differential scanning calorimetry using a Mettler Toledo DSC823e. Liquid crystal phases were determined by polarized light microscopy using a Nicon-HCS400 microscope with an Instec STC200 temperature-controlled stage in 3 μm liquid crystal cells. The magnitude of the spontaneous polarization was measured by the triangular wave method.

X-ray experiments were temperature-controlled with an Instec STC200 hotstage, and data were collected using a point detector mounted on a Huber four-circle goniometer at either of the following: Synchrotron radiation at beamline X10A of the National Synchrotron Light Source (NSLS), Brookhaven National Laboratory, or Cu K(R) radiation from a Rigaku UltraX-18 rotating anode generator, operated by the Liquid Crystal Materials Research Center, University of Colorado-Boulder.

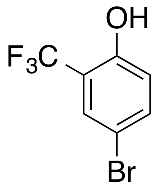

2

4-Bromo-2-(trifluoromethyl) phenol (**2**)

To a stirred solution of 2-hydroxybenzotrifluoride (25.2 g, 155 mmol, 1 eq) in acetonitrile (250 mL) at -20 °C under argon atmosphere was added 1 M tetrafluoroboric acid diethyl ether complex (23.3 mL, 171 mmol, 1.1 eq). After stirring for 5 minutes N-bromosuccinamide (30.43 g, 171 mmol, 1.1 eq) was added in small portions over two hours. The reaction was stirred an additional 2 hours at which point it was quenched with saturated sodium bisulfite. The reaction mixture was extracted from diethyl ether (3x 150 mL) and the combined organics were washed with brine and dried over sodium sulfate. The product was isolated by flash chromatography (1:1 hexanes : methylene chloride) to afford 33.28g (138 mmol, 89%) of **2** as a colourless solid. ^{1}H NMR (300 MHz, Chloroform-*d*): 7.65 - 7.57 (m, 1H), 7.51 - 7.40 (m, 1H), 6.89 (dtd, *J* = 8.7, 0.6 Hz, 1H). ^{13}C NMR (75 MHz, CDCl$_3$): 153.64, 153.62, 153.59, 136.00, 135.99, 129.72, 129.65, 129.58, 129.51, 128.46, 124.84, 121.23, 119.17, 118.74, 118.32, 117.62, 111.61.

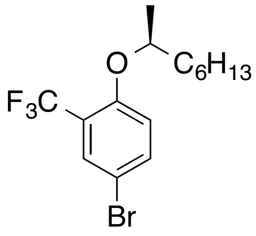

3

<u>*4-bromo-1-(S)-2-octyloxy2-(trifluoromethyl) benzene* (**3**)</u>

To a stirred solution of **2** (5g, 20.7 mmol, 1eq), triphenyl phosphine (8.16 g, 31.1 mmol, 1.5 eq), (*R*)-2-octanol (3.62 mL, 28.8 mmol, 1.1 eq) at 5 °C, under argon atmosphere, was added diethyl azodicarboxylate (4.92 mL, 31.1 mmol, 1.5 eq) dropwise. The mixture was allowed to warm to room temperature slowly and stirred an additional 16 hours. The reaction mixture was dried in vacuo and isolated by column chromatography (5:1 hexanes : ethyl acetate) to afford 7.03 g of **3** as a clear liquid (19.9 mmol, 96%). ^{1}H NMR (300 MHz, Chloroform-*d*): 7.68 (dd, *J* = 2.5, 0.7 Hz, 1H), 7.56 (ddd, *J* = 8.9, 2.6, 0.7 Hz, 1H), 6.89 (dt, *J* = 8.8, 0.8 Hz, 1H), 4.46 (h, *J* = 6.1 Hz, 1H), 1.84 - 1.53 (m, 2H), 1.51 - 1.24 (m, 10H), 0.97 - 0.85 (m, 3H). ^{13}C NMR (75 MHz, CDCl$_3$): 155.45, 155.43, 155.41, 135.70, 135.68, 135.67, 130.24, 130.17, 130.10, 130.02, 128.20, 124.58, 121.95, 121.53, 121.12, 120.97, 120.71, 117.35, 115.46, 111.23, 75.22, 36.19, 31.73, 29.17, 25.13, 22.56, 19.24, 14.03.

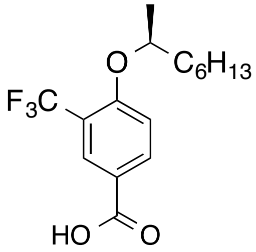

4

4-(S)-2-octyloxy-3-(trifluoromethyl)benzoic acid (**4**)

To a solution of **3** (2.0 g, 5.66 mmol, 1 eq) in THF (100 mL) charged with a stir bar at -78 ^{o}C was added 1.6 M n-butyl lithium in hexanes (3.9 mL, 6.79 mmol, 1.2 eq) and stirred 45 minutes. The mixture was allowed to warm to room temperature and stir an additional 10 minutes before being cooled to -78 ^{o}C, at which point a large excess of solid CO_2 was added. The mixture was stirred an additional 2 hours and warmed to room temperature. The reaction was quenched with 50 mL of $NH_4Cl_{(aq)}$ (sat.) and the THF was removed in vacuo. The mixture was extracted with Et_2O (3 x 100 mL) and the organic layers were combined, washed with H_2O (1 x 50 mL) and brine (1 x 50 mL), dried over Na_2SO_4, and concentrated. The product was isolated by flash chromatography (2:1 hexanes:EtOAc) to afford 0.816 g of **4** a colourless solid (2.56 mmol, 45%).

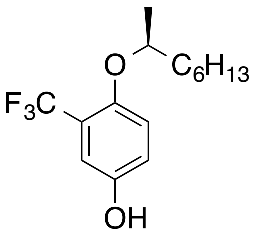

5

4-(S)-2-octyloxy-3-(trifluoromethyl) phenol (**5**)

To a solution of **3** (5g, 14.2 mmol, 1 eq) in THF (100 mL) charged with a stir bar at -78 °C was added 1.6 M n-butyl lithium in hexanes (11 mL, 17.0 mmol, 1.2 eq) and stirred 45 minutes. The mixture was allowed to warm to room temperature and stirred for 10 minutes before being cooled to -78 °C, at which point trimethyl borate (1.9 mL, 17.0 mmol, 1.2 eq) was added dropwise. The mixture was stirred an additional hour and warmed to room temperature. The reaction was quenched with 5 mL of methanol, 8 mL of 30% hydrogen peroxide in H_20 and 2.83 g of NaOH in 20 mL of H_20 and stirred overnight. The THF was removed in vacuo, and the mixture acidified with 10% $HCl_{(aq)}$. The mixture was extracted with Et_2O (3 x 100 mL) and the organic layers were combined, washed with H_2O (1 x 50 mL) and brine (1 x 50 mL), dried over Na_2SO_4, and concentrated. The product was isolated by flash chromatography (5:1 hexanes:EtoAc) to afford 3.55g of **5** as a colourless oil (12.1 mmol, 86%). ^{1}H NMR (300 MHz, Chloroform-*d*): 7.07 (d, *J* = 2.9 Hz, 1H), 7.01 - 6.84 (m, 2H), 5.30 (s, 1H), 4.37 (h, *J* = 6.1 Hz, 1H), 1.84 - 1.67 (m, 1H), 1.67 - 1.51 (m, 1H), 1.52 - 1.21 (m, 12H), 0.99 - 0.83 (m, 3H). ^{13}C NMR (75 MHz, $CDCl_3$): 150.21, 150.19, 148.36, 128.74, 125.13, 121.52, 120.73, 120.33, 119.52, 119.51, 115.95, 114.31, 114.24, 114.17, 114.09, 75.50, 36.34, 31.76, 29.24, 25.23, 22.57, 19.38, 14.08, 14.05.

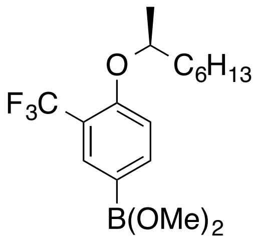

6

B-[4-(S)-2-octyloxy-3-(trifluoromethyl)phenyl]- dimethyl ester boronic acid **(6)**

To a solution of **3** (2.80 g, 7.93 mmol, 1.0 eq) in THF (75 mL) charged with a stir bar was added, at -78 °C, 1.6 M n-butyl lithium in hexanes (5.45 mL, 8.72 mmol, 1.1 eq) dropwise under argon atmosphere. The mixture was stirred an additional hour at which point it was warmed to room temperature and stirred for 10 minutes. The mixture was then cooled to -78 °C at which point trimethyl borate (1 mL, 8.72 mmol, 1.1 eq) was added dropwise. The mixture was stirred an additional hour and then warmed to room temperature, quenched with 5 mL of methanol and stirred overnight. The mixture was concentrated to afford a yellow oil which was taken up in diethyl ether (100 mL) and washed twice with H_2O 2 x 50 mL) and once with brine (50 mL). The organic layer was dried over Na_2SO_4, filtered and concentrated under reduced pressure to afford 2.54 g (7.333 mmol, 93%) of **6** a colourless oil. **6** was used without further purification.

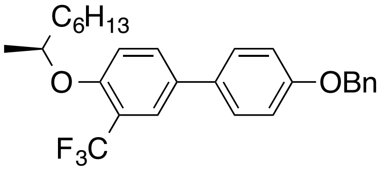

7

4-(4-(S)-2-octyloxy-3-(trifluoromethyl)phenyl)benzyloxy benzene (**7**)

To a 3-necked flask fitted with a reflux condenser was added **6** (2.10 g, 6.07 mmol, 1 eq), K_2CO_3 (4.20 g, 30.4 mmol, 5 eq), H_2O (50 mL) and THF (75 mL). The mixture was degassed with argon for 1h. In a separate flask tetrakis triphenylphosphine palladium (350 mg, 0.30 mmol, 0.05 eq) was taken up in 25 mL of THF and freeze-pump-thawed three times at which point it was added to a solution of 4-benzyloxy bromobenzene (1.76 g, 6.67 mmol. 1 eq) in 25 mL of THF, which had been degassed 1 h with argon, via cannula. This mixture was allowed to stir 10 minutes before being added to the boronic ester mixture via cannula. The reaction mixture was then heated to reflux and stirred overnight. The mixture was then cooled to room temperature, diluted with water and extracted with diethyl ether (3x 100 mL). The combined organic layers were dried over Na_2SO_4, filtered and concentrated under reduced pressure. Flash chromatography (8:1 hexanes : EtOAc) afforded 2.75 g (6.02 mmol, 99%) of **7** as a colourless oil.

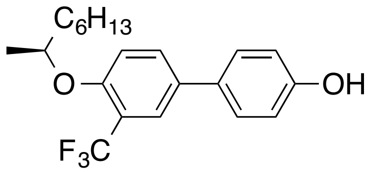

8

4-(4-(S)-2-octyloxy-3-(trifluoromethyl)phenyl)phenol (**8**)

To a three-necked flask charged with a stirbar was added **7** (2.52 g, 5.52 mmol, 1 eq) and 75 mL EtOH and 75 mL CH_2Cl_2. The reaction mixture was put under inert atmosphere and 10% Palladium on Carbon (0.590 g, 0.252 mmol, 0.1 eq) was added. The reaction mixture was then put under an atmosphere of H_2. The reaction was monitored by TLC and stirred ca. 3h. The reaction mixture was then filtered through celite and the desired compound was isolated by flash chromatography (4:1 hexanes:EtOAc) to afford 1.85 g (5.05 mmol, 91%) of **8** as a colourless oil. ^{1}H NMR (300 MHz, Chloroform-*d*): 7.77 (d, *J* = 2.3 Hz, 1H), 7.63 (dd, *J* = 8.6, 2.4 Hz, 1H), 7.51 - 7.40 (m, 2H), 7.06 (d, *J* = 8.7 Hz, 1H), 7.01 - 6.89 (m, 2H), 5.39 (s, 1H), 4.54 (h, *J* = 6.1 Hz, 1H), 1.92 - 1.76 (m, 1H), 1.67 (ddd, *J* = 13.4, 10.5, 5.1 Hz, 1H), 1.59 - 1.26 (m, 12H), 0.99 - 0.88 (m, 3H). ^{13}C NMR (75 MHz, $CDCl_3$): 155.29, 155.26, 154.89, 132.69, 132.36, 131.00, 130.98, 128.03, 125.64, 125.53, 125.46, 125.39, 125.32, 122.02, 120.05, 119.65, 116.02, 115.84, 114.29, 114.25, 74.99, 36.37, 31.79, 29.25, 25.25, 22.60, 19.45, 19.40, 14.08.

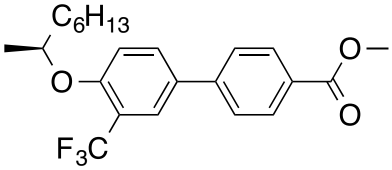

9

Methyl 4-(4-(S)-2-octyloxy-3-(trifluoromethyl)phenyl)benzoate (**9**)

To a 3-necked flask fitted with a reflux condenser was added **6** (2.54 g, 7.33 mmol, 1 eq), K_2CO_3 (5.06 g, 36.7 mmol, 5 eq), H_2O (50 mL) and THF (75 mL). The mixture was degassed with argon for 1 h. In a separate flask tetrakis triphenylphosphine palladium (424 mg, .37 mmol, 0.05 eq) was taken up in 25 mL of THF and freeze-pump-thawed three times at which point it was added to methyl 4-iodobenzoate in 25 mL of THF, which had been degassed 1 h with argon, via cannula. This mixture was allowed to stir 10 minutes before being added to the boronic ester mixture via cannula. The reaction mixture was then heated to reflux and stirred overnight. It was then cooled to room temperature, diluted with water and extracted with diethyl ether (3x 100 mL). The combined organic layers were dried over Na_2SO_4, filtered and concentrated under reduced pressure. Flash chromatography (8:1 hexanes : EtOAc) afforded 2.41 g (5.90 mmol, 80%) of a 9 as colourless solid. ^{1}H NMR (300 MHz, Chloroform-*d*): 8.15 - 8.04 (m, 2H), 7.82 (d, *J* = 2.3 Hz, 1H), 7.76 - 7.56 (m, 3H), 7.07 (d, *J* = 8.7 Hz, 1H), 4.53 (h, *J* = 6.1 Hz, 1H), 3.94 (s, 3H), 1.84 - 1.72 (m, 1H), 1.72 - 1.57 (m, 1H), 1.52 - 1.23 (m, 12H), 0.99 - 0.82 (m, 4H). ^{13}C NMR (75 MHz, $CDCl_3$): 155.40, 155.37, 155.00, 148.35, 132.80, 132.47, 131.11, 131.09, 129.36, 128.14, 125.75, 125.64, 125.57, 125.50, 125.43, 122.13, 120.56, 120.16, 119.76, 119.36, 118.52, 116.13, 115.94, 114.40, 114.36, 75.70, 75.10, 36.48, 31.90, 29.36, 25.35, 22.71, 19.56, 19.51, 14.19.

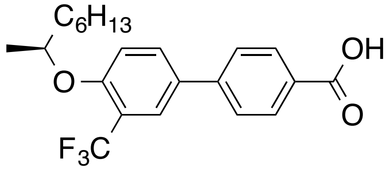

10

4-(4-(S)-2-octyloxy-3-(trifluoromethyl)phenyl)benzoic acid (**10**)

To a round-bottomed-flask charged with a stir bar was added **9** (2.290 g, 5.61 mmol, 1 eq), NaOH (0.673 g, 16.8 mmol, 3 eq), 50 mL EtOH and 50 mL H_2O. The flask was fixed with a condenser and the reaction mixture was heated to reflux and stirred overnight. The mixture was then cooled to room temperature and acidified with conc. HCl dropwise and a colourless precipitate formed. The volume was reduced by about half and then filtered. The colourless solid was recrystallized from hexanes to afford 1.87g (4.75 mmol, 85%) of **10** as a colourless solid. ^{1}H NMR (300 MHz, Acetone-d_6): 11.29 (s, 1H), 8.18 - 8.07 (m, 2H), 8.02 - 7.91 (m, 2H), 7.88 - 7.77 (m, 2H), 7.44 - 7.34 (m, 1H), 4.84 - 4.67 (m, 1H), 1.88 - 1.59 (m, 2H), 1.59 - 1.24 (m, 10H), 0.93 - 0.81 (m, 3H).^{13}C NMR (75 MHz, Acetone): 167.33, 144.55, 133.16, 132.19, 131.19, 130.15, 127.43, 126.52, 126.45, 115.66, 75.60, 37.07, 32.52, 29.91, 25.85, 23.22, 19.74, 14.31.

Coupling:

Esters were formed via Steglich coupling. A general procedure follows:

To a round bottomed flask charged with a stirbar was added the appropriate carboxylic acid, alcohols and dimethylamino pyridine (amounts vary, see specific reactions) were taken up in ca. 50 mL of CH_2Cl_2. The reaction mixture was put under inert atmosphere at which point DCC was added in a single portion (amounts vary, see specific reactions). The mixture was stirred overnight. The products were isolated by flash chromatography (8–15:1 hexanes : EtOAc) to afford colourless solids, except where noted.

Core A:

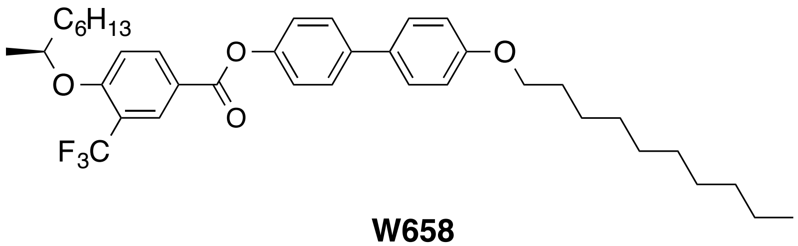

W658

4-(4-decyloxyphenyl)phenyl 4-(1-(S)-methylheptyloxy)-3-trifluoromethyl benzoate (**W658**)

4-(4-decyloxyphenyl)phenol (0.903 g, 2.76 mmol, 1.1 eq), **4** (0.800 g, 2.51 mmol, 1.0 eq), DMAP (0.460 g, 3.77 mmol, 1.5 eq), DCC (0.777 g, 3.77 mmol, 1.5 eq). Yield: 1.34 g (85%). ^{1}H NMR (300 MHz, Chloroform-*d*): 8.48 - 8.41 (m, 1H), 8.33 (dd, *J* = 8.8, 2.2 Hz, 1H), 7.66 - 7.46 (m, 4H), 7.31 - 7.19 (m, 2H), 7.08 (d, *J* = 8.9 Hz, 1H), 7.04 - 6.92 (m, 2H), 4.61 (h, *J* = 6.1 Hz, 1H), 4.01 (t, *J* = 6.5 Hz, 2H), 1.92 - 1.58 (m, 4H), 1.59 - 1.21 (m, 25H), 0.96 - 0.84 (m, 6H). ^{13}C NMR (75 MHz, $CDCl_3$): 164.24, 160.66, 158.96, 149.85, 138.96, 135.72, 132.81, 130.07, 130.00, 128.25, 127.88, 122.00, 120.82, 120.08, 119.66, 114.97, 113.27, 75.70, 68.26, 36.29, 32.06, 31.86, 29.75, 29.72, 29.57, 29.48, 29.45, 29.28, 26.22, 25.22, 22.84, 22.69, 19.46, 14.27, 14.20. HRMS (ESI+) calc'd. for $C_{38}H_{49}F_3LiO_4$: 633.3743; found: 633.3738.

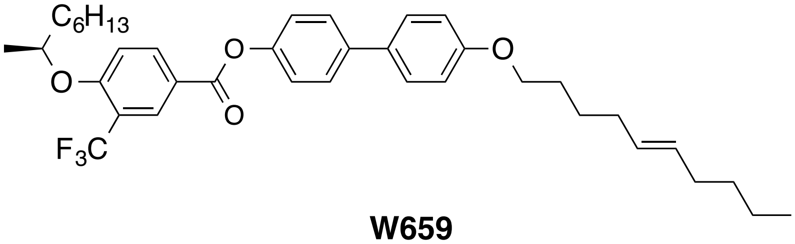

W659

4-(4-(E-5-decenyloxy))phenyl 4-(1-(S)-methylheptyloxy)-3-trifluoromethyl benzoate (**W659**)

4-(4-*E*-dec-5-enyloxyphenyl)phenol (0.896 g, 2.76 mmol, 1.1 eq), **4** (0.800 g, 2.51 mmol, 1.0 eq), DMAP (0.460 g, 3.77 mmol, 1.5 eq), DCC (0.777 g, 3.77 mmol, 1.5 eq). Yield: 1.02 g (65%). ^{1}H NMR (300 MHz, Chloroform-*d*): 8.44 (d, *J* = 2.2 Hz, 1H), 8.33 (dd, *J* = 8.8, 2.2 Hz, 1H), 7.66 - 7.46 (m, 4H), 7.31 - 7.19 (m, 2H), 7.13 - 6.92 (m, 3H), 5.44 (qd, *J* = 3.4, 1.5 Hz, 2H), 4.61 (h, *J* = 6.1 Hz, 1H), 4.01 (t, *J* = 6.5 Hz, 2H), 2.15 - 1.94 (m, 4H), 1.87 - 1.21 (m, 19H), 0.90 (ddt, *J* = 7.1, 5.9, 1.7 Hz, 6H). ^{13}C NMR (75 MHz, $CDCl_3$): 164.24, 160.66, 160.64, 158.93, 149.85, 138.95, 135.71, 132.83, 131.15, 130.07, 130.00, 129.81, 128.25, 127.88, 125.10, 122.00, 121.49, 120.81, 120.08, 119.66, 114.96, 113.27, 75.70, 68.10, 36.29, 32.43, 32.41, 31.94, 31.86, 29.28, 28.89, 26.17, 25.22, 22.69, 22.36, 19.46, 14.20, 14.12. HRMS (ESI+) calc'd. for $C_{38}H_{47}F_3LiO_4$: 631.3586; found: 631.3583.

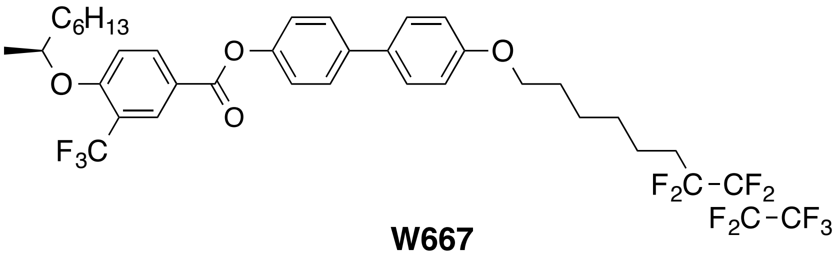

W667

4-(4-7,7,8,8,9,9,10,10,10nonafluorodecylphenyl)phenyl 4-(1-(S)-methylheptyloxy)-3-trifluoromethyl benzoate (**W667**)

4 (0.456 g, 1.43 mmol, 1.0 eq), 4-(4-7,7,8,8,9,9,10,10,10nonafluorodecyyloxyphenyl)phenol (0.700 g, 1.43 mmol, 1.0 eq), EDCI (0.330 g, 1.72 mmol, 1.2 eq), DMAP (0.210 g, 1.72 mmol, 1.2 eq). Yield: 0.886 g (79%). ^{1}H NMR (300 MHz, Chloroform-*d*): 8.44 (d, *J* = 2.2 Hz, 1H), 8.33 (dd, *J* = 8.8, 2.2 Hz, 1H), 7.66 - 7.46 (m, 4H), 7.31 - 7.20 (m, 2H), 7.08 (d, *J* = 8.9 Hz, 1H), 7.02 - 6.92 (m, 2H), 4.61 (h, *J* = 6.1 Hz, 1H), 4.02 (t, *J* = 6.3 Hz, 2H), 2.22 - 1.97 (m, 2H), 1.92 - 1.21 (m, 21H), 0.95 - 0.84 (m, 3H). HRMS (ESI+) calc'd. for $C_{38}H_{40}F_{12}LiO_4$: 795.2895; found: 795.2829.

Core B:

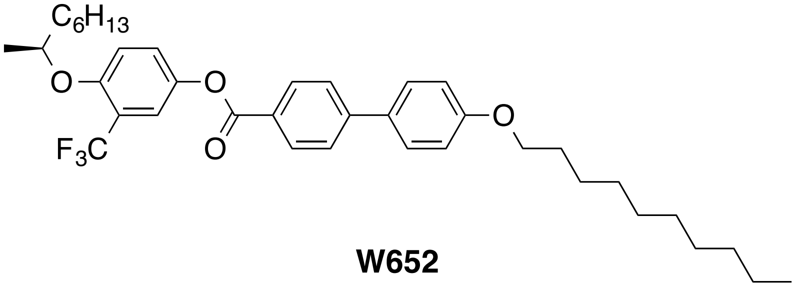

W652

4-(1-(S)-methylheptyloxy)-3-trifluoromethyl 4-(4-decyloxyphenyl) benzoate (**W652**)

4-(4-decyloxyphenyl)benzoic acid (1.32g, 3.74 mmol, 1.1 eq), **5** (1.00g, 3.40 mmol, 1.0 eq), DMAP (0.623 g, 5.10 mmol, 1.5 eq), DCC (1.05g, 5.10 mmol, 1.5 eq). Yield: 1.95 g (92%). ^{1}H NMR (300 MHz, Chloroform-*d*): 8.27 - 8.16 (m, 2H), 7.75 - 7.64 (m, 2H), 7.66 - 7.54 (m, 2H), 7.44 (d, *J* = 2.8 Hz, 1H), 7.34 (dd, *J* = 9.0, 2.9 Hz, 1H), 7.01 (dd, *J* = 8.8, 3.4 Hz, 3H), 4.47 (h, *J* = 6.0 Hz, 1H), 4.02 (t, *J* = 6.5 Hz, 2H), 1.90 - 1.71 (m, 3H), 1.72 - 1.21 (m, 26H), 0.95 - 0.84 (m, 6H). ^{13}C NMR (75 MHz, $CDCl_3$): 165.40, 159.79, 154.18, 146.32, 143.13, 132.02, 130.87, 128.54, 127.22, 126.77, 126.30, 125.08, 121.47, 121.07, 120.99, 120.92, 120.63, 120.21, 115.15, 114.62, 77.58, 77.36, 77.16, 76.74, 75.43, 68.32, 36.47, 32.06, 31.91, 29.74, 29.72, 29.56, 29.54, 29.48, 29.40, 29.36, 26.20, 25.35, 22.84, 22.73, 19.55, 14.28, 14.22. HRMS (ESI+) calc'd. for $C_{38}H_{49}F_3LiO_4$: 633.3743; found: 633.3730.

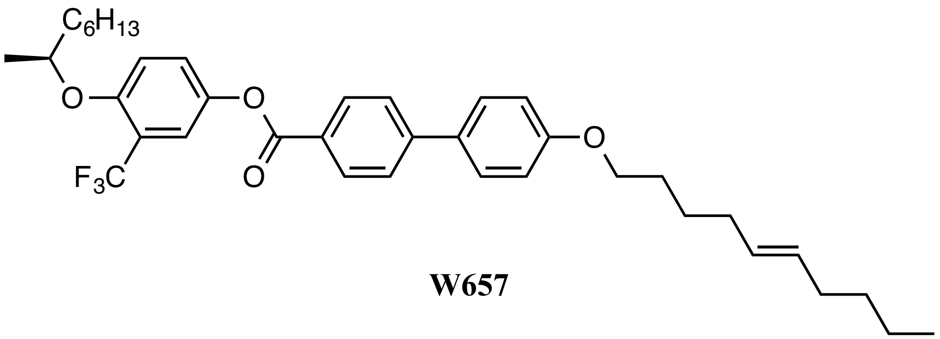

W657

4-(1-(S)-methylheptyloxy)-3-trifluoromethyl 4-(4-(E-5-decenyloxyphenyl)) benzoate (**W657**)

4-(4-*E*-dec-5-enyloxyphenyl)benzoic acid (0.840g, 2.38 mmol, 1 eq), **5** (0.77g, 2.68 mmol, 1.1 eq), DMAP (0.440 g, 3.57 mmol, 1.5 eq), DCC (0.74g, 3.57 mmol, 1.5 eq). Yield 1.27 g (78%). ^{1}H NMR (300 MHz, Chloroform-*d*): 8.27 - 8.17 (m, 2H), 7.75 - 7.54 (m, 4H), 7.44 (d, *J* = 2.8 Hz, 1H), 7.34 (dd, *J* = 9.0, 2.9 Hz, 1H), 7.07 - 6.95 (m, 3H), 5.44 (qd, *J* = 3.6, 1.9 Hz, 2H), 4.47 (h, *J* = 6.1 Hz, 1H), 4.03 (t, *J* = 6.5 Hz, 2H), 2.15 - 1.91 (m, 4H), 1.81 (dddd, *J* = 13.6, 11.8, 10.0, 6.5 Hz, 3H), 1.69 - 1.21 (m, 17H), 0.98 - 0.84 (m, 6H). ^{13}C NMR (75 MHz, $CDCl_3$): 165.40, 159.75, 154.19, 154.15, 146.31, 143.13, 132.04, 131.21, 130.87, 129.77, 128.54, 127.23, 126.77, 126.30, 125.08, 121.47, 121.07, 120.99, 120.92, 120.62, 120.21, 115.14, 114.62, 77.58, 77.36, 77.16, 76.74, 75.43, 68.17, 36.47, 32.43, 32.40, 31.94, 31.91, 29.36, 28.84, 26.15, 25.35, 22.73, 22.36, 19.55, 14.22, 14.12. HRMS (ESI+) calc'd. for $C_{38}H_{47}F_3LiO_4$: 631.3586; found: 631.3582.

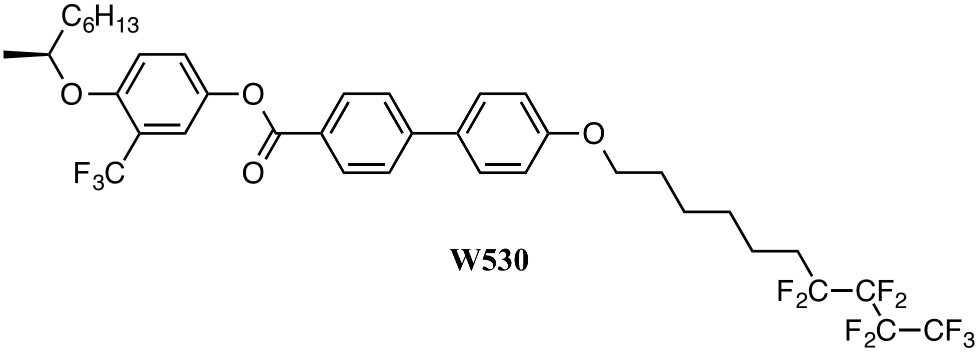

W530

4-(1-(S)-methylheptyloxy)-3-trifluoromethyl 4-(4-7,7,8,8,9,9,10,10,10 nonafluorodecyloxyphenyl) benzoate (**W530**)

4-(4-7,7,8,8,9,9,10,10,10-nonafluorodecylocyphenyl)benzoic acid (0.420g, 0.813 mmol, 1 eq), **5** (0.240g, 0.813 mmol, 1 eq), DMAP (0.120 g, 0.976 mmol, 1.2 eq), DCC (0.201 g, 0.976 mmol, 1.2 eq). Yield 0.542 g (86%).

Core C:

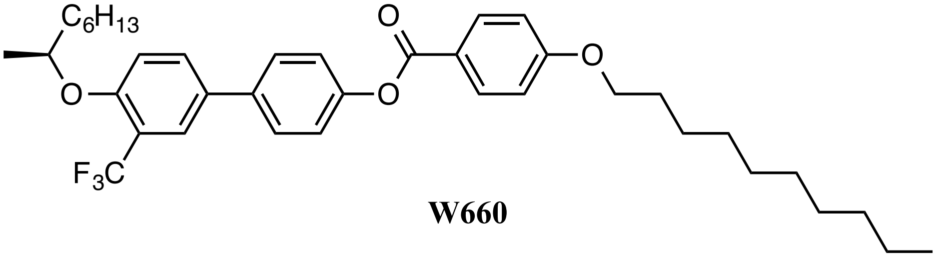

W660

*4-(4-(1-(S)-methylheptyloxy)-3-trifluoromethylphenyl)phenyl 4-decyloxybenzoate (**W558**)*

8 (0.600 g, 1.64 mmol, 1.0 eq), 4-decyloxybenzoic acid (0.501 g, 1.80 mmol, 1.1 eq), DMAP (0.300 g, 2.46 mmol, 1.5 eq), DCC (0.508 , 2.46 mmol, 1.5 eq). Yield: 0.777 g (76%). ^{1}H NMR (300 MHz, Chloroform-*d*): 8.22 - 8.10 (m, 2H), 7.78 (d, *J* = 2.4 Hz, 1H), 7.71 - 7.52 (m, 3H), 7.33 - 7.22 (m, 1H), 7.10 - 6.93 (m, 3H), 4.52 (h, *J* = 6.1 Hz, 1H), 4.05 (t, *J* = 6.5 Hz, 2H), 1.91 - 1.40 (m, 7H), 1.44 - 1.24 (m, 22H), 0.95 - 0.83 (m, 6H). ^{13}C NMR (75 MHz, $CDCl_3$): 165.14, 163.75, 155.88, 155.85, 150.58, 137.52, 132.46, 132.09, 131.55, 127.89, 126.05, 125.98, 125.65, 122.38, 122.03, 121.56, 120.25, 119.85, 114.46, 114.26, 75.06, 68.49, 36.49, 32.05, 31.91, 29.71, 29.52, 29.47, 29.36, 29.25, 26.13, 25.36, 22.84, 22.72, 19.60, 14.27, 14.22. HRMS (ESI+) calc'd. for $C_{38}H_{49}F_3LiO_4$: 633.3743; found: 633.3712.

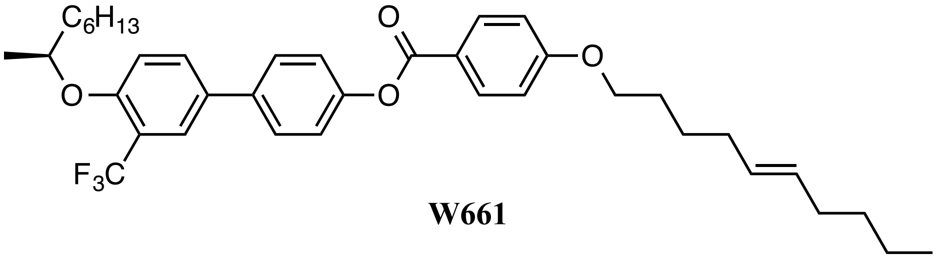

W661

4-(4-(1-(S)-methylheptyloxy)-3-trifluoromethylphenyl)phenyl 4-(E-5-decenyloxy) benzoate (**W661**)

8 (0.600 g, 1.64 mmol, 1.0 eq), 4-*E*-dec-5-enyloxybenzoic acid (0.501 g, 1.80 mmol, 1.1 eq), DMAP (0.300 g, 2.46 mmol, 1.5 eq), DCC (0.508 , 2.46 mmol, 1.5 eq). Yield: 0.914 g (89%). ^{1}H NMR (300 MHz, Chloroform-*d*): 8.22 - 8.10 (m, 2H), 7.81 - 7.51 (m, 4H), 7.33 - 7.21 (m, 2H), 7.10 - 6.92 (m, 3H), 5.54 - 5.34 (m, 2H), 4.52 (h, *J* = 6.1 Hz, 1H), 4.13 - 4.00 (m, 2H), 2.24 - 1.70 (m, 5H), 1.68 - 1.22 (m, 16H), 1.01 - 0.81 (m, 6H). ^{13}C NMR (75 MHz, $CDCl_3$): 165.14, 163.71, 155.87, 150.57, 137.54, 132.48, 132.46, 132.08, 131.56, 131.31, 129.65, 127.89, 126.06, 125.99, 125.92, 122.38, 122.03, 121.58, 120.25, 119.85, 114.46, 114.44, 114.26, 77.58, 77.36, 77.16, 76.74, 75.06, 68.34, 36.48, 32.42, 32.35, 31.93, 31.91, 29.36, 28.67, 26.07, 25.36, 22.72, 22.36, 22.32, 19.60, 14.22, 14.12. HRMS (ESI+) calc'd. for $C_{38}H_{47}F_3LiO_4$: 631.3586; found: 631.3574.

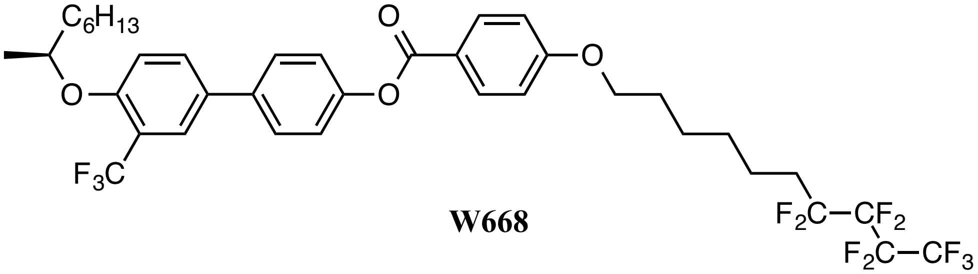

W668

4-(4-(1-(S)-methylheptyloxy)-3-trifluoromethylphenyl)phenyl 4-7,7,8,8,9,9,10,10,10 nonafluorodecyloxybenzoate (**W668**)

8 (0.500 g, 1.36 mmol, 1.0 eq), 4-7,7,8,8,9,9,10,10,10-nonylfluorodecyloxybenzoic acid (0.600, 1.36 mmol, 1.0 eq), EDCI (0.313 g, 1.64 mmol, 1.2 eq), DMAP (0.200 g, 1.64 mmol, 1.2 eq). Yield: 0.931g (87%). ^{1}H NMR (300 MHz, Chloroform-*d*): 8.23 - 8.11 (m, 2H), 7.78 (d, *J* = 2.3 Hz, 1H), 7.72 - 7.52 (m, 3H), 7.33 - 7.22 (m, 1H), 7.10 - 6.93 (m, 3H), 4.52 (h, *J* = 6.1 Hz, 1H), 4.06 (t, *J* = 6.3 Hz, 2H), 2.22 - 1.97 (m, 2H), 1.94 - 1.22 (m, 20H), 0.95 - 0.82 (m, 3H). ^{13}C NMR (75 MHz, CDCl$_3$) ? 165.10, 163.59, 155.89, 155.87, 155.85, 150.56, 137.55, 132.48, 132.08, 131.57, 131.55, 129.26, 127.90, 126.12, 126.05, 125.98, 125.91, 125.65, 122.37, 122.04, 121.74, 120.26, 119.86, 119.45, 118.43, 114.43, 114.27, 77.58, 77.36, 77.16, 76.74, 75.07, 68.14, 36.49, 31.91, 31.15, 30.85, 30.55, 29.37, 29.01, 28.98, 25.88, 25.37, 22.72, 20.27, 20.22, 20.17, 19.59, 14.21. HRMS (ESI+) calc'd. for $C_{38}H_{40}F_{12}LiO_4$: 795.2895; found: 795.2876.

Core D:

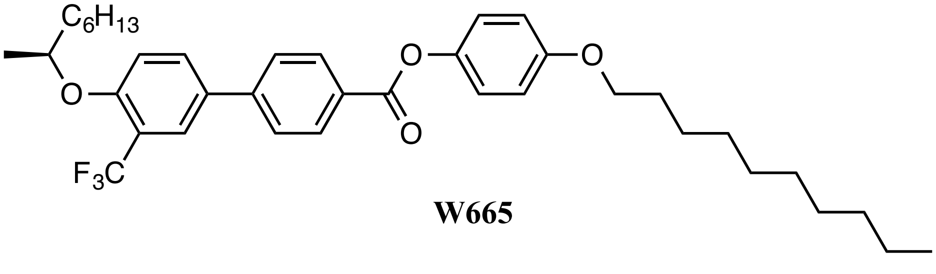

W665

4-decyloxyphenyl 4-(1-(S)-methylheptyloxy)-3-trifluoromethylphenyl benzoate (**W665**)

10 (0.650 g, 1.65 mmol, 1.0 eq), 4-decyloxyphenol (0.390 g, 1.55 mmol, 1.0 eq), DMAP (0.228 g, 1.86 mmol, 1.2 eq), DCC (0.385 , 1.86 mmol, 1.2 eq). Yield: 0.835 g (86%). ^{1}H NMR (300 MHz, Chloroform-*d*): 8.32 - 8.18 (m, 2H), 7.90 - 7.81 (m, 1H), 7.74 (dd, *J* = 8.7, 2.4 Hz, 1H), 7.70 - 7.65 (m, 2H), 7.21 - 7.03 (m, 3H), 6.99 - 6.88 (m, 2H), 4.54 (h, *J* = 6.1 Hz, 1H), 3.97 (t, *J* = 6.5 Hz, 2H), 1.89 - 1.59 (m, 5H), 1.55 - 1.19 (m, 28H), 0.99 - 0.77 (m, 6H). ^{13}C NMR (75 MHz, $CDCl_3$): 165.50, 157.07, 156.64, 144.78, 144.38, 131.82, 131.32, 130.95, 128.42, 126.79, 126.32, 126.25, 125.53, 122.52, 121.92, 120.48, 120.08, 115.27, 114.32, 75.19, 68.60, 36.44, 32.06, 31.90, 29.74, 29.72, 29.56, 29.48, 29.43, 29.35, 26.20, 25.34, 22.84, 22.72, 19.58, 14.28, 14.22. HRMS (ESI+) calc'd. for $C_{38}H_{49}F_3LiO_4$: 633.3743; found: 633.3733.

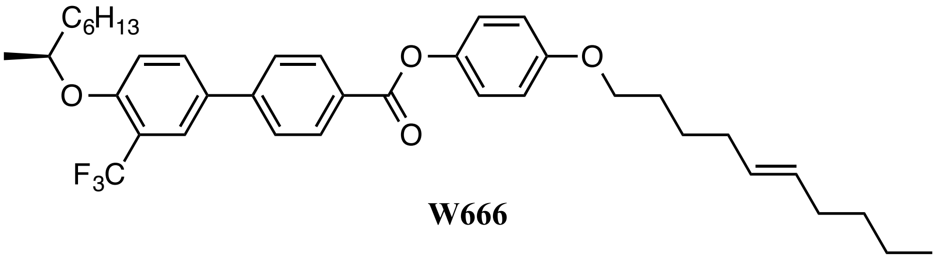

W666

4-(E-5-decenyloxyphenyl 4-(1-(S)-methylheptyloxy)-3-trifluoromethylphenyl benzoate (**W666**)

10 (0.650 g, 1.65 mmol, 1.0 eq), 4-*E*-dec-5-enyloxyphenol (0.380 g, 1.55 mmol, 1.0 eq), DMAP (0.240 g, 1.98 mmol, 1.2 eq), DCC (0.380 , 1.98 mmol, 1.2 eq). Yield: 1.00 g (99%). ^{1}H NMR (300 MHz, Chloroform-*d*): 8.31 - 8.20 (m, 2H), 7.85 (dd, *J* = 2.4, 0.8 Hz, 1H), 7.80 - 7.70 (m, 1H), 7.70 - 7.62 (m, 2H), 7.20 - 7.04 (m, 3H), 7.00 - 6.88 (m, 2H), 5.54 - 5.33 (m, 2H), 4.55 (h, *J* = 6.1 Hz, 1H), 3.97 (t, *J* = 6.5 Hz, 2H), 2.14 - 1.93 (m, 4H), 1.91 - 1.21 (m, 21H), 0.98 - 0.82 (m, 6H). ^{13}C NMR (75 MHz, CDCl$_3$): 165.48, 157.04, 156.64, 156.62, 144.77, 144.39, 131.82, 131.31, 131.16, 130.94, 129.79, 128.41, 126.78, 126.31, 126.24, 126.17, 125.53, 122.52, 121.92, 120.48, 120.07, 115.25, 114.32, 75.19, 68.44, 36.44, 32.43, 32.40, 31.94, 31.90, 29.34, 28.87, 26.15, 25.33, 22.71, 22.36, 19.57, 14.21, 14.12. HRMS (ESI+) calc'd. for $C_{38}H_{47}F_3LiO_4$: 631.3586; found: 631.3576.

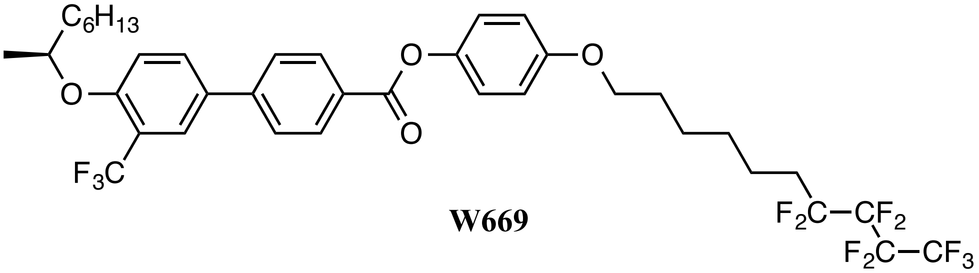

W669

4-7,7,8,8,9,9,10,10,10 nonafluorodecyloxyphenyl 4-(1-(S)-methylheptyloxy)-3-trifluoromethylphenyl benzoate (**W669**)

10 (0.500 g, 1.27 mmol, 1.0 eq) 4-7,7,8,8,9,9,10,10,10-nonylfluorodecyloxy-phenol (0.523 g, 1.27 mmol, 1.0 eq), EDCI (0.292 g, 1.52 mmol, 1.2 eq), DMAP (0.186 g, 1.52 mmol, 1.2 eq). Yield: 0.875 g (87%). ^{1}H NMR (300 MHz, Chloroform-*d*): 8.31 - 8.20 (m, 2H), 7.89 - 7.81 (m, 1H), 7.80 - 7.62 (m, 3H), 7.23 - 7.04 (m, 3H), 7.00 - 6.88 (m, 2H), 4.63 - 4.46 (m, 1H), 3.98 (t, *J* = 6.3 Hz, 2H), 2.22 - 1.96 (m, 2H), 1.91 - 1.21 (m, 21H), 0.95 - 0.83 (m, 3H). ^{13}C NMR (75 MHz, CDCl$_3$): 165.50, 156.94, 156.66, 156.64, 144.81, 144.49, 131.82, 131.31, 130.95, 128.39, 126.80, 126.39, 126.32, 126.25, 126.18, 125.54, 122.59, 121.92, 120.49, 120.09, 115.24, 114.33, 75.20, 68.24, 36.44, 31.90, 31.17, 30.87, 30.58, 29.35, 29.18, 29.00, 25.93, 25.34, 22.72, 20.23, 20.17, 19.57, 14.21. HRMS (ESI+) calc'd. for $C_{38}H_{40}F_{12}LiO_4$: 795.2895; found: 795.2887.

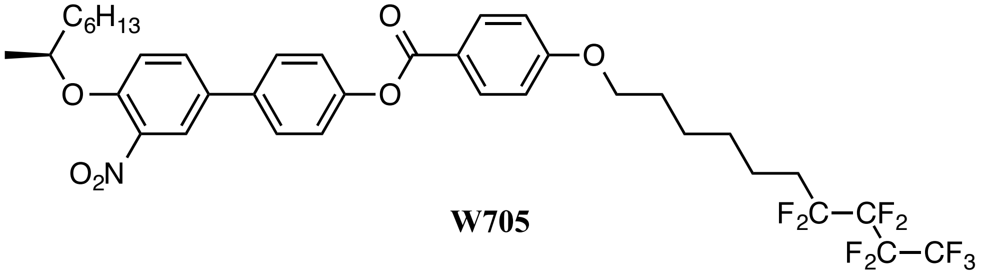

W705

4-(4-(1-(S)-methylheptyloxy)-3-nitrphenyl)phenyl 4-7,7,8,8,9,9,10,10,10 nonafluorodecyloxybenzoate (**W705**)

^{1}H NMR (300 MHz, Chloroform-*d*): 8.22 - 8.10 (m, 2H), 8.00 (d, *J* = 2.4 Hz, 1H), 7.70 (dd, *J* = 8.7, 2.4 Hz, 1H), 7.64 - 7.53 (m, 2H), 7.35 - 7.23 (m, 2H), 7.13 (d, *J* = 8.8 Hz, 1H), 7.04 - 6.92 (m, 2H), 4.54 (h, *J* = 6.1 Hz, 1H), 4.06 (t, *J* = 6.3 Hz, 2H), 2.22 - 1.96 (m, 2H), 1.94 - 1.21 (m, 24H), 0.94 - 0.83 (m, 3H). ^{13}C NMR (75 MHz, $CDCl_3$) ? 164.89, 163.49, 150.87, 150.81, 141.10, 136.17, 132.57, 132.35, 131.93, 127.76, 123.78, 122.42, 121.48, 116.12, 114.30, 77.44, 77.22, 77.01, 76.59, 68.01, 36.25, 31.73, 31.00, 30.71, 29.18, 28.86, 28.82, 25.73, 25.26, 22.58, 20.12, 20.07, 19.57, 14.07. HRMS (ESI+) calc'd. for $C_{37}H_{40}F_9LiO_6$: 772.2872; found: 772.2878.

2.7 References

1. Garoff, S. and Meyer, R. *Physical Review Letters* **1977**, *38*, 848.

2. de Vries, A. *Mol. Cryst. Liq. Cryst. Lett.* **1977**, *41*, 27.

3. Walba, D. M.; Korblova, E.; Eshdat, L.; Biewer, M. C.; Yang, H.; Jones, C.; Nakata, M.; Talarico, M.; Shao, R. and Clark, N. A. *Journal of the SID*, **2007**, 15/8, 1.

4. Glaser, M. and Clark, N. A. *Phys. Rev. E.*, **2002**, *66*, 021711.

5. a) Hori, K. and Endo, K. *Bull. Chem. Soc. Japan*, **1993**, *66*, 46. b) Hori, K.; Kawahara, S. and Ito, K. *Ferroelectrics*, **1993**, *147*, 91.

6. a) Li, L.; Jones, C. D.; Magolan, J. and Lemieux, R. P. *J. Mater. Chem.* **2007**, *17*, 2313. b) Rupar, I.; Mulligan, K. M.; Roberts, J. C.; Nonnenmacher, D.; Giesselmann, F. and Lemieux, R. P. *J. Mater. Chem. C* **2013**, *1*, 3729.

7. a) Gorkunov, M. V.; Giesselmann, Lagerwall, J. P. F.; Sluckin, T. J. and Osipov, M. A. *Phys. Rev. E* **2007**, *75*, 060701(R). b) Gorkunov, M. V.; Osipov, M. A.; Lagerwall, J. P. F. and Giesselmann, F. Phys. Rev. E **2007**, *76*, 051706.

8. Wang, L. *et al.* in Proceedings of the 26th Display Research Conference of the Society for Information Display, Kent, USA (Society for Information Display, CA, USA, 2006), p. 189.

9. Tschierske, C. *J. Mater. Chem.* **1998**, *8*, 1485.

10. Prasad, S. K.; Rao, D. S. S.; Sridevi, S.; Lobo, C. V.; Ranta, B. R.; Naciri, J. and Shashidhar, R. *Phys. Rev. Lett.* **2009**, *102*, 147802.

11. Kost-Smith, Z. V.; Beale, P. D.; Clark, N. A. and Glaser, M. A. *Phys. Rev. E* **2013**, *87*, 050502(R).

12. Rappaport, A. G.; Williams, P. A.; Thomas, B. N.; Clark, N. A.; Ros, M. B. and Walba, D. M. *Appl. Phys. Lett.* **1995**, *67*, 362.

13. Shao, R.; Maclennan, J. E.; Clark, N. A.; Dyer, D. J. and Walba, D. M. *Liquid Crystals* **2001**, *28*, 117.

14. Williams, P. A.; Komitov, L.; Rappaport, A. G.; Thomas, B. N.; Clark, N. A.; Walba, D. M. and Day, G. W. *Liq. Cryst.* **1993**, *14*, 1095.

15. Walba, D. M.; Ros, M. B.; Sierra, T.; Rego, J. A.; Clark, N. A.; Shao, R.; Wand, M. D.; Vohra, R. T.; Arnett, K. E. and Velsco, S. P. *Ferroelectrics* **1991**, *121*, 247.

16. Santismo, E. E. (**2007**) *Effects of Confinement on Chemical Reactions*, ProQuest.

17. Kapernaum, N.; Walba, D. M.; Korblova, E.; Zhu, C.; Jones, C.; Shen, Y.; Clark, N. A. and Giesselmann, F. *ChemPhysChem* **2009**, *10*, 890.

18. Mitsunobu, O. *Synthesis* **1981**, 1.

19. Neises, B.; Steglich, W. *Angew. Chem. Int. Ed.* **1978**, *17*, 522.

20. Miyaura, N.; Yamada, K. and Suzuki, A. *Tetrahedron Letters* **1979**, *20*, 3437.

21. Yang, H.; Wang, L.; Shao, R.; Clark, N. A.; Ortega, J.; Etxebarria, J.; Albouy, P.-A.; Walba, D. M. and Keller, P. *J. Mater. Chem.* **2009**, *19*, 7208.

Chapter 3. Effect of Lateral Substituent on Bulk Properties

3.1 Intro

Having established that materials built upon the **Core B** scaffold reliably possess both the de Vries SmA* and SmC* phase, the lateral polar group was altered to determine if the promotion of the de Vries SmA* phase, even without strongly out-of-layer suppressing tails, is general. The lateral trifluoromethyl group of Core B was replaced with a lateral hydrogen, methyl, chloro and nitro group. Structure-property relationships were developed and the impact of tail and lateral polar group on tilt angle, polarization, birefringence, clearing point and width of the SmA* phase was determined.

The development of a library of chemically similar de Vries SmA* compounds is important since it allows for tuning material properties, such as: tilt angle; electroclinic tilt susceptibility; polarization; phase transition temperature and phase transition width, through mixing. These mixtures could be used to optimize the host for a high-throughput chirality detector designed by the Walba group, where very large tilt susceptibility is required.[1]

3.2 Design and Synthesis

The lateral groups of hydrogen, methyl, chloro and nitro were chosen for this series of compounds due to a large range in size and transverse dipole. To prepare the series with the lateral hydrogen groups (Scheme 3-1) 4-hydroxyphenylbenzoate, **12**, was coupled to (*R*)-2-octanol, via Mitsunobu coupling[2], to afford **13**. The benzoic acid protecting group was removed via saponification to afford the mono-substituted hydroquinone derivative **14**, which was subsequently coupled to 4-(4'-alkoxyphenyl)benzoic acid derivatives with n-decyl, *E*-5-decenyl and 7,7,8,8,9,9,10,10,10-nonafluorodecyl tails via Steglich coupling[3] to afford **W697**, **W698** and **W699**, respectively.

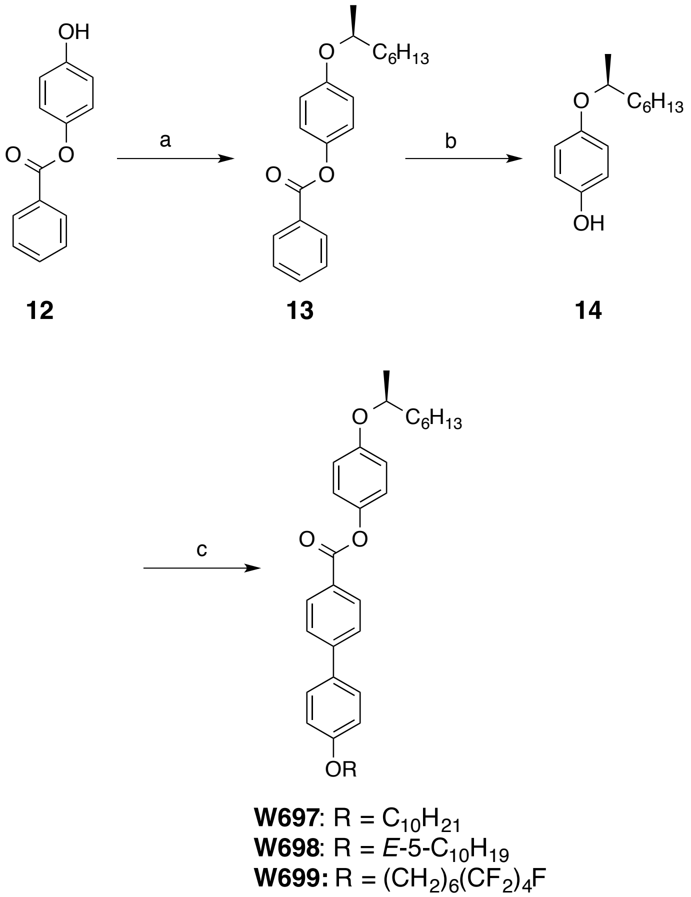

Scheme 0-1 a) (R)-2-octanol, P((Ph)$_3$)$_4$, DEAD, THF b) NaOH, H$_2$O, EtOH c) 4-(4'-alkoxyphenyl)benzoic acid, EDC, DMAP, CH$_2$Cl$_2$

To prepare the series with the methyl lateral polar group (Scheme 3-2) methylhydroquinone, **15**, was regioselectively protected at the less sterically hindered hydroxyl group with pivalic anhydride to afford mono-substituted hydroquinone intermediate **16.** This was the coupled to (*R*)-2-octanol via Mitsunobu coupling[2] to afford **17.** The pivalic ester group was cleaved via saponification to afford mono-substituted hydroquinone derivative **18.** This was subsequently coupled to 4-(4'-alkoxyphenyl)benzoic acid derivatives with n-decyl, *E*-5-decenyl and 7,7,8,8,9,9,10,10,10-nonafluorodecyl tails via Steglich coupling[3] to afford **W733**, **W734** and **W735**, respectively.

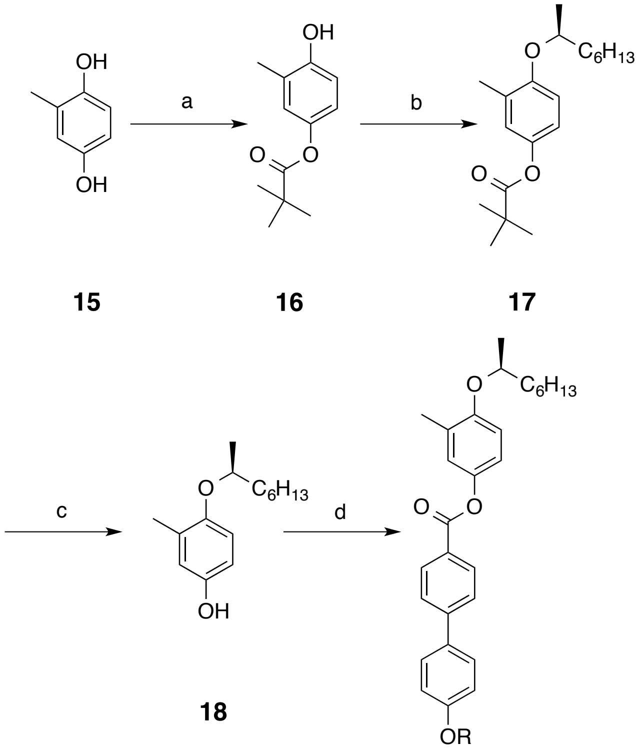

15 **16** **17**

18

W733: R = $C_{10}H_{21}$
W734: R = *E*-5-$C_{10}H_{19}$
W735: R = $(CH_2)_6(CF_2)_4F$

Scheme 0-2 a) Pivalic anhydride, CH2Cl2 b) (R)-2-octanol, $P((Ph)_3)_4$, DEAD, THF c) NaOH, H_2O, EtOH d) 4-(4’-alkoxyphenyl)benzoic acid, EDC, DMAP, CH_2Cl_2

To prepare the series with the chloro lateral polar group (Scheme 3-3) 4-hydroxyphenylbenzoate, **12**, was regioselectively chlorinated by treatment with N-chlorosuccinamide to afford intermediate **19**. This was subsequently coupled to (*R*)-2-octanol via Mitsunobu coupling[2] to afford **20**, which subsequently underwent saponification, to remove the benzoic acid, to afford mono-substituted hydroquinone derivative **21**. This was then coupled to 4-(4’-alkoxyphenyl)benzoic acid derivatives with n-decyl, *E*-5-decenyl and 7,7,8,8,9,9,10,10,10-nonafluorodecyl tails via Steglich coupling[3] to afford **W713**, **W714** and **W715**, respectively.

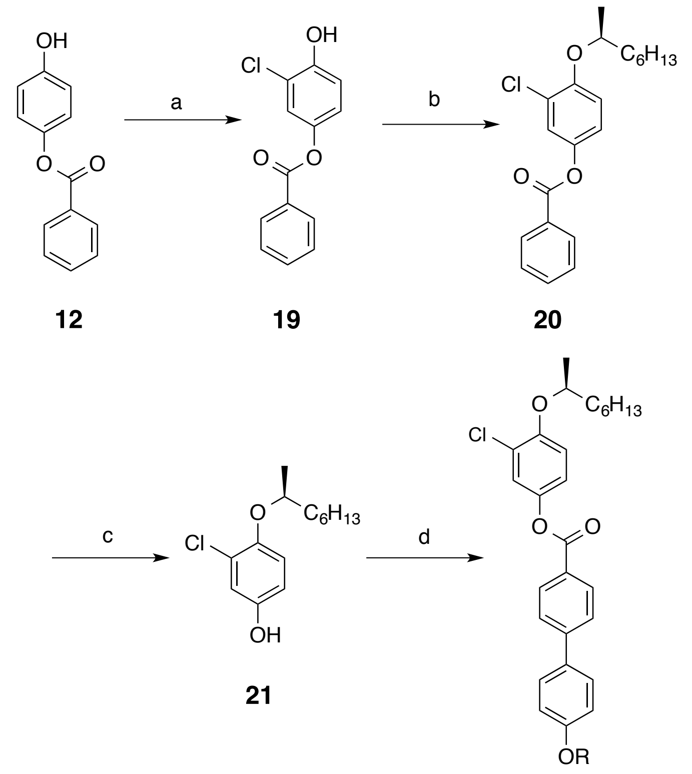

W713: R = $C_{10}H_{21}$
W714: R = *E*-5-$C_{10}H_{19}$
W715: R = $(CH_2)_6(CF_2)_4F$

Scheme 0-3 a) N-Chlorosuccinimide, p-Toluenesulfonic acid, CH_2Cl_2 b) (*R*)-2-octanol, $P((Ph)_3)_4$, DEAD, THF c) NaOH, H_2O, EtOH d) 4-(4'-alkoxyphenyl)benzoic acid, EDC, DMAP, CH_2Cl_2

To prepare the series with the nitro lateral polar group (Scheme 3-4) 4-hydroxyphenylbenzoate, **12**, was regioselectively nitrated by treatment with sodium nitrite and hydrochloric acid with catalytic acetic anhydride to afford intermediate **22.**[4] This was subsequently coupled to (*R*)-2-octanol via Mitsunobu coupling[2] to afford **23**, which was then subjected to saponification conditions to remove the benzoic acid group to afford mono-substituted hydroquinone derivative **24.** This was subsequently coupled to 4-(4'-alkoxyphenyl)benzoic acid derivatives with n-decyl, *E*-5-decenyl and 7,7,8,8,9,9,10,10,10-nonafluorodecyl tails via Steglich coupling[3] to afford **W314**, **W717** and **W718**, respectively.

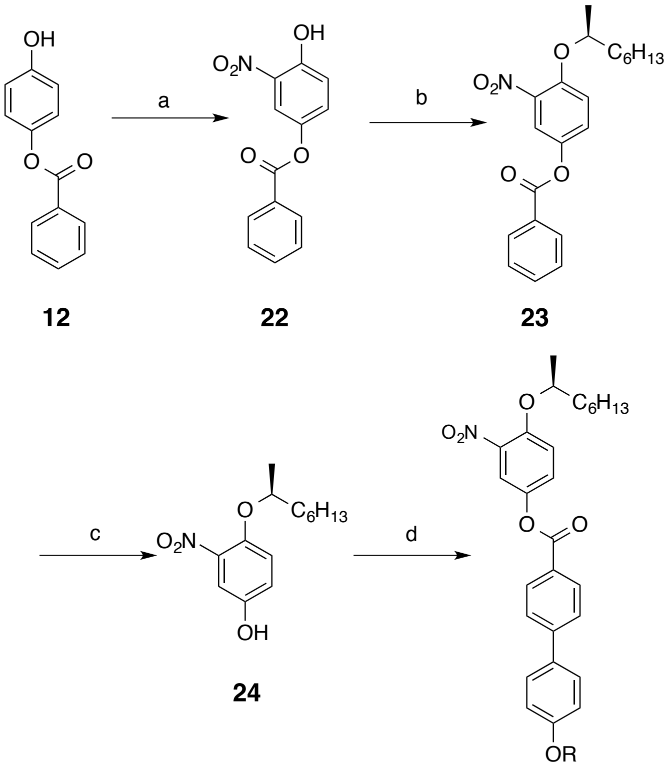

12 **22** **23** **24**

W314: R = $C_{10}H_{21}$
W717: R = *E*-5-$C_{10}H_{19}$
W718: R = $(CH_2)_6(CF_2)_4F$

Scheme 0-4 a) Sodium nitrite, $HCl_{(aq)}$, acetic anhydride, EtOAc b) (*R*)-2-octanol, $P((Ph)_3)_4$, DEAD, THF c) NaOH, H_2O, EtOH d) 4-(4'-alkoxyphenyl)benzoic acid, DCC, DMAP, CH_2Cl_2

In the following sections the effect of the lateral polar group and tail on materials built on the **Core B** scaffold will be examined.

3.3 Effect of Hydrogen as Lateral Polar Group

3.3.1 W697

W697 employs an n-decyloxy tail on the **Core B** scaffold with a lateral hydrogen in place of the trifluoromethyl group, and is a known compound.[5] This compound lacks a strongly of out-of-layer suppressing group, but may form the de Vries SmA* phase due to the strongly de Vries promoting core, as seen with **W652**, which has the same arrangement of aromatic units, but with a lateral trifluoromethyl group. The SmA* phase forms from the isotropic melt at 142 °C and transitions to the SmC* phase, via a weakly first order phase transition, at 124 °C, as seen in the DSC (Figure 3.1). At 70 °C the SmC* transitions to a higher order smectic phase, evidenced by the relatively low transition energy change relative to a SmC* - Cr transition energy. All phase transition temperatures are on cooling. The nature of this higher order smectic was not evaluated. By DSC the higher order smectic phase transitions into two additional phases very close in phase transition temperatures. The lowest temperature phase is crystal, while the intermediate phase is unidentified. The SmC* phase of **W697**, as observed by PLM, transitions directly to the crystal phase. The layer spacing of of **W697** in the SmA* phase increases from 35.7 Å at 148 °C to 36.3 Å at 130 °C, which corresponds to .033 Å K^{-1}. This is ca. 5x larger than **W652**, which shows the de Vires SmA* phase. The X-Ray layer spacing of **W697** is shown in Figure 3.2. The 36.3 Å layer spacing of **W697** is shorter than the estimated molecular length of 37.8 Å. At $T-T_{A-C}$ = -10 K the layer spacing is 34.2 Å, which is a ca. 4% shrinkage.

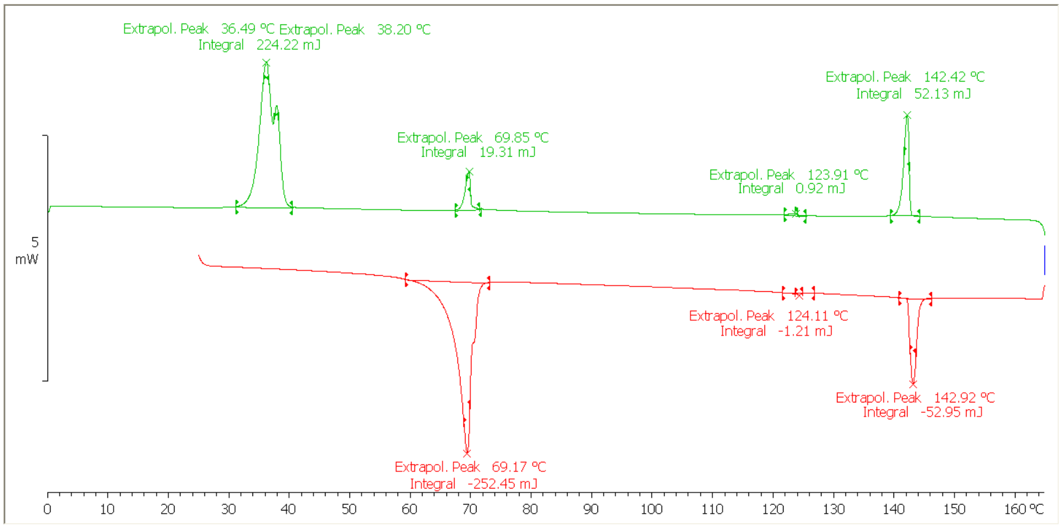

Figure 0.1 DSC of W697

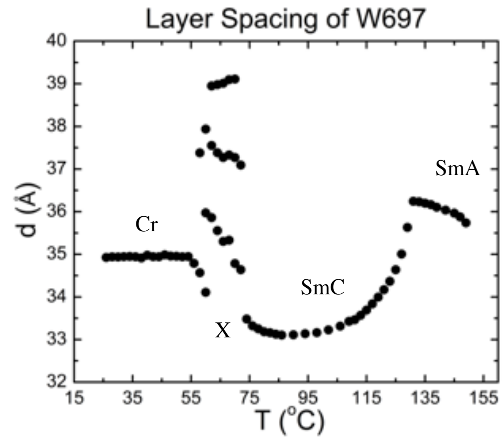

Figure 0.2 Layer spacing of W697 as a function of temperature.

W697 behaves like a de Vries SmA* with a weakly first order SmA* - SmC* phase transition in how it reacts to the application of an electric field near the SmA* - SmC* phase transition temperature. Unlike prototypical de Vries materials (e.g. **W530**) showing strongly first order SmA* - SmC* phase transitions, **W697** does not show a strong sigmoidal response in the tilt vs. applied field (Figure 3.3), much like **W652**. The saturated tilt of **W697** in the SmA* phase is ca. 18^{o}, which is slightly larger than the X-Ray tilt 17^{o}. The saturated tilt of **W697** is lower than the 27^{o} of **W652**. The saturated tilt of 18^{o} is only observed at 20 V mm^{-1} at ca. 2 K above the SmA* - SmC* phase transition. This indicates a fairly weak electroclinic effect, since the saturation occurs so close to the SmA* - SmC* phase transition, despite a pronounced electroclinic tilt. **W697** shows a very small increase in birefringence near the SmA* - SmC* phase transition, as shown in Figure 3.4. At $T\text{-}T_{A\text{-}C}$ = 2 K the birefringence increases from 0.146 at 10 V μm^{-1} to 0.149 at 20 V μm^{-1}, which is a 2% increase. This relatively small increase is significantly less than the 7% change in birefringence observed in **W652**. The smaller tilt angle of **W697**, relative to **W652**, could explain the difference in birefringence change. The birefringence at $T–T_{A\text{-}C}$ = -5 K is 0.155, which is a 6% change relative to the SmA* phase. Changes in birefringence from the SmA* to SmC* phase are a strong indicator of de Vries SmA* materials. The 6% increase in birefringence is similar to the 8% observed in **W652**. The field induced polarization in the SmA* phase is too small to measure. The P_s of the SmC* phase at $T\text{-}T_{A\text{-}C}$ = -5 K is 43 nC cm^{-2}, which is about half of that of the chemically similar **W652**. The smaller polarization is likely a result of the smaller transverse dipole.

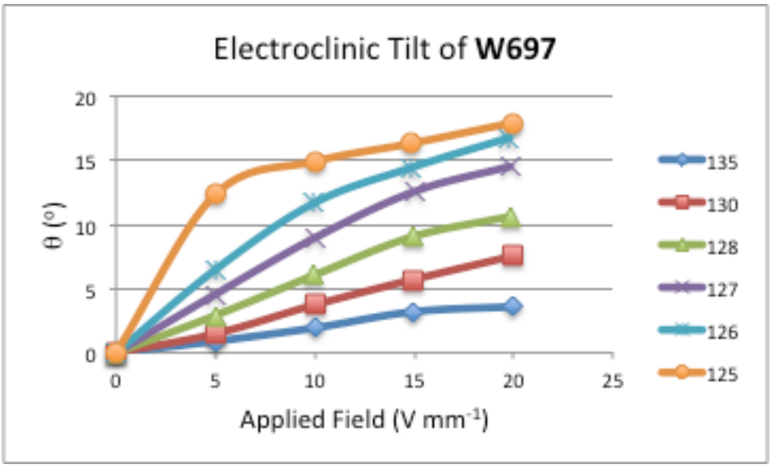

Figure 0.3 The electroclinic tilt of W697 as a function of applied field at various temperatures in the SmA* phase

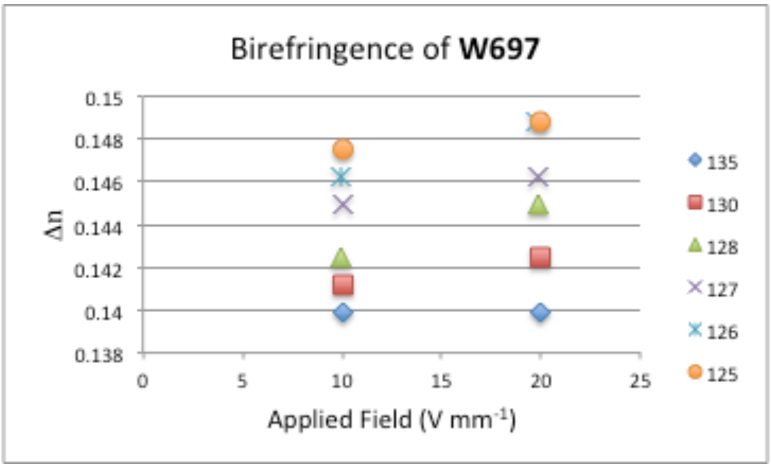

Figure 0.4 The birefringence (Δn) of W697 as a function of applied field at various temperatures in the SmA* phase.

3.3.2 W698

W698 employs an *E*-5-decenyloxy tail on the same core as **W697**. The unsaturation in the tail seems to be surprisingly strong at suppressing out-of-layer fluctuations, inducing strongly first order SmA* - SmC* phase transitions. As such, **W698** is expected to form the de Vries SmA* phase with properties similar to **W657**. The SmA* phase forms from the isotropic melt at 115 °C and transitions to the SmC* phase, via a first order phase transition, at 110 °C, which transitions to the crystal phase at 51 °C, on cooling. The DSC for **W698** is shown in Figure 3.5. The layer spacing of the SmA* phase is roughly constant at 33.7 Å across the entire SmA* phase temperature range, as shown in Figure 3.6. This behaviour is similar to **W657**, however, the layer spacing of **W698** is 1.7 Å larger than **W657**, suggesting a tilt cone with a smaller angle. The layer spacing of **W698** is significantly shorter than the estimated molecular length of 37.5 Å. The layer spacing of **W698** at $T-T_{A-C}$ = -10 K, is 30.6 Å, which corresponds to a layer shrinkage of ca. 8%. This is similar to the 7% of **W657**.

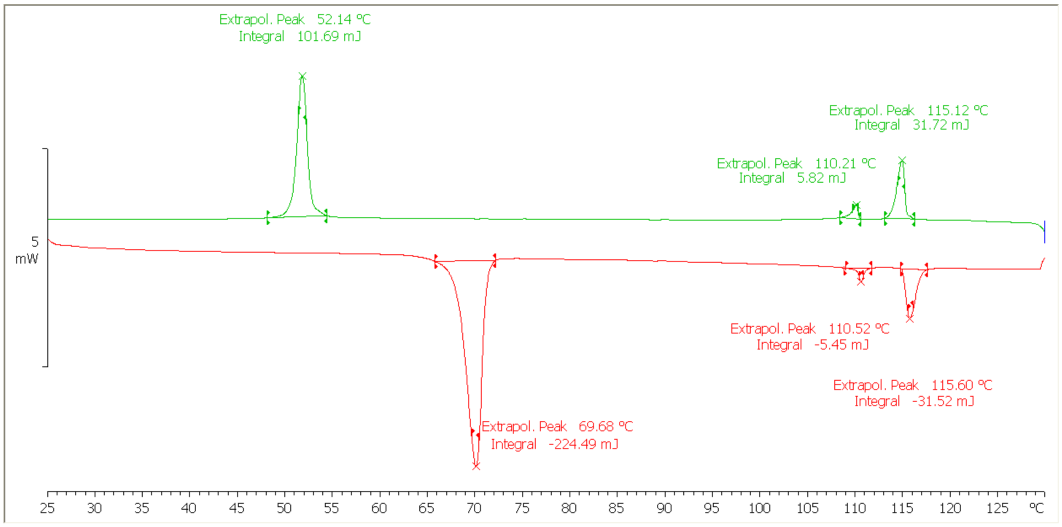

Figure 0.5 DSC of W698

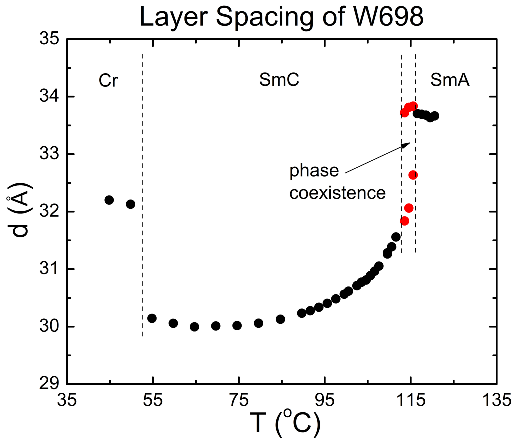

Figure 0.6 Layer spacing of W698 as a function of temperature.

W698 behaves like a prototypical de Vries SmA* in the electrooptic response. The application of an electric field near the SmA* - SmC* phase transition temperature results in a weakly sigmoidal response, as shown in Figure 3.7. The saturated tilt of **W698** in the SmA* phase is ca. 22°, which is smaller than the calculated X-Ray tilt of 26°. The saturated electroclinic tilt of **W698** is significantly lower than the 33° seen in **W657**. The saturated tilt of 22° is achieved at 12 V mm^{-1} at ca. 1 K above the SmA* - SmC* phase transition. This indicates a fairly weak electroclinic effect, since the saturation only occurs so close to the SmA* - SmC* phase transition, despite a pronounced electroclinic tilt. **W698** is capable of reaching saturation only ca. 1 K above the SmA* - SmC* transition, while **W657** shows saturation ca. 5 K above the SmA* - SmC* phase transition. The part of the sigmoidal response with the largest e_c occurs over ca. 7 V μm^{-1}. This is rather broad suggesting that the coupling between the electric field and the transverse dipole is small. **W657** shows similarly broad regions where the e_c increases, however these occur far from the SmA* - SmC* phase transition (Figure 2.20). Additionally the field-induced SmC* phase of **W698** is only evident at T-T$_{A\text{-}C}$ = 1 K, whereas **W657** shows the field-induced SmC* phase at T-T$_{A\text{-}C}$ =

7 K, further suggesting a stronger coupling of the field to the transverse dipole in **W657**, relative to **W698**. The birefringence of **W698** increases from 0.142 at 4 V μm^{-1} to 0.153 at 20 V mm^{-1} at $T-T_{A-C} = 1$ K, as shown in Figure 3.8. This corresponds to an 8% increase, which is significantly smaller than the 25% increase observed in **W657**. The smaller cone angle of **W698** could explain the difference. The birefringence of **W698** shows a similar sigmoidal response as the electroclinic tilt, as expected from modified Langevin models. The birefringence at $T–T_{A-C} = -5$ K is 0.164, which corresponds to a 15% increase. The field induced polarization in the SmA* phase is too small to measure. The P_s of the SmC* phase at $T-T_{A-C} = -5$ K is 70 nC cm^{-2}, which is ca. 3x smaller than **W657**. Potential reasons for the increase in polarization are discussed in 2.4.5.

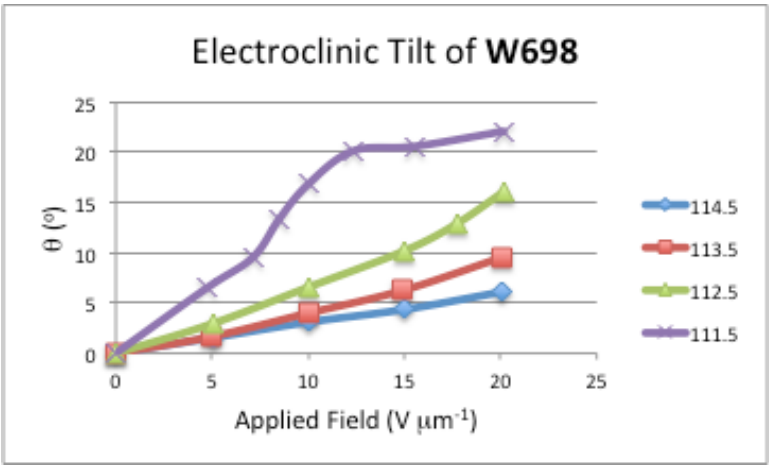

Figure 0.7 The electroclinic tilt of W698 as a function of applied field at various temperatures in the SmA* phase

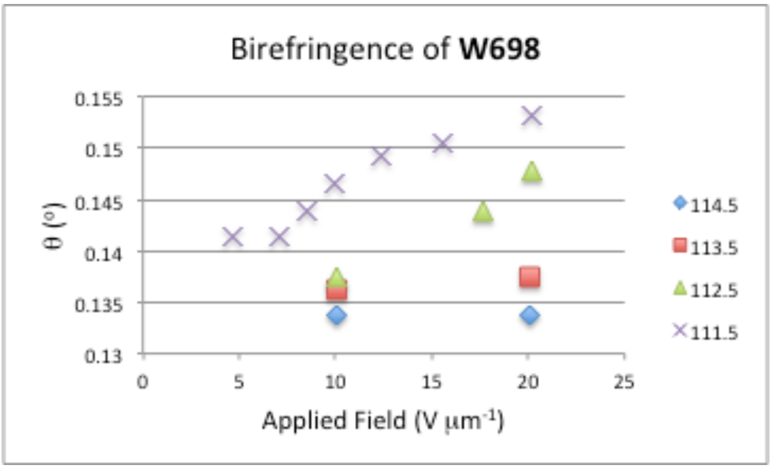

Figure 0.8 The birefringence (Δn) of W698 as a function of applied field at various temperatures in the SmA* phase.

3.3.3 W699

W699 employs a 7,7,8,8,9,9,10,10,10-nonylfluoro decyloxy tail on the same core as **W697** and **W698**. The semi-fulorinated tail has been shown to be a out-of-layer suppressing group, which tends to promote the de Vries SmA* phase.[6] The SmA* phase of **W699** forms from the isotropic melt at 172 °C and transitions to the SmC* phase, via a weakly first order phase transition at 154 °C and then transitions into the crystal phase at 86 °C, on cooling. The DSC for **W699** is shown in Figure 3.9. The layer spacing of the SmA* phase is roughly constant at 35.4 Å throughout the entire SmA* temperature range, which is consistent with prototypical de Vries SmA* materials. The X-Ray layer spacing of **W699** is shown in Figure 3.10. This is significantly smaller than the estimated molecular length of 38.3 Å. The layer spacing of the SmA* phase **W699** is 1.6 Å larger than chemically similar **W530**, suggesting a smaller tilt cone angle. The layer spacing of **W699** at $T\text{-}T_{A\text{-}C}$ = -10 K is is 33.4 Å, which corresponds to a layer shrinkage of ca. 6%, which is similar to the 4% observed in **W530**.[7]

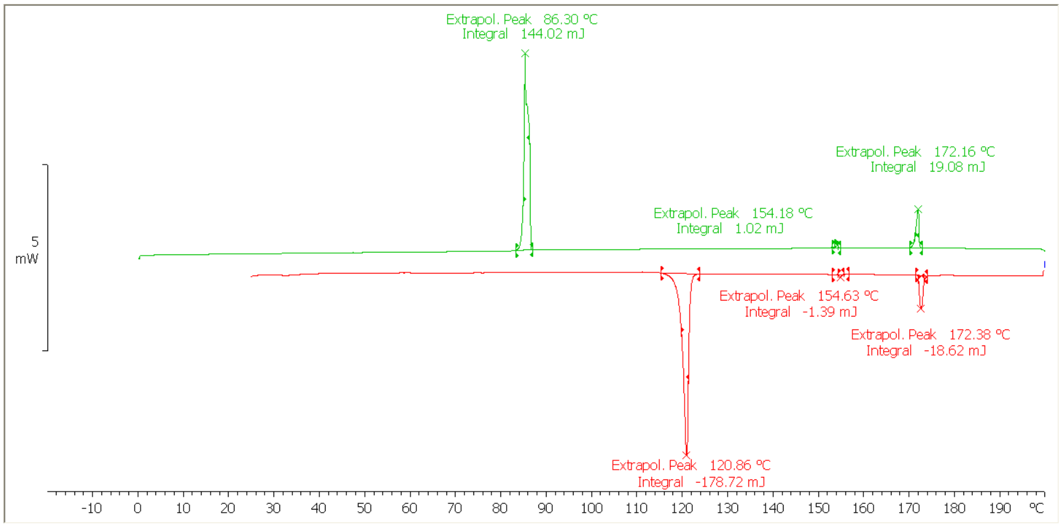

Figure 0.9 DSC of W699

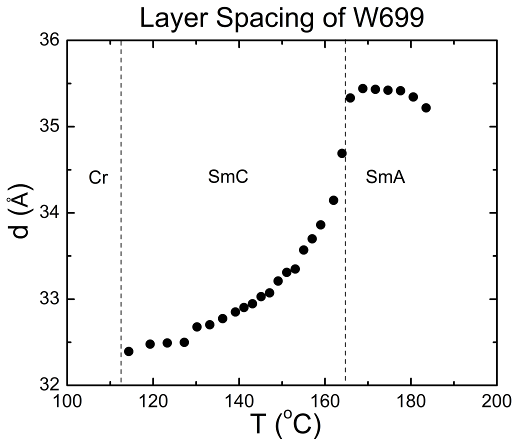

Figure 0.10 Layer spacing of W699 as a function of temperature.

W699 behaves like a de Vries SmA* material with a weakly first order SmA* - SmC* phase transition in the electrooptic response. The application of an electric field just above the SmA* - SmC* phase transition temperature results in a non-sigmoidal response (Figure 3.11). The saturated tilt of **W699** in the SmA* phase is ca. 23°, which is larger than the X-Ray tilt of 24°. The saturated electroclinic tilt of **W699** is smaller than the chemically similar **W530**,[7] which shows a saturated tilt of 33°. The saturated tilt of 23° is only achieved at 20 V mm^{-1} at ca. 1 K above the SmA* - SmC* phase transition. This indicates a fairly weak electroclinic effect, since the saturation only occurs very near the SmA* - SmC* phase transition (T-T_{A-C} = 1 K), despite a pronounced electroclinic tilt. At T-T_{A-C} = 1 K the birefringence of **W699** increases from 0.102 at 2.5 V μm^{-1} to 0.117 at 20 V μm^{-1}, as shown in Figure 3.12. This corresponds to an increase of 15%, which is smaller than the 30% seen in **W530**. The birefringence at T–T_{A-C} = -5 K 0.131, which is an increase of 28%. The field induced polarization in the SmA* phase is too small to measure. The P_s at T-T_{A-C} = -5 K is 36 nC cm^{-2}, which is 3.1x smaller than **W530.**[7]

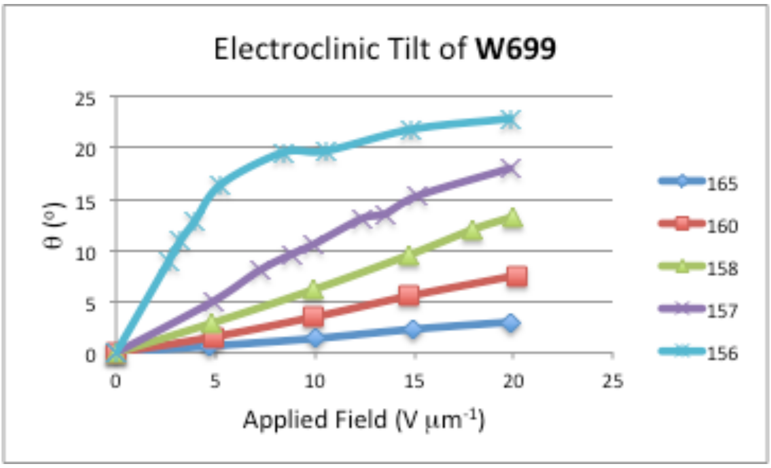

Figure 0.11 The electroclinic tilt of W699 as a function of applied field at various temperatures in the SmA* phase

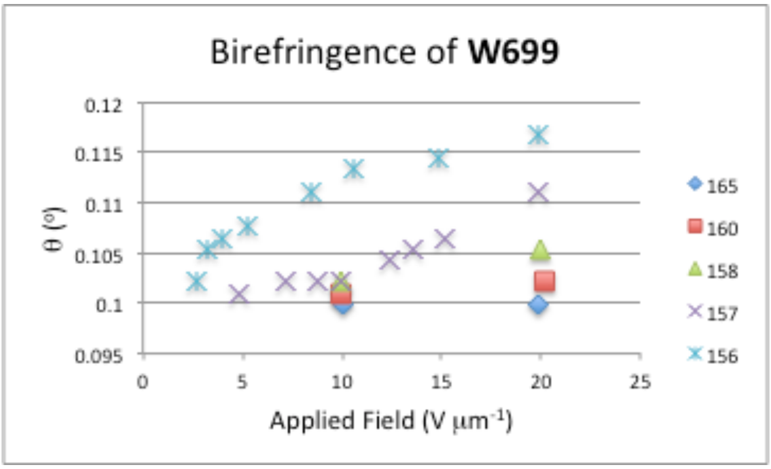

Figure 0.12 The birefringence (Δn) of W699 as a function of applied field at various temperatures in the SmA* phase.

3.4 Effect of Methyl as Lateral Polar Group

3.4.1 W733

W733 employs an n-decyl tail on the scaffold of **Core B** with a lateral methyl group in place of the trifluoromethyl group. The SmA* phase forms from the isotropic melt at 110 ^{o}C and transitions to the SmC* phase, via a weakly first order phase transition, at 90 ^{o}C, which transitions to the crystal phase at 18 ^{o}C, on cooling. The DSC of W733 is shown in Figure 3.13. The layer spacing of the SmA* phase of **W733** increases from 34.9 Å at 118 ^{o}C to 35.5 Å at 99 ^{o}C, as shown in Figure 3.14. This corresponds to an increase of 0.032 Å K^{-1}, which is similar to the rate of expansion in **W697** and ca. 5x larger than the rate of expansion of **W652**. The layer spacing of **W733** at the SmA* - SmC* phase transition (35.5 Å) is much shorter than the estimated molecular length of ca. 37.8 Å. At $T-T_{A-C}$ = -10 K the layer spacing is 32.7 Å, which corresponds to a layer shrinkage of 8%.

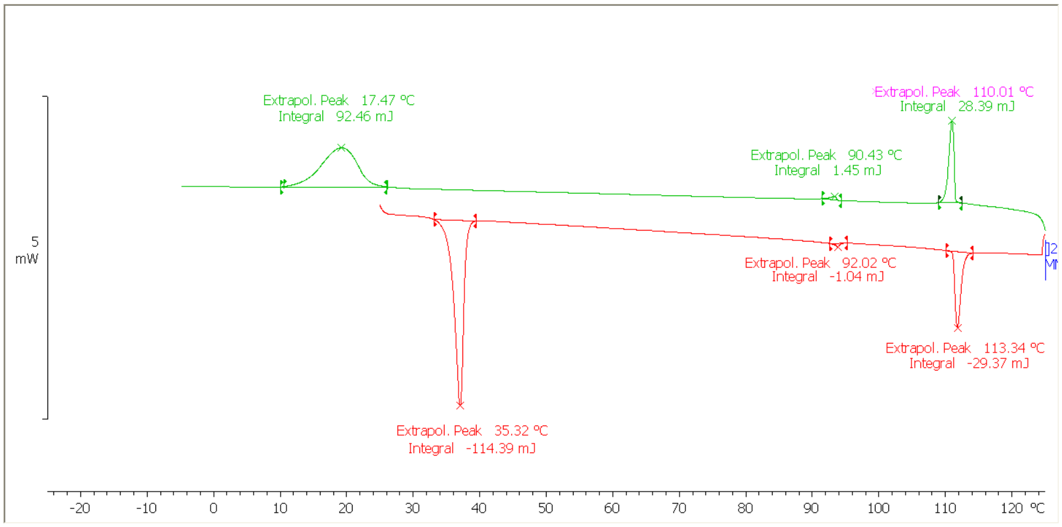

Figure 0.13 DSC of W733

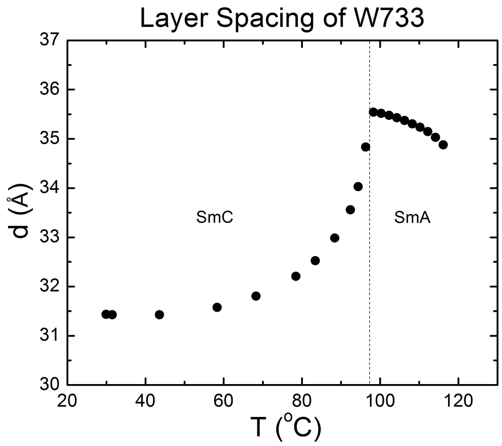

Figure 0.14 Layer spacing of W733 as a function of temperature.

W733 behaves like a de Vries SmA* with a weakly first order SmA* - SmC* phase transition in how it reacts to the application of an electric field. The saturated tilt of **W733**, in the SmA* phase, is 18° (Figure 3.15), which is smaller than the X-Ray tilt of 21°. It is possible that insufficient electric fields were applied to reach saturation, as the X-Ray tilt should be smaller than the optical tilt. The small transverse dipole of **W733** could be responsible for the lack of saturation. The saturated tilt of **W733** is approximately the same as the saturated tilt of **W697**, but much lower than the 27° of **W652.** The saturated tilt of

Bibliography

Andersson, G.; Dahl, I.; Komitov, L.; Laggerwall, S. T.; Skarp, K. and Stebler. B. *J. Appl. Phys.* **1989**, *66*, 4983.

Bartolino, R.; Doucet, J.and Durand, G. *Ann. Phys. (Paris)*, **1978**, *3*, 389.

Bondi., A. *J. Phys. Chem.* **1964**, *68*, 441.

Clark, N. A.; Bellini, T.; Shao, R.; Coleman, D.; Bardon, S. Link, D. R.; Maclennan, J. E.; Chen, X. Wand, M. D.; Walba, D. M.; Rudquist, P. and Lagerwall, S. T. *Appl. Phys. Lett.* **2002**, *80*, 4097.

Clark, N. A. and Lagerwall, S. *Appl. Phys. Lett.* **1980**, *36*, 899.

Collings, P. J. Liquid Crystals: Nature's Delicate Phase of Matter; Princeton University Press: Princeton, **1990**.

Davidson, M. W. *http://micro.magnet.fsu.edu/primer/techniques/polarized/berekcompensator.html.*

Demus, D.; Goodby, J.; Gray, G. W.; Spiess, H.-W. and Vill, V. (**1998**). Handbook of Liquid Crystals. Weinheim: Wiley VCH.

de Vries, A. *Mol. Cryst. Liq. Cryst. Lett.* **1977**, *41*, 27.

Garoff, S. and Meyer, R. *Physical Review Letters* **1977**, *38*, 848.

Glaser, M. and Clark, N. A. *Phys. Rev. E.*, **2002**, *66*, 021711.

Gorkunov, M. V.; Giesselmann, Lagerwall, J. P. F.; Sluckin, T. J. and Osipov, M. A. *Phys. Rev. E* **2007**, *75*, 060701(R).

Gorkunov, M. V.; Osipov, M. A.; Lagerwall, J. P. F. and Giesselmann, F. Phys. Rev. E **2007**, *76*, 051706.

Hansch, C.; Leo, A.; Taft, R. W. *Chem. Rev.* **1991**, *91*, 165.

Hori, K. and Endo, K. *Bull. Chem. Soc. Japan*, **1993**, *66*, 46.

Hori, K.; Kawahara, S. and Ito, K. *Ferroelectrics*, **1993**, *147*, 91.

18^{o} is only achieved at 20 V mm^{-1} at ca. 1 K above the SmA* - SmC* phase transition. This indicates a fairly weak electroclinic effect, since the saturation occurs so close to the SmA* - SmC* phase transition, despite a pronounced electroclinic tilt. The birefringence of **W733** increases from 0.147 at 5 V μm^{-1} to 0.152 at 20 V mm^{-1}, at T-T$_{A-C}$ = 2 K, as shown in Figure 3.16. This is a 3% increase, which is similar to the 2% increase seen in **W697** and smaller than the 7% of **W652.** The birefringence at T–T$_{A-C}$ = -5 K is 0.158, which a 7% increase from the SmA* phase. The field induced polarization in the SmA* phase is too small to measure. The P$_{s}$ of the SmC* phase at T-T$_{A-C}$ = -5 K is 31 nC cm^{-2}, which is ca. 70% the polarization of **W697** and 33% the polarization of **W652** at the same reduced temperature.

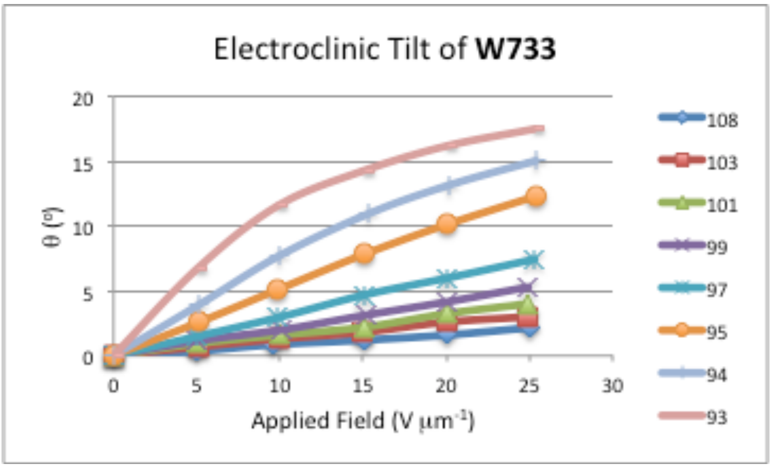

Figure 0.15 The electroclinic tilt of W733 as a function of applied field at various temperatures in the SmA* phase

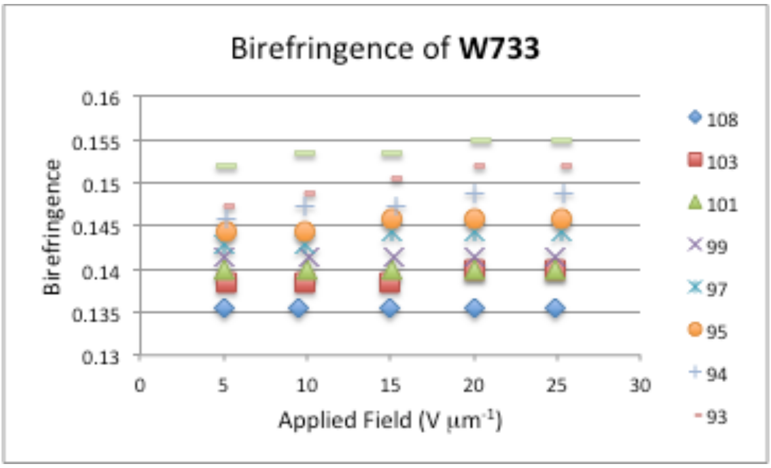

Figure 0.16 The birefringence (Δn) of W733 as a function of applied field at various temperatures in the SmA* phase.

3.4.2 W734

W734 employs an *E*-5-decenyl tail on the same core as **W733**. The SmA* phase forms from the isotropic melt at 78 ^{o}C and transitions to the SmC* phase, via a strongly first order phase transition at 76 ^{o}C and subsequently forms the crystal phase at 22 ^{o}C, on cooling, as shown in Figure 3.17. The layer spacing of the SmA* phase is approximately constant at 32.5 Å across the entire SmA* phase temperature range, as shown in Figure 3.18. The layer spacing of the SmA* phase at the SmA* - SmC* phase transition is significantly shorter than the estimated molecular length of 37.5 Å. The layer spacing of **W734** is 29.2 Å at $T-T_{A-C}$ = -10 K, which is a layer shrinkage of ca. 10%, which is significantly larger than expected for de Vries SmA* materials.

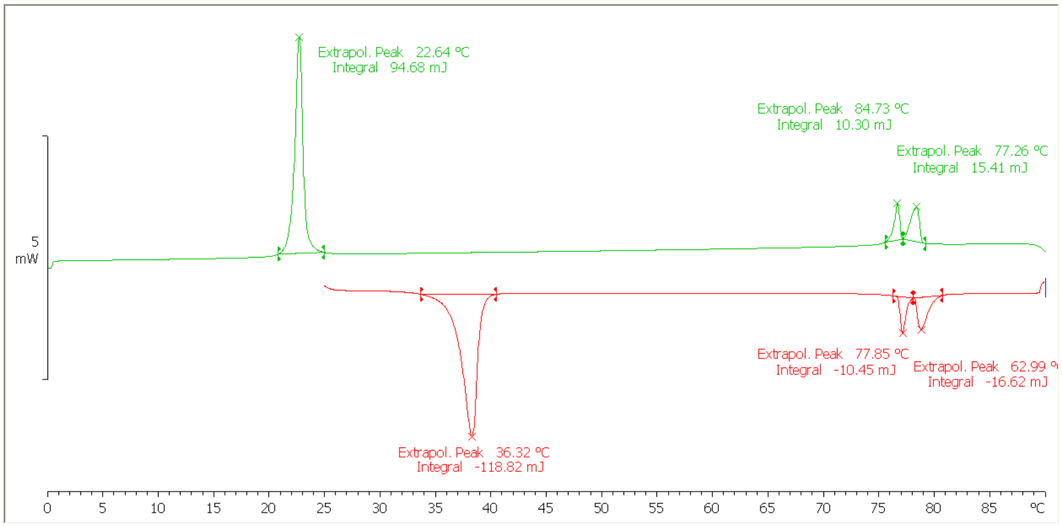

Figure 0.17 DSC of W734

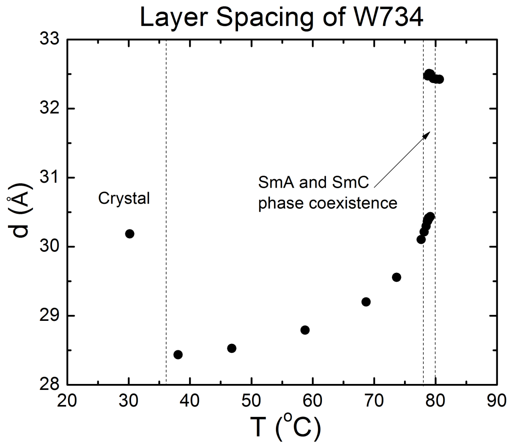

Figure 0.18 Layer spacing of W734 as a function of temperature.

It is difficult to ascertain the electrooptic response of **W734** in the SmA* phase. The application of an electric field at $T\text{-}T_{A\text{-}C}$ = 2 K shows a very weak electroclinic effect with e_c = 0.33 ° μm V^{-1}, with a saturated tilt of 5° at 20 V μm V^{-1}. At $T–T_{A\text{-}C}$ = 1 K the tilt susceptibility increases to ca. 0.67 ° μm V^{-1}, as shown in Figure 3.19. Above applied fields of ~7.5 V μm the sample undergoes a field-induced realignment. The sample gets much brighter and the angle at which the sample aligns with the crossed polarizers changes. It is possible that this is a field induced SmC* phase, however, the change in alignment is unexpected as a field-induced SmC* phase should have the same alignment as the SmA* phase. The average of the two tilt angles of the field-induced SmC* phase should be the same angle at which extinction occurs in the SmA* phase. Since the sample realigns, the saturated tilt of **W734** in the SmA* phase could not be measured. Since the electroclinic tilt at T-$T_{A\text{-}C}$ = 2 K is particularly small and does not reach saturation, i.e. a field induced SmC* phase, the electroclinic effect is considered weak, especially when compared to the chemically similar **W698**, which shows a saturated tilt of 22° and **W657**, which shows a saturated tilt of 33°. The surprisingly small saturated tilt angle of W734 could be a result of the very narrow SmA* phase (ca. 2 K). While the tilt of SmA* materials is largest near the SmA* - SmC* phase transition, at T-$T_{A\text{-}C}$ = 1 K **W734** is only 2 K below the isotropic – SmA* phase transition, thus **W734** is simultaneously close to the isotropic - SmA* and SmA* - SmC* phase transitions. This could be the origin of the anomalously small electroclininc effect. Additionally, **W734** has a very small transverse dipole, which would reduce the coupling to the electric field and lower the optical tilt. The birefringence of **W734** shows very little change in the SmA*, as shown in Figure 3.20. The small change is a result of the birefringence being immeasurable at larger applied fields, due to the field-induced reorientation or the director. The birefringence at T–$T_{A\text{-}C}$ = -5 K is 0.162, which corresponds to an increase of 35%, which is larger than the birefringence change of both **W698** and **W657**. This large birefringence change from the SmA* - SmC* phase is consistent with a de Vries SmA* - SmC* phasetransition. The field induced polarization in the SmA* phase is too small to measure. The P_s at T-$T_{A\text{-}C}$ = -5 K is 62 nC cm^{-2}, which is 88% of the polarization of **W699** and 30% the polarization of **W657**.

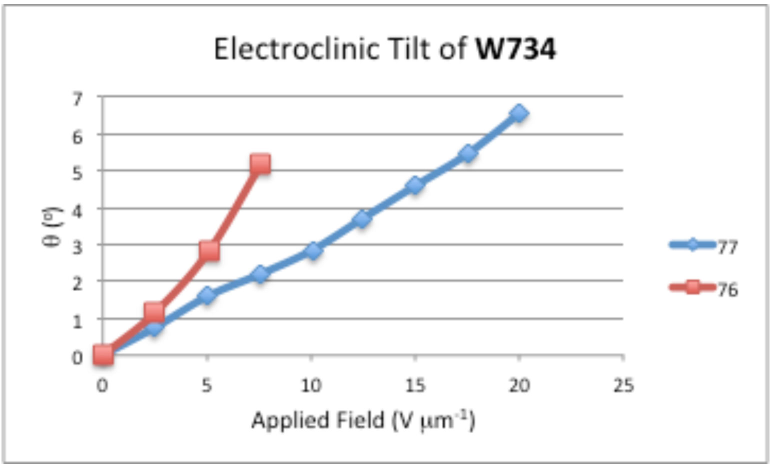

Figure 0.19 The electroclinic tilt of W734 as a function of applied field at various temperatures in the SmA* phase

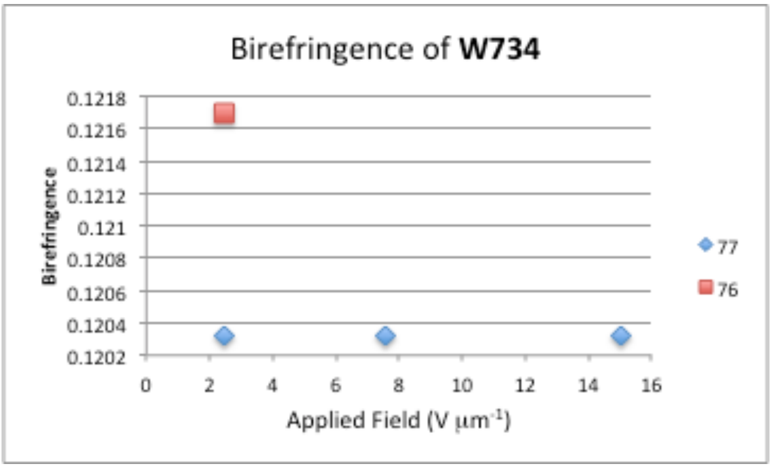

Figure 0.20 The birefringence (Δn) of W734 as a function of applied field at various temperatures in the SmA* phase

3.4.3 W735

W735 employs a 7,7,8,8,9,9,10,10,10-nonylfluoro decyloxy tail on the same core as **W733** and **W734.** The SmA* phase forms from the isotropic melt at 141 ^{o}C and transitions to the SmC* phase, via a first order phase transition, at 117 ^{o}C and transitions to the crystal phase at 4 ^{o}C, on cooling. The DSC for **W735** is shown in Figure 3.21. The layer spacing of the SmA* phase is roughly constant at 33.7 Å across the entire SmA* phase temperature range, as shown in Figure 3.22. This behaviour is consistent with de Vries SmA* materials with strongly first order SmA* - SmC* phase transitions, such as **W530.** The layer spacing of 33.7 Å is significantly shorter than the estimated molecular length of 38.3 Å, and is approximately the same as **W530**,[7] which would suggest they possess similar cone angles. The layer spacing of **W735** at T-T_{A-C} = -10 K is 31.7 Å, which is a layer shrinkage of 6%.

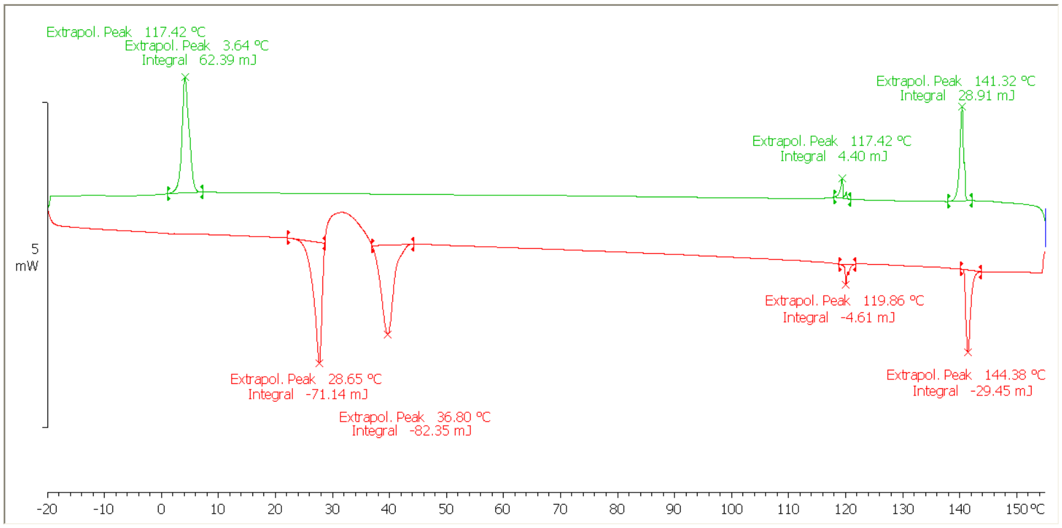

Figure 0.21 DSC of W735

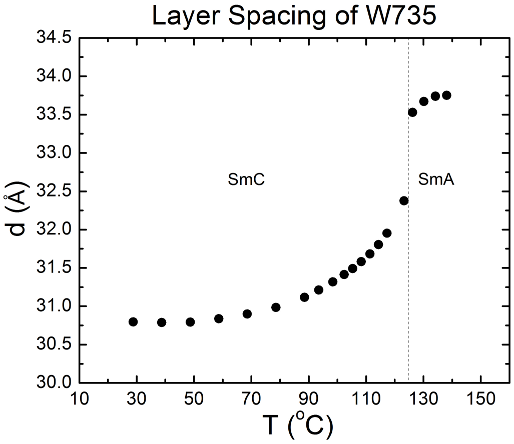

Figure 0.22 Layer spacing of W735 as a function of temperature.

W735 behaves like a prototypical de Vries SmA* material with strongly first order SmA* - SmC* phase transition in the electrooptic response. The application of an electric at T-T_{A-C} = 1 K shows a sigmoidal response in the electroclininc tilt, as shown in Figure 3.23. The saturated tilt of W735 is 28°, which is larger than the 23° seen in **W699** and smaller than the 33^{o} seen in **W530**. The strongly first order SmA* - SmC* phase transition may explain why the saturated tilt of **W735** is larger than in **W699**, as **W735** possesses a field-induced SmC* phase. The saturated tilt of **W735** is smaller than **W530**, which also shows a strongly first order SmA* - SmC* phase transition.[7] This is somewhat surprising since the tilt angle is expected to be the same based on layer spacing. This anomaly could be the result of lower coupling of the transverse dipole to the electric field in **W735** relative to **W530**, or the lateral polar group has some effect on the fully extended molecular length, which is not taken into account in the estimate. Tilt saturation in **W735** is only observed above 15 V μm^{-1} at $T-T_{A-C}$ = 1 K. This indicates a fairly weak electroclinic effect, since the saturation occurs close to the SmA* - SmC* phase transition, despite a large electroclinic tilt. The birefringence of **W735** increases from 0.091 at 5 V μm^{-1} to 0.108 at 20 V μm^{-1} at $T-T_{A-C}$ = 1 K, as shown in Figure 3.24. This is a 19% increase in birefringence, which is similar to the 15% seen in **W699**, but much smaller than the 30% observed in **W530**. The sigmoidal shape in the birefringence vs. applied field is expected based on a modified Langevin model. The birefringence at $T–T_{A-C}$ = -5 K is 0.136, which corresponds to a 50% increase from the SmA* to SmC* phase. The field induced polarization in the SmA* phase is too small to measure, however, it would be expected to show two peaks in the polarization revesal current. The P_s of **W735** at $T-T_{A-C}$ = -5 K is 27 nC cm^{-2}, which is 1.3x smaller than **W699** and 4x smaller than **W530**[7] at the same reduced temperature.

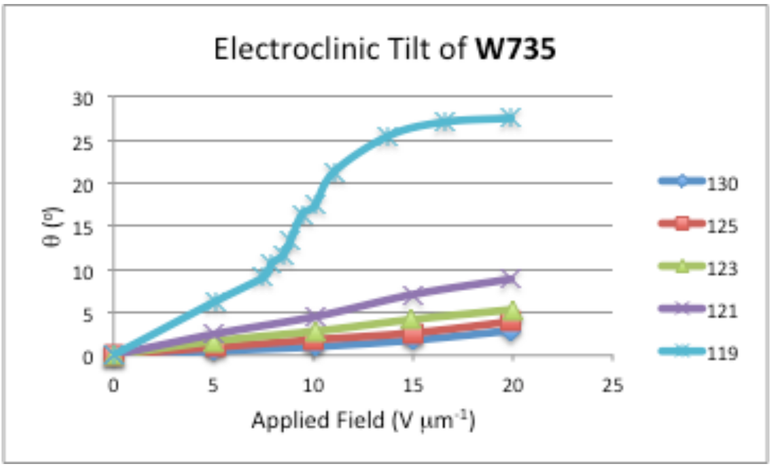

Figure 0.23 The electroclinic tilt of W735 as a function of applied field at various temperatures in the SmA* phase

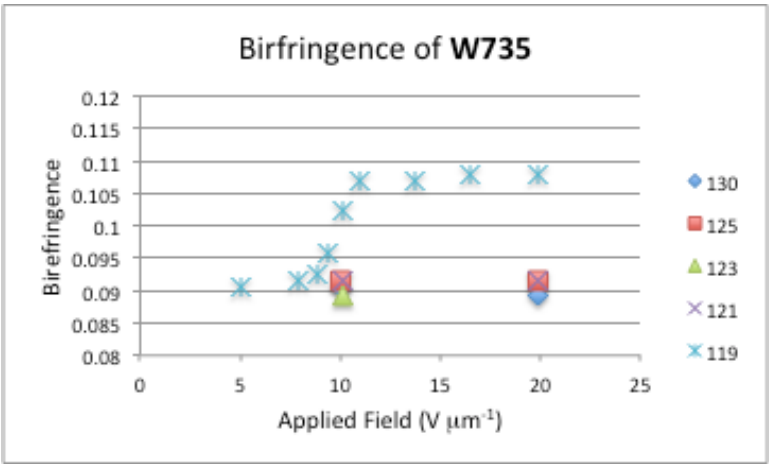

Figure 0.24 The birefringence (Δn) of W735 as a function of applied field at various temperatures in the SmA* phase.

3.5 Effect of Chloro as Lateral Polar Group

3.5.1 W713

W713 employs an n-decyloxy tail on the scaffold of **Core B** with a lateral chloro group in place of the trifluoromethyl group. The SmA* phase forms from the isotropic melt at 122 ^{o}C and transitions to the SmC* phase, via a weakly first order phase transition at 105 ^{o}C, which then transitions to the crystal phase at 30 ^{o}C, on cooling. The DSC of **W713** is shown in Figure 3.25. The layer spacing of the SmA* phase rises from 34.0 Å at 127 ^{o}C to 34.4 Å at 109 ^{o}C, as shown in Figure 3.26. This layer expansion is consistent with de Vries materials with a weakly first order SmA* - SmC* phase transition, such as **W652**, **W697** and **W733**, all of which are built on the scaffold of Core B with an n-decyloxy tail. The layers expand at a rate of 0.022 Å K^{-1}. The rate of layer expansion is smaller than **W697** and **W733**, but smaller than **W652**. The layer spacing of **W713** at the SmA* - SmC* phase transition is much shorter than the estimated molecular length of 37.8 Å. At $T-T_{A-C} = -10$ K the layer spacing is 31.9 Å, which is a layer shrinkage of 7%.

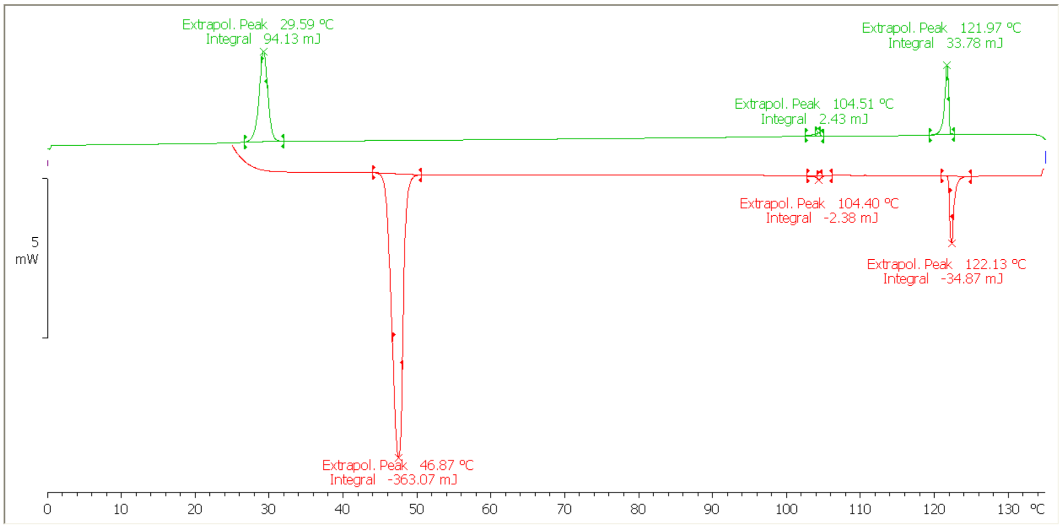

Figure 0.25 DSC of W713

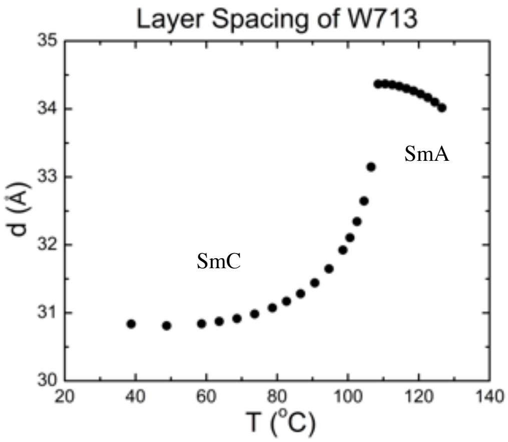

Figure 0.26 Layer spacing of W713 as a function of temperature.

W713 behaves like a de Vries SmA* material with a weakly first order SmA* - SmC* phase transition in how it reacts to the application of an electric field near the SmA* - SmC* phase transition temperature. The saturated tilt of **W713** in the SmA* phase is 23° (Figure 2.27), which slightly larger than the X-Ray tilt of 22°. The saturated tilt of **W713** larger than the 18° of both **W699** and **W733**, but is lower than the 27° of **W652**. The saturated tilt of ca. 23° is achieved at 20 V mm^{-1} at as far as 3 K above the SmA* - SmC* phase transition. This indicates a significantly stronger electroclinic effect than **W697** and **W733** which only show saturation at ca. 1 K above the SmA* - SmC* phase transition, suggesting a stronger coupling to the electric field. The birefringence of **W713** increases from 0.131 at 5 V μm^{-1} to 0.140 at 20 V μm^{-1} at T-T$_{A\text{-}C}$ = 2 K, as shown in Figure 2.28. This corresponds to a 7% increase. The increase in birefringence is similar to the field-induced increase seen in **W699**, **W733** and **W652**. The birefringence at T – T$_{A\text{-}C}$ = -5 K in the SmC* phase is 0.150, which corresponds to a 15% increase from the SmA* to SmC* phase. The field induced-polarization in the SmA* phase could be measured T-T$_{A\text{-}C}$ = 1 K. The reduced polarization vs. applied filed is shown in Figure 3.29. The relationship between P$_s$ and applied field is linear, which is unexpected since once saturation is achieved, at ca. 10 V μm^{-1}, the polarization should not change significantly. The largest measurable polarization in the SmA* phase is 9 nC cm^{-2}. The P$_s$ of the SmC* phase at T-T$_{A\text{-}C}$ = -5 K is 87 nC cm^{-2}. The spontaneous polarization of **W713** is 2x larger than that of **W699**, 2.8x larger than that of **W733** and 93% the spontaneous polarization of **W652**.

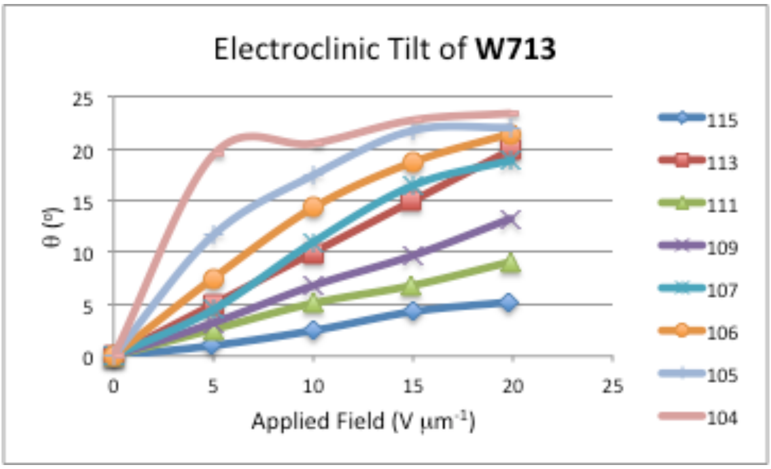

Figure 0.27 The electroclinic tilt of W713 as a function of applied field at various temperatures in the SmA* phase

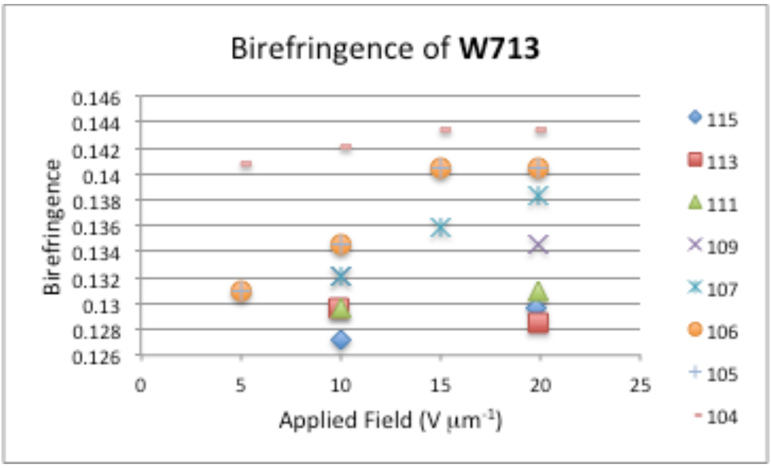

Figure 0.28 The birefringence (Δn) of W713 as a function of applied field at various temperatures in the SmA* phase.

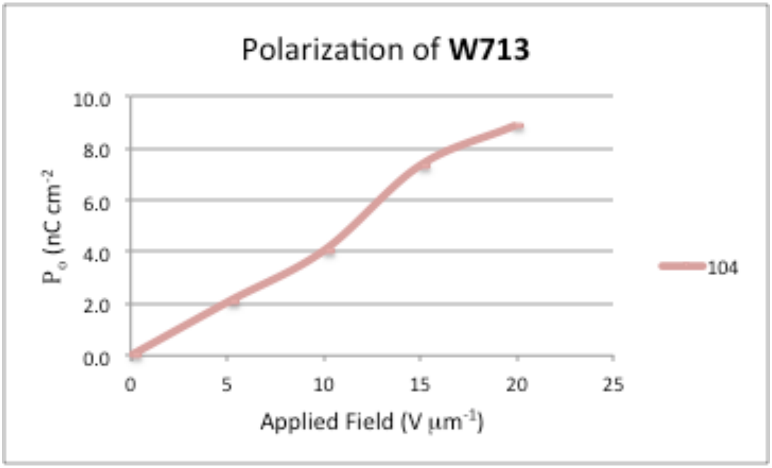

Figure 0.29 Field-induced polarization of W713

3.5.2 W714

W714 employs an *E*-5-decenyloxy tail on the same core as **W713**. The SmA* phase forms from the isotropic melt at 92 °C and transitions to the SmC* phase, via a first order phase transition at 86 °C and into the crystal phase at 27 °C, on cooling. The DSC for **W714** is shown in Figure 3.30. The layer spacing of the SmA* phase is roughly constant at 32.1 Å from ca. 95 °C to 88 °C. This behaviour is consistent with a de Vries SmA* phase. The layer spacing of **W714** is shown in Figure 3.31. **W714** does not show coexistence between the SmA* phase and SmC*, which is indicative of a first order phase transition, however, the layers contract sharply at 88 °C, suggesting a first order phase transition. The layer spacing of 32.1 Å is significantly shorter than the estimated fully extended molecular length of 37.5 Å. The layer spacing of **W714** is 29.6 Å at T-T$_{A-C}$ = -10 K, resulting in a layer shrinkage of ca. 8%.

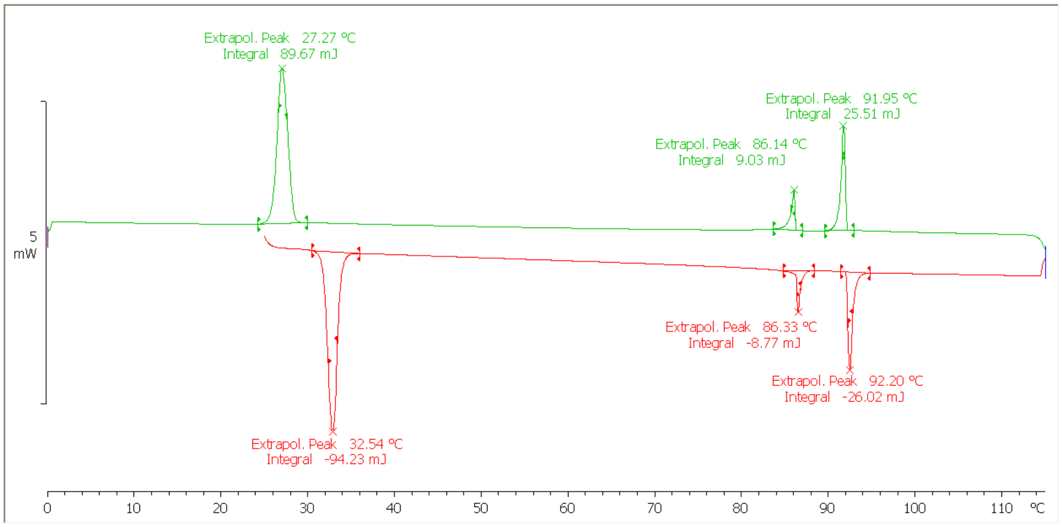

Figure 0.30 DSC of W714

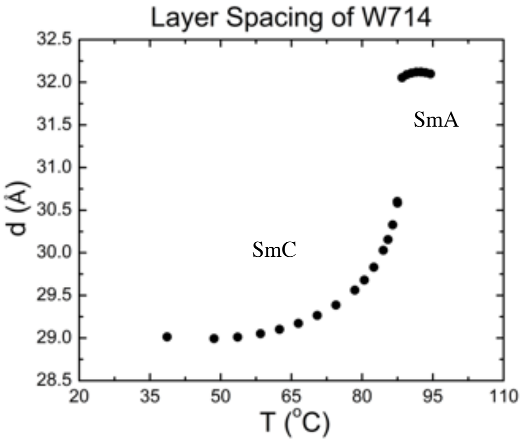

Figure 0.31 Layer spacing of W714 as a function of temperature.

W714 behaves like a prototypical de Vries SmA* material with a strongly first order SmA* - SmC* phase transition in the electrooptic response. The application of an electric at $T\text{-}T_{A\text{-}C}$ = 2 K a strong sigmoid response in the electroclinic tilt as a function of applied field is observed, as shown in Figure 3.32. The saturated tilt of W714 is 29^{o}, which smaller than the X-Ray tilt of 27^{o}. The X-Ray tilt should be smaller than the optical tilt and the discrepancy could be explained by the crude nature of the estimation of the molecular length. The saturated tilt of **W714** is larger than **W698** and smaller than **W657**. The saturated tilt of **W714** cannot be compared to the tilt of **W734**, since the alignment of W734 changes with the application of electric fields above ca. 7.5 V μm^{-1}. Tilt saturation in **W714** is observed at temperatures as high as T-T$_{A-C}$ = 3 K. This is at a higher reduced temperature than **W698**, in which saturation is only observed at T-T$_{A-C}$ = 1 K. This indicates a relatively strong electroclinic effect, since the field-induced SmA – SmC* phase transition occurs so far away from the SmA* - SmC* phase transition. The birefringence of **W714** increases from 0.118 at 2.5 V mm^{-1} to 0.142 at 20 V mm^{-1} at T-T$_{A-C}$ = 1 K, as shown in Figure 3.33. This is a 20% increase in birefringence from the de Vries SmA* to the field-induced SmA* phase. The birefringence change of **W714** is larger than both **W699** and **W734**, but a little smaller than **W657**. The sigmoidal shape in the birefringence vs. applied field plot mirrors the electroclininc tilt as a function of applied field, as expected. The birefringence at T–T$_{A-C}$ = -5 K is 0.146, which is similar a 20% increase from the SmA* to the SmC* phase. The field-induced polarization in the SmA* phase is only measurable at T-T$_{A-C}$ = 1K and is shown in Figure 3.34. The polarization reversal current shows two peaks, like prototypical de Vries SmA* materials **W657** and **W530**, and the polarization seems to increase linearly. It is expected to, however, follow the sigmoidal shape of both the birefringence and tilt. The very small magnitude of polarization may be the origin of this discrepancy. The P$_s$ of the SmC* phase at T-T$_{A-C}$ = -5 K is 148 nC cm^{-2}, which is 2.1x larger than the polarization of **W699**, 2.8x larger than the polarization of **W734** and 70% of the polarization of **W657**, at the same reduced temperature.

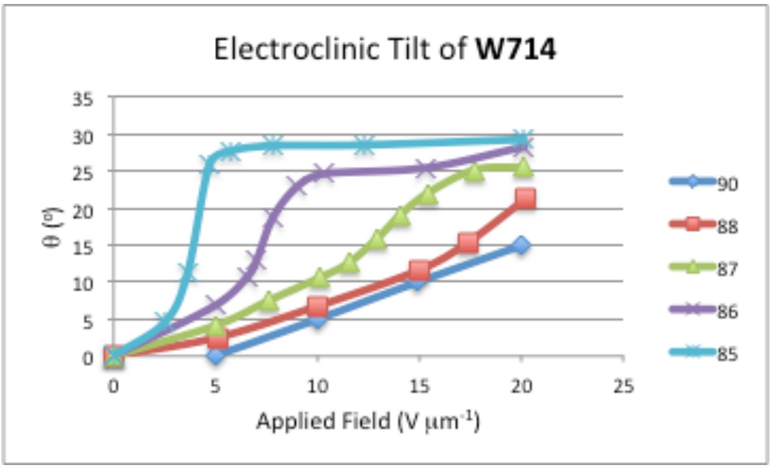

Figure 0.32 The electroclinic tilt of W714 as a function of applied field at various temperatures in the SmA* phase

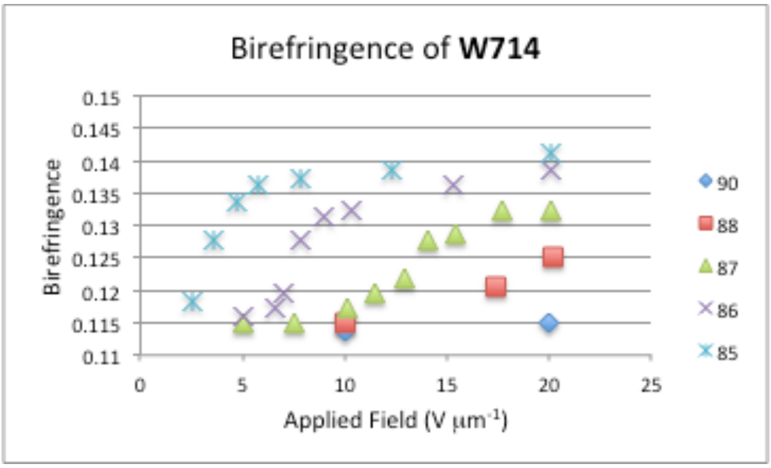

Figure 0.33 The birefringence (Δn) of W714 as a function of applied field at various temperatures in the SmA* phase.

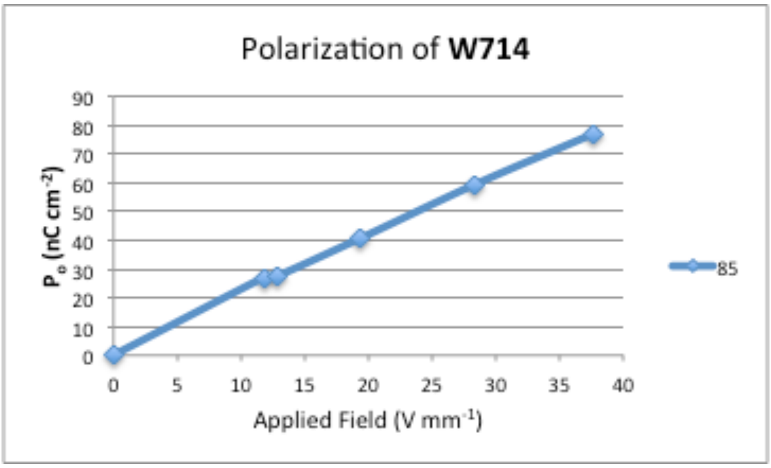

Figure 0.34 Field-induced polarization of W714

3.5.3 W715

W715 employs a 7,7,8,8,9,9,10,10,10-nonylfluoro decyloxy tail on the same core as **W713** and **W714**. The SmA* phase forms from the isotropic melt at 151 °C and transitions to the SmC* phase, via a weakly first order phase transition at 120 °C and transitions into the crystal phase at 18 °C, on cooling. The DSC for **W715** is shown in Figure 3.35. The layer spacing of the SmA* phase is roughly constant at 34.4 Å over the entire SmA* phase range, which is consistent with materials that form the de Vries SmA* phase with a strongly first order SmA* - SmC* phase transition, such as **W530**. The layer spacing of **W715** is shown in Figure 3.36. The layer spacing of **W715** at the SmA* - SmC* phase transition is 34.4 Å and is significantly shorter than the estimated molecular length of 38.3 Å. This value is intermediate between the chemically similar materials **W699** (35.4 Å), **W735** (33.7 Å) and **W530** (33.8 Å). The layer spacing of **W735** is 32.8 Å at $T-T_{A-C}$ = -10 K, which is a layer shrinkage of 5%.

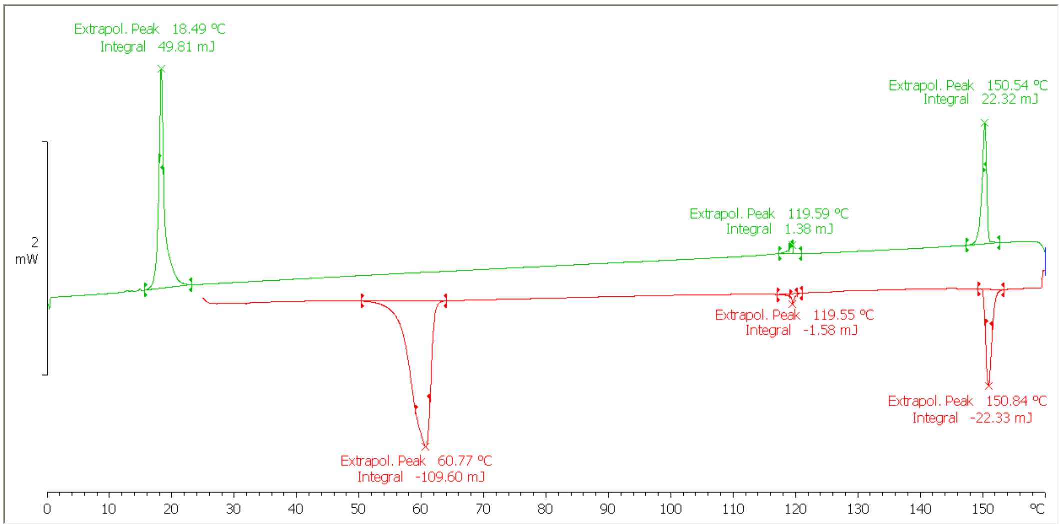

Figure 0.35 DSC of W715

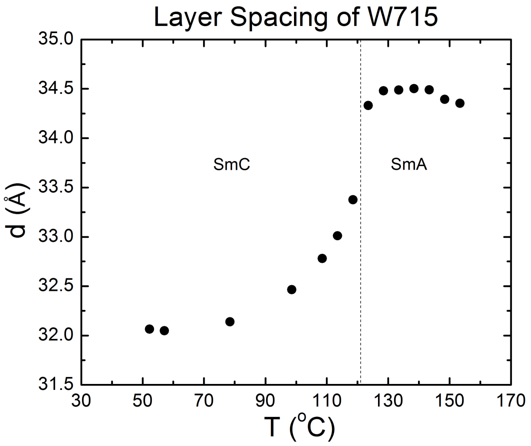

Figure 0.36 Layer spacing of W715 as a function of temperature.

W715 behaves like a de Vries SmA* material with a weakly first order phase transition in the electrooptic response, like **W699**, as shown in Figure 3.37. The saturated tilt angle of **W715** is 27^o and is equal to the saturated tilt of **W735**, larger than the 23^o saturated tilt of **W699**, but smaller than the 33^o saturated tilt of **W530**. Tilt saturation in **W715** is first observed above 15 V μm^{-1} at 1 K above the SmA* - SmC* phase transition, although at 20 V μm^{-1} at T-T_{A-C} = 2 K, the tilt angle is very close to saturation. This indicates a fairly weak electroclinic effect, since the saturation only occurs so close to the SmA* - SmC* phase transition, despite a pronounced electroclinic tilt, upwards of 20^o, at T-T_{A-C} = 5 K. The tilt saturation of **W715** occurs closer to the SmA* - SmC* phase transition that **W713** and **W714**, both of which possess the chloro lateral polar group. The birefringence of **W715** increases from 0.099 at 2 V μm^{-1} to 0.120 at 20 V mm^{-1}at T – T_{A-C} = 1 K, as shown in Figure 3.38. This corresponds to a 21% increase in birefringence from low to high applied field at T-T_{A-C} = 1 K. The 21% increase of **W715** is larger than the 15% of **W699**, similar to the 19% increase of **W735**, and smaller than the 30% of **W530**. The shape of the birefringence vs. applied field curve of **W715** strongly mirrors the shape of the electroclinic tilt vs. applied field curve, as expected. The birefringence at T–$T_{A\text{-}C}$ = -5 K 0.130, which corresponds to a 31% increase from the SmA* phase to the SmC* phase. The field-induced polarization in the SmA* at is only measurable at T-$T_{A\text{-}C}$ = 1 K. A plot of polarization vs. applied field for **W715** is shown in Figure 3.39. The polarization increases linearly, which is surprising since the polarization vs. applied field curve should closely resemble the electroclinic tilt and birefringence curves. The very small polarization may be the origin of the anomalous shape, as the error of the measurement is large relative to the magnitude of the polarization. There is only one peak in the polarization reversal current, further suggesting this is a weakly first order SmA* - SmC* phase transition, similar to **W652**. The P_s of **W715** at T-$T_{A\text{-}C}$ = -5 K is 78 nC cm^{-2}, which is 2.2x larger than the polarization of **W699**, 2.9x larger than the polarization of **W735** and 74% of the polarization of **W530**, at the same reduced temperature.

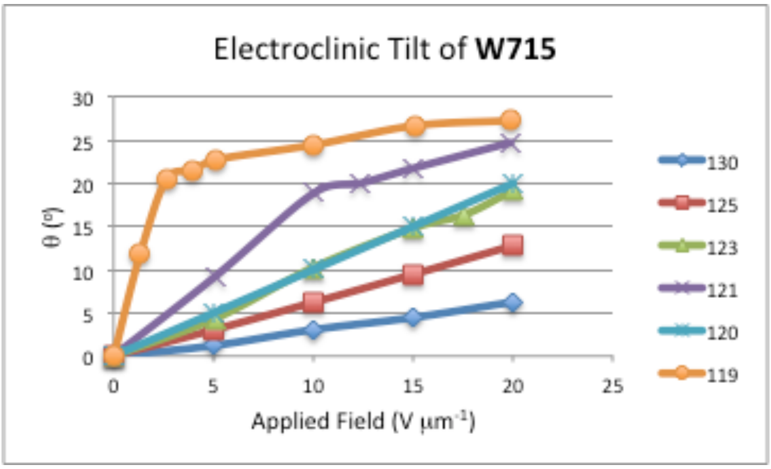

Figure 0.37 The electroclinic tilt of W715 as a function of applied field at various temperatures in the SmA* phase

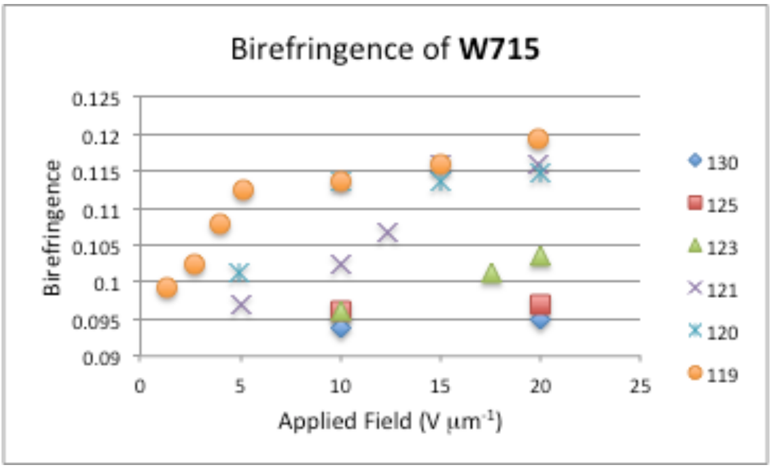

Figure 0.38 The birefringence (Δn) of W715 as a function of applied field at various temperatures in the SmA* phase.

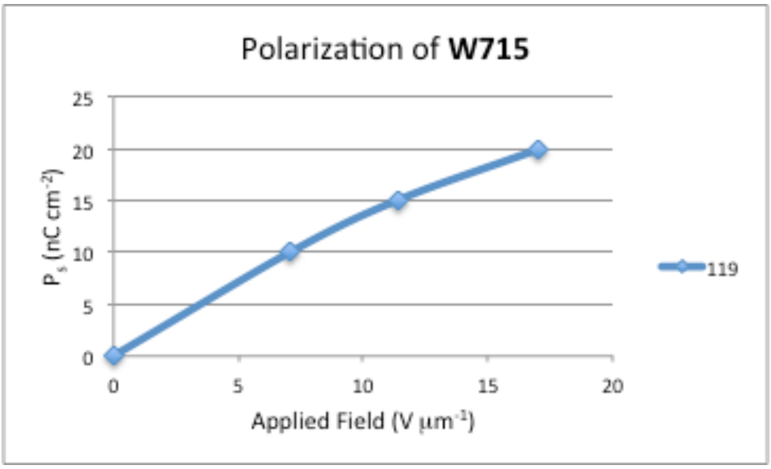

Figure 0.39 Field-induced polarization of W715

3.6 Effect of Nitro as Lateral Polar Group

3.6.1 W314

W314 employs an n-decyloxy tail on the **Core B** scaffold with a lateral nitro group replacing the trifluoromethyl group. **W314** is a known material first reported by the Walba lab in 1991 and was reported to possesses nearly no electroclinic effect, although it does possess one of the largest spontaneous polarizations in the SmC* phase of a calamitic liquid crystal.[8] The lack of strong electroclinic effect, given the strong electroclinic effects of all compounds built on the **Core B** scaffold, such as n-decyloxy possessing analogues **W652**,

W697, **W733** and **W713**, was surprising. **W314** was resynthesized and its properties examined. The SmA* phase forms from the isotropic melt at 115 °C and transitions to the SmC* phase, via a weakly first order phase transition at 91 °C and transitions to the crystal phase at 22 °C. These phase transitions are consistent with literature values.[8] The DSC of **W314** is shown in Figure 3.40. These phase transitions are consistent with the literature values. The layer spacing of the SmA* phase of **W314** increases from 33.2 Å at 123 °C to 33.5 Å at 95 °C. This is a rate of increase of 0.011 Å K^{-1}. **W314** possesses a layer spacing of 33.5 Å at the SmA* - SmC* phase transition, which is significantly shorter than the estimated molecular length of 37.8 Å. The X-Ray layer spacing of **W314** is shown in Figure 3.41. This suggests that W314 is de Vries, which is previously unreported. At T-T$_{A-C}$ = -10 K the layer spacing is 31.8 Å, which corresponds to a layer shrinkage of 5%.

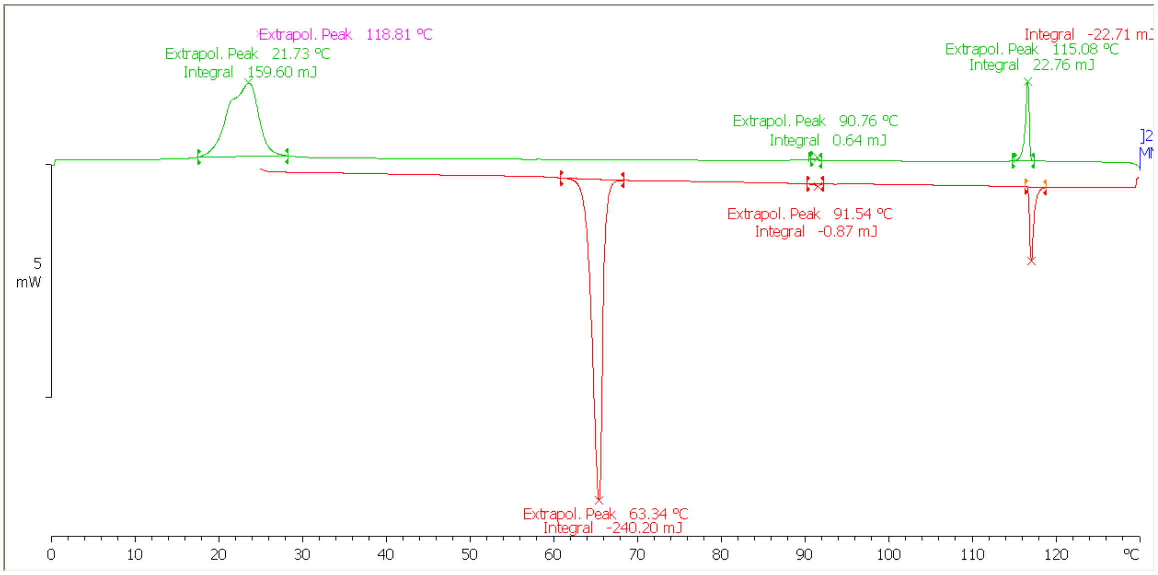

Figure 0.40 DSC of W314

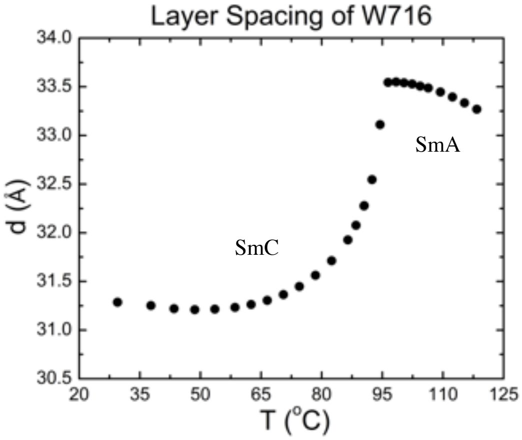

Figure 0.41 Layer spacing of W314 as a function of temperature.

Contrary to published results,[8] **W314** has a very strong electrooptic response. **W314** behaves like a de Vries SmA* with a weakly first order SmA* - SmC* phase transition in the electrooptic response near the SmA* - SmC* phase transition temperature. The saturated tilt of **W713** in the SmA* phase is 24°, as shown in Figure 3.42, which is lower than the X-Ray tilt of 28°. The optical tilt should be larger than the X-Ray tilt, suggesting that either the crude estimate of the molecular length is inaccurate or the molecules do not reach saturation. The saturated tilt of 24° is larger than that observed in chemically similar **W697** and **W733**, approximately equal to the saturated tilt of **W713**, and smaller than the 26° seen in **W652**. The saturated tilt of **W314** is achieved at 20 V μm^{-1} at as far as 4 K above the SmA* - SmC* phase transition. This indicates a largerer electroclinic effect than **W697**, **W733**, **W713** and W652, evidenced by saturation of the electroclinic tilt occurring further from the SmA* - SmC* phase tranisition. The birefringence of **W314** increases from 0.145 at 10 V μm^{-1} to 0.155 at 20 V mm^{-1} at T-T$_{A\text{-}C}$ = 4 K. This corresponds to a 7% increase, which is similar to increases observed in chemically similar de Vries SmA* materials with a weakly first order SmA* - SmC* phase transition, **W699**, **W733**, **W713** and **W652**. The birefringence as a function of applied field is shown in Figure 3.43. The birefringence at T–T_{A-C} = -5 K is 0.162, which corresponds to a 12% increase in birefringence from the SmA* phase to the SmA* phase. This behaviour is consistent with a de Vries SmA* - SmC* phase transition. The field induced-polarization in the SmA* phase could be measured as high as T-T_{A-C} = 4 K, which is further away from the SmA* - SmC* phase transition than **W713** and **W652**. This is likely a result of the larger transverse dipole of the nitro analogue relative to chloro or trifluoromethyl. The field-induced polarization vs. applied filed is shown in Figure 3.44. Only one peak is observed in the polarization reversal current, which is consistent with de Vries materials with weakly first order SmA* - SmC* phase transitions. The polarization vs. applied filed curve mirrors the electrooptic tilt vs. applied field curve well, as expected. The maximum field-induced polarization of **W314** is 206 nC cm^{-2}. The polarization of **W314** at T-T_{A-C} = -5 K is 269nC cm^{-2}. The polarization of **W314** is 6.2x larger than the polarization of **W699**, 8.7x larger than the polarization of **W733**, 3.1x larger than **W713** and 2.9x larger than **W652**.

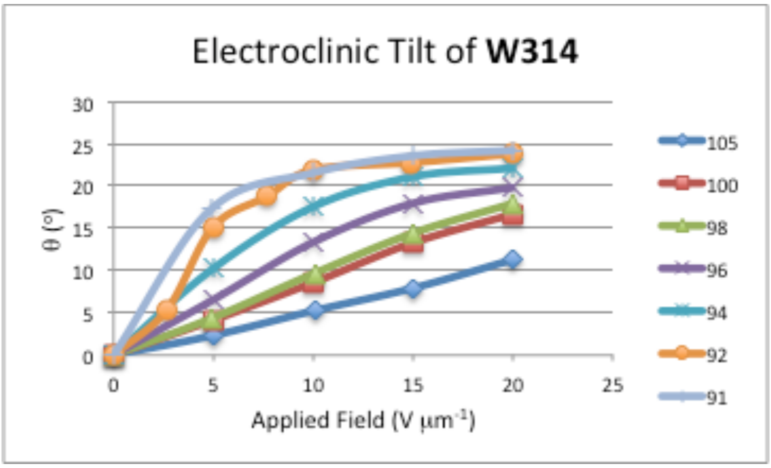

Figure 0.42 The electroclinic tilt of W314 as a function of applied field at various temperatures in the SmA* phase

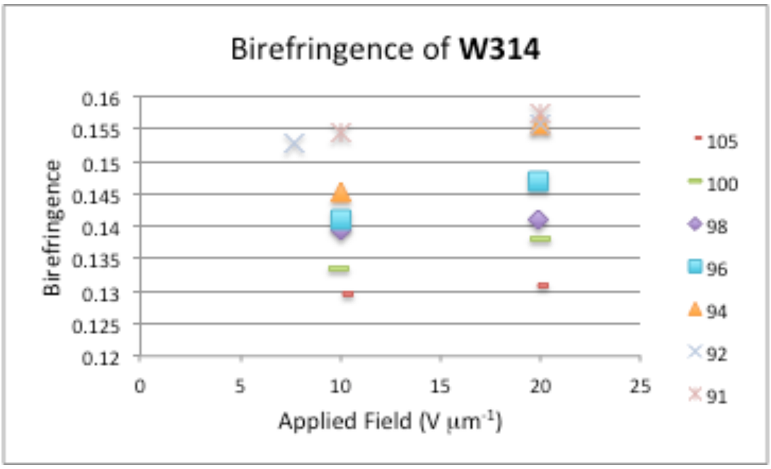

Figure 0.43 The birefringence (Δn) of W314 as a function of applied field at various temperatures in the SmA* phase.

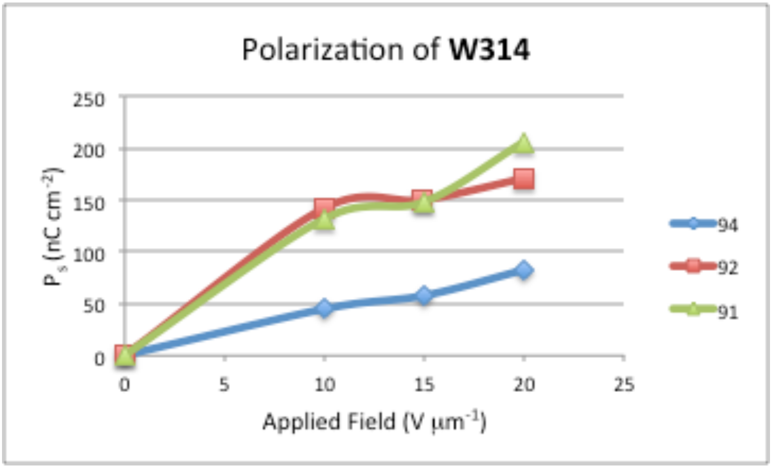

Figure 0.44 Field-induced polarization of W314 at various temperatures

3.6.2 W717

W717 employs a *E*-5-decenyloxy tail on the same core as W314. The SmA* phase forms from the isotropic melt at 89 ^{o}C and transitions to the SmC* phase, via a weakly first order phase transition at 72 ^{o}C, which trasitions to a crystal phase at 12 ^{o}C. The DSC for **W717** is shown in Figure 3.45. The SmA* - SmC* phase transition has the lowest transition energy relative to all other E-5-decenyl compounds in this series. This results in a first order phase transition more similar to W314 than W657, a prototypical de Vries SmA* possessing compound with a strongly first order phase transition that showns a field-induced SmA* - SmC* phase transition. The layer spacing of the SmA* phase shows two distinct regions. At high temperature, on cooling, the layers expand from 31.6 Å at 93 ^{o}C to 31.8 Å at 85 ^{o}C. The layers then begin to contract and the layer spacing at the SmA* - SmC* phase transition temperature is 31.7 Å. The X-Ray layer spacing as a function of temperature of W717 is shown in Figure 3.46. This behaviour is not consistent with prototypical de Vries SmA* materials with strongly first order SmA* - SmC* phase transitions. The layer spacing of 31.7 Å at the SmA* - SmC* phase transition is significantly shorter than the estimated extended molecular length of 37.5 Å. The layer spacing of **W717** is 30.2 Å at $T-T_{A-C}$ = -10 K, which corresponds to a 5% layer shrinkage.

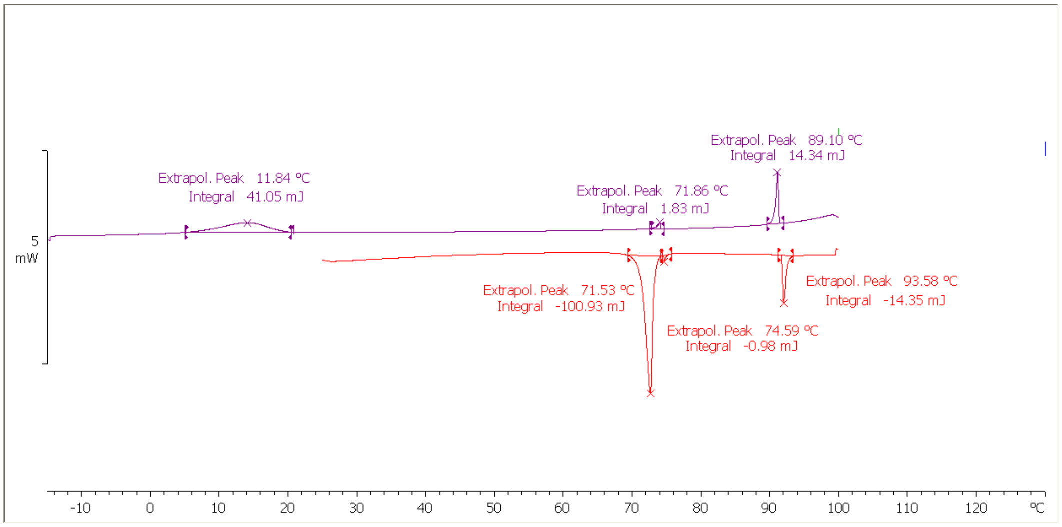

Figure 0.45 DSC of W717

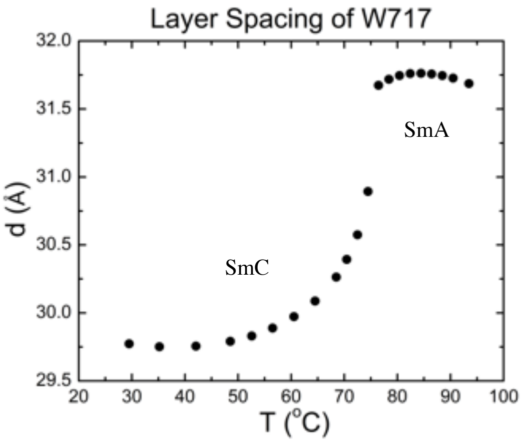

Figure 0.46 Layer spacing of W717 as a function of temperature.

W717 behaves like a de Vries SmA* material with a weakly first order SmA* - SmC* phase transition in the electrooptic response. The saturated tilt of W717 is 27°, which is reached at 15 V μm^{-1} at T-T$_{A\text{-}C}$ = 2 K. The plot of the electroclinic tilt vs. applied field is shown in Figure 3.47. The saturated tilt of **W717** is 27° is larger than the 22° seen in **W698**, approximately the same as the chlorinated analogue **W714** and smaller than the trifluoromethyl analogue **W657**. The saturated tilt can not be compared to the methyl analogue **W734**, since **W734** reorients with large applied fields and the saturated tilt could not be measured. Surprisingly **W717** does not show a strongly sigmoidal response in the electroclinic tilt vs. applied field, like all other compounds in this series with an *E*-5-decenyloxy tail. This is due to a weakly first order SmA* - SmC* phase transition, however, why **W717** does not show a strong SmA* - SmC* phase transition is unknown. Strangely, **W415**, which possesses a core that does not promote the de Vries SmA* phase as well as the **Core B** analogues, shows a strongly first order SmA* - SmC* phase transition and sigmoidal response in the electroclinic tilt vs. applied field.[9] Tilt saturation in **W717** is observed 2 K above the SmA* - SmC* phase transition, which suggests a stronger electroclinic effect than **W699**, **W734**, which show saturation at T-$T_{A\text{-}C}$ = 1 K, approximately the same as **W714**, which shows saturation at T-$T_{A\text{-}C}$ = 2K, and much lower than **W657**, which shows tilt saturation as high as T-$T_{A\text{-}C}$ = 5 K. The birefringence of **W717** increases from 0.129 at 2 V μm^{-1} to 0.148 at 20 V μm^{-1} at T-$T_{A\text{-}C}$ = 1 K. The plot of birefringence vs. applied field is shown in Figure 3.48. The increase in birefringence at T-$T_{A\text{-}C}$ = 1 K is 15%, which is larger than the 8% birefringence increase seen in **W699**, but less than the 20% and 25% seen in **W714** and **W657**, respectively. The shape of the birefringence vs. applied field plot closely mirrors the shape of the electroclininc tilt vs. applied field plotas expected. The birefringence at T–$T_{A\text{-}C}$ = -5 K in the SmC* phase is 0.154, which corresponds to a 19% increase. The field-induced polarization of **W717** is shown in Figure 3.49. The maximum field-induced polarization of **W717** is 98 nC cm^{-2}. This is ca. 50% the field-induced polarization of W716. This is anomalous since other compounds built on the core B scaffold with an *E*-5 decenyloxy tail show polarization values 1.8x larger than the decyloxy analogues. The origin of this discrepancy is currently being investigated. The P_s of the SmC* phase at T-$T_{A\text{-}C}$ = -5 K is 420 nC cm^{-2}. This is larger than the P_s of **W314** at the same reduced polarization, which is consistent with the other compounds in this series. The polarization of **W717** is 6x larger than the polarization of **W698**, 6.7x larger than the polarization of **W734**, 2.8x larger than the polarization of **W714** and 2x larger than the polarization of **W657**, at the same reduced temperature. Amazingly, the polarization of **W717** 1.5x larger than **W314**, a material renowned for very large polarization, at the same reduced temperature. At 30 ^{o}C, well below the SmA* - SmC* phase transition, the P_s is measured to be 784 nC cm^{-2}, which is amongst the largest polarizations measured for calamitic liquid crystals.

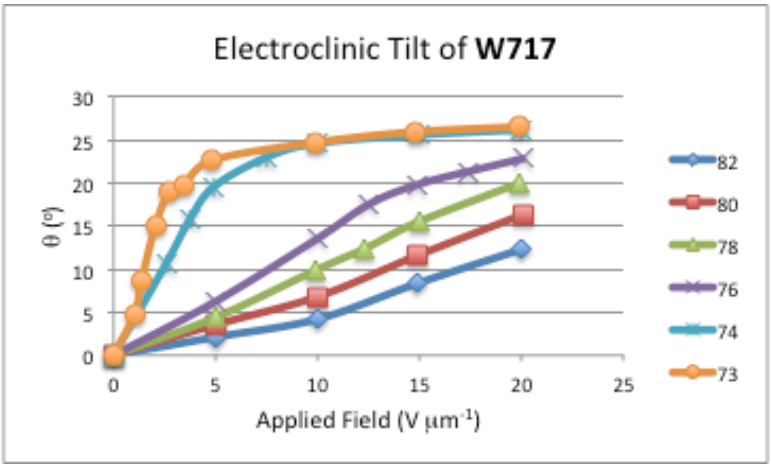

Figure 0.47 The electroclinic tilt of W717 as a function of applied field at various temperatures in the SmA* phase

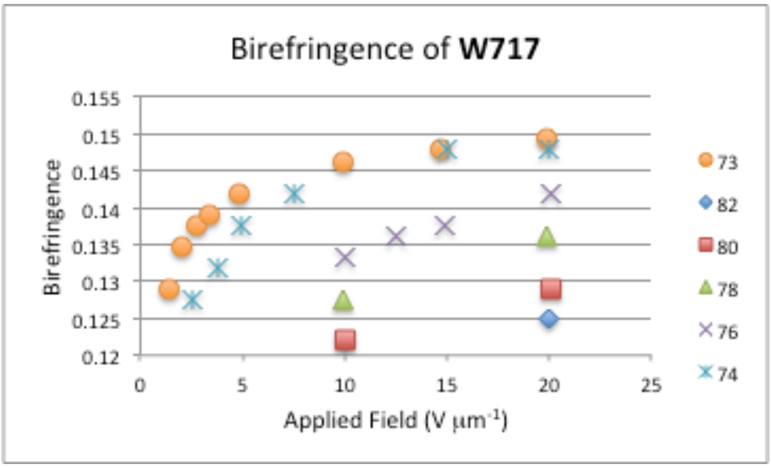

Figure 0.48 The birefringence (Δn) of W717 as a function of applied field at various temperatures in the SmA* phase

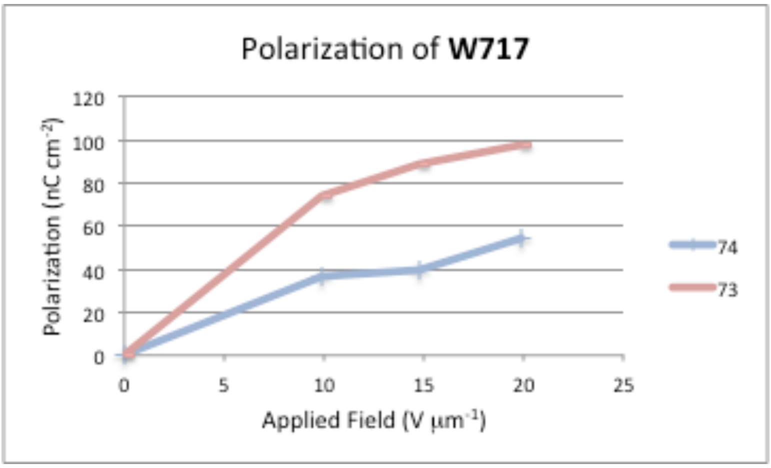

Figure 0.49 Field-induced polarization of W717 at various temperatures

3.6.3 W718

W718 employs a 7,7,8,8,9,9,10,10,10-nonylfluoro decyloxy tail on the same core as **W314** and **W717**. The SmA* phase forms from the isotropic melt at 147 ^{o}C and transitions to the SmC* phase, via weakly first order phase transition, at 83 ^{o}C which transitions to the crystal phase at 9 ^{o}C. The DSC for **W715** is shown in Figure 3.50. The layer spacing of the SmA* phase increases from 34.1 Å at 155 ^{o}C to 34.8 Å at 100 ^{o}C. The layers then contract to 34.7 Å before transitioning to the SmC* phase at 89 ^{o}C . The X-Ray layer spacing of **W718** is shown in Figure 3.51. This behaviour is consistent with a traditional SmA* phase with a weakly first order SmA* - SmC* phase transition. The layer spacing of 34.7 Å is significantly shorter than the fully estimated molecular length of 38.3 Å. The layer spacing of **W718** at $T\text{-}T_{A\text{-}C}$ = -10 K is 33.5 Å, which corresponds to a 4% layer shrinkage.

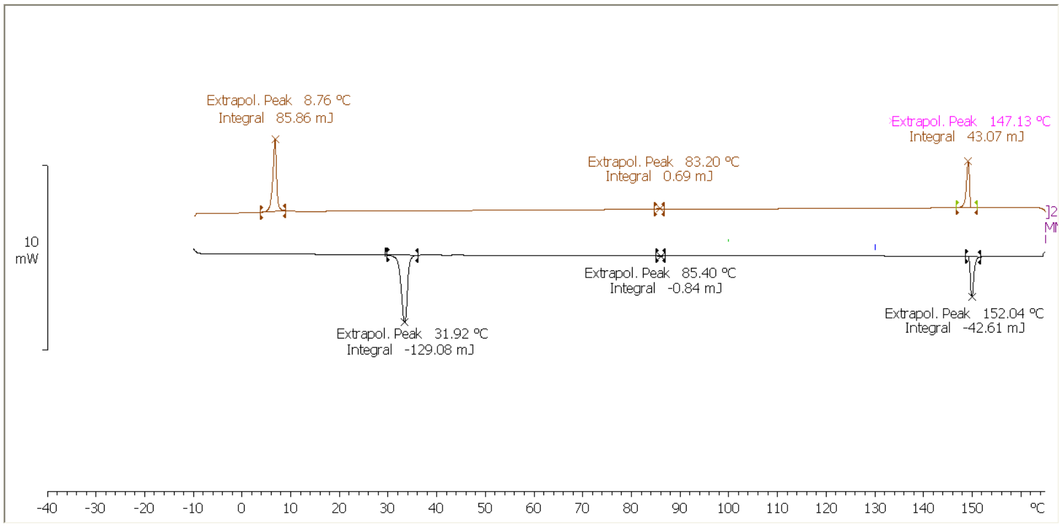

Figure 0.50 DSC of W718

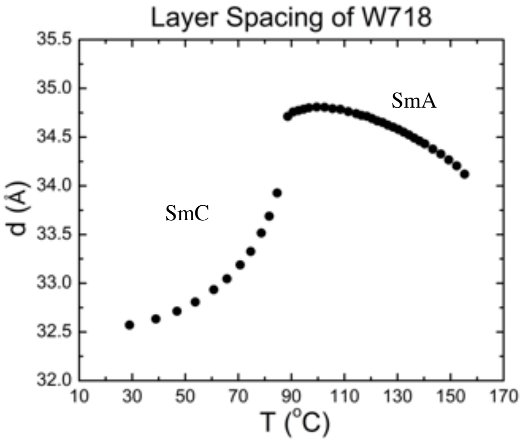

Figure 0.51 Layer spacing of W718 as a function of temperature.

W718, much like **W699** and **W715**, behaves like a de Vries SmA* material with a weakly first order SmA* - SmC* phase transition in the electrooptic response. The saturated tilt angle of W718 is 27^o, which is larger than the calculate X-Ray tilt of 25^o. The tilt vs. applied field response of W718 is shown in Figure 3.52. The saturated tilt of **W718** is approximately the same as the saturated tilt of the chemically similar semi-fluorinated tail possessing materials **W735** and **W715**, larger than 23^o of **W699** and smaller than the 33^o seen in **W530**.[7] Additionally, the saturated tilt angle is approximately the same as **W717**, which possesses the same core, an achiral tail expected to suppress out-of-layer fluctuations and a weakly first order SmA* - SmC* phase tranisiton. Tilt saturation of **W718** is observed as far above the SmA* - SmC* phase transition as 5 K at 20 V μm^{-1}. This indicates a strong electroclinic effect, since the saturation occurs so far above the SmA* - SmC* phase transition. The birefringence of **W718** increases from 0.097 at 2 V μm^{-1} to 0.117 at 20 V mm^{-1}, at T-T$_{A\text{-}C}$ = 1 K. This represents a 21% increase in the birefringence, which is much larger than the 15% of **W699**, very similar to the 19% and 20% of **W735** and **W718**, respectively, but smaller than the 30% seen in **W530**. The birefringence response to an electric field of **W718** is shown in Figure 3.53. The birefringence vs. applied field response strongly resembles the tilt vs. applied field, as expected. The birefringence at T–T$_{A\text{-}C}$ = -5 K is 0.125, which represents a 29% increase from the SmA* phase. The field induced polarization in the SmA* at was measurable at 20 V μm^{-1} at temperatures as high as T-T$_{A\text{-}C}$ = 5 K. The polarization vs. applied field curve closely resembles both the electroclinic tilt and birefringence vs. applied field plots, as expected, and is shown in Figure 3.54. The maximum field-induced polarization is 205 nC cm^{-2}, which is approximately the same as **W314.** There is only 1 peak in the polarization reversal current, which is consistent with a weakly first order SmA* - SmC* phase transition. The P$_s$ of **W718** at T-T$_{A\text{-}C}$ = -5 K is 274 nC cm^{-2}, which is 7.8x larger than the polarization of **W699**, 10.5x larger than the polarization of **W735**, 3.6x larger than the polarization of **W715** and 2.6x larger than **W530**[7] at the same reduced temperature.

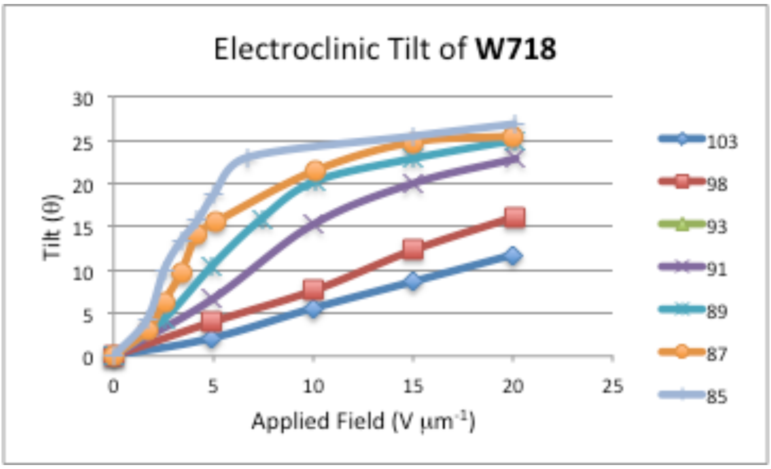

Figure 0.52 The electroclinic tilt of W718 as a function of applied field at various temperatures in the SmA* phase

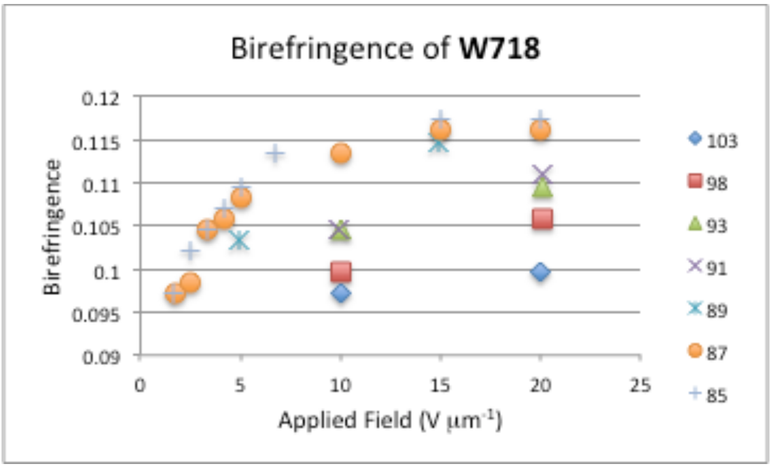

Figure 0.53 The birefringence (Δn) of W718 as a function of applied field at various temperatures in the SmA* phase.

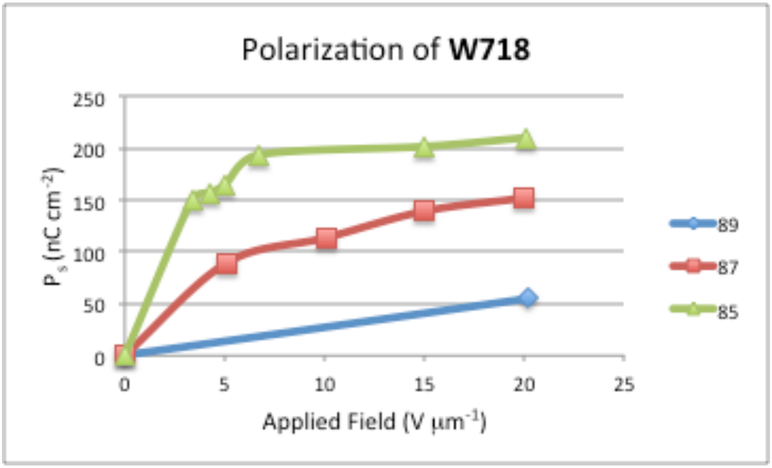

Figure 0.54 Field induced polarization of W718 at various temperatures

3.7 Trends

Having synthesized many derivatives built on the **Core B** scaffold and measured their physical and electrooptic properties the development of structure-property relationships for the design of new materials was performed. Not all measured properties showed significant differences, some important properties such as the clearing point, width of the SmA* phase, the saturated electroclinic tilt in the SmA* phase, the change in birefringence within the SmA* phase with an applied field as well as the change from the SmA* phase to the SmC* phase and the polarization in the SmC* phase showed strong structure-based differences. Specifically, the effect of the non-chiral tail and lateral polar group will be investigated.

3.7.1 Effect of Lateral Polar Group and Tail on the Clearing Point

The clearing point, which is the temperature at which the liquid crystal transitions to the isotropic liquid phase, depends on the size of the lateral polar group and the electronegativity. The clearing points, volume of lateral polar group and Hammett parameters (σ) for compounds built on the **Core B** scaffold are shown in Table 3.1. In the following sections the average was determined by either summing the values of materials with the same lateral polar group (e.g. **W697**, **W698** and **W699** for the lateral hydrogen group) or same tail (e.g. **W698**, **W734**, **W714**, **W657** and **W717** for the E-5-decenyloxy tail) and dividing by three or five, respectively. This method isolates the effect of the lateral polar group, as the tails are identical in all series, and the tails, as the cores are identical between the series. The series possessing the lateral hydrogen group (**W697/W698/W699**) shows the highest average clearing point of 143 °C. The hydrogen atom has the lowest volume[10] and fourth lowest σ.[11] The series possessing the lateral chloro group has the second highest average clearing point of 121 °C. The chloro group is the second smallest lateral group[10] and has the third highest σ.[11] If the effect were entirely steric the lateral methyl group should have the third highest average clearing point. The nitro group, however, which is larger than methyl by 6 cm^{-3} $mole^{-1}$,[10] has an average clearing point of 118 °C, which is ca. 8 K higher than the average of the lateral methyl group. This suggests a dipolar component in the clearing point. Finally, the series possessing the lateral trifluoromethyl group show the lowest average clearing point of 71 °C. The trifluoromethyl group is significantly larger than other lateral groups investigated and likely impacts the ability of cores to close-pack in layers. These results suggest that, unsurprisingly, either the size or polarity of the lateral polar group can be used to tune the clearing point to move mesogenic properties to a convenient temperature range.

The clearing point is strongly affected by the achiral tail. The semi-fluorinated tail shows the highest average clearing point of 141 °C. Semi-fluorinated tails are known to strongly promote mesogenicity and smectic phases.[12] The *E*-5-decenyloxy tail shows the lowest average clearing point of 83 °C. The shape anisotropy of the tail is likely the cause of the clearing point suppression. The *E*-5-decenyloxy tail, relative to the decyloxy, is significantly more kinked.[13] The larger volume of tail, in the absence of strongly nano-phase segregating moieties, such as fluorination on silanes, suppresses the close-packing of cores, which suppresses the clearing point. This is similar to the incorporation of branching in an n-alkoxy tail. A summary of the clearing point, van der Waals volume[10] and the Hammett substituent constant[11] for compounds built on the **Core B** scaffold is summarized in Table 3.1.

Lateral Group	Achiral Tail	Compound	SmA* - I (°C)	VDW Volume (cm^3 $mole^{-1}$)	σ
	alkyl	**W697**	142	7	0
Hydrogen	alkenyl	**W698**	115	7	0
	semi-fluoro	**W699**	172	7	0
	alkyl	**W733**	111	13.7	-0.17
Methyl	alkenyl	**W734**	78	13.7	-0.17
	semi-fluoro	**W735**	140	13.7	-0.17
	alkyl	**W713**	122	12	0.23
Chloro	alkenyl	**W714**	92	12	0.23
	semi-fluoro	**W715**	151	12	0.23
	alkyl	**W652**	79	42.6	0.54
Trifluoromethyl	alkenyl	**W657**	40	42.6	0.54
	semi-fluoro	**W530**	94	42.6	0.54
	alkyl	**W314**	115	18	0.78
Nitro	alkenyl	**W717**	91	18	0.78
	semi-fluoro	**W718**	148	18	0.78

Table 0.1 Summary of the clearing point, van der Waals volume and the Hammett substituent constant for compounds built on the Core B scaffold

3.7.2 Effect of Lateral Polar Group and Tail on the Width of the SmA Phase*

Like the clearing point, the width of the SmA* phase seems to depend on the size and dipole moment of the lateral polar group. The methyl group, which is the third largest lateral group[10] and has the smallest transverse dipole, [14] as suggested by the Boulder Model for prediction of spontaneous polarization in the SmC* phase,[15] shows the narrowest average SmA* phase, with an average width of 12 K. The hydrogen group is the smallest group[10] with the second smallest transverse dipole.[14] The average width of the SmA* phase of materials with a lateral hydrogen group is 14 K. The chloro group is the second smallest[10] and possesses the third highest transverse dipole.[14] The average width of the SmA* phase of LCs possessing a lateral chloro group is similar to the lateral hydrogen and methyl and is 18 K. LCs possessing the lateral nitro and trifluoromethyl group show significantly wider SmA* phases than the other analogues. The average width of the SmA* phase of LCs possessing the trifluoromethyl group is 34 K and the average width of the SmA* phase of the nitro possessing series is 35 K. The series possessing the nitro group has a significantly larger transverse dipole,[14] while the trifluoromethyl group is significantly larger than the nitro group. Based on the Glaser model, the de Vries SmA* phase is expected to form sub-optical domains of close-packed coherently tilted molecules with no azimuthal correlation between domains, while the SmC* phase shows close-packed coherently tilted molecules, suggesting that the average distance between cores is larger in the de Vries SmA* phase.[16] Since the trifluoromethyl group is particularly bulky, relative to the other groups investigated, it is likely that the SmA* phase broadens to suppress the SmC* phase, which would bring the cores closer together. The nitro group is not much larger than the methyl group, suggesting that there may be an electrostatic component which is responsible for the unusually broad SmA* phase.

The semi-fluorinated tail promotes the SmA* phase the best relative to the n-decyloxy and *E*-5-decenyloxy tails. The average width of the SmA* phase in analogues of **Core B** is 39 K. Semi-fluorinated tails are well known to promote smectic phases compared to hydrocarbon tails.[12] The decyloxy tail has an average SmA* width of 20 K, which is higher than the 8 K average of the E-5-decenyloxy tail. Since the E-5-decenyloxy tail shows de Vries properties and abnormally large polarizations, incorporation of alkene tails with the unsaturation at other positions should be explored (*vide infra*). A summary of the width of the SmA* phase in different compounds is shown in Table 3.2.

Lateral Group	Achiral Tail	Compound	Width of SmA* phase (K)
	alkyl	**W697**	19
Hydrogen	alkenyl	**W698**	5
	semi-fluoro	**W699**	18
	alkyl	**W733**	13
Methyl	alkenyl	**W734**	2
	semi-fluoro	**W735**	21
	alkyl	**W713**	17
Chloro	alkenyl	**W714**	6
	semi-fluoro	**W715**	31
	alkyl	**W652**	29
Trifluoromethyl	alkenyl	**W657**	12
	semi-fluoro	**W530**	60
	alkyl	**W314**	24
Nitro	alkenyl	**W717**	17
	semi-fluoro	**W718**	63

Table 0.2 Summary of the saturated tilt for compounds built on the Core B scaffold.

3.7.3 Effect of Lateral Polar Group and Tail on the Saturated Electroclinic Tilt

The saturated tilt in the SmA* phase seems to depend weakly on the size of the lateral polar group. The series with a lateral hydrogen possesses the smallest lateral group[10] and the lowest average saturated tilt in the SmA* phase, with an average of 21^{o}. The lateral methyl group has the next lowest average of 23^{o}. The average only incorporates two analogues (**W733** and **W735**). **W734**, which possesses the E-5-decenyloxy tail, is not included in the average since it shows reorientation with large electric fields and the saturated tilt could not be measured. The E-5-decenyloxy analogues show the highest saturated tilt suggesting that the average of the methyl group series is lower than the series with more polar groups (chloro, trifluoromethyl and nitro) since the saturated tilt of **W734** is not included. From the other series the average tilt of the methyl series can be extrapolated to ca. 25°. The chloro series has an average saturated tilt in the SmA* phase of 27°, which is approximately the same as the methyl series, which has a slightly larger lateral polar group. The nitro series has a saturated tilt of 26°. This is intermediate between the chloro and methyl series and the lateral polar group is slightly larger than methyl. The series with a lateral trifluoromethyl shows the largest saturated tilt of 31°. The trifluoromethyl group is much larger than the other lateral groups, which could be the origin of the larger saturated tilt.

The nature of the achiral tail shows a large effect on the saturated tilt of the SmA* phase of materials built on the **Core B** scaffold with varying lateral polar groups. The compounds with a decyloxy tail show the smallest average tilt of 22°. The *E*-5-decenyloxy series shows an average tilt of 28°. This value does not include the 7° saturated tilt observed in **W734**, since it shows realignment with larger applied fields and the saturated tilt could not be measured. The saturated tilt of LCs with a semi-fluorinated tail is 28°, like the alkenyl series. The core seems to be promoting the de Vries SmA* phase while the tail impacts the tilt. The decenyloxy and semi-fluorinated tails suppress out-of-layer fluctuations to a greater extent than the decyloxy tail. This means that the cores in the decenyloxy and demi-fluorinated LCs are closer together on the time average. The cores get closer together with increasing tilt, suggesting that the entropy lost to the suppression of out-of-layer fluctuations is offset by an enthalpic gain by the cores close packing. A summary of the saturated tilt of compounds built on the **Core B** scaffold is shown in Table 3.3.

Lateral Group	Achiral Tail	Compound	Saturated θ_{opt} SmA* (°)
Hydrogen	alkyl	**W697**	18
	alkenyl	**W698**	22
	semi-fluoro	**W699**	23
Methyl	alkyl	**W733**	18
	alkenyl	**W734**	7*
	semi-fluoro	**W735**	28
Chloro	alkyl	**W713**	23
	alkenyl	**W714**	29
	semi-fluoro	**W715**	27
Trifluoromethyl	alkyl	**W652**	27
	alkenyl	**W657**	33
	semi-fluoro	**W530**	33
Nitro	alkyl	**W314**	24
	alkenyl	**W717**	26
	semi-fluoro	**W718**	27

Table 0.3 The saturated tilt of compounds built on the Core B scaffold.

3.7.4 Summary of the Effect of Lateral Polar Group and Tail on the Birefringence

An increase in birefringence with an applied electric field is a characteristic of the de Vries SmA* phase. The birefringence of compounds built on the **Core B** scaffold was measured at low and high field to verify all compounds are de Vries SmA* LCs. A summary of the minimum and maximum birefringence near the SmA* - SmC* phase transition as well as the birefringence at T-T_{A-C} = 5 K for compounds built on the Core B scaffold is shown in Table 3.4. The birefringence at low field does not seem to be strongly influenced by the lateral polar group. The birefringence of the series with the lateral hydrogen group possesses the highest average birefringence of 0.130. The series with a lateral nitro, methyl and trifluoromethyl have approximately the same average birefringence, with values of 0.124, 0.120 and 0.122, respectively. The series with the lateral chloro group shows the smallest average birefringence of 0.116, which is not greatly different than the nitro, methyl and trifluoromethyl analogues, as the error in the birefringence is ca. 0.003.

Similarly, the average birefringence for all series in the SmC* phase is very similar, ranging from 0.142 to 0.153, with chloro being the lowest and trifluoromethyl the highest.

The birefringence seems to be strongly impacted by the nature of the achiral tail. The decyloxy tail shows the highest average birefringence (0.149) with weak electric fields. The *E*-5-decenyloxy tail shows intermediate average birefringence (0.126). This is likely a result of a larger X-Ray tilt than the decyloxy analogues, as birefringence decreases with increasing tilt up to 45° in de Vries SmA* LCs. This is supported by the birefringence of the decyloxy and *E*-5-decenyloxy series having nearly identical birefringence with large applied fields in the SmA* phase and in the SmC* phase. The semi-fluorinated series has the lowest average birefringence at both low and high applied electric fields. The tail should not contribute to the birefringence directly, since light interacts with electrons of the conjugated π system of the core significantly more than the tails. The largest difference between the semi-fluorinated series and the hydrocarbon analogues is the density of molecules. The semi-fluorinated tail has a larger cross section the than the hydrocarbon analogues (35-75% larger), which would lead to fewer molecules per unit area as the molecules will be further apart.[6] Since the saturated tilt of the decenyloxy and semi-fluorinated compounds are approximately equal, the lower areal density is likely the cause of the lower birefringence of the semi-fluorinated series.

All compounds show large changes in birefringence from the SmA* to the SmC* phase. This is characteristic of de Vries materials.

Lateral Group	Achiral Tail	Compound	Δn_{min} (SmA*)	Δn_{max} (SmA*)	Δn (SmC*)
Hydrogen	alkyl	**W697**	0.146	0.149	0.155
	alkenyl	**W698**	0.143	0.153	0.164
	semi-fluoro	**W699**	0.102	0.117	0.131
Methyl	alkyl	**W733**	0.147	0.152	0.158
	alkenyl	**W734**	0.122	0.122	0.162
	semi-fluoro	**W735**	0.091	0.108	0.136
Chloro	alkyl	**W713**	0.131	0.14	0.15
	alkenyl	**W714**	0.118	0.142	0.146
	semi-fluoro	**W715**	0.099	0.12	0.13
Trifluoromethyl	alkyl	**W652**	0.155	0.165	0.167
	alkenyl	**W657**	0.12	0.16	0.16
	semi-fluoro	**W530**	0.093	0.121	0.131
Nitro	alkyl	**W314**	0.145	0.155	0.162
	alkenyl	**W717**	0.129	0.148	0.154
	semi-fluoro	**W718**	0.097	0.117	0.125

Table 0.4 Summary of the minimum and maximum birefringence near the SmA* - SmC* phase transition as well as the birefringence at $T\text{-}T_{A\text{-}C}$ = 5 K for compounds built on the Core B scaffold.

3.7.5 Summary of the Effect of Lateral Polar Group and Tail on the Spontaneous Polarization

The magnitude of the spontaneous polarization in the SmC* phase at $T\text{-}T_{A\text{-}C}$ = 5 K increases with increasing transverse dipole. The polarization of compounds built on the **Core B** scaffold and the dipole of substituted benzene[14] are shown in Table 3.5. The lateral polar group with the lowest average spontaneous polarization is the methyl group. While the dipole is larger than benzene, the dipole points from the methyl to the benzene, which is in the opposite direction on the methylheptyloxy tail.[15] This means these two dipoles cancel and the net polarization is smaller than the series with lateral hydrogen groups. The average spontaneous polarization for the lateral methyl series is 40 nC cm^{-2}, while the series with the lateral hydrogen group has an average spontaneous polarization at $T\text{-}T_{A\text{-}C}$ = 5 K of 50 nC cm^{-2}. Chloro is the next most electronegative group (μ = 1.54 D),[14] suggesting that the polarization should be higher than the lateral hydrogen and methyl series. The average polarization of the lateral chloro series is 104 nC cm^{-2}, which is 2.6x larger than the lateral methyl series and 2.1x larger than the lateral hydrogen series. The trifluoromethyl series has the second highest average P_s at $T-T_{A-C}$ = 5 K of 130 nC cm^{-2}, and the second highest transverse dipole (μ = 2.86 D)[14]. Finally, the series with the lateral nitro group, which is the series with the largest transverse dipole (μ = 4.28 D)[14] shows the largest P_s at $T-T_{A-C}$ = 5 K, with an average polarization of 322 nC cm^{-2}.

Compounds with the same lateral polar group and a decyloxy tail or 7,7,8,8,9,9,10,10,10-nonafluorodecyloxy tail show approximately the same spontaneous polarization, with the fluorinated analogue showing a slightly lower polarization. This could be a result of the bulkier semi-fluorinated tail. The increased molecular volume reduced the number of molecules per unit area. Given the large difference in birefringence between the decyloxy series and semi-fluorinated series, which suggests a large density difference, there may also be a difference in rotational distribution of the transverse dipole. The *E*-5-decenyloxy tail shows a polarization that is 1.8x larger than the decyloxy and semi-fluorinated analogues, on average. The origin of this effect was discussed in Section 2.4.5.

Lateral Group	Achiral Tail	Compound	μ X-Ph (D)	P_s (T-T_{A-C} = 5 K)
	alkyl	**W697**		43
Hydrogen	alkenyl	**W698**	0	70
	semi-fluoro	**W699**		36
	alkyl	**W733**		31
Methyl	alkenyl	**W734**	0.31	62
	semi-fluoro	**W735**		27
	alkyl	**W713**		87
Chloro	alkenyl	**W714**	1.54	148
	semi-fluoro	**W715**		78
	alkyl	**W652**		94
Trifluoromethyl	alkenyl	**W657**	2.86	209
	semi-fluoro	**W530**		105
	alkyl	**W314**		269
Nitro	alkenyl	**W717**	4.28	420
	semi-fluoro	**W718**		277

Table 0.5 A summary of the dipole moment (D) of the benzene derivatives of the lateral polar group from compounds built on the Core B scaffold and the corresponding spontaneous polarization at T-T_{A-C} = 5 K.

3.8 New Materials to Supplement this Work

From the structure-property relationships developed in Section 3.7 some features for next-generation de Vries materials include: strongly electronegative lateral polar groups for large polarization (which is related to switching speed) and broader SmA* phases, as well as large lateral polar groups for lowering the clearing point, broadening the SmA* phase and increasing the saturated tilt. Since the trifluoromethyl group is particularly good at promoting these desirable properties, incorporation of a trifluorosilyl group is an excellent choice for new materials (**25**). While the VDW volume of the SiF_3 group could not be found in the literature, it is expected to be larger than the CF_3 group since silicon has a larger volume than carbon. The dipole of trifluorophenyl silane could not be found in the literature, however, the dipole moment of trifluoromethyl silane is 2.34 D,[14] which is approximately the same a s 1,1,1,-trifluoroethane, which has a dipole moment of 2.35 D.[14]

LCs built on the **Core B** scaffold with a lateral trifluorosilane group would be expected to show broad SmA* phases, lower clearing points, larger saturated tilt in the SmA* phase and approximately the same polarization as their trifluoromethyl analogues.

The LCD industry is moving away from esters and incorporating difluoroether linking-groups for improved hydrolytic stability. There is very little in the literature, outside of patents, about the effect of replacing ester groups with difluoroether moieties, so the effect of phase morphology is unknown at this time. It would be particularly interesting if incorporated into materials built on the **Core B** scaffold, replacing the ester linking group (**26**). This substitution is particularly interesting since it tests the dipolar hypothesis of the particularly strong core-core interactions of **Core B** (2.4.5). The 4-alkoxyphenylbenzoate shows a very large longitudinal dipole, which would be severely reduced by conversion of the ester to a difluoroether. This reduction in dipole reduces the core-core interactions and should suppress the de Vries SmA* phase.

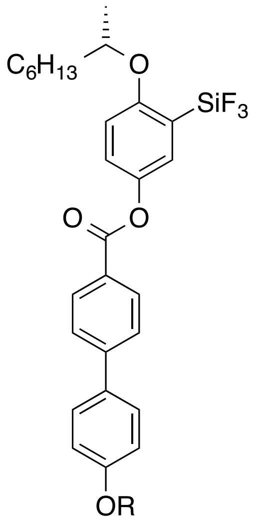

25

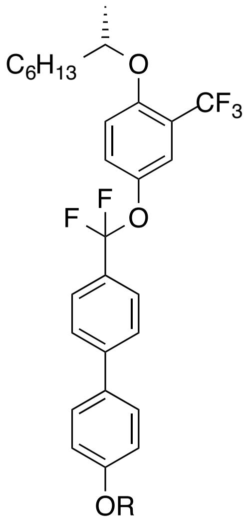

26

3.9 Synthesis

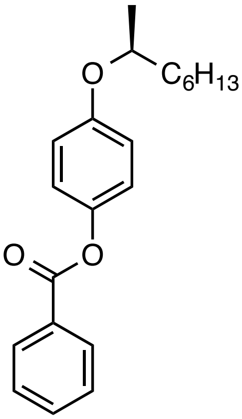

13

4-(1-(*S*)-methylheptyloxy) benzoate (**13**)

To a stirred solution of 4-Hydroxyphenyl benzoate (**12**) (2.54g, 1.19 mmol, 1eq), triphenyl phosphine (4.06, 15.5 mmol, 1.3 eq), (*R*)-2-octanol (2.07 mL, 13. mmol, 1.1 eq) at 5 °C under inert atmosphere was added diethyl azodicarboxylate (2.4 mL, 15.5 mmol, 1.3 eq) dropwise. The mixture was allowed to warm to room temperature slowly and stirred an additional 16 hours. The reaction mixture was dried in vacuo and isolated by column chromatography (10:1 hexanes : ethyl acetate) to afford 2.88 g of **13** as a clear liquid (8.8 mmol, 74%). ^{1}H NMR (300 MHz, Chloroform-*d*) δ 8.27 - 8.16 (m, 2H), 7.70 - 7.45 (m, 3H), 7.19 - 7.06 (m, 2H), 6.93 (dd, *J* = 8.9, 2.0 Hz, 2H), 4.43 - 4.23 (m, 1H), 1.84 - 1.22 (m, 13H), 1.00 - 0.85 (m, 3H). ^{13}C NMR (75 MHz, $CDCl_3$) δ 165.63, 156.10, 144.28, 133.96, 133.70, 133.57, 130.23, 129.80, 128.90, 128.80, 128.63, 128.54, 122.50, 116.64, 74.61, 36.61, 31.93, 29.40, 25.66, 22.73, 19.86, 14.21, 14.19.

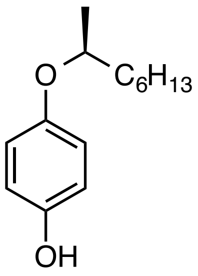

14

<u>4-(1-(*S*)methylheptyloxy) phenol (**14**)</u>

To a round-bottomed-flask charged with a stir bar was added 4-((*S*)-2-octyloxy)phenyl benzoate (2.88g, 8.8 mmol, 1 eq), NaOH (1.06 g, 24.5 mmol, 3 eq), 150 mL EtOH and 100 mL H_2O. The flask was fixed with a condenser and the reaction mixture was heated to reflux overnight. The mixture was then cooled to room temperature and conc. HCl was added dropwise until the mixture was ca. pH 1. The volume was reduced by about half and extracted with diethyl ether (3 x 50 mL). The product was isolated by column chromatography (5:1 hexanes : ethyl acetate) to afford 1.63g (7.90 mmol, 88%) of **14** as a colourless liquid. ^{1}H NMR (300 MHz, Chloroform-*d*) δ 6.85 - 6.69 (m, 4H), 5.47 (s, 1H), 4.29 - 4.12 (m, 1H), 1.81 - 1.62 (m, 1H), 1.61 - 1.19 (m, 11H), 0.97 - 0.82 (m, 3H). ^{13}C NMR (75 MHz, $CDCl_3$) δ 152.03, 149.67, 117.88, 116.11, 75.64, 36.51, 31.82, 29.31, 25.58, 22.61, 19.81, 14.09.

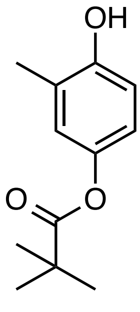

16

4-hydroxy-3-methylphenyl 2, 2-dimethylpropanoate (**16**)

To a stirred solution of methylhydroquinone (3g, 24.2 mmol, 1 eq) in 75 mL anhydrous CH2Cl2 at ca. 5 °C under inert atmosphere was added pivalic anhydride (4.5g, 24.2 mmol, 1eq) in 25 mL of anhydrous toluene. The reaction mixture was allowed to warm to room temperature slowly and stirred an additional 16 hours at which point the solvent was removed in vacuo and the product was isolated by column chromatography (4:1 hexanes : EtOAc) to afford 2.03g (9.75 mmol) as a colourless solid. . ^{1}H NMR (300 MHz, Chloroform-*d*) - 6.83 (dt, *J* = 2.2, 0.8 Hz, 1H), 6.77 - 6.75 (m, 2H), 4.63 (s, 1H), 2.25 (d, *J* = 0.7 Hz, 3H), 1.36 (s, 9H). ^{13}C NMR (75 MHz, $CDCl_3$) - 178.07, 151.55, 144.37, 125.14, 123.69, 119.66, 115.53, 39.15, 27.31, 15.99.

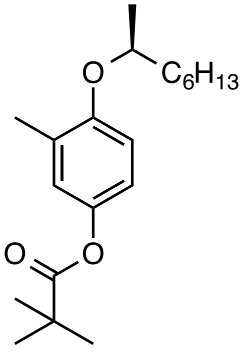

17

4-(1-(S)-methylheptyloxy)-3-methylphenyl 2, 2-dimethylpropanoate (**17**)

To a stirred solution of pivilate protected (2.03g, 9.75 mmol, 1 eq), triphenyl phosphine (3.33g, 12.7 mmol, 1.3 eq), (*R*)-2-octanol (2.0 mL, 12.7 mmol, 1.3 eq) at 5 °C under inert atmosphere was added diethyl azodicarboxylate (3.33 mL, 12.7 mmol, 1.3 eq) dropwise. The mixture was allowed to warm to room temperature slowly and stirred an additional 16 hours. The reaction mixture was dried in vacuo and isolated by column chromatography (12:1 hexanes : ethyl acetate) to afford 2.67 g of a clear liquid (8.3 mmol, 85%). ^{1}H NMR (300 MHz, Chloroform-*d*) - 6.88 - 6.72 (m, 3H), 4.37 - 4.20 (m, 1H), 2.24 - 2.14 (m, 3H), 1.78 - 1.22 (m, 22H), 0.94 - 0.83 (m, 3H). ^{13}C NMR (75 MHz, $CDCl_3$) - 177.73, 154.01, 143.98, 129.12, 123.65, 118.99, 113.37, 74.70, 39.11, 36.75, 31.96, 29.47, 27.32, 25.66, 22.75, 19.99, 14.23.

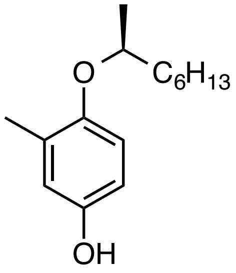

18

4-(1-(S)-methylheptyloxy)-3-methyl phenol (**18**)

To a round-bottomed-flask charged with a stir bar was added methyl (2.67g, 8.33 mmol, 1 eq), NaOH (1.00 g, 25.0 mmol, 3 eq), 50 mL EtOH and 50 mL H2O. The flask was fixed with a condenser and the reaction mixture was heated to reflux overnight. The mixture was then cooled to room temperature and conc. HCl was added dropwise until the mixture was ca. pH 1. The volume was reduced by about half and extracted with diethyl ether (3 x 50 mL). The product was isolated by column chromatography (5:1 hexames : ethyl acetate) to afford 1.72g (7.24 mmol, 87%) as a colourless liquid. ^{1}H NMR (300 MHz, Chloroform-*d*) - 6.73 (d, *J* = 8.6 Hz, 1H), 6.67 - 6.55 (m, 2H), 4.19 (h, *J* = 6.0 Hz, 1H), 2.18 (s, 3H), 1.84 - 1.66 (m, 1H), 1.66 - 1.22 (m, 10H), 0.99 - 0.84 (m, 3H). ^{13}C NMR (75 MHz, $CDCl_3$) - 150.33, 149.33, 129.89, 118.00, 115.98, 112.93, 75.96, 36.75, 31.95, 29.48, 25.67, 22.73, 19.99, 16.63, 14.20.

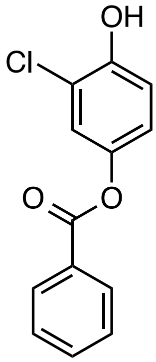

19

4-hydroxy-3-chlorophenyl benzoate (**19**)

To a stirred solution of 4-hydroxyphenylbenzoate (3.00 g, 14.0 mmol, 1.0 eq) in acetonitrile (100 mL) at -20 ºC under inert atmosphere was added a catalytic amount of anhydrous p-toluenesulfonic acid (ca. 10 drops). After stirring for 5 minutes N-chlorosuccinamide (2.00 g, 14.7 mmol, 1.1 eq) was added portionwise over two hours. The reaction was allowed to continue an additional 2 hours at which point it was quenched with saturated sodium bisulfite. The reaction mixture was extracted from diethyl ether (3x 50) and the combined organics were washed with brine and dried over sodium sulfate. The product was isolated by flash chromatography (1:1 hexanes : methylene chloride) to afford 1.6 g (6.43 mmol, 46%) of a colourless solid. ^{1}H NMR (300 MHz, Chloroform-*d*) - 8.24 - 8.13 (m, 2H), 7.71 - 7.59 (m, 1H), 7.52 (ddt, *J* = 8.2, 6.7, 1.1 Hz, 2H), 7.25 (t, *J* = 1.5 Hz, 1H), 7.05 (d, *J* = 1.5 Hz, 2H), 5.59 (s, 1H). ^{13}C NMR (75 MHz, $CDCl_3$) - 165.42, 149.55, 144.15, 133.93, 130.32, 129.27, 128.77, 122.53, 121.94, 119.99, 116.57.

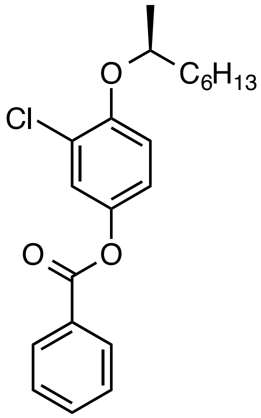

20

*4-(1-(S)-methylheptyloxy-3-chlorophenyl benzoate (**20**)*

To a stirred solution of 3-chloro-4-Hydroxyphenyl benzoate (1.35 g, 5.43 mmol, 1.0 eq), triphenyl phosphine (2.14 g, 8.15 mmol, 1.5 eq), (*R*)-2-octanol (0.843 g, 6.57 mmol, 1.2 eq) at 5 ºC under inert atmosphere in a sonicating bath was added diethyl azodicarboxylate (1.3 mL, 8.15 mmol, 1.5 eq) dropwise. The mixture was subjected to sonics for additional 2 hours. The reaction mixture was dried in vacuo and isolated by column chromatography (8:1 hexanes : ethyl acetate) to afford 1.51 g of a clear liquid (4.18 mmol, 77%). ^{1}H NMR (300 MHz, Chloroform-*d*) - 8.24 - 8.14 (m, 2H), 7.71 - 7.58 (m, 1H), 7.52 (ddt, *J* = 8.3, 6.9, 1.2 Hz, 2H), 7.28 (d, *J* = 2.8 Hz, 1H), 7.07 (dd, *J* = 8.9, 2.8 Hz, 1H), 6.96 (d, *J* = 9.0 Hz, 1H), 4.45 - 4.28 (m, 1H), 1.91 - 1.73 (m, 1H), 1.73 - 1.22 (m, 12H), 0.99 - 0.80 (m, 3H). ^{13}C NMR (75 MHz, $CDCl_3$) - 165.30, 152.05, 144.15, 133.81, 130.27, 129.37, 128.71, 124.59, 123.89, 120.72, 115.95, 76.67, 36.53, 31.91, 29.38, 25.52, 22.72, 19.86, 14.21.

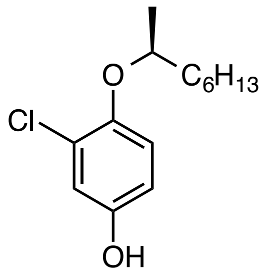

21

4-(1-(S)-methylheptyloxy-3-chloro phenol (**21**)

To a round-bottomed-flask charged with a stir bar was added chloro (1.5gg, 4.17 mmol, 1.0 eq), NaOH (0.500 g , 12.5 mmol, 3 eq), 40 mL ^{i}PrOH and 10 mL H_2O. The flask was fixed with a condenser and the reaction mixture was heated to reflux overnight. The mixture was then cooled to room temperature and conc. HCl was added dropwise until the mixture was ca. pH 1. The volume was reduced by about half and extracted with diethyl ether (3 x 50 mL). The product was isolated by column chromatography (5:1 hexames : ethyl acetate) to afford 0.974 g (3.79 mmol, 91%) as a colourless liquid. ^{1}H NMR (300 MHz, Chloroform-*d*) - 6.92 - 6.77 (m, 2H), 6.66 (dd, *J* = 8.8, 3.0 Hz, 1H), 5.64 (s, 1H), 4.30 - 4.12 (m, 1H), 1.86 - 1.68 (m, 1H), 1.58 (ddt, *J* = 13.1, 8.9, 5.8 Hz, 1H), 1.49 - 1.19 (m, 12H), 0.97 - 0.82 (m, 3H). ^{13}C NMR (75 MHz, $CDCl_3$) - 150.30, 147.89, 125.68, 119.26, 117.55, 114.55, 78.15, 36.51, 31.90, 29.41, 25.53, 22.71, 19.84, 14.19.

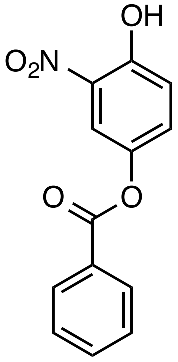

22

<u>*4-hydroxy-3-nitrophenyl benzoate* (**22**)</u>

To a stirred solution of sodium nirtrite (1.2g, 14.0 mmol, 1 eq) in 25 mL of H_2O at ca. 5 ºC was added 15 mL of conc. $HCl_{(aq)}$ dropwise. After 5 minutes 4-hydroxyphenylbenzoate (3.00 g, 14.0 mmol, 1.0 eq) in diethyl ether (100 mL) was added dropwise followed by ca. 10 drops of acetic anhydride. The mixture was stirred an additional 16 hours and the organic layer was isolated. The product was isolated by column chromatography (5:1 hexanes : EtOAc) to afford 3.15g (12.2 mmol, 87%) as a yellow solid. ^{1}H NMR (300 MHz, Chloroform-*d*) - 10.52 (d, *J* = 0.4 Hz, 1H), 8.27 - 8.13 (m, 2H), 8.01 (dd, *J* = 2.8, 0.4 Hz, 1H), 7.74 - 7.60 (m, 1H), 7.60 - 7.42 (m, 3H), 7.33 - 7.18 (m, 1H).

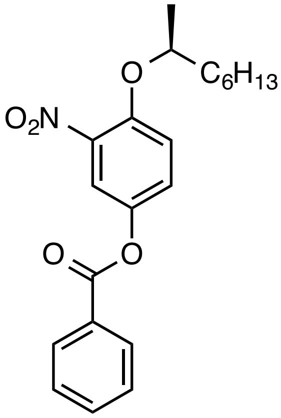

23

4-(1-(S)-methylheptyloxy)-3-nitrophenyl benzoate (**23**)

To a stirred solution of 3-nitro-4-hydroxyphenyl benzoate (1.50 g, 5.79 mmol, 1.0 eq), triphenyl phosphine (2.27 g, 8.69 mmol, 1.5 eq), (*R*)-2-octanol (0.904 g, 6.94 mmol, 1.2 eq) at 5 °C under inert atmosphere in a sonicating bath was added diethyl azodicarboxylate (1.3 mL, 8.15 mmol, 1.5 eq) dropwise. The mixture was subjected to sonics for additional 2 hours. The reaction mixture was dried in vacuo and isolated by column chromatography (8:1 hexanes : ethyl acetate) to afford 1.61 g of a yellow liquid (4.34 mmol, 75%). ^{1}H NMR (300 MHz, Chloroform-*d*) - 8.26 - 8.12 (m, 2H), 7.76 - 7.58 (m, 2H), 7.58 - 7.45 (m, 2H), 7.39 (dd, *J* = 9.1, 2.9 Hz, 1H), 7.11 (d, *J* = 9.2 Hz, 1H), 4.50 (h, *J* = 6.1 Hz, 1H), 1.90 - 1.19 (m, 13H), 0.98 - 0.82 (m, 3H). ^{13}C NMR (75 MHz, $CDCl_3$) - 164.97, 149.59, 142.87, 140.49, 134.07, 130.27, 130.24, 128.83, 128.76, 128.68, 127.31, 122.70, 119.15, 116.55, 77.04, 36.30, 31.79, 29.24, 25.30, 22.65, 19.59, 14.14.

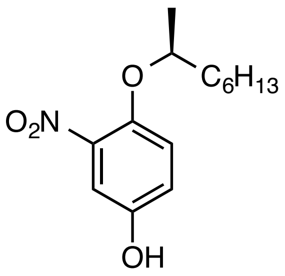

24

4-(1-(S)-methylheptyloxy)-3-nitro phenol (**24**)

To a round-bottomed-flask charged with a stir bar was added nitro (1.60 g, 4.31 mmol, 1.0 eq), NaOH (0.500 g , 12.5 mmol, 2.9 eq), 40 mL ^{i}PrOH and 10 mL H_2O. The flask was fixed with a condenser and the reaction mixture was heated to reflux overnight. The mixture was then cooled to room temperature and conc. HCl was added dropwise until the mixture was ca. pH 1. The volume was reduced by about half and extracted with diethyl ether (3 x 50 mL). The product was isolated by column chromatography (5:1 hexames : ethyl acetate) to afford 1.02 g (3.82 mmol, 88%) as a yellow liquid. ^{1}H NMR (300 MHz, Chloroform-*d*) - 7.32 (d, *J* = 3.0 Hz, 1H), 7.11 - 6.91 (m, 2H), 6.22 - 6.12 (m, 1H), 4.35 (h, *J* = 6.1 Hz, 1H), 1.83 - 1.48 (m, 2H), 1.49 - 1.15 (m, 10H), 0.93 - 0.78 (m, 3H). ^{13}C NMR (75 MHz, $CDCl_3$) - 149.12, 145.84, 140.90, 121.86, 118.69, 112.16, 77.84, 36.32, 31.80, 29.27, 25.34, 22.64, 19.62, 14.12.

Esters were formed using Steglich coupling. A general procedure follows:

To a round bottomed flask charged with a stirbar was added the appropriate carboxylic acid, alcohols and dimethylamino pyridine (amounts vary, see specific reactions) were taken up in ca. 30 mL of CH_2Cl_2. The reaction mixture was put under intert atmosphere at which point EDC was added in a single portion (amounts vary, see specific reactions). The mixture was stirred overnight. The products were isolated by flash chromatography (8:1 hexanes:EtOAc) to afford colourless solids.

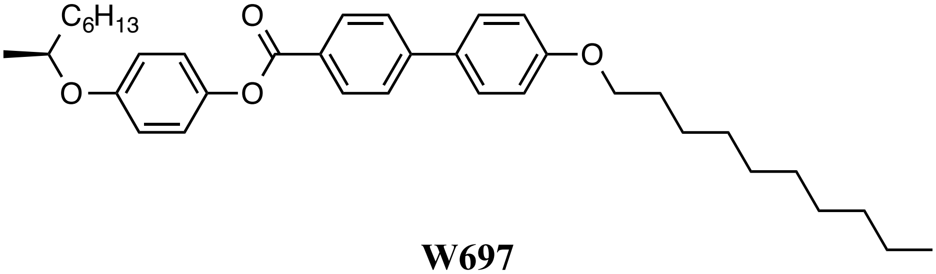

W697

*4-(1-(S)-methylheptyloxy) 4-(4-decyloxyphenyl) benzoate* (**W697**)

4-((*S*)-2-octyloxy)phenol (0.456, 2.21 mmol, 1.1 eq), 4-(4-decyloxyphenyl)benzoic acid (0.713g, 2.01 mmol, 1.0 eq), EDCI 0.677 g, 3.02 mmol, 1.5 eq), EDCI (0.368 g, 3.02 mmol, 1.5 eq). Yield: .916 g (84%). ^{1}H NMR (300 MHz, Chloroform-*d*) - 8.28 - 8.17 (m, 1H), 7.74 - 7.54 (m, 2H), 7.18 - 7.06 (m, 1H), 7.06 - 6.86 (m, 2H), 4.02 (t, *J* = 6.5 Hz, 1H), 1.90 - 1.66 (m, 2H), 1.66 - 1.21 (m, 14H), 0.95 - 0.83 (m, 3H). ^{13}C NMR (75 MHz, CDCl$_3$) - 165.67, 159.70, 156.10, 146.00, 144.38, 132.15, 130.81, 128.52, 127.77, 126.70, 122.58, 116.70, 115.12, 74.69, 68.31, 36.65, 32.05, 31.97, 29.74, 29.72, 29.55, 29.48, 29.44, 29.40, 26.20, 25.70, 22.84, 22.76, 19.90, 14.28, 14.24. HRMS (ESI+) calc'd for $C_{37}H_{50}LiO_4$: 581.3602; found: 581.3588.

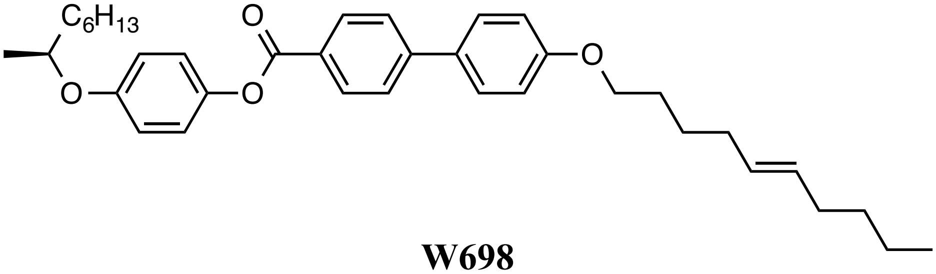

W698

4-(1-(S)-methylheptyloxy) 4-(4-E-5-decenyloxyphenyl) benzoate (**W698**)

4-((*S*)-2-octyloxy)phenol (0.450, 2.18 mmol, 1.2 eq), 4-(4-*E*-dec-5-enyloxyphenyl)benzoic acid (0.640g, 1.82 mmol, 1.0 eq), EDCI 0.453 g, 2.37 mmol, 1.3 eq), EDCI (0.290 g, 2.37 mmol, 1.3 eq). Yield: .845 g (86%). ^{1}H NMR (300 MHz, Chloroform-*d*) - 8.28 - 8.17 (m, 1H), 7.74 - 7.54 (m, 2H), 7.18 - 7.06 (m, 1H), 7.06 - 6.86 (m, 2H), 5.43 (qd, *J* = 3.6, 1.8 Hz, 1H), 4.02 (t, *J* = 6.5 Hz, 1H), 2.21 - 1.93 (m, 2H), 1.90 - 1.67 (m, 2H), 1.66 - 1.45 (m, 2H), 1.45 - 1.21 (m, 7H), 0.98 - 0.84 (m, 3H). ^{13}C NMR (75 MHz, $CDCl_3$) - 165.67, 159.66, 156.10, 145.99, 144.37, 132.17, 131.20, 130.81, 129.77, 128.52, 127.78, 126.70, 122.58, 116.70, 115.11, 74.69, 68.15, 36.65, 32.43, 32.40, 31.97, 31.94, 29.44, 28.84, 26.14, 25.71, 22.77, 22.36, 19.90, 14.25, 14.12. HRMS (ESI+) calc'd for $C_{37}H_{48}LiO_4$: 563.3713; found: 563.3702.

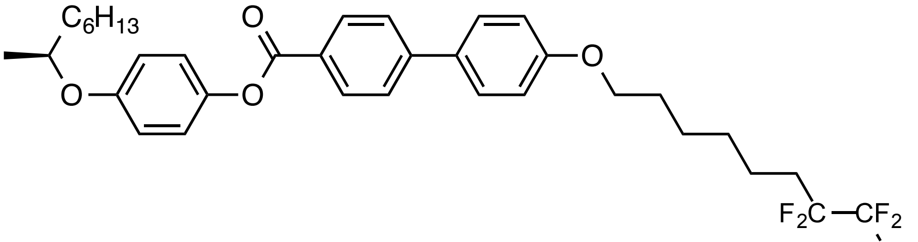

W699

4-(1-(S)-methylheptyloxy) 4-(4-7,7,8,8,9,9,10,10,10-nonafluorodecyloxyphenyl) benzoate (**W699**)

4-((*S*)-2-octyloxy)phenol (0.2.13, 0.95 mmol, 1.1 eq), 4-(4-7,7,8,8,9,9,10,10,10-nonafluorodecylocyphenyl)benzoic acid (0.450g, 0.87 mmol, 1.0 eq), EDCI 0.221 g, 1.13 mmol, 1.3 eq), EDCI (0.140 g, 1.13 mmol, 1.3 eq). Yield: .540 g (88%). ^{1}H NMR (300 MHz, Chloroform-*d*) δ 8.29 - 8.18 (m, 2H), 7.77 - 7.48 (m, 4H), 7.24 - 7.07 (m, 2H), 7.06 - 6.87 (m, 4H), 4.42 - 4.18 (m, 1H), 4.03 (t, *J* = 6.3 Hz, 2H), 2.21 - 1.97 (m, 2H), 1.93 - 1.21 (m, 18H), 0.90 (m, 6H). ^{13}C NMR (75 MHz, $CDCl_3$) δ 165.65, 159.55, 156.11, 145.94, 144.38, 132.32, 131.02, 130.81, 128.94, 128.55, 127.84, 126.71, 122.57, 116.71, 115.08, 74.69, 68.30, 67.95, 38.88, 36.66, 31.97, 31.16, 30.87, 30.51, 29.44, 29.15, 29.08, 29.00, 25.93, 25.70, 23.89, 23.14, 22.76, 20.22, 20.17, 19.90, 14.24, 14.20, 11.11. HRMS (ESI+) calc'd for $C_{37}H_{41}F_9LiO_4$: 727.3021; found: 727.3013.

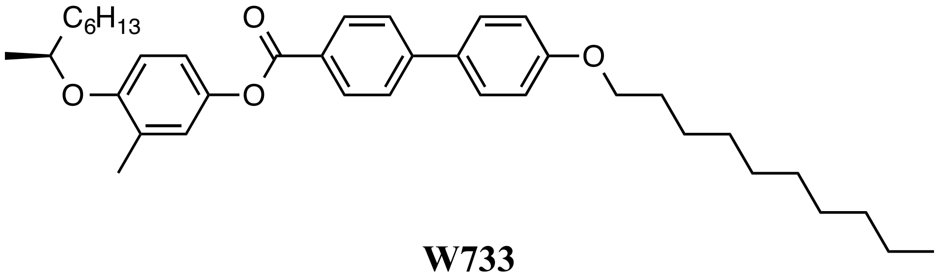

W733

4-(1-(S)-methylheptyloxy)-3-methyl 4-(4-decyloxyphenyl) benzoate (**W733**)

3-methyl-4-((*S*)-2-octyloxy)phenol (0.400, 1.69 mmol, 1.0 eq), 4-(4-decyloxyphenyl)benzoic acid (0.719 g, 2.03 mmol, 1.2 eq), EDCI 0.485 g, 2.54 mmol, 1.5 eq), EDCI (0.310 g, 2.54 mmol, 1.5 eq). Yield: .903 g (93%). ^{1}H NMR (300 MHz, Chloroform-*d*) - 8.28 - 8.17 (m, 2H), 7.74 - 7.54 (m, 4H), 7.07 - 6.93 (m, 4H), 6.84 (d, *J* = 8.6 Hz, 1H), 4.33 (h, *J* = 6.0 Hz, 1H), 4.02 (t, *J* = 6.5 Hz, 2H), 2.24 (s, 3H), 1.90 - 1.69 (m, 3H), 1.65 - 1.22 (m, 26H), 0.96 - 0.84 (m, 6H). ^{13}C NMR (75 MHz, $CDCl_3$) - 165.78, 159.67, 154.24, 145.91, 143.85, 132.16, 130.77, 129.21, 128.49, 127.88, 126.66, 123.91, 119.29, 115.10, 113.32, 74.67, 68.29, 36.78, 32.05, 31.98, 29.74, 29.71, 29.55, 29.48, 29.40, 26.20, 25.69, 22.83, 22.76, 20.03, 16.73, 14.27, 14.24. HRMS (ESI+) calc'd for $C_{38}H_{52}LiO_4$: 579.4026; found: 579.4005.

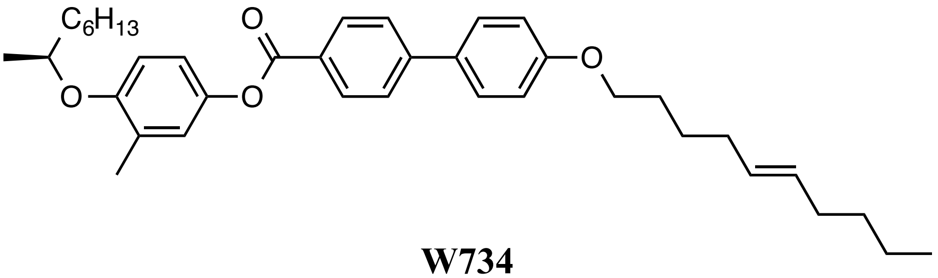

W734

4-(1-(S)-methylheptyloxy)-3-methyl 4-(4-E-5-decenyloxyphenyl) benzoate (**W734**)

3-methyl-4-((*S*)-2-octyloxy)phenol (0.400, 1.69 mmol, 1.0 eq), 4-(4-*E*-dec-5-enyloxyphenyl)benzoic acid (0.715 g, 2.03 mmol, 1.2 eq), EDCI 0.485 g, 2.54 mmol, 1.5 eq), EDCI (0.310 g, 2.54 mmol, 1.5 eq). Yield: 0.933 g (97%). ^{1}H NMR (300 MHz, Chloroform-*d*) - 8.30 - 8.19 (m, 2H), 7.75 - 7.56 (m, 4H), 7.08 - 6.94 (m, 4H), 6.86 (d, *J* = 8.6 Hz, 1H), 5.46 (qd, *J* = 3.5, 1.8 Hz, 2H), 4.35 (h, *J* = 6.1 Hz, 1H), 4.04 (t, *J* = 6.5 Hz, 2H), 2.25 (t, *J* = 0.6 Hz, 3H), 2.17 - 1.95 (m, 4H), 1.93 - 1.70 (m, 3H), 1.70 - 1.23 (m, 18H), 0.99 - 0.86 (m, 6H). ^{13}C NMR (75 MHz, $CDCl_3$) - 165.80, 159.64, 154.25, 145.92, 143.85, 132.20, 131.19, 130.78, 129.77, 129.22, 128.51, 127.90, 126.67, 123.91, 119.29, 115.10, 113.33, 74.68, 68.15, 36.78, 32.43, 32.40, 31.98, 31.93, 29.48, 28.84, 26.14, 25.69, 22.76, 22.36, 20.04, 16.73, 14.24, 14.12. HRMS (ESI+) calc'd for $C_{38}H_{50}LiO_4$: 577.3869; found: 577.3865.

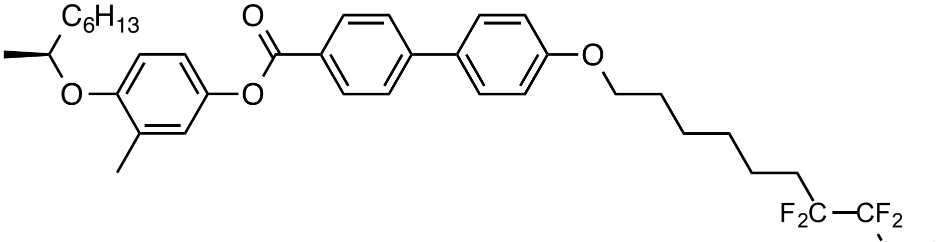

W735

4-(1-(S)-methylheptyloxy)-3-methyl 4-(4-7,7,8,8,9,9,10,10,10-nonafluorodecyloxyphenyl) benzoate (**W735**)

3-methyl-4-((*S*)-2-octyloxy)phenol (0.2.13, 0.95 mmol, 1.1 eq), 4-(4-7,7,8,8,9,9,10,10,10-nonafluorodecylocyphenyl)benzoic acid (0.450g, 0.87 mmol, 1.0 eq), EDCI 0.221 g, 1.13 mmol, 1.3 eq), EDCI (0.140 g, 1.13 mmol, 1.3 eq). Yield: .540 g (88%). ^{1}H NMR (300 MHz, Chloroform-*d*) - 8.28 - 8.17 (m, 2H), 7.73 - 7.54 (m, 4H), 7.06 - 6.92 (m, 4H), 6.84 (d, *J* = 8.7 Hz, 1H), 4.33 (h, *J* = 5.9 Hz, 1H), 4.03 (t, *J* = 6.3 Hz, 2H), 2.28 - 1.96 (m, 5H), 1.92 - 1.23 (m, 19H), 0.95 - 0.84 (m, 3H). ^{13}C NMR (75 MHz, $CDCl_3$) - 165.79, 159.53, 154.27, 145.87, 143.85, 132.36, 130.80, 129.24, 128.55, 127.96, 126.69, 123.91, 119.29, 115.08, 113.34, 74.70, 67.96, 36.79, 31.98, 30.87, 29.49, 29.15, 29.00, 25.93, 25.69, 22.77, 20.23, 20.04, 16.73, 14.24. HRMS (ESI+) calc'd for $C_{38}H_{43}F_9LiO_4$: 741.3178; found: 741.3179.

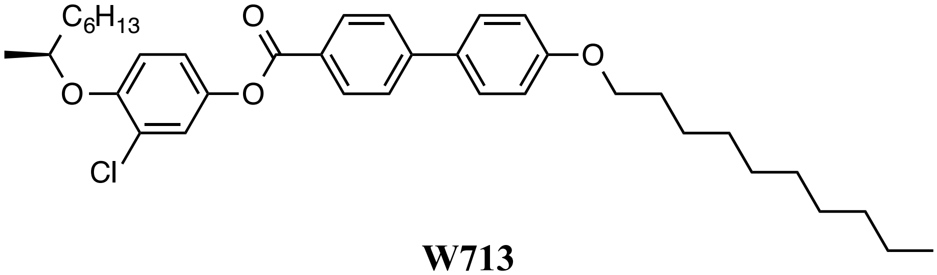

W713

4-(1-(S)-methylheptyloxy)-3-chloro 4-(4-decyloxyphenyl) benzoate **(W713)**

3-chloro-4-((*S*)-2-octyloxy)phenol (0.362, 1.41 mmol, 1.0 eq), 4-(4-decyloxyphenyl)benzoic acid (0.500 g, 1.41 mmol, 1.0 eq), EDCI 0.350 g, 1.83 mmol, 1.3 eq), EDCI (0.225 g, 1.83 mmol, 1.3 eq). Yield: 0.790 g (94%). ^{1}H NMR (300 MHz, Chloroform-*d*) - 8.27 - 8.16 (m, 2H), 7.77 - 7.54 (m, 4H), 7.29 (d, *J* = 2.7 Hz, 1H), 7.15 - 6.92 (m, 4H), 4.37 (h, *J* = 6.1 Hz, 1H), 4.02 (t, *J* = 6.6 Hz, 2H), 1.81 (tdd, *J* = 9.7, 7.2, 4.8 Hz, 3H), 1.72 - 1.54 (m, 1H), 1.52 - 1.22 (m, 24H), 0.96 - 0.84 (m, 6H). ^{13}C NMR (75 MHz, $CDCl_3$) - 165.28, 159.74, 152.02, 146.21, 144.25, 132.00, 130.83, 128.50, 127.29, 126.71, 124.61, 123.95, 120.78, 115.99, 115.11, 76.71, 68.29, 36.56, 32.04, 31.93, 29.73, 29.71, 29.55, 29.47, 29.41, 29.39, 26.19, 25.55, 22.83, 22.75, 19.89, 14.27, 14.23. HRMS (ESI+) calc'd for $C_{37}H_{49}ClLiO_4$: 599.3479; found: 599.3470.

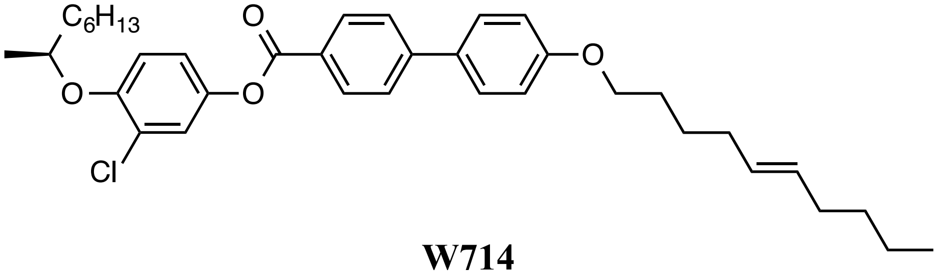

W714

4-(1-(S)-methylheptyloxy)-3-chloro 4-(4-E-5-decenyloxyphenyl) benzoate **(W714)**

3-chloro-4-((*S*)-2-octyloxy)phenol (0.364, 1.42 mmol, 1.0 eq), 4-(4-*E*-dec-5-enyloxyphenyl)benzoic acid (0.500 g, 1.41 mmol, 1.0 eq), EDCI 0.353 g, 1.84 mmol, 1.3 eq), EDCI (0.225 g, 1.84 mmol, 1.3 eq). Yield: 0.360 g (43%). ^{1}H NMR (300 MHz, Chloroform-*d*) - 8.28 - 8.17 (m, 2H), 7.79 - 7.56 (m, 4H), 7.31 (d, *J* = 2.8 Hz, 1H), 7.15 - 6.94 (m, 4H), 5.46 (qd, *J* = 3.6, 1.9 Hz, 2H), 4.39 (h, *J* = 6.1 Hz, 1H), 4.04 (t, *J* = 6.5 Hz, 2H), 2.17 - 1.95 (m, 3H), 1.84 (dddd, *J* = 13.5, 9.9, 6.2, 4.6 Hz, 3H), 1.74 - 1.22 (m, 16H), 1.02 - 0.82 (m, 6H). ^{13}C NMR (75 MHz, $CDCl_3$) - 165.30, 159.71, 152.04, 146.22, 144.25, 132.05, 131.19, 130.85, 129.76, 128.52, 127.31, 126.74, 124.62, 123.96, 120.79, 116.01, 115.12, 76.73, 68.15, 36.56, 32.42, 32.39, 31.93, 29.41, 28.83, 26.13, 25.56, 22.75, 22.35, 19.90, 14.24, 14.12, 14.12. HRMS (ESI+) calc'd for $C_{37}H_{49}ClLiO_4$: 596.3314; found: 596.3293.

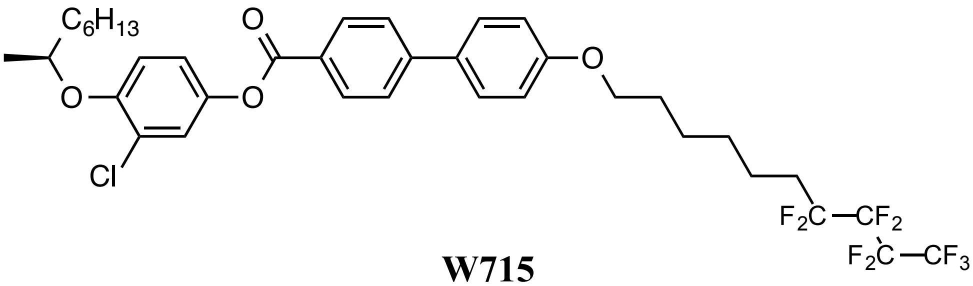

W715

4-(1-(S)-methylheptyloxy)-3-chloro 4-(4-7,7,8,8,9,9,10,10,10-nonafluorodecyloxyphenyl) benzoate (**W715**)

3-chloro-4-((*S*)-2-octyloxy)phenol (0.298, 1.16 mmol, 1.0 eq), 4-(4-7,7,8,8,9,9,10,10,10-nonafluorodecylocyphenyl)benzoic acid (0.600 g, 1.16 mmol, 1.0 eq), EDCI 0.298 g, 1.51 mmol, 1.3 eq), EDCI (0.185 g, 1.51 mmol, 1.3 eq). Yield: .630 g (72%). ^{1}H NMR (300 MHz, Chloroform-*d*) - 8.27 - 8.16 (m, 2H), 7.74 - 7.54 (m, 4H), 7.29 (d, *J* = 2.8 Hz, 1H), 7.13 - 6.92 (m, 4H), 4.37 (h, *J* = 6.1 Hz, 1H), 4.03 (t, *J* = 6.3 Hz, 2H), 2.22 - 1.96 (m, 2H), 1.93 - 1.21 (m, 21H), 0.95 - 0.84 (m, 3H). ^{13}C NMR (75 MHz, $CDCl_3$) - 165.30, 159.61, 152.05, 146.17, 144.25, 132.20, 130.86, 128.56, 127.37, 126.76, 124.63, 123.97, 120.79, 116.01, 115.09, 76.74, 67.95, 36.57, 31.94, 31.14, 30.86, 30.85, 30.56, 29.42, 29.14, 28.99, 25.93, 25.56, 22.75, 20.22, 20.16, 19.90, 14.23.

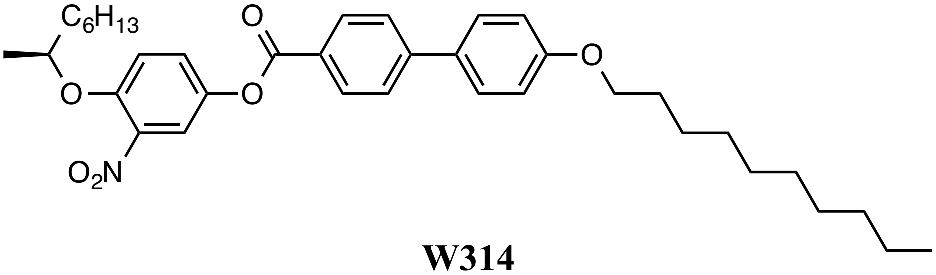

W314

4-(1-(S)-methylheptyloxy)-3-nitro 4-(4-decyloxyphenyl) benzoate (**W314**)

3-nitro-4-((*S*)-2-octyloxy)phenol (0.411, 1.54 mmol, 1.0 eq), 4-(4-decyloxyphenyl)benzoic acid (0.600 g, 1.69 mmol, 1.2 eq), EDCI (0.383 g, 2.0 mmol, 1.5 eq), DMAP (0.100 g, 0.77 mmol, 0.5 eq). Yield: 0.830 g (89%). ^{1}H NMR (300 MHz, Chloroform-*d*) - 8.27 - 8.15 (m, 2H), 7.77 - 7.54 (m, 5H), 7.40 (dd, *J* = 9.1, 2.9 Hz, 1H), 7.11 (d, *J* = 9.2 Hz, 1H), 7.04 - 6.96 (m, 2H), 4.50 (h, *J* = 6.1 Hz, 1H), 4.02 (t, *J* = 6.5 Hz, 2H), 1.81 (dtt, *J* = 13.2, 6.3, 3.4 Hz, 3H), 1.74 - 1.21 (m, 26H), 0.95 - 0.83 (m, 6H). ^{13}C NMR (75 MHz, $CDCl_3$) - 165.04, 159.82, 149.65, 146.53, 143.01, 140.60, 131.89, 130.92, 128.54, 127.42, 126.81, 126.77, 119.29, 116.60, 115.15, 77.14, 68.31, 36.38, 32.05, 31.87, 29.74, 29.71, 29.55, 29.47, 29.39, 29.32, 26.19, 25.40, 22.84, 22.73, 19.69, 14.27, 14.22. HRMS (ESI+) calc'd for $C_{37}H_{49}LiNO_6$: 610.3720; found: 610.3709.

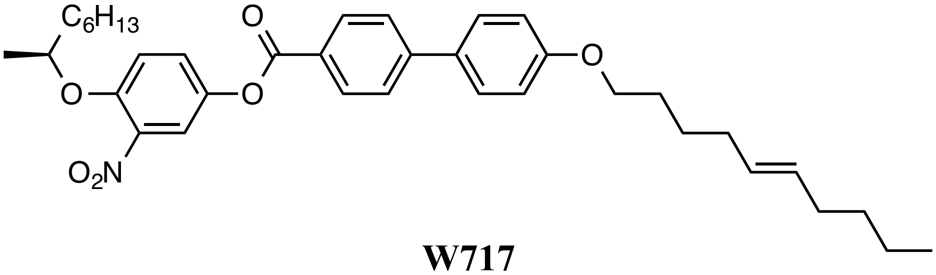

W717

4-(1-(S)-methylheptyloxy)-3-nitro 4-(4-E-5-decenyloxyphenyl) benzoate (**W717**)

3-nitro-4-((*S*)-1-methylheptyloxy)phenol (0.415, 1.55 mmol, 1.0 eq), 4-(4-*E*-dec-5-enyloxyphenyl)benzoic acid (0.600 g, 1.68 mmol, 1.2 eq), EDCI (0.383 g, 2.0 mmol, 1.5 eq), DMAP (0.100 g, 0.77 mmol, 0.5 eq). Yield: 0.805 g (85%). ^{1}H NMR (300 MHz, Chloroform-*d*) - 8.26 - 8.16 (m, 2H), 7.77 - 7.54 (m, 5H), 7.40 (dd, *J* = 9.1, 2.9 Hz, 1H), 7.11 (d, *J* = 9.2 Hz, 1H), 7.04 - 6.96 (m, 2H), 5.43 (qd, *J* = 3.6, 1.9 Hz, 2H), 4.50 (h, *J* = 6.1 Hz, 1H), 4.02 (t, *J* = 6.5 Hz, 2H), 2.15 - 1.93 (m, 4H), 1.91 - 1.73 (m, 3H), 1.74 - 1.21 (m, 17H), 0.97 - 0.83 (m, 6H).^{13}C NMR (75 MHz, $CDCl_3$) - 165.03, 159.79, 149.65, 146.52, 143.01, 140.60, 131.91, 131.20, 130.92, 129.75, 128.54, 127.42, 126.81, 119.29, 116.60, 115.14, 77.13, 68.15, 36.38, 32.42, 32.39, 31.92, 31.87, 29.32, 28.82, 26.13, 25.39, 22.72, 22.35, 19.68, 14.22, 14.12. HRMS (ESI+) calc'd for $C_{37}H_{47}LiNO_6$: 608.3563; found: 610.3556.

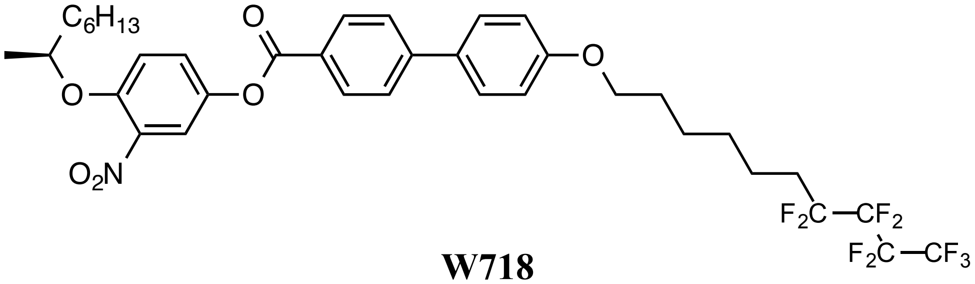

W718

4-(1-(S)-methylheptyloxy)-3-nitro 4-(4-7,7,8,8,9,9,10,10,10-nonafluorodecyloxyphenyl) benzoate (**W718**)

3-nitro-4-((*S*)-2-octyloxy)phenol (0.330, 1.23 mmol, 1.1 eq), 4-(4-7,7,8,8,9,9,10,10,10-nonafluorodecylocyphenyl)benzoic acid (0.550 g, 1.07 mmol, 1.0 eq), EDCI 0.290 g, 1.50 mmol, 1.5 eq), DMAP (0.071 g, 0.58 mmol, 0.5 eq). Yield: .708 g (86%). ^{1}H NMR (300 MHz, Chloroform-*d*) - 8.27 - 8.16 (m, 2H), 7.78 - 7.55 (m, 5H), 7.40 (dd, *J* = 9.1, 2.9 Hz, 1H), 7.11 (d, *J* = 9.2 Hz, 1H), 7.04 - 6.96 (m, 2H), 4.50 (h, *J* = 6.1 Hz, 1H), 4.03 (t, *J* = 6.3 Hz, 2H), 2.21 - 1.96 (m, 2H), 1.93 - 1.23 (m, 21H), 0.95 - 0.83 (m, 3H). ^{13}C NMR (75 MHz, $CDCl_3$) - 165.03, 159.68, 149.67, 146.48, 143.01, 140.61, 132.07, 130.93, 128.58, 127.42, 126.83, 119.30, 116.61, 115.12, 77.16, 67.97, 36.39, 31.88, 31.16, 30.86, 30.57, 29.33, 29.14, 29.00, 25.93, 25.41, 22.74, 20.23, 20.17, 19.69, 14.22. HRMS (ESI+) calc'd for $C_{37}H_{40}F_9LiNO_6$: 772.2872; found: 772.2879.

3.10 References

1. Walba, D. M.; Eshdat, L.; Korblova, E.; Shao, R. and Clark, N. A. *Angew. Chem. Int. Ed.* **2007**, 46, 1473.

2. Mitsunobu, O. *Synthesis* **1981**, 1.

3. Neises, B.; Steglich, W. *Angew. Chem. Int. Ed.* **1978**, *17*, 522

4. Keller, P. *Bull. Soc. Chim. Fr.* **1994**, *131*, 27.

5. Onishi, H.; Kamimura, T.; Sakurai, T. and Higuchi, R. *Jpn. Kokai Tokkyo Koho* **1998**, JP 63037192 A 19880217.

6. Rieker, T. P. and Janulus, E. P. *Phys. Rev. E.* **1995**, *52*, 2688.

7. a) L. Wang et al., in Proceedings of the 26th Display Research Conference of the Society for Information Display, Kent, USA (Society for Information Display, CA, USA, 2006), p. 189. b) Shen, Y.; Wang, L,; Shao, R.; Gong, T.; Zhu, C.; Yang, H.; Maclennan, J. E.;Walba, D. M. and Clark, N. A. *Phys. Rev. E* **2013**, *88*, 062504.

8. Walba, D. M.; Ros, M. B.; Clark, N. A.; Shao, R.; Robinson, M. G.; Liu, J. Y.; Johnson, K. M. and Doroski, D. *J. Am. Chem. Soc.* **1991**, *113*, 5471.

9. a) Walba, D. M.; Ros, M. B.; Sierra, T.; Rego, J. A.; Clark, N. A.; Shao, R.; Wand, M. D.; Vohra, R. T.; Arnett, K. E. and Velsco, S. P. *Ferroelectrics* **1991**, *121*, 247. b) Kapernaum, N.; Walba, D. M.; Korblova, E.; Zhu, C.; Jones, C.; Shen, Y.; Clark, N. A. and Giesselmann, F. *ChemPhysChem* **2009**, *10*, 890.

10. Bondi., A. *J. Phys. Chem.* **1964**, *68*, 441.

11. Hansch, C.; Leo, A.; Taft, R. W. *Chem. Rev.* **1991**, *91*, 165

12. Tschierske, C. *J. Mater. Chem.* **1998**, *8*, 1485.

13. Santismo, E. E. (**2007**) *Effects of Confinement on Chemical Reactions*, ProQuest

14. Weast, R. C., ed. (**1981**). *CRC Handbook of Chemistry and Physics* (62nd ed.). Boca Raton, FL: CRC Press.

15. Wand, M. D.; Vohra, R. T.; Walba, D. M.; Clark, N. A. and Shao, R. *Mol. Cryst. Liq. Cryst.* **1991**, *202*, 183.

16. Kost-Smith, Z. V.; Beale, P. D.; Clark, N. A. and Glaser, M. A. *Phys. Rev. E* **2013**, *87*, 050502(R).

Bibliography

Andersson, G.; Dahl, I.; Komitov, L.; Laggerwall, S. T.; Skarp, K. and Stebler. B. *J. Appl. Phys.* **1989**, *66*, 4983.

Bartolino, R.; Doucet, J.and Durand, G. *Ann. Phys. (Paris)*, **1978**, *3*, 389.

Bondi., A. *J. Phys. Chem.* **1964**, *68*, 441.

Clark, N. A.; Bellini, T.; Shao, R.; Coleman, D.; Bardon, S. Link, D. R.; Maclennan, J. E.; Chen, X. Wand, M. D.; Walba, D. M.; Rudquist, P. and Lagerwall, S. T. *Appl. Phys. Lett.* **2002**, *80*, 4097.

Clark, N. A. and Lagerwall, S. *Appl. Phys. Lett.* **1980**, *36*, 899.

Collings, P. J. Liquid Crystals: Nature's Delicate Phase of Matter; Princeton University Press: Princeton, **1990**.

Davidson, M. W. *http://micro.magnet.fsu.edu/primer/techniques/polarized/berekcompensator.html.*

Demus, D.; Goodby, J.; Gray, G. W.; Spiess, H.-W. and Vill, V. (**1998**). Handbook of Liquid Crystals. Weinheim: Wiley VCH.

de Vries, A. *Mol. Cryst. Liq. Cryst. Lett.* **1977**, *41*, 27.

Garoff, S. and Meyer, R. *Physical Review Letters* **1977**, *38*, 848.

Glaser, M. and Clark, N. A. *Phys. Rev. E.*, **2002**, *66*, 021711.

Gorkunov, M. V.; Giesselmann, Lagerwall, J. P. F.; Sluckin, T. J. and Osipov, M. A. *Phys. Rev. E* **2007**, *75*, 060701(R).

Gorkunov, M. V.; Osipov, M. A.; Lagerwall, J. P. F. and Giesselmann, F. Phys. Rev. E **2007**, *76*, 051706.

Hansch, C.; Leo, A.; Taft, R. W. *Chem. Rev.* **1991**, *91*, 165.

Hori, K. and Endo, K. *Bull. Chem. Soc. Japan*, **1993**, *66*, 46.

Hori, K.; Kawahara, S. and Ito, K. *Ferroelectrics*, **1993**, *147*, 91.

Inui, S.; Iimura, N.; Suzuki, T.; Iwane, H.; Miyachi, K.; Takanishi, Y. and Fukuda, A. *J. Mater. Chem.* **1996**, *6*, 671.

Inukai, T.; Saitoh, S.; Inoue, H.; Miyazawa, K.; Terashima, K. and Furukawa, K. *Mol. Cryst. Liq. Cryst.* **1986**, *141*, 251.

Kapernaum, N.; Walba, D. M.; Korblova, E.; Zhu, C.; Jones, C.; Shen, Y.; Clark, N. A. and Giesselmann, F. *ChemPhysChem* **2009**, *10*, 890.

Keller, P. *Bull. Soc. Chim. Fr.* **1994**, *131*, 27.

Kost-Smith, Z. V.; Beale, P. D.; Clark, N. A. and Glaser, M. A. *Phys. Rev. E* **2013**, *87*, 050502(R).

Li, L.; Jones, C. D.; Magolan, J. and Lemieux, R. P. *J. Mater. Chem.* **2007**, *17*, 2313.

Meyer, R. B. ; Liebert, L.; Strzelecki, L. and Keller, P. *J. Phys. (France)*, **1975**, *36*, L-69.

Mitsunobu, O. *Synthesis* **1981**, 1.

Miyaura, N.; Yamada, K. and Suzuki, A. *Tetrahedron Letters* **1979**, *20*, 3437.

Murphy, D. B.; Spring, K. R.; Fellers, T. J.; Davidson, M. W. *http://www.microscopyu.com/articles/polarized/birefringenceintro.html.*

Neises, B.; Steglich, W. *Angew. Chem. Int. Ed.* **1978**, *17*, 522.

Onishi, H.; Kamimura, T.; Sakurai, T. and Higuchi, R. *Jpn. Kokai Tokkyo Koho* **1998**, JP 63037192 A 19880217.

Particle Sciences – Technical Briefs, **2012**, Vol. 04.

Prasad, S. K.; Rao, D. S. S.; Sridevi, S.; Lobo, C. V.; Ranta, B. R.; Naciri, J. and Shashidhar, R. *Phys. Rev. Lett.* **2009**, *102*, 147802.

Rappaport, A. G.; Williams, P. A.; Thomas, B. N.; Clark, N. A.; Ros, M. B. and Walba, D. M. *Appl. Phys. Lett.* **1995**, *67*, 362.

Rieker, T. P. and Janulus, E. P. *Phys. Rev. E.* **1995**, *52*, 2688.

Rupar, I.; Mulligan, K. M.; Roberts, J. C.; Nonnenmacher, D.; Giesselmann, F. and Lemieux, R. P. *J. Mater. Chem. C* **2013**, *1*, 3729.

Santismo, E. E. (**2007**) *Effects of Confinement on Chemical Reactions*, ProQuest.

Schubert, C. P. J.; Bogner, A; Porada, J. H.; Ayub, K.; Andrea, T.; Giesselmann, F. and Lemieux, R. P. *J. Mater. Chem. C*, **2014**, *2*, 4581.

Shao, R.; Maclennan, J. E.; Clark, N. A.; Dyer, D. J. and Walba, D. M. *Liquid Crystals* **2001**, *28*, 117.

Shen, Y.; Wang, L,; Shao, R.; Gong, T.; Zhu, C.; Yang, H.; Maclennan, J. E.;Walba, D. M. and Clark, N. A. *Phys. Rev. E* **2013**, *88*, 062504.

Stegemeyer; H.; Meister, R.; Hoffmann, U.; Sprick, A. and Becker, A. *J. Mater. Chem.* **1995**, *5*, 2183.

Tschierske, C. *J. Mater. Chem.* **1998**, *8*, 1485.

Walba, D. M.; Eshdat, L.; Korblova, E.; Shao, R. and Clark, N. A. *Angew. Chem. Int. Ed.* **2007**, 46, 1473.

Walba, D. M.; Korblova, E.; Eshdat, L.; Biewer, M. C.; Yang, H.; Jones, C.; Nakata, M.; Talarico, M.; Shao, R. and Clark, N. A. *Journal of the SID*, **2007**, 15/8, 1.

Walba, D. M.; Ros, M. B.; Clark, N. A.; Shao, R.; Robinson, M. G.; Liu, J. Y.; Johnson, K. M. and Doroski, D. *J. Am. Chem. Soc.* **1991**, *113*, 5471.

Walba, D. M.; Ros, M. B.; Sierra, T.; Rego, J. A.; Clark, N. A.; Shao, R.; Wand, M. D.; Vohra, R. T.; Arnett, K. E. and Velsco, S. P. *Ferroelectrics* **1991**, *121*, 247.

Wand, M. D.; Vohra, R. T.; Walba, D. M.; Clark, N. A. and Shao, R. *Mol. Cryst. Liq. Cryst.* **1991**, *202*, 183.

Wang, L. *et al.*, in Proceedings of the 26th Display Research Conference of the Society for Information Display, Kent, USA (Society for Information Display, CA, USA, 2006), p. 189.

Weast, R. C., ed. (**1981**). *CRC Handbook of Chemistry and Physics* (62nd ed.). Boca Raton, FL: CRC Press.

Williams, P. A.; Komitov, L.; Rappaport, A. G.; Thomas, B. N.; Clark, N. A.; Walba, D. M. and Day, G. W. *Liq. Cryst.* **1993**, *14*, 1095.

Yang, H.; Wang, L.; Shao, R.; Clark, N. A.; Ortega, J.; Etxebarria, J.; Albouy, P.-A.; Walba, D. M. and Keller, P. *J. Mater. Chem.* **2009**, *19*, 7208.